STATISTICAL HADRONIZATION AND MULTI PARTICLE PRODUCTION IN HIGH ENERGY INTERACTIONS

A THESIS

Submitted to the
FACULTY OF SCIENCES
PANJAB UNIVERSITY, CHANDIGARH
for the degree of

DOCTOR OF PHILOSOPHY

2018

SANDEEP SHARMA

DEPARTMENT OF PHYSICS
CENTRE OF ADVANCED STUDY IN PHYSICS
PANJAB UNIVERSITY
CHANDIGARH, INDIA

DEPARTMENT OF PHYSICS
Centre of Advanced Study in Physics
PANJAB UNIVERSITY, CHANDIGARH-160 014 (INDIA)
Fax: ++91-172-2783336
Phone: ++91-172-2541741
EPABX: ++91-172-2534466, 2534446
Email: casphypu.ac.in

CORRECTION CERTIFICATE

It is certified that there were no specific corrections recommended by the examiner of **Mr. Sandeep Sharma** in his Ph.D. thesis **"Statistical Hadronization and Multi Particle Production in High Energy Interactions".** The thesis submitted by **Mr. Sandeep Sharma** in the present form, is acceptable.

(Prof. Navdeep Goyal)
Dept. of Physics,
P.U., Chandigarh
(Chairperson)

(Prof. Shakeel Ahmed)
Department of Physics
AMU, Aligarh
(External Examiner)

(Prof. Manjit Kaur)
Department of Physics
P.U., Chandigarh
(Supervisor)

Chairperson
Department of Physics
Panjab University
Chandigarh-160014

PANJAB UNIVERSITY CHANDIGARH
STUDENT APPROVAL FORM FOR ELECTRONIC THESIS SUBMISSION

Thesis Title	STATISTICAL HADRONIZATION AND MULTI PARTICLE PRODUCTION IN HIGH ENERGY INTERACTIONS
Name of the Research Scholar	SANDEEP SHARMA
Supervisor / Co-Supervisors	PROF. MANJIT KAUR
Department/Centre	DEPARTMENT OF PHYSICS

STUDENT AGREEMENT

1. I represent that my thesis is my original work. Proper attribution has been given to all outside sources. I understand that I am solely responsible for obtaining any needed copyright permissions. I have obtained needed written permission statements(s) from the owner(s) of each third-party copyrighted matter to be included in my work, allowing electronic distribution (if such use is not permitted by the fair use doctrine) which will be submitted to Panjab University Chandigarh.
2. I hereby grant to the university and its agents the irrevocable, non-exclusive, and royalty-free license to archive and make accessible my work in whole or in part in all forms of media, now or hereafter known. I agree that the document mentioned above may be made available for worldwide access.

REVIEW, APPROVAL AND ACCEPTANCE

The thesis mentioned above has been reviewed and accepted by the student`s advisor, on behalf of the program; I/We verify that this is the final, approved version of the student's thesis including all changes required.

It is certified that electronic copy of thesis is the same as submitted in print form and as per the Shodhganga format.

EMBARGO AGREEMENT (OPTIONAL)

Kindly tick the appropriate option:

☐ No Embargo requested

☐ Embargo request for 6 months

☐ Embargo request for 1 Year

☐ Embargo request for 2 Year

Please specify the reasons for Embargo:

- The student is applying for a patent on an invention or procedure documented in the thesis and does not wish to make the contents public until the patent application has been filed.
- The thesis contains sensitive and/or classified information
- Immediate release of the thesis may impact an existing or potential publishing agreement.
- If any other, please specify:-

____

____

__Note:__ Research scholars are requested to please fill this form and get it signed from their supervisor/co-supervisors and HOD with proper stamp/seal and save the scanned copy of same in the CD (thesis).

Sandeep Sharma
Signature of the Research Scholar

M Kaur
Supervisor
Name: (MANJIT KAUR)

Co-Supervisor
Name:

Co-Supervisor
Name:

Navdeep
Chairperson
Department of Physics
Panjab University
Chandigarh-160014
Head of the Department

Acknowledgements

This thesis would not have been possible without generous assistance and support of many people so I take this occasion to express my heartfelt gratitude to all those who helped me in different ways in the completion of my Ph.D. thesis.

First of all, I pay my regards to the Almighty for giving me blessings, love and enough courage to handle different phases in my life.

I heartily pay my regards to my supervisor Prof. Manjit Kaur for her immense contribution, significant direction, commitment, inspiration, ceaseless help and blessings. Words are less to thank her for the care and motherly love she gave me during the course of Ph.D. Her kindness, dedication towards every task, punctuality and management skills still inspire me. Whenever I felt stressed during the course, she was always there to inspire and motivate me. Her encouragement, guidance and support helped me in all the time of research and writing of this thesis.

It is my pleasure to acknowledge the assistance and help of Dr. Virginia Azzolini, due to whose outstanding commitment, I could attain so much knowledge in the task of Data Certification at the CMS. It was a great experience working with her. She always answered all kinds of questions and remained cooperative in every situation. Her enthusiasm, leadership and commitment to the CMS deeply inspired me.

I am thankful to the present and former Chairpersons, Department of Physics, Panjab University for providing me with adequate facilities to work in the department. The research work has been supported by Department of Science and Technology (DST). I am highly thankful to the organization for their continued support. I

am very grateful to Prof. Vipin Bhatnagar, Prof. J.B.Singh, Prof. Suman Beri and CMS Office staff of PU-EHEP group for their cooperation throughout my research work. I am thankful to India-CMS Collaboration for conducting the regular meetings and discussions which helped alot in my research work.

I would like to thank all my colleagues in PU-EHEP lab, Aayushi, Anterpreet, Amandeep, Aman, Ankita, Geetanjali, Genius, Harjot, Jyoti, Kuldeep, Manisha, Priyanka, Rajat, Ridhi, Sandeep Hundal, Sandeep Kaur, Sonia and Sunil who were always there for helping me out from all kinds of problems with their suggestions and discussions and creating enjoyable environment in the lab. I appreciate the help and support of my friends and well wishers Anjali, Aviraj, Bharti, Neha, Dr. Bikram, Harkawal, Harpreet, Richa, Mahak, Kavita, Swati, Shailza, Shaurya Nath, Shagun and Jagbir. They all helped me in some direct or indirect way during the course.

I feel much indebted to my friends Amrinder Partap Singh, Sudesh Thakur and Shivani for their encouragement, care, understanding and precious friendship. They have borne all my dissapointments and frustrations but have always been with me during the ups and downs in my life. I am thankful to my friends for their wonderful support in my life and hope it will always continue in this way. Their valuable and fruit-ful suggestions kept me on right track in these years. It is very hard to find friends like them and no words can acknowledge their support.

All of my work would have been impossible without the patience and incredible support of my family. I am indebted to my parents Mr. Gian Chand and Mrs. Saroj for their unconditional love, understanding, blessings, in believing and supporting me in every situation. They have made countless sacrifices in their life for me. My father was always the first with whom I shared all my worries and tensions during the course. The prayers and blessings of my mother gave me strength to accomplish this task smoothly. I would also like to acknowledge my sister Disha, my brother-in-law Amit for the encouragement and constant support. A special acknowledgement goes to my niece, Prisha Kaushik. Her activities were stress buster for me during the thesis writing time.

I would like to thank and pay my regards to Late Dr. Kuldeep Kumar for his phenomenal contribution in my academics. The way he taught the complex equations of 'Quantum Mechanics' is simply incredible. His hard work and dedication was truly inspiring.

Finally, I would like to thank everyone who was important to the successful realization of the thesis, as well as express my apology that I could not mention personally one by one.

Date: (Sandeep Sharma)

Abstract

The particle collisions at very high centre of mass energies are the finest tools to understand underlying dynamics of multiparticle production in such collisions. Various high energy accelerators have been built to collide particles such as hadrons, leptons and heavy ions to study the fundamental physics and the particles produced in these collisions are recorded in the particle detectors to extract the information about their charges, momenta and energies. The number of particles produced in the final state after the interaction is termed as particle multiplicity and the distribution of these final states particles produced is known as multiplicity distribution (MD). Study of charged particle multiplicity distributions provides an understanding of the particle production mechanism, as the particles produced in these interactions follow certain production rules and conservation laws. Various theoretical and phenomenological models based on hydrodynamics, thermodynamics and statistics have been successfully used in describing the distributions of these final state particles. The data from collider experiments recorded by any detector has to pass through several stages of filtering, before the final set of data meaningful for the physics analysis is obtained. Various stages involve triggering, monitoring, certifications and validations, phase space checks and finally kinematical cuts for the specific analysis.

In this thesis study of multiparticle production and analysis of charged particle multiplicity distributions, correlations amongst the particles produced and dependence of mean multiplicity on the centre of mass energy is presented. For the hadronic analysis, data from proton-proton collisions collected with the CMS detector at centre of mass energies, $\sqrt{s}$ = 0.9, 2.36 and 7 TeV, antiproton-proton data from the UA5 detector at $\sqrt{s}$ = 200, 540 and 900 GeV and the leptonic collisions taken from the L3 and the OPAL experiments at LEP at $\sqrt{s}$ = 91 to 206 GeV energies are studied. Results from the various models like the Negative Binomial Distribution, NBD, Gamma, Shifted Gamma, the Weibull and the Tsallis gas model are compared with the experimental data. Detailed analysis shows that the Tsallis model is the most successful in describing the experimental data for all types of

interactions, from the lower to the higher energies. Most of the results from this work are published in various international journals.

Contents

List of Figures

List of Tables

Chapter 1

Introduction

The word “science” has originated from the Latin word “scientia” which means “knowledge” in English. Science is a way to answer all the fundamental questions regarding natural phenomena occurring around us in our day-to-day life. It covers multiple fields of study. Particle physics is one amongst the important fields of science which provides us information about the fundamental particles of the Universe. Particle physics is one of the branches of science which aims at understanding the basic constituents of matter and the forces which govern the interactions between them. The Standard Model of particle physics is the framework which describes properties of the fundamental particles and their interactions. The fundamental particles consist of fermions (leptons and quarks) and the gauge bosons. The gauge bosons are the mediators of the four fundamental forces of interaction that exist in nature. These four forces are the gravitational force, the electromagnetic force, the weak force and the strong force. The Standard Model explains the electromagnetic, weak and strong interactions with the help of these gauge bosons. The Standard Model consists of 13 gauge bosons which include eight gluons, W^+, W^- and Z boson, the photon and the Higgs boson. Quantum Electrodynamics (QED) is the theory of electromagnetic force and explains the interaction between light and matter. QED is associated with the charged elementary particles like electrons and positrons and shows that the interaction between these particles is mediated by the massless photon. On other hand, theory of the strong interactions is described by the Quantum Chromodynamics (QCD) which explains how the interaction between the quarks is mediated by the massless gluons. The quarks and gluons carry ‘colour charge’. Due to colour confinement property of the QCD, which states “All the natural existing particles are colourless in nature”, the quarks can not exist freely in nature but bind themselves into the colourless particles called hadrons like protons, neutrons, pions etc. To study the structure and properties of these sub-atomic particles they need to be probed, explored and investigated at the level of nuclear distance which is typically of order $\sim 1\ fm$. This can be done by accelerating the particles using particle accelerators and then colliding them at very high energies. The final products of these collisions are recorded in the particle detectors which are then analyzed carefully to obtain the important information about the structure and properties of these fundamental particles.

High energy particle accelerators are usually used as the particle colliders to obtain the information about structure of matter and kinds of interactions involving high momentum transfers. During the last three decades various particle colliders like the Large Electron Positron collider (LEP) at CERN in Geneva, HERA at DESY in Germany, the KEKB at KEK in Japan, the RHIC at Brookhaven National Laboratory in USA, the Tevatron at Fermi National Accelerator Laboratory and the Large Hadron Collider (LHC) at CERN, Geneva have played significant role in major discoveries in the field of particle physics. In 1954 European Organization for Nuclear Research (CERN) was established in Geneva to provide particle physics laboratory to study the nuclei and the interaction between elementary particles at high energies. The W^+, W^- and Z bosons were discovered in UA1 and UA5 experiments in CERN’s Super proton antiproton collider (SPS) with $\sqrt{s} = 540$ GeV. The Large Electron Positron collider (LEP) at CERN measured the properties of these bosons precisely. At present, network of six accelerators and a decelerator are operated by CERN which are involved in the operation of Large Hadron Collider, a successor of the LEP. The Large Hadron Collider at CERN is the biggest and the most powerful particle collider of present time where protons are accelerated and collided at enormously high energies to probe the internal structure of protons. Since protons are not elementary particles, these are made up of quarks, so these proton collisions are viewed as interaction between the quarks and gluons. Problems that are being addressed at the LHC include discovery of the Higgs boson that provides the mass to elementary particles, nature of dark matter, extra dimensions to validate string theory, search for any super symmetric partners to extend the Standard Model, asymmetry between matter and antimatter in the universe and search for physics beyond Standard Model (BSM).

In high energy collisions, particles are made to collide with a total relativistic momenta much greater than their rest masses. In these high energy interactions two particles collide together to produce hundreds of particles in final state from a variety of processes. These collisions can be hadronic, leptonic or heavy-ion interactions. In case of leptonic collisions lepton-antilepton annihilate to form virtual neutral boson like photon, γ or Z^0 which with time decays to produce other elementary particles, mostly lighter hadrons or mesons. In hadronic collisions the quarks and gluons inside the two hadrons interact via quark-quark, quark-gluon and gluon-gluon interactions to produce a large number of particles. These processes can be summarized in the form of reaction, for leptonic collision as $l\text{-}l \rightarrow X$, where l is the lepton or for hadronic collisions as $h\text{-}h \rightarrow X$, where h is the hadron or for hadron-nucleus collision as $h\text{-}A \rightarrow X$, with A being the nucleus. X in the final state of these reactions can be any number of particles. The particles produced during the collisions are recorded by the detectors which provide information about the charge, momentum and energy of each particle produced. The multitude of particles produced in the final state after the collision, is termed as particle multiplicity and the distribution of these final state particles produced during the collision is known as multiplicity distribution. The charged particle multiplicity is one of the key measurements in these high energy interactions which provides the information about particle production mechanism. Several theoretical and phenomenological models based on statistics, hydrodynamics and thermodynamics have been successful in describing the distribution of these final state particles.

The work presented in the thesis is based upon the study of multiparticle production and analyses of the charged particle multiplicity distribution P_n as a function of number of charged particles, n, at high energy particle collisions, correlations amongst the produced particles and dependence of average multiplicity on the centre of mass energy in leptonic, hadronic and hadron-nucleus interactions. Various models like the negative binomial distribution (NBD), Gamma, Shifted Gamma, the Weibull and the Tsallis gas model have been used to describe the multiplicity distributions and the results from these models have been compared with the experimental data obtained from the LEP, the Proton-Antiproton Collider (SPS) and the LHC experiments. The organization of thesis is as follows:

Chapter 2 presents a brief overview of fundamental interactions, the Standard Model of particle physics, Quantum Electrodynamics, QED, the theory of electromagnetic interactions along with the theory of strong interactions, Quantum Chromodynamics, QCD. Different kinds of high energy interactions and the mechanism of particle production are also discussed in this chapter.

Chapter 3 describes the basic principle of particle acceleration, general structure of high energy particle detector, brief overview of particle accelerators and colliders including the Large Electron Positron Collider (LEP), the Tevatron, the Large Hadron Collider (LHC) and their detectors. Main emphasis is on the Compact Muon Solenoid (CMS) detector of LHC, as part of work presented in the thesis utilizes the CMS detector features. The brief overview of various sub-detectors of the CMS experiment along with the experimental conditions is given in this chapter.

Chapter 4 deals with Data Quality Monitoring using the Compact Muon Solenoid (CMS) detector at the Large Hadron Collider, CERN. In this chapter description of how the raw data from detector is scrutinized, validated and certified is discussed in brief. All these processes play vital role in the data analyses as it is only after all these processes data is made available to the various CMS sub groups for different analyses. Results of validation for the data taken by the CMS during period 2015-16 and certification results for the 2017 CMS data are also shown.

Chapter 5 describes the statistical hadronization of multiparticle production during high energy particle collisions. Various phenomenological, theoretical and statistical approaches used to describe the behaviour of particles produced in high energy interactions are discussed in this chapter.

Chapter 6 presents the results of multiplicity distributions obtained by using several models and theoretical approaches. Results from these models have been compared with the experimental data of multiplicity from various collider experiments at the LEP, the UA5 and the LHC. Experimental data in e^+e^- collisions at center of mass energy ranging from $\sqrt{s} = 91$ GeV to 206 GeV from the LEP experiments, L3 and OPAL, in $\bar{p}p$ collisions at $\sqrt{s} = 200$, 540 and 900 GeV in restricted pseudorapidity windows as well as in full phase space from the UA5 experiment conducted at Proton-Antiproton collider ($Sp\bar{p}S$) have been analyzed. Analysis of data of proton-proton collisions from the CMS detector at the LHC at center of mass energies ranging from $\sqrt{s} = 0.9$ to 7 TeV in different pseudorapidity windows for charged particle multiplicities has been done and presented in the thesis. Moments which provide the information about the correlation of particles are also calculated and compared with the experimental data, in each case

Chapter 7 summarizes the results and conclusions of the work done and presented in this thesis.

Chapter 2

Theoretical Background

Particle physics can be described very well using the theories and laws that govern the interactions between the elementary particles. Kinematics and dynamics of these interactions are the finest way to understand the concept of energy and matter. Gravitational force due to the mass of particle, electromagnetic force as a result of charges on particles, strong and weak forces inside the atom at subatomic scales play an important role in particle physics. Structure of matter at the subatomic scale can be obtained by colliding particles at high energy. Very high energy particle accelerators [1] are used for colliding the particles leading to interactions, which are used for studying the dynamics and kinematics of interactions and exploring the structure of matter at fundamental level. Present day knowledge of matter at this scale is very well described by the Standard Model [2, 3]. Details of fundamental particles, their interactions, the Standard Model, Quantum Chromodynamics, which describes the strong interactions and theory of high energy particle interactions are discussed briefly in this chapter.

2.1 Fundamental Interactions

In nature, four fundamental forces are known to exist; gravitational, electromagnetic, strong and weak. These forces are characterized on the basis of important criteria, the type of particles that experience the force, the range over which the force is effective and the nature of the particles that mediate the force. Basic characteristics of these interactions are illustrated in figure 2.1

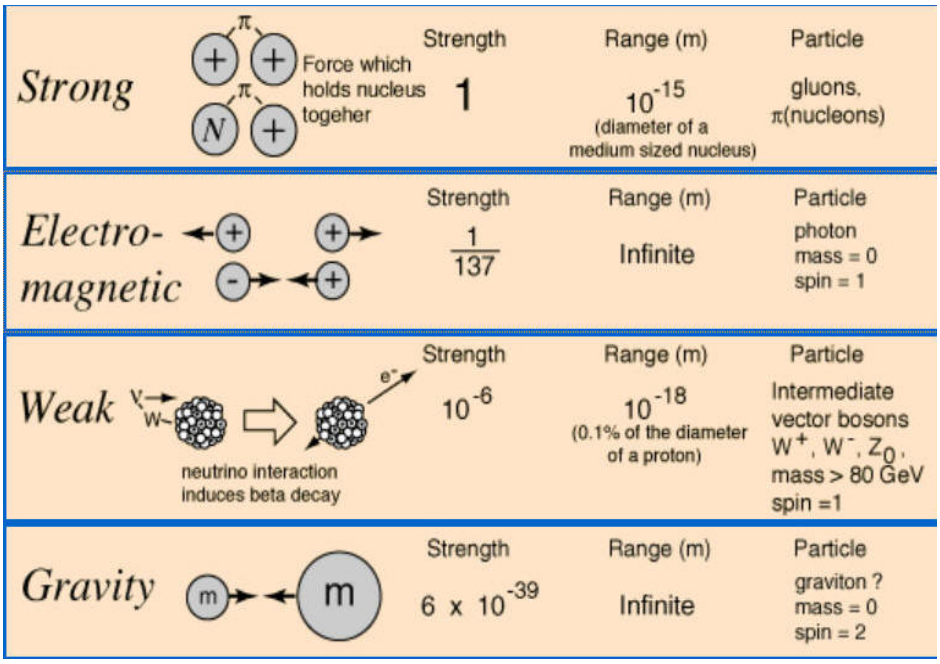

	Strength	Range (m)	Particle
Strong Force which holds nucleus togeher	1	10^{-15} (diameter of a medium sized nucleus)	gluons, π(nucleons)
Electro-magnetic	$\frac{1}{137}$	Infinite	photon mass = 0 spin = 1
Weak neutrino interaction induces beta decay	10^{-6}	10^{-18} (0.1% of the diameter of a proton)	Intermediate vector bosons W^+, W^-, Z_0, mass > 80 GeV spin =1
Gravity	6×10^{-39}	Infinite	graviton ? mass = 0 spin = 2

Figure 2.1: The basic features of four fundamental forces of nature. Image source: http://hyperphysics.phy-astr.gsu.edu/hbase/Forces/funfor.html

- The electromagnetic interaction exists between all particles which possess charge. This force is characterized by $1/r^2$ dependence on distance, where r is the separation between the centers of two charged particles. It is a long range force extending over infinite distance and is mediated by the exchange of massless photon [4].

- Strong force, the strongest of the four fundamental forces, is responsible for holding nucleons together inside the nucleus against the electromagnetic repulsive force due to the presence of protons inside the nucleus. This force acts between the particles carrying colour quantum number with a very short range ($\sim$ 1 femtometer) and arises from an exchange of the quantum of strong colour field known as the gluon [5].

- The weak interaction is accountable for the beta decay process and hence conversion of a neutron in to proton, electron and antineutrino. This force arises due to exchange of intermediate vector bosons $W^{\pm}$ and Z^0. The exchange of $W^{\pm}$ leads to the charged-current (CC) weak interaction and the exchange of Z^0 leads to a neutral-current (NC) weak interaction. Since the intermediate vector bosons are massive, hence weak interaction is of very short range [6].

- The gravitational force, mediated by the graviton, is the weakest in magnitude and have infinite range. However graviton is yet to be discovered and its mass measured. The gravitational interaction between the two particles, similar to electromagnetic interaction, is characterized by the $1/r^2$ dependence on distance. Since this force has infinite range, the mediating particle (graviton) is expected to be massless and is purely an attractive force.

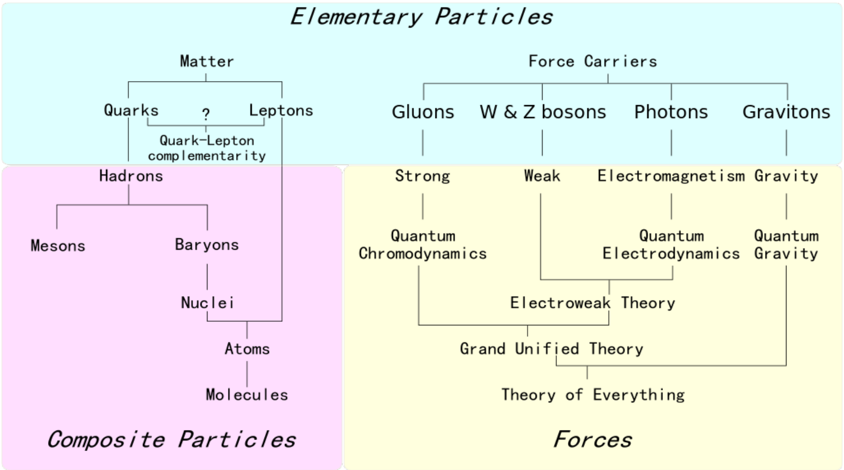

Figure 2.2: Overview of elementary particles and the interaction forces. Image source: https://goo.gl/images/cDnL8X

Earlier concept about the terrestrial gravity, that pulls things down to earth, and the astronomical gravity, which holds the planets in to their orbits around the Sun was unclear, whether they were the same or different. Newton showed that both terrestrial and astronomical gravities are the same. The other significant contribution about the unification was made by James Clerk Maxwell, who showed that, electric and magnetic forces both can be united in to a single interaction known as electromagnetic interaction. The weak interactions were unknown for some time. S. Glashow, A. Salam and S. Weinberg brought forward the concept of unification of weak and electromagnetic forces. They proposed 'electroweak theory' [7, 8], which considers the electromagnetic and weak forces as different manifestations of a single electroweak interaction. The theory has also been verified by collider experiments at CERN in 1983. As a natural extension of electroweak theory it is observed that at sufficiently high energies, the strong interaction and electroweak interaction have convergence similar to that between the electromagnetic and weak interactions. This lead to the proposal of unification theory of strong, weak and electromagnetic interactions, known as grand-unified theory, GUT [9]. The unified interaction due the unification of three forces is characterized by one unified coupling constant. This implies that α_S, coupling constant of strong interactions, α_e, electromagnetic coupling constant and weak coupling constant, α_w will converge together at very high energy of order $\sim 10^{16}$ GeV, at a GUT scale. Till date no strong evidence has been found which could describe the Grand Unified Theory. The unification of grand-unified interaction and gravitational interaction is known as 'Theory of Everything' (TOE) [10], giving rise to a universal interaction as shown in figure 2.2. Grand unification is the intermediate step towards the establishment of the Theory of Everything. It is a theoretical framework which can explain and unify all the aspects of physics of the Universe together. At present TOE is one of the major unsolved problems of physics on which physicists are working.

2.2 The Standard Model of Particle Physics

The Standard Model (SM) [11] of elementary particle physics is a framework that describes all the elementary particles and their interactions. It incorporates the theories of the electromagnetic, weak and strong forces, but excludes theory of gravitation. SM describes the Universe in terms of matter and force carriers. The building units of matter are particles called fermions, with spin-1/2 and categorized into leptons and quarks. Quarks exist in bound states as hadrons, containing either two or three quarks: quark anti-quark pair (mesons) and three quarks (baryons), instead of existing individually.

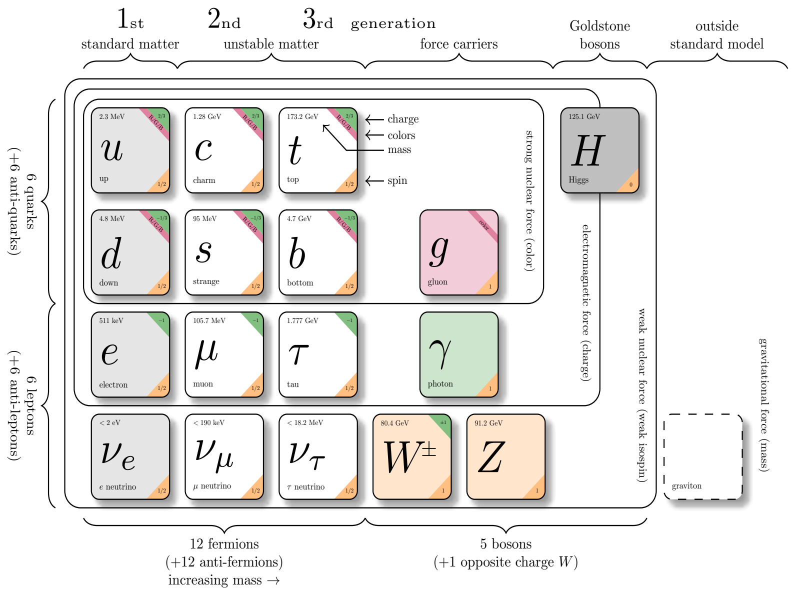

Figure 2.3: The Standard Model of elementary particles with the three generations of matter, gauge bosons and the Higgs boson. Image source: http://www.texample.net/tikz/examples/model-physics

The fundamental forces in the SM are mediated through the exchange of bosons having spin-1. The photon, γ, is the carrier of the electromagnetic interaction, eight gluons mediate the strong interaction whereas the weak interaction is mediated by the W and Z bosons. Higgs, a spin-0 scalar boson, is a quantum excitation of the Higgs field. It plays an important role in the Standard Model and was discovered in 2012 at the Large Hadron Collider (LHC). Higgs mechanism is associated with the Higgs field which explains why the photon is massless whereas W, Z bosons are massive. SM is mathematically consistent and the framework for it is provided by Quantum Field Theory (QFT). The Standard Model can be defined mathematically using SU(3) x SU(2) x U(1) local gauge symmetry [12, 13]. The three factors of the gauge symmetry lead to the three fundamental interactions, strong, electromagnetic and weak. The SU(3) term defines the strong interaction between quarks and gluons, with three degrees of freedom of colour charge. SU(2) x U(1) gauge group defines the electroweak interaction which is a combination of the weak and electromagnetic interactions. The Standard Model predictions have been well verified in the past by various experiments at the Large Electron Positron collider (LEP) in e^+e^- collisions and at the Tevatron in proton-antiproton collisions, at high energies. Figure 2.3 describes the particle constituents of the Standard Model according to which all visible matter of the Universe is made up of basic building units called fundamental particles, categorized in three generations each of quarks and leptons, which interact via three of the four fundamental forces electromagnetic, strong and weak. In addition to quarks and leptons, field bosons complete the picture of SM along with the Higgs Boson, which is responsible for Electroweak symmetry breaking via Higgs Mechanism [14]. Interaction summary between all the fundamental particles and forces are shown in figure 2.4 and their properties are described in the following sections.

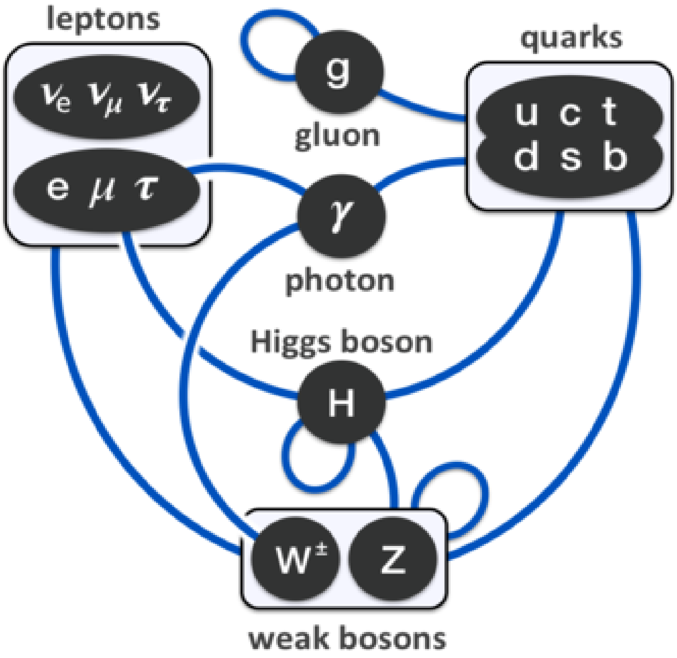

Figure 2.4: Schematic diagram summarizing the interactions amongst the elementary particles. Image source: https://en.wikipedia.org/wiki/Standard-Model

2.2.1 Leptons

Leptons are half integral spin particles, which do not take part, in strong interaction, carry either one unit of charge or zero charge [15]. Lepton group has six different species of particles; three of them are charged and the other three are neutral. The charged leptons are electron (e), muon (μ) and tau (τ), which are negatively charged and have distinct masses. Each charged lepton has an associated neutral partner known as neutrino ν_e, ν_μ, and ν_τ. Neutrinos are considered as massless in the SM, but the experimental observations confirm that the neutrinos have non zero masses [16]. Each of the six leptons has a distinct anti-particle, known as antilepton. The mass of an antilepton is same as that of the lepton, but all of other electric or magnetic properties, e.g. charge, lepton number, etc., are opposite.

Lepton	Symbol	Mass (Nev/c^2)	Charge	Mean life (sec)	spin	Antiparticle
Electron	e^-	0.511	-1	stable	1/2	e^+
e-neutrino	ν_e	$< 2.2 \text{ x } 10^{-6}$	0	stable	1/2	$\bar{\nu_e}$
Muon	μ^-	105.7	-1	$2.2 \text{ x } 10^{-6}$	1/2	μ^+
μ-neutrino	ν_μ	< 0.17	0	stable	1/2	$\bar{\nu_\mu}$
Tau	τ^-	1777	-1	$2.9 \text{ x } 10^{-13}$	1/2	τ^-
τ-neutrino	ν_τ	< 15.5	0	stable	1/2	$\bar{\nu_\tau}$

Table 2.1: Leptons and their characteristics

Some properties of the leptons are listed in Table 2.1. Each lepton is assigned a lepton number, L $(L_{e^-}, L_{\mu^-}, L_{\tau^-})$ equal to 1 and each antilepton $(L_{e^+}, L_{\mu^+}, L_{\tau^+})$ the lepton number is - 1 . All other particles which are non-leptonic have lepton number of 0. In all interactions involving leptons each of the lepton numbers is conserved separately in order to obey conservation laws i.e conservation of muon number, conservation of electron number and conservation of tau number. Another important property of leptons is the helicity, which tells the direction of particle's spin relative to its momentum. When the direction of the spin of a particle is the same as the direction of its motion, it is called right handed where as left handed particles are those which have spin and motion in opposite direction as shown in figure 2.5. All leptons in the Standard Model are normally considered as left handed, where as antileptons as right handed.

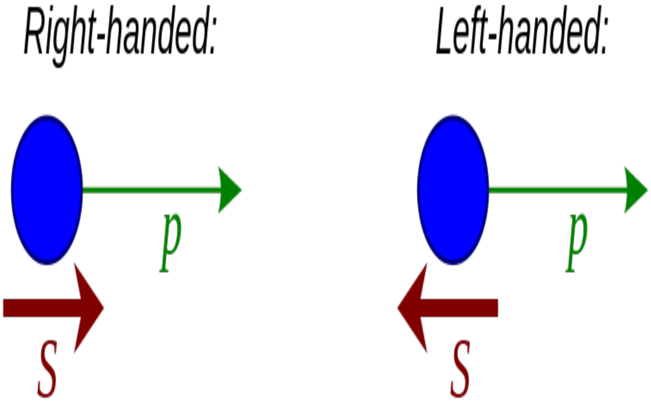

Figure 2.5: Leptons with right handed and left handed chirality. Image source: http://www.wikiwand.com/en/Chirality_(physics)

2.2.2 Quarks

The important building blocks of matter are quarks which are fractionally charged, half integral spin and strongly interacting objects, form the composites known as hadrons: mesons ($\bar{q}q$ state) [1] and baryons (qqq state) [2]. There are six different flavours of quarks: up (u), down (d), strange (s), charm (c), bottom (b) and top (t). The anti-particles of these quarks, i.e., antiquarks have opposite signs of electric charge, baryon number, strangeness, charmness, bottomness and topness. The properties of the quarks are tabulated in Table 2.2.

The mesons [17] have integral spin and are the constituent combinations of a quark and an antiquark. The baryons [17] have half integral spin and are constituent combination of three quarks. Since quarks, having half integral spin, are fermions

---

[1] Meson: $\bar{q}q$ state with zero or integral spin

[2] Baryon: qqq state with half integral spin

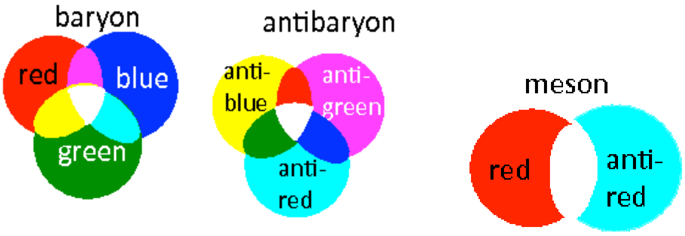

Figure 2.6: The colour constituents of baryons, antibaryons and a meson. Image source: http://inspirehep.net/record/1615882

Quark	Symbol	Mass (GeV/c^2)	Charge (e)	Strangeness S	spin	Antiparticle
Up	u	0.002	+(2/3)	0	1/2	$\bar{u}$
Down	d	0.005	-(1/3)	0	1/2	$\bar{d}$
Strange	s	0.5	-(1/3)	-1	1/2	$\bar{s}$
Charm	c	1.5	+(2/3)	0	1/2	$\bar{c}$
Top	t	174	+(2/3)	0	1/2	$\bar{t}$
Bottom	b	4.3	-(1/3)	0	1/2	$\bar{b}$

Table 2.2: Characteristics of quarks

and hence follow the Pauli's exclusion Principle, no two quarks in the baryon, qqq state, can have exactly the same properties. So another quantum number, 'colour' with a three-fold degree of freedom, for the quark is introduced to resolve this problem. The quarks have three primary colour charges: red (r), green (g) and blue (b); whereas antiquarks have complementary colours: Cyan ($\bar{r}$), magenta ($\bar{g}$) and yellow ($\bar{b}$).

All particle states observed in nature are colourless; baryons have a colour state (rgb) and mesons exist in a pair of colour-anticolour quarks as shown in figure 2.6. Gluons are bicoloured and the exchange particles for the colour force between quarks, similar to the exchange of photons in the electromagnetic force between two charged particles. The gluon-exchange process changes the colour of the quarks and the colour of individual quarks changes continually as the gluons are exchanged as shown in figure 2.7.

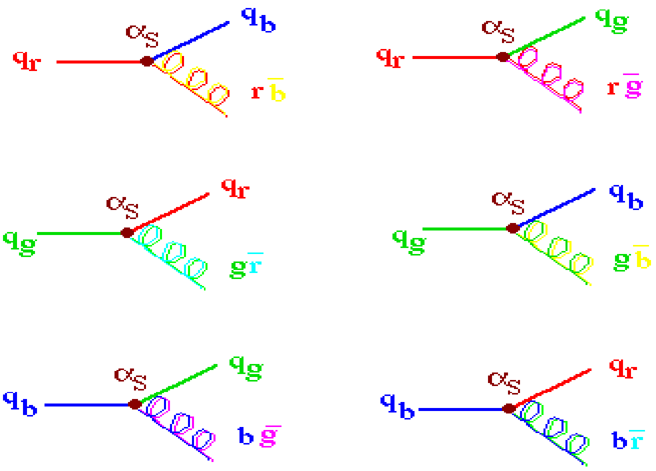

Figure 2.7: A Feynman diagram of gluon exchange process of quarks. Image source: https://faraday.physics.utoronto.ca/PVB/DBailey/SubAtomic/Lectures/LectF23

2.2.3 Bosons

The interaction between two particles is mediated by the exchange of another particle between them. The particles which are exchanged, are known as field bosons and are the carrier of the force (interaction). These particles follow Bose-Einstein statistics and have zero or integral spins. The carriers of weak interaction are known as intermediate vector bosons. There are two types of such intermediate vector bosons: neutral and charged. The neutral vector boson (Z) is of spin one with mass almost 97 times the mass of the proton. The charged boson (W) is also spin one particle with charge either +e or -e. The mass of W-boson is around 85 times the mass of the proton. Since the masses of the force carriers are very high, so the weak interactions are of short range. The particles exchanged, among the quarks to produce the strong interaction, are known as the gluons. A total of eight gluons are postulated by the quark model. A gluon carries a colour and an anti-colour. The emission or absorption of a gluon by a quark changes colour of the quark as described above.

The force carrier of the electromagnetic interaction is a neutral massless particle, photon. Since the photon has no mass, the electromagnetic interaction is of long range and follows $1/r^2$ dependence. We can consider that the unification of electromagnetic forces and weak forces, is the manifestation of a single electroweak

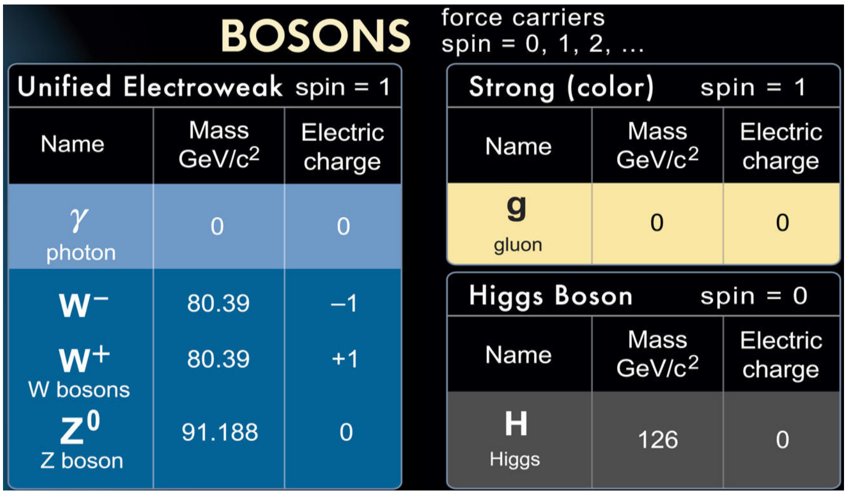

BOSONS force carriers
spin = 0, 1, 2, ...

Unified Electroweak spin = 1

Name	Mass GeV/c^2	Electric charge
γ photon	0	0
W$^-$	80.39	–1
W$^+$ W bosons	80.39	+1
Z^0 Z boson	91.188	0

Strong (color) spin = 1

Name	Mass GeV/c^2	Electric charge
g gluon	0	0

Higgs Boson spin = 0

Name	Mass GeV/c^2	Electric charge
H Higgs	126	0

Figure 2.8: Fundamental bosons in the Standard Model of particle physics. Image source: http://www.cpepphysics.org/images/Bosons.jpg

force in the electroweak theory. The electroweak force is mediated by four massless bosons and hence is a long range force. Three of these bosons acquire mass by the phenomenon of 'Spontaneous Symmetry Breaking'. These three massive bosons are $W^{\pm}$ and Z-bosons, which also reduce the range of weak part of the electroweak interaction. The fourth electroweak boson, the photon remains mass less and hence the range of the electromagnetic force remains infinite. The field bosons and their properties are summed in figure 2.8.

2.3 Quantum Electrodynamics

Quantum Electrodynamics (QED) is the relativistic quantum field theory of electromagnetic force and explains the interaction between light and matter. QED is associated with the charged elementary particles like electrons and positrons and mathematically describes the interaction between these particles as mediated by the massless photon. As QED interactions involve the charged fermions and photons so the Lagrangian, $\mathcal{L}$ of QED consists of the Lagrangian due to free charged Dirac fermions [18] and the Lagrangian of the electromagnetic field. i.e. $\mathcal{L} = \mathcal{L}_{\mathcal{D}} + \mathcal{L}_{e.m}$. Thus Lagrangian density can be written in the form [19]

$$\mathcal{L} = \mathcal{L}_{\mathcal{D}} + \mathcal{L}_{e.m} = \bar{\psi}(x)(\iota\gamma^{\mu}\partial_{\mu} - m)\psi(x) \; - \; \frac{1}{4}F_{\mu\nu}F^{\mu\nu} \tag{2.1}$$

where ψ is the spin 1/2 field (fermion field), γ_{μ} [3] represents the Dirac matrices, ∂_{μ} [4] represents the co-variant derivative and the $F_{\mu\nu}$ is the electromagnetic field tensor describing the electromagnetic field coupling strength. Field strength tensor can be written in terms of 4-vector potential A^{μ} ($\equiv A^0$, $\mathbf{A}$)[5] in the co-variant form as;

$$F_{\mu\nu} = \partial_{\mu}A_{\nu} - \partial_{\nu}A_{\mu} \tag{2.2}$$

Where the components of the field strength tensor are the components of electric and magnetic fields;

$$F_{\mu\nu} = \begin{bmatrix} 0 & E^1 & E^2 & E^3 \\ -E^1 & 0 & -B^3 & B^2 \\ -E^2 & B^3 & 0 & -B^1 \\ -E^3 & -B^2 & B^1 & 0 \end{bmatrix} \tag{2.3}$$

Under the transformation of $A^{\mu} \rightarrow A'^{\mu} = A^{\mu} + \partial_{\mu}\, \theta(x)$; field strength tensor, $F_{\mu\nu}$ and hence Lagrangian, $\mathcal{L}_{e.m}$ remains invariant. In the transformation $\theta(x)$ is the differentiable function of space time and hence values of A^{μ} are different at each space-time point. Such transformations are called 'local gauge transformation'.

The Lagrangian of the free Dirac field, $\mathcal{L}_D$ remains invariant under transformation $\psi(x) \rightarrow \psi'(x) = e^{-\iota eQ\theta}\, \psi(x)$, where e is the unit of electric charge, which is basically the charge of the electron and Q is the charge of the particle. In this transformation θ is a global parameter having same value at all space-time points. Due

---

[3] γ_{μ} is 4 x 4 Dirac matrices which follow the anti-commuting relation, $\{\gamma^{\mu}, \gamma_{\nu}\} = 2g_{\mu\nu}$ with $g^{\mu\nu}$ is the metric tensor having components = diag(1,-1,-1,-1)

[4] 4-gradient partial derivative in space-time coordinates given by $\partial_{\mu} = \frac{\partial}{\partial x_{\mu}}$ with μ = x, y, z, t

[5] A^{μ} is a 4-vector potential which can be expressed in terms of a scalar quantity A^0 and a 3 vector $\mathbf{A}$

to involvement of this global parameter such transformations are called as 'global gauge transformation'. If θ is made a function of space-time then the Lagrangian, $\mathcal{L}_D$ fails to remain invariant and changes, and is given by equation (2.4).

$$\mathcal{L}_{\psi'(x)} = \bar{\psi}'(x)(\iota\gamma^{\mu}\partial_{\mu} - m)\psi'(x) \tag{2.4}$$

$$= \mathcal{L}_{\psi(x)} + eQ(\partial_{\mu}\theta)\bar{\psi}(x)\gamma^{\mu}\psi(x) \tag{2.5}$$

The extra term at right side includes $\partial_{\mu}\theta$ that transforms like a 4-vector. To compensate this term another 4-vector, (Let's say A^{μ}), is needed to be introduced in the Lagrangian. The new Lagrangian in this case is given by;

$$\mathcal{L}_{\psi(x)} = \bar{\psi}(x)(\iota\gamma^{\mu}\partial_{\mu} - m)\psi(x) + eQ\bar{\psi}(x)\gamma^{\mu}\psi(x)A^{\mu} \tag{2.6}$$

This new Lagrangian remains invariant under local gauge transformation of $\psi(x) \rightarrow \psi'(x) = e^{-\iota eQ\theta(x)}\ \psi(x)$ and $A^{\mu} \rightarrow A'^{\mu} = A^{\mu} + \partial_{\mu}\ \theta(x)$. The transformed Lagrangian in this case is;

$$\mathcal{L}_{\psi'(x)} \;=\; \bar{\psi}'(x)(\iota\gamma^{\mu}\partial_{\mu} - m)\psi'(x) + eQ\bar{\psi}'(x)\gamma^{\mu}\psi'(x)A'^{\mu} \tag{2.7}$$

$$= \bar{\psi}(x)(\iota\gamma^{\mu}\partial_{\mu} - m)\psi(x) + eQ(A'^{\mu} - \partial_{\mu}\theta(x))\bar{\psi}'(x)\gamma^{\mu}\psi'(x) \tag{2.8}$$

It is clear that equations (2.8) and (2.6) are same if $A'^{\mu} = A^{\mu} + \partial_{\mu}.\ \theta(x)$. This is the same transformation under which the free Lagrangian of electromagnetic field remains invariant. This 4-vector A^{μ} is named as photon field. Adding this new Dirac Lagrangian to the Lagrangian of $e.m$ field we have the Lagrangian of QED [20] which describes the dynamics of charged fermions and photon.

$$\mathcal{L}_{QED} = \bar{\psi}(x)(\iota\gamma^{\mu}\partial_{\mu} - m)\psi(x) - \frac{1}{4}F_{\mu\nu}F^{\mu\nu} - eQ\bar{\psi}(x)\gamma^{\mu}\psi(x)A^{\mu} \tag{2.9}$$

The last term of the Lagrangian represents the interaction of charged fermions with electromagnetic field, photon and is responsible for the creation and annihilation of the particle with the help of photon field. QED was the first successful quantum field theory which incorporated the ideas of particle creation and annihilation into a consistent framework. The mathematical expressions to describe the behaviour of subatomic particles in the electromagnetic interactions are represented by a series of pictorial representation called 'Feynman diagrams'. Feynman diagram [21] consists of points, vertices, and lines attached to the points. It represented in time-space axes and defined by three key actions.

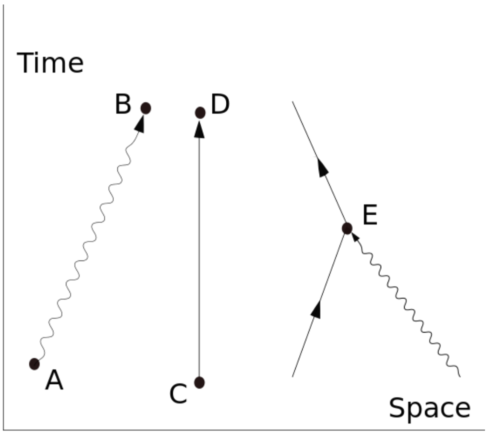

Figure 2.9: Three basic processes involved in a Feynman diagram. Image source: http://www.wikiwand.com/en/Quantum_electrodynamics

- An exchange particle, called gauge boson (e.g. photon, γ) going from one place and time to another place and time.
- A charged particle (e.g. e^+ or e^-) going from one place and time to another place and time.
- Emission or absorption of a gauge boson by a charged particle at a certain place and time.

These actions are represented by a wavy line for the photon, a straight line for charged particle and a junction of two straight lines and a wavy one for a vertex to represent absorption or emission of a photon by a charged particle as shown in figure 2.9. It is to be noted that particle line moving backwards in time in the Feynman diagram represents the anti-particle going forward. Interaction of two oppositely charged particles (e^+/e^-) is the simplest example which can be described by using

QED. The charged particles like electron and positron (antiparticle) annihilate to form the photon which further decays to form the electron-positron pair. This process is known as 'Bhabha scattering' and Feynman diagram for this process is shown in figure 2.10.

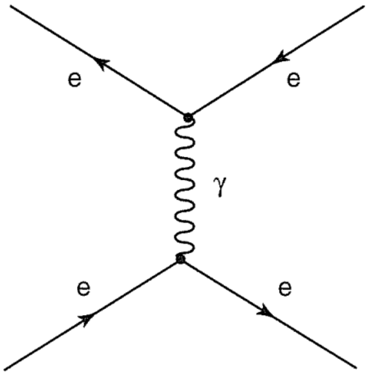

Figure 2.10: A Feynman diagram for 'Bhabha scattering', $e^{+}e^{-}$ coulomb attraction. Image source: http://www.wikiwand.com/en/Quantum_electrodynamics

The Feynman diagrams help us in determining the order of process from number of vertices involved in the QED interactions. The lowest order physical processes in QED which involve of only two charged particles and one photon, are second order processes as it involve the Feynman diagrams with two vertices e.g. 'Bhabha scattering'. But there is a possibility that QED interactions involve an infinite number of photons making the processes complex. These processes can have higher-order contributions due to involvement of multiple exchange of photons. Figure 2.11 shows the processes with fourth order contributions coming from the Feynman diagrams. These diagrams are called loop diagrams and can yield infinite number of contributions. There are infinite number of ways in which photon can divide its momentum between the electron and positron on the internal loop to follow energy-momentum conservation. In order to perform the precise mathematical calculations, like cross section calculations, all these infinite contributions need to be considered which is impossible. This problem of infinite contributions is removed with a process called re-normalization. Richard Feynman [22], Julian Schwinger [23] and Sin'Itiro

Tomonga [24] shared the Noble Prize for this work. Re-normalization process treats the infinities by readjusting the values of quantities like coupling constant, normalization of propagators to compensate for effects of their self-interactions. This process of readjusting the quantities simply eliminates the infinities by cancelling the positive infinities to negative infinities and leads to finite number of Feynman diagrams. Renormalizability allows the QED to predict the values of observables, like cross section, in very close agreement with the experiments. For details of renormalization refer to [25].

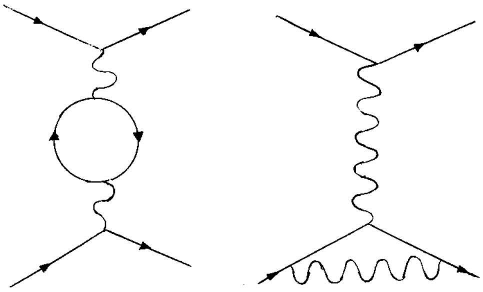

Figure 2.11: Fourth order contributions from a Feynman diagram. Image source: http://jefferywinkler.com/standardmodel2.html

2.4 Quantum Chromodynamics

The theory of strong interactions is known as 'Quantum Chromodynamics' (QCD) due to the property of 'colour' for the quarks. Two important features of the QCD are briefly described below;

- **Quark confinement** : Although it is predicted that hadrons themselves are not the fundamental particles, they are further constituted by point-like particles called quarks. But, no quark has been isolated till date since its prediction. This feature has been explained by Quantum Chromodynamics (QCD) [26] through the mechanism of quark confinement [27]. The explanation of the quark confinement is given by the idea that the attractive force between two quarks inside a hadron goes on increasing as the quarks are moved apart from their equilibrium spacing. Therefore, more and more energy is required to increase their separation. This increased energy is utilized to form a new quark-antiquark pair rather than isolating the quarks present inside the hadrons. This quark-antiquark pair results in the formation of a meson. An example of the quark confinement is explained in figure 2.12. Two quarks, q_1 and q_2, inside a hadron are pulled apart by providing energy to increase their separation. The energy, thus provided, ends up with the formation of new quark-antiquark pair, q_3 and q_4, rather than isolation of the former two quarks.

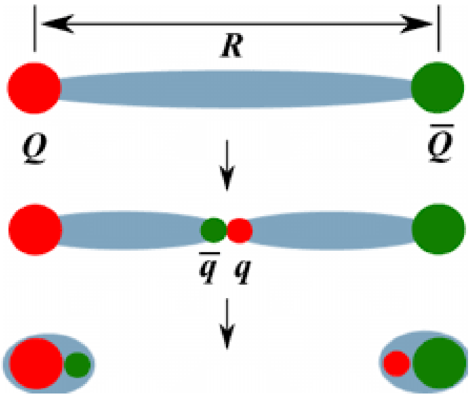

Figure 2.12: Pictorial representation of quark confinement. Image source: http://inspirehep.net/record/841791

- **Asymptotic freedom** : The behaviour of quarks at short distances and at high energies, where momentum transfer is large, is explained by the term 'asymptotic freedom' [28]. In QCD, interactions between the quarks occur via exchange of gluons with certain momentum, Q. When quarks inside the hadrons come closer, the force between them becomes very weak in a way that it decreases asymptotically. As a consequence quarks behave as free, weakly bound and non-interacting particles. This behaviour is known as 'asymptotic freedom'.

Both asymptotic freedom and confinement are the consequences of behavior of QCD coupling constant α_S, which determines the strength of interaction between quarks and gluons. The dependence of α_S on the energy scale Q is mathematically given by

$$\alpha_S(Q^2) = \frac{4\pi}{b\ ln(Q^2/\Lambda^2_{QCD})^2} \tag{2.10}$$

where b = (33 - $2n_f$)/3, n_f is the number of active quark flavors and Λ_{QCD} is the QCD scale parameter with the dimension of energy and Q denotes the momentum transfer. Experimentally measurements of Λ_{QCD} yield values of around 200 GeV. The perturbation coupling becomes very large at the scale Λ_{QCD}. The equation (2.10) [26] shows that confinement of quarks and gluons inside hadrons is actually a consequence of the growth of coupling at low energy scale, which decreases at high energy scale. The behavior of the QCD coupling is the result of the non-abelian nature of the strong interaction which is characterized by the presence of self interaction of gauge bosons. Figure 2.13 shows the variation of strong coupling constant α_S with Q, obtained from various experimental observations [29]. According to Particle Data Group (PDG) [29] , the current world average value of the strong coupling constant at the scale of mass of Z boson is $\alpha_S(M_Z) = 0.1181 \pm 0.0011$.

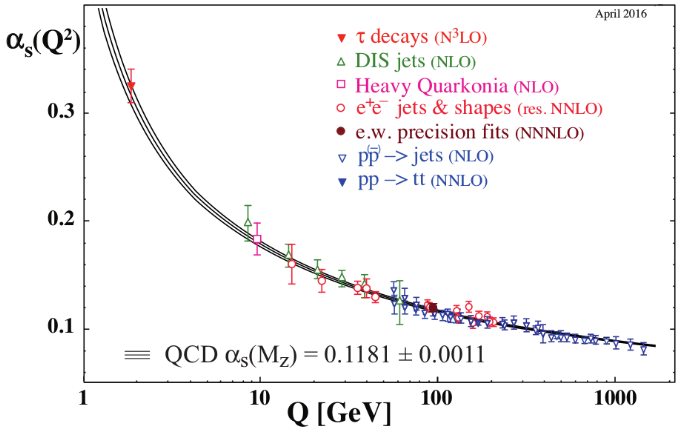

Figure 2.13: Different experimental determinations of the strong coupling constant α_S evolved at the energy scale Q are shown as a function of Q. Plot taken from [29]

2.4.1 Perturbative and non-perturbative QCD

The property of asymptotic freedom allows a perturbation treatment for calculations of QCD when the separation between partons is very small, corresponding to a high energy probe. In most of the cases, making predictions with QCD is extremely difficult, due to the infinite number of possible topologically-in-equivalent interactions. But at short distances, the coupling is very small. As a result this infinite number of terms can be approximated accurately by a finite number of terms. This is achieved by the pQCD [30], which means perturbative QCD (pQCD) allows for the prediction of an observable (e.g. the scattering cross section) to be expressed in terms of finite expansions of power series in coupling constant α_S, in which a simple system is "perturbed" by higher order corrections:

$$f = f_1 + f_2\alpha_s + f_3\alpha_s^2 \tag{2.11}$$

for example f_1 can be the scattering cross section. The pQCD calculation of an observable associated with a given scattering process is determined by summing up over the amplitudes of all Feynman diagrams associated with the scattering as described in reference [30]. Due to colour confinement one cannot observe free quarks and gluons, so most of the strong interaction processes can not be calculated directly using perturbative QCD. Hence pQCD can not be applied at the longer distances or at low to moderate energy/momentum values. The Best example to describe the non-perturbative part in QCD is the hadron physics [31] and its structure. In order to study the complete scattering processes like lepton-hadron or hadron-hadron scattering processes, QCD factorization theorem [32] is used. According to this theorem such processes can be divided into two parts, a soft part containing the non-perturbative long-range dynamics for low-moderate momentum exchange, and a hard part, which encodes the quark-gluon sub-processes calculated using pQCD, for the high-momentum exchange between the quarks in the hadron-hadron scattering and between the lepton and quarks of a hadron in lepton-hadron scattering.

2.5 High Energy Interactions

In high energy collisions of hadrons and leptons, a large number of particles are produced through different interaction channels. The interaction amongst different categories of particles are discussed below.

2.5.1 Leptonic Collisions

Leptonic collision [33] processes are much simpler than the hadronic collisions [34]. Being the elementary particles and due to the point like nature of leptons, like electrons and positrons (and their antiparticles), leptonic collision processes are much clean and suitable for accurate experimental measurements. Other advantage of leptonic annihilation is that all of the center of mass energy is available for particle production and there are no remnants. Collision between an electron and a positron leads to creation of virtual particle like a Z boson [35] or a photon or a pair of W boson, W^+ and W^-, via the annihilation process. These virtual particle then decay instantly to produce other elementary particles, which are then detected by the particle detectors. Figure 2.14 represents the production of hadrons from the electron-positron collision. This whole process can be summarized as;

$$e^+e^- \rightarrow (Z^0/\gamma)^* \rightarrow W^\pm \rightarrow q\bar{q} \rightarrow \text{hadrons}$$

.

From a theoretical point of view, the production of hadrons from the leptons ($e^+e^- \rightarrow$ hadrons) can be understood as a succession of three phases as shown in figure 2.15. These phases are electroweak phase, perturbative QCD phase and non perturbative QCD phase. First phase, the electroweak phase, directly involves collision of the leptons (electron and positron) which annihilate to produce virtual photon or Z boson or pair of W boson, $W^\pm$, which then decay instantly into a quark-antiquark ($q\bar{q}$) pair. In second perturbative QCD phase a large number of quarks and gluons (partons) are produced from the quark-antiquark $q\bar{q}$ pair created in the electroweak phase. Quantum Chromodynamics (QCD) provides the expla-

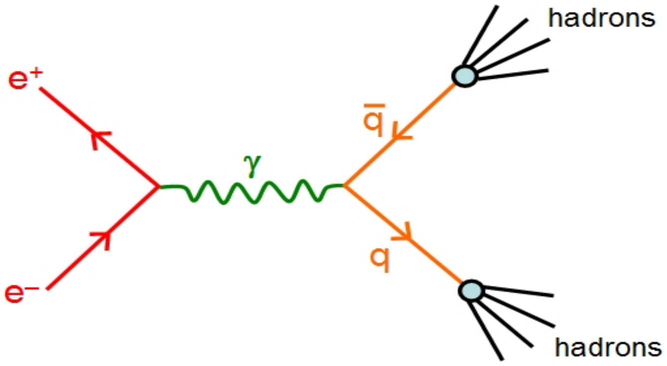

Figure 2.14: Hadron production in the leptonic collision process. Image source: https://www.quantumdiaries.org/tag/petra/

nation of production of the large number of partons. In QCD, multi partons are produced due to the interactions between quarks and gluons. These interactions lead to the formation of additional quark-antiquark pairs and gluons (i.e. partons) in a cascading process called as parton showers. At larger distances and smaller energies perturbation theory can not be used to explain the formation of particles. In the third non perturbative QCD phase coloured partons formed in the second phase fragment together to form colourless hadrons. This process of formation of colourless hadrons from coloured partons is called as hadronization. Some of the hadrons formed during hadronization can be unstable and decay into the smaller and stable final state particles which are recorded in the detector.

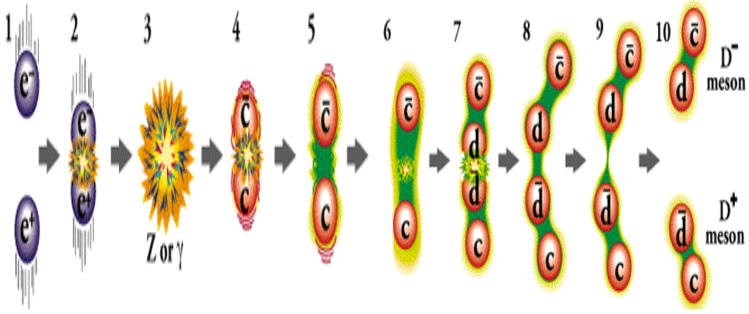

Figure 2.15: Pictorial representation of electron-positron collision and its outcome. Image source: http://www.particleadventure.org/eedd.html

2.5.2 Hadronic Collisions

Interaction processes are complex and influenced by strong interactions in hadronic collisions. These collisions are basically the interaction between the quarks and gluons which are the constituents of the interacting hadrons. Incoming hadrons provide "broad-band" beams of partons which posses varying fractions of the momenta of their parent hadrons. The probability that determines which of the constituents interact, is governed by the parton distribution functions [36] $f(x, Q^2)$, which depend on the momentum fraction x of the interacting parton and the momentum transfer Q^2 in the interaction. Momentum fraction, x, is defined as fraction of momentum carried by the interacting parton (quark or gluon) from the total available momenta whereas Q^2 is defined as the momentum which is exchanged during the interaction between the particles.

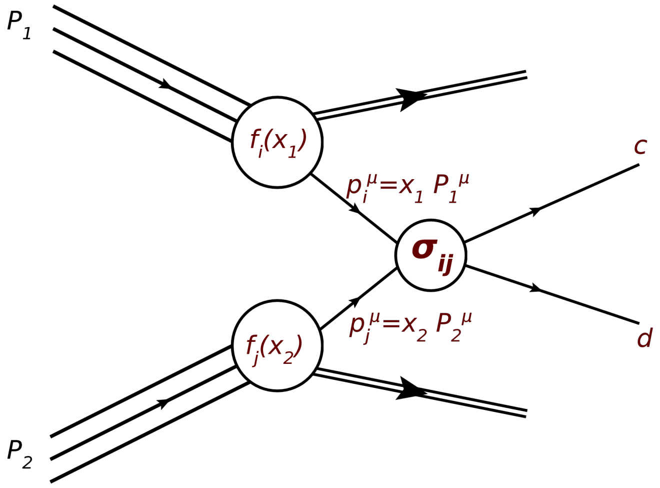

Figure 2.16: Hadronic collision with hard interaction between partons. Image source: http://inspirehep.net/record/1251416/plots

Most of the partonic interactions in the hadron-hadron collisions are soft, leading to small momentum transfer (Q^2) described by non pQCD. Where as hard interactions involve the processes having large momentum transfer and may lead to the new physics. In this region the strong interaction can be described by perturbative QCD only. With sufficiently large momentum transfer, the interaction between two hadrons can be viewed as interactions between the constituents of hadrons (figure 2.16). So the interacting parton $i(j)$ carries a sufficiently large momentum fraction to probe the inner structure of the other hadron 1(2). The remaining partons inside the colliding hadrons participate only minimally in the interaction. The cross section for a hard scattering process initiated by two hadrons is given by

$$\sigma^{12\to cd} = \int_0^1 dx_1 dx_2 \sum_{i,j} f_i(x_1, Q^2) f_j(x_2, Q^2) \times \hat{\sigma}^{ij\to cd} \tag{2.12}$$

In the hard process momenta are given by $p_i = x_1 P_1$, and $p_j = x_2 P_2$. In most of the cases $x_1 = x_2$. The short-distance cross section for the scattering of partons from A and B is denoted by σ^{ij}. The sum is over all partonic processes which produce particles c and d.

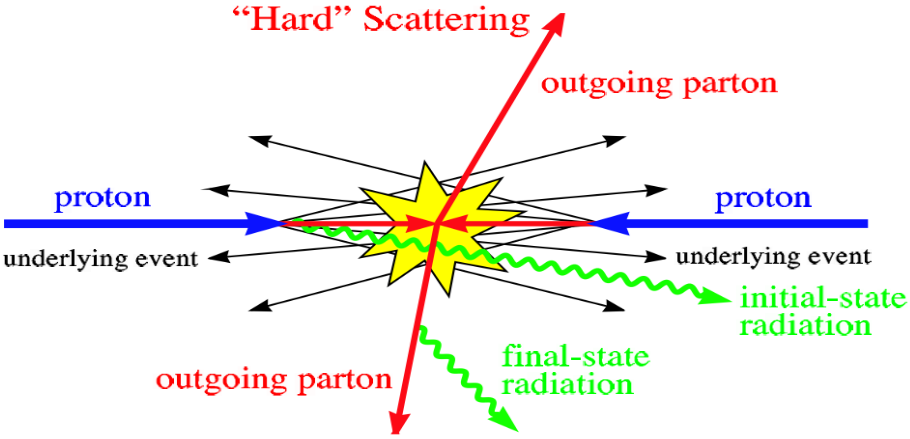

Figure 2.17: Overview of all the processes involved in hadronic collision. Image source: http://inspirehep.net/record/853601/plots

The presence of a significant number of soft interactions [6] between colliding hadrons, possible multiple parton interactions and gluon radiation from the initial partons before the hard interactions, initial state radiation-ISR as defined below, complicate things even further. Figure 2.17 shows the proton-proton collision in

---

[6] Soft Interactions: Interactions in which low energy particles are involved. The momentum transfer between the particles in such cases is very small, i.e. $p_T < 1$ GeV

which 2 to 2 parton scattering has occurred. In addition to the hard scattering [7], there is a secondary interaction which is not associated with the primary leading hardest parton-parton process. The event (particle production) coming due to this secondary interaction process is called as ‘Underlying Event (UE)’ [37]. UE can be semi-hard or soft interaction process due to the energy scale which is typically of order $\leq$ 1 GeV. Main components of UE are initial and final state radiations, multiple parton interaction at low transverse momentum and beam beam remnants. Initial state radiation (ISR) and final state radiation (FSR) are defined as emission of photon or gluon by the incoming and outgoing partons respectively and are shown in figure 2.18. The particles that come from the splitting of the protons and do not participate in the initial-state radiation, hard-scattering process and final state radiation are referred as ‘beam beam remnants’. The steps involved in production of particles in hadronic collision are shown in figure 2.19 and can be described in following processes :

Incoming Beams: Two particle ($p/\bar{p}$) bunched beams approaching each other with equal and opposite momenta at very high energies.

Initial State Radiation is defined as showering of radiation from the incoming particles. In ISR one of the partons (quark or gluon) from the incoming particle (protons) emits radiations like photons or gluons before interacting with partons of the other particles. This emission of radiation leads to the reduction of beam energy available for the collisions. They can branch like q → qg, q → γg or g →gg.

Hard Interaction: It occurs between two partons with momentum transfer with $p_T > 1$ GeV from the beam which produces outgoing partons. It is also possible to have more than one hard scattering in the same collision, leading to the so called multiple parton interaction. The interacting partons carry only a fraction of the total beam energy, and some of the partons are called beam remnants, since they do not participate in the collision.

Semi Hard and Soft Interactions (Underlying Event): Several semi-hard

---

[7] Hard Interactions: Interactions which involve high energy partons. The momentum transfer between the partons is large in these interactions, i.e. $p_T > 1$ GeV

interactions occur between other partons. Soft processes like single, double and non diffractive processes will be discussed in detail in the next section.

Final State Radiation: After the collisions of two hadrons, the outgoing scattered particles may emit radiations like photon or gluon. This emission of radiations and branchings of the outgoing partons (q → qg, q → γg or g →gg) is called as 'Final State Radiation (FSR)'. These processes become more relevant at higher energies.

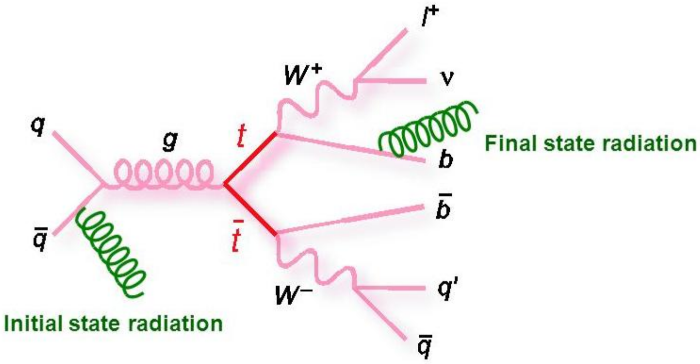

Figure 2.18: A Feynman diagram representing the final state radiation, FSR and initial state of radiation, ISR in quark-antiquark interaction. Image source: https://slideplayer.com/slide/8029144/

Hadronization: In a process which involves outgoing partons (quarks and gluons), a large number of hadrons can be seen due to parton fragmentation. Due to confinement, a net colour charge cannot exist freely, thus the produced partons are not observed in nature. Instead, partons join together in colourless combinations leading to the process of hadronization [38]. This process of hadronization leads to a collimated spray of hadrons which is referred to as a jet.

Decay: If the hadrons produced during fragmentation are unstable, they decay in to lighter stable particles.

2.5.3 Interaction Processes

Hadronic interactions consist of both hard scattering and soft scattering. Hard scattering processes can be described very well using perturbative QCD. But soft

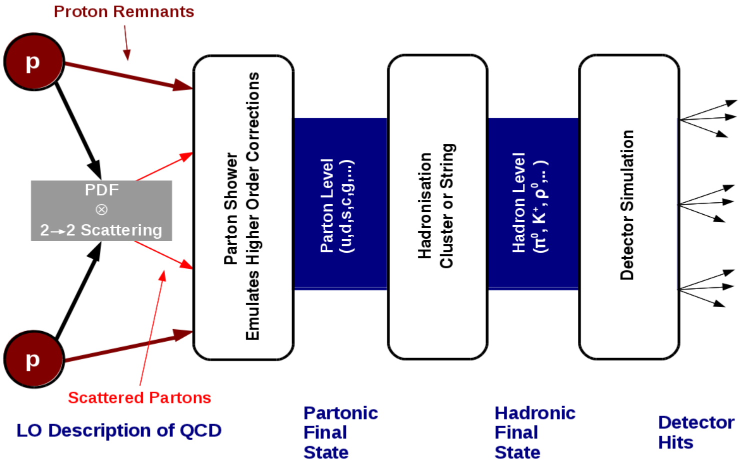

Figure 2.19: The basic steps involved in the production of particles in a hadronic collision. Image source: http://inspirehep.net/record/1251416/plots

processes which dominate the collision can not be described by pQCD. The hadronic interaction can further be divided in to elastic and inelastic interaction by looking in to the outcome or final state of collisions.

Elastic Scattering: Elastic scattering is a collision between two particles in which final and initial states are the same e.g. $\mathrm{a} + \mathrm{b} \rightarrow \mathrm{a} + \mathrm{b}$. The total momentum of the two particles after the interaction is equal to their total momentum before the collision. For instance, at the LHC two protons are produced after collisions of two protons;

$$\mathrm{p} + \mathrm{p} \rightarrow \mathrm{p} + \mathrm{p}$$

Inelastic Scattering: In an inelastic scattering final and initial states are different from each other. Several other particles are produced after the collisions. e.g. the collision of two protons;

$$\mathrm{p} + \mathrm{p} \rightarrow \mathrm{x} + ..$$

Inelastic interactions can be classified into non diffractive and diffractive processes [39].

- Non Diffractive: In ND process, exchange of colour charge takes place between the colliding particles which results in production of more hadrons from the two colliding particles. These ND interactions are dominant in hadronic collisions and consist of around 55 % of total events produced by all scattering processes.

- Diffractive : In QCD, Pomeron (IP) is considered as a flavourless and colourless multiple gluon combination or a glue-ball. Diffraction occurs when the Pomeron is exchanged and interacts with the proton to produce a diffractive system. In a diffractive process there is very small transfer of energy between the two interacting protons, but one or both protons fragment to produce multi particle final states (hadrons). Diffractive processes can be further divided in to Single and Double diffractive processes. In SD only one of the incoming particles fragments to produce more particles while the other incoming particle remains intact with small alteration of momentum. In DD both the incoming particles fragment to produce more particles. In addition to above mentioned processes there is one more type of process in which single diffractive process is suppressed. This process is called as inelastic non-single-diffractive (NSD) process and defined as sum of non diffractive and double diffractive processes. These processes are shown in figure 2.20.

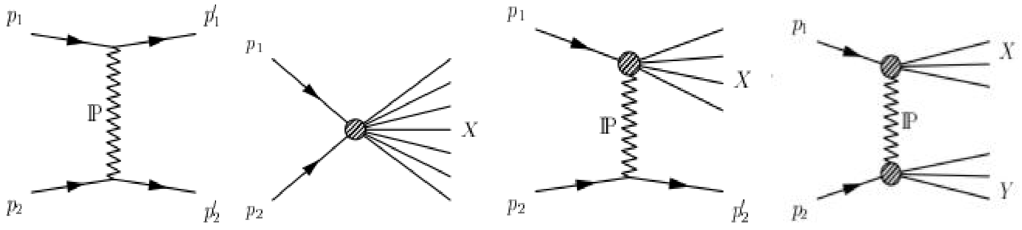

Figure 2.20: Types of Diffraction processes from left to right a) Elastic scattering b) Inelastic scattering c) Single diffractive process d) Double diffractive process. Image source: http://www.desy.de/2011summerstudents/2014/reports/

Interaction between any two particles like hadrons can be described in terms of cross section. The cross section gives the measure of probability of particle production and is calculated by measuring the number of particles produced. To find the probability of particle production in the interaction process total cross section needs to be measured. The total cross section for hadronic process like pp collision is calculated by summing the cross sections of elastic and inelastic processes .i.e.

$$\sigma_{total} = \sigma_{el} + \sigma_{inel} = \sigma_{el} + (\sigma_{SD} + \sigma_{DD} + \sigma_{ND}) \tag{2.13}$$

2.5.4 Multi-Particle Production in High Energy Interactions

In high energy collisions, both the colliding and the produced objects can be hadrons, mesons or leptons which are recorded in the particle detectors designed suitably to record different kinds of particles. The multitude of particles [40] produced in relativistic collisions follow certain production rules which can be predicted in terms of various models, some of them including the laws of statistical mechanics. A number of phenomenological approaches have been brought forward to characterize the multi-particle production in high energy interactions. Many of the physical observable of the collisions follow distributions in the phase space as predicted by these models within the statistical fluctuations. An observable which is the first one to be measured and accounted for in any experiment is the charged particle multiplicity [41, 42]. Being the key observable of high energy collisions, study of charged multiplicity distributions provides notable constraints for models of multi-particle production. Several models [43–45] combining statistics and thermodynamics have been successful in the description of particle production in a systematic way. These statistical thermodynamical models have been developed to understand the high energy collisions by considering the produced particles as a gaseous system in which entropy of the system is taken into consideration. Thus, concepts from statistical mechanics and ensemble theory play an important role to study the characteristic properties of charged particle production.

Multi particle production in high energy collisions can result in any number of particles. Nearly all the models make predictions for charged particle multiplicity variable. In addition, the dependence of this variable on the rapidity [46] (y= $\frac{1}{2}$ ln $\frac{E+P_L}{E-P_L}$) and on the transverse momentum yields important information about the particle dynamics. The LHC being the highest energy *pp* collider produces hundred of particles of different kinds having a wide range of energies and rapidities. The proton proton interactions at LHC lead to a huge amount of data at the highest collision energy which motivated us to analyze these data. The work reported in the thesis is based on various aspects of the multi-particle production. In the present study the regularity and irregularities in multiplicity distributions and characteristic properties of charged particle production at high energy leptonic and hadronic collisions using various models have been investigated. Details of such models are explained in chapters 5 and 6.

Bibliography

[1] R. Fernow, “Introduction to Experimental Particle Physics”, Cambridge University Press (1989)

[2] D. J. Griffiths, “Introduction to Elementary Particles”, John Wiley and Sons, New York (2008)

[3] H. D. Perkins, “Introduction to High Energy Physics”, Cambridge University Press (2000)

[4] R. Feynman, “QED: The Strange Theory of Light and Matter”, Princeton University Press (1985)

[5] F. Halzen, A. Martin, “Quarks & Leptons: An Introductory Course in Modern Particle Physics”, John Wiley and Sons, New York (1984)

[6] S. Wolfram, “Introduction to the Weak Interaction”, (1974)

[7] A. Salam, J. C. Ward, “Weak and electromagnetic interactions”, J. C. Nuov. Cim. **11**, 568 (1959)

[8] A. Salam, “Gauge Unification of Fundamental Forces”, Rev. Mod. Phys. **52**, 525 (1980)

[9] A. J. Buras, J. Ellis, M. K. Gaillard, D. V. Nanopoulos, “Aspects of the grand unification of strong, weak and electromagnetic interactions”, Nucl. Phys. B. **135**, 66 (1978)

[10] J. Ellis, “The superstring: theory of everything, or of nothing?”, Nature **323**, 595 (1986)

[11] M. Herrero, “The standard model”, NATO Sci. Ser. C. **534**, 1 (1999)

[12] F. Englert and R. Brout, “Broken Symmetry and the Mass of Gauge Vector Mesons”, Phys. Rev. Lett. **13**, 321 (1964)

[13] P. W. Higgs, “Broken Symmetries and the Masses of Gauge Bosons”, Phys. Rev. Lett. **13**, 508 (1964)

[14] T. C. Hill and M. L. Lederman, “Beyond the God Particle”, Prometheus Books, (2013)

[15] H. Harari, “Three generations of quarks and leptons”, Proceedings of the XII Rencontre de Moriond, **SLAC-PUB-1974**, 170 (1977)

[16] B. Pontecorvo, “Neutrino Experiments and the Problem of Conservation of Leptonic Charge”, JETP **26**, 984 (1968)

[17] M. Gell-Mann, “Symmetries of baryons and mesons”, Phys. Rev. **125**, 1067 (1962)

[18] P. A. M. Dirac, “Principles of Quantum Mechanics”, Int. Ser. Mono. Phys., Oxford University Press, 255 (1982)

[19] S. Aguilar, “Introductory Quantum Electrodynamics”, (2016)

[20] R. Feynman, “Mathematical Formulation of Quantum Theory of Electromagnetic Interaction”, Phys. Rev. **80 (3)**, 440 (1950)

[21] M. Peskin, D. Schroeder, “An introduction to quantum field theory”, Westview Press (1995)

[22] R. Feynman, “Space-Time approach to Quantum Electrodynamics”, Phys. Rev. **76 (6)**, 769 (1949)

[23] J. Schwinger, "On Quantum Electrodynamics and Magnetic moment of the Electron", Phys. Rev. **73 (4)**, 416 (1948)

[24] S. Tomonaga, "On a Relativistically Invariant Formulation of Quantum Electrodynamics", Prog. Theor. Phys. **1**, 27 (1946)

[25] L. Ryder, "Quantum Field Theory", Cambridge University Press (1996)

[26] R. Ellis, W. J. Stirling and B. R. Webber, "QCD and collider physics", Camb. Monogr. Part. Phys. Nucl. Phys. Cosmol. **8**, 1 (1996)

[27] J. Greensite, "An introduction to the confinement problem", Springer ISBN 978-3-642-14381-6, (2011)

[28] D. J. Gross, F. Wilczek, "Ultraviolet behavior of non-abelian gauge theories", Phys. Rev. Lett. **30**, 1343 (1973)

[29] C. Patrignani et al. (Particle Data Group), "Review of Particle Physics", Chin. Phys. C **40**, 100001 (2016)

[30] G. Sterman et al., "Handbook of Perturbative QCD", Rev. Mod. Phys. **67**, 157 (1995)

[31] J. J. Cobos-Martnez, "Non-perturbative QCD and hadron physics", J. Phys. Conf. Ser. **761**, 012036 (2016)

[32] J. C. Collins, D. E. Soper, G. Sterman, "Factorization of Hard Processes in QCD", Adv. Ser. Direct. High Energy Phys. **5**, 1 (1988)

[33] F. J. Gilman, "Electron-Positron Annihilation and the Structure of Hadrons", Stud. Nat. Sci. **9**, 29 (1975)

[34] M. L. Mangano, "QCD and the physics of hadronic collisions", Physics-Uspekhi **53**, 109 (2010)

[35] L3 Collaboration, "Z Boson Pair-Production at LEP", Phys. Lett. B **572**, 133 (2003)

[36] D. Sopera, “Parton distribution functions”, Nucl. Phys. B - Proceedings Supplements **53**, 69 (1997)

[37] R. Field, “The Underlying Event in Hard Scattering Processes”, eConfC010630, **501**, UFIFT-HEP-01 (2001)

[38] B. Webber, “Fragmentation and Hadronization”, Int. J. Mod. Phys. A **15**, 577 (2000)

[39] E. Berger et. al., “Diffractive hard scattering”, Nucl. Phys. B **286**, 704 (1987)

[40] E. De Wolf, J. J. Dumont and F. Verbeure, “Comparative study of charged multiplicity distributions”, Nucl. Phys. B **87**, 325 (1975)

[41] I. M. Dremin, “Quantum Chromodynamics and Multiplicity Distributions”, Physics Uspekhi **37**, 715 (1994)

[42] I. Dremin, “Commands of QCD multiplicity distributions in small phase space bins”, Phys. Lett. B **341**, 95 (1994)

[43] Z. Koba, D. Weingarten, “Use of density correlations in testing models of particle production”, Lett. al Nuov. Cim. **8**, 303 (1973)

[44] Z. Koba, H. B. Nielsen, P. Olesen, “Scaling of multiplicity distributions in high-energy hadron collisions”, Nucl. Phys. B **40**, 317 (1972)

[45] S. Hegyi, “Log-KNO scaling: A new empirical regularity at very high energies?”, Phys. Lett. B **467**, 126 (1999)

[46] K. J. Eskola, K. Kajantie, P. V. Ruuskanen, K. Tuominen, “Rapidity dependence of particle production in ultrarelativistic nuclear collisions”, Phys. Lett. B **543**, 208 (2002)

Chapter 3

High Energy Particle Accelerators During Last Three Decades

High energy physics commonly known as Particle Physics is the study of the fundamental forces of nature and the particles, their behaviour and interactions at very high energies. To study the physics at very high energy we need to probe at very small distance, which is small compared to nuclear radius (~ 1 fm). To achieve this, highly energetic subatomic particles are used as probes. In order to produce beams of such particles with large momenta, they need to be accelerated using particle accelerators. This makes the particle accelerators very important research tool in high energy physics. In this chapter, high energy particle accelerators [1] which are used for the study of elementary particle physics are described. Electron-proton collider HERA (Hadron Elektron Ringanlage) at DESY, antiproton-proton collider (Tevatron) at Fermilab, electron-positron collider LEP (Large Electron Positron Collider) and proton-proton collider, LHC (Large Hadron Collider) at CERN are amongst the largest particle colliders which have been used in the last three decades to explore the frontiers of particle physics. The detailed description about the general structure of modern day high energy particle detector, the principle of acceleration of particles and the experimental set up of the accelerators used in the analyses are briefly described in this chapter. The LHC and the CMS detector have been described in detail due to our participation in the CMS experiment.

3.1 Principle of Particle Acceleration

A particle accelerator is a device which uses electromagnetic fields to increase the velocity of charged particles to nearly the speed of light. Accelerators can be classified broadly in to two classes: electrostatic accelerators and electrodynamic accelerators. Electrostatic accelerators make use of static electric fields to accelerate the particles whereas electrodynamic accelerators use varying electromagnetic field (oscillating radio frequency fields) for acceleration purpose. Electrostatic accelerators are generally known as high voltage D.C. accelerators as a constant high voltage is built up between the two terminals of an evacuated tube and particles are accelerated on their passage across the space. In these types of accelerators the gain in the energy is limited to the accelerating voltage of the machine. Cockcroft-Walton machine [2] and the Van de Graaff machine [3] are the best examples of electrostatic accelerators. As electrostatic accelerators can increase the energy of charged particles upto MeV only, so in order to increase the energy of particles to higher magnitudes electrodynamic accelerators are used which use the mechanism of resonant circuits or cavities inspired by oscillating RF fields. Electrodynamic accelerators can be classified in to linear and circular accelerators.

3.1.1 Linear Accelerator

A Linear Accelerator which is often called as '*linac*' accelerates the particles in a straight line by using oscillating radio frequency (RF) fields. The RF fields give a series of accelerating kicks in correct phase at a series of electrode gaps as shown in figure 3.1. The accelerator consists of array of hollow, metallic cylindrical drift tubes (plates) which are separated by small gaps and are enclosed in an evacuated glass chamber. An alternating field of high energy is applied on these drift tubes. When the particles approach towards a drift tube they get attracted towards it due to an opposite polarity charge applied to the tube. The polarity of the tube is switched when particles pass through the tube, this makes the tube to repel the particles and accelerate them towards the next plate. Till date Stanford Linear Accelerator, SLAC, (electron-positron collider) is the longest linear accelerator in the world having length of 3 km. More information about the SLAC can be found in reference [4]. It can accelerate electrons/positrons up to 50 GeV

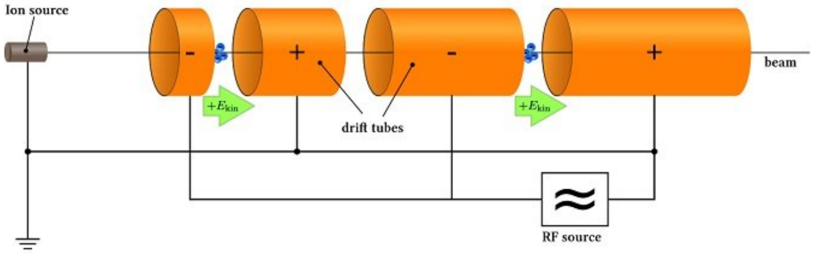

Figure 3.1: Principle of a linear acceleration

3.1.2 Circular Accelerator

In circular accelerators, particles move in a circular path to achieve the desired energy. Electromagnets are used to bend the particle's tracks in to a circle. The ring topology used in circular accelerators allows the continuous acceleration of particles because of the continuous movement of the particles. Circular accelerator can be classified in to three types namely, Cyclotron, Synchrocyclotron and Synchrotron, depending upon the requirement of desired value of energy of the particles. Cyclotrons use a pair of hollow 'D'-shaped electrodes (metal plates), separated by a narrow gap, for the acceleration of the particles. The two Dees facing each other are placed between the two poles of electromagnet which provides static magnetic field perpendicular to the Dees. This field is used to bend the path of a particle into a circular orbit. The charged particles are injected at the center of this gap and due to the magnetic field, particles move in a circular path with constant speed inside the

Dees. A high frequency alternating voltage is applied across the gap between the Dees. The frequency is set in such a way that the particles complete one complete round during a single cycle of the voltage. The frequency, f, of the RF field in the static magnetic field, B, should match the resonance frequency of particle of charge, q and rest mass, m as

$$f = \frac{qB}{2\pi m} \tag{3.1}$$

Every time when the particles cross the gap, the polarity of the Dee is reversed in order to provide the accelerating kick to the particles. This push increases the speed of the particles and causes them to move in a circle with larger radius with every rotation. The particles move in a spiral path outward from the middle to the edge of the Dees. A small voltage on a metal plate allows the beam to leave the cyclotron and hit the desired target located at the exit point at the edge of the bombardment chamber [5]. The final velocity, v, achieved by a particle while moving in the Dees of radius, R, is given by;

$$v = \frac{qBR}{2m} \tag{3.2}$$

Cyclotrons can accelerate the particles upto energy of few MeVs which corresponds to a speed upto 0.1 c only. So in order to achieve the higher velocity and energy, modifications in the Cyclotrons need to be done. Synchrocyclotron is other type of circular accelerator with few modifications in the conventional form of Cyclotron. In Synchrocyclotron only one Dee is used and the frequency of the RF electric field is varied, decreased continuously instead of keeping it constant as in the case of Cyclotron, to take care the effects of relativity on the particles. The particles get accelerated when they enter or leave the Dee. The another way of achieving high energy particles is by keeping frequency of the RF electric field constant but increasing the magnetic field. A circular accelerator working on the principle of increasing magnetic field is known as Isochronous Cyclotron. Using the above two ways particles can achieve the velocity around 80 % of the speed of light. Even these two modifications of cyclotron could not accelerate the particles at energy of

GeV order. Another modification of Cyclotron lead to the evolution of Synchrotron which could accelerate the particles with the velocity almost equivalent to speed of light (99.9999 % of c). Synchrotron is a circular accelerator in which a ring of constant radius is used to accelerate the particle beam. To accelerate the particles while considering relativistic effects on particles, the magnetic field strength is varied with time (instead of space as in the case of Isochronous Cyclotron). Magnetic field is increased in order to keep the radius of the orbit nearly constant during the process of acceleration. The disadvantage of Synchrotron is that it can not accelerate the particles direct from zero energy. So particle beams need to be pre-accelerated before injection into main ring. The Large Electron-Positron Collider, The Large Hadron Collider at CERN, The Tevatron at FermiLab are the examples of Synchrotron and are described in the following sections.

3.2 General Structure of a High Energy Particle Detector

The purpose of a particle detector is to record the particles produced that pass through it after being produced in a collision or a decay - an ‘event’, to visualize their tracks, to measure their energies and momenta, to record time of fight and to identify their identity. The exact position where the event occurs is known as the interaction point. It is necessary to know the mass and momentum of the particles to identify them. Depending on the type of the particles and forces to be studied, various detectors have been designed. In particle physics, a hermetic detector, also known as a 4π detector, is a particle detector which is designed to observe all possible decay products of an interaction between subatomic particles in a collider. It covers a large area around the interaction point and consists of layers of sub-detectors each specializing in a particular type of particle or property. They are typically cylindrical having different types of detectors wrapped around each other. These are known as hermetic because their construction is such that the motion of particles is ceased at the boundaries of the chamber and the particles do not move beyond the seals. These detectors cover solid angle nearly of 4π steradians around the interaction point and hence are named as 4π detectors. The first 4π detector was the 'Mark I' at the Stanford Linear Accelerator Center (SLAC) which lead to the discoveries of J/ψ particle and τ lepton. Its basic design has been used for all modern collider detectors. The interactions of the fundamental particles at colliders involve very large exchanges of energy and therefore involve large transverse momenta. So the large angular coverage is taken into account for modern particle physics detectors. Some of the modern day particle detectors which are in use in accelerators such as Large hadron collider at CERN include CMS, ATLAS and LHCb or CDF and Dϕ at Tevatron are hermetic detectors. The accelerators and detectors are often situated underground to provide the maximum possible shielding from natural radiations such as cosmic rays.

3.2.1 Components of a Hermetic Detector

The main components of a hermetic or a prototype detector are described in this section.

- **Vertex detector**: It is a high resolution position detector to identify the location of the collision as closely as possible and thus identifying very short-lived particles. The particles leave small electric charges in the squares they cross on traveling through the thin chips as shown in figure 3.2. The location of these deposits can be recorded electronically and these can be connected to reconstruct the track of the particles. Due to small size of electronic squares the position of the charged particle can be measured with microscopic level of accuracy. The position where any charged particle has been created is known as the vertex and can be found by drawing each path back to where it meets with one or more paths as the charged particles are always produced in pairs of equal and opposite charges.
- **Tracker**: A tracking detector unveils the track followed by a charged particle

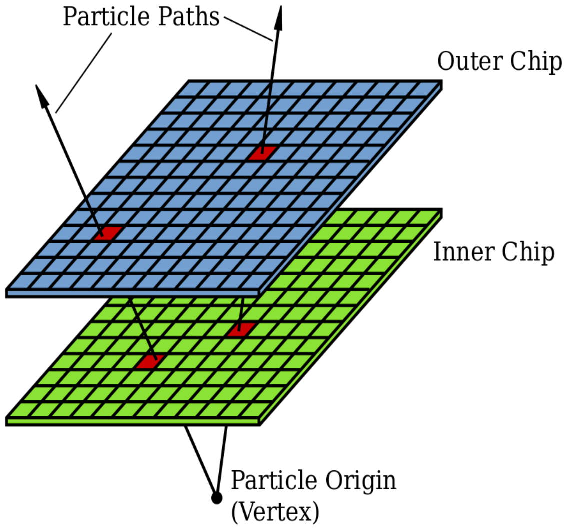

Figure 3.2: Vertex detector

by the trails left behind. The tracking system plots the helix path traced by a charged particle that curves in a magnetic field by localizing it in space in fine segmented layers of detecting material, usually silicon. The tracks are not visible directly in the modern tracking devices. The tiny electric signals are recorded by the computers which are then reconstructed by a computer program and displayed on the screen. The curvature of the path helps to know the charge and momentum of the particle. A strong magnetic field is used to identify the particles produced as it bends the particle's path into a curve.

- **Large Superconducting magnet**: This produces a strong magnetic field to bend the tracks of charged particles in the tracking detectors and provides their momenta. The curvature helps in identifying the charge of the particle and measuring the momentum.

- **Time Projection Chamber (TPC)**: It measures the three dimensional coordinate at many points along the track of a charged particle. When there are large numbers of tracks within a small angular cone, it is important to have the 3 dimensional information. The transverse coordinates are determined by wire proportional chambers at the ends of the TPC while the longitudinal (z) coordinate is obtained from the time taken by the charged particles to drift to the ends of the TPC.

- **Calorimeters**: A calorimeter measures the energy lost by a particle on travelling through it. It is designed to slow down the particles and to absorb their energy into a material. Calorimeters consist of layers of passive or absorbing high-density material such as lead having layers of active medium such as solid lead-glass or liquid argon.

  There are two types of calorimeters :

  The Electromagnetic Calorimeter (ECAL): It measures the energy of light particles - electrons and photons - as they interact electrically with the charged particles inside the matter. Electrons, positrons create a cascade of photons and electron-positron pairs known as electromagnetic shower which spreads due to Compton scattering and the photoelectric effect. The photons being neutral do not leave tracks in the Central Tracking Detector (CTD) but produce an electromagnetic shower in the ECAL. The electrons and positrons, being charged, leave tracks in the CTD and give rise to a shower in the ECAL.

  The Hadronic Calorimeter (HCAL): The hadronic calorimeters are specialized in absorbing hadrons such as protons and neutrons which interact through the strong nuclear force. The charged hadrons leave tracks in all the layers of detectors upto the HCAL and deposit all their energies. The neutral hadrons do not leave tracks in any of the layers of the detectors but produce showers and deposit their energies in the HCAL. The calorimeters can stop or absorb most of the known particles except muons and neutrinos.

- **Muon Chambers**: Only the muons and neutrinos, out of all the known stable particles, can pass through the calorimeter without depositing most or all of their energy. They interact very little with matter and can travel long distances through the dense matter. The charged muons can be detected by having an additional tracking system outside the calorimeters whereas the neutrinos are practically undetectable as they escape completely without being tracked in any of the layers. Their presence can be detected from the missing energy carried by them.

Figure 3.3 schematically represents all the basic components, Interaction Point (I.P), Tracker system, Calorimeters and Muon System, of a hermetic detector as mentioned above.

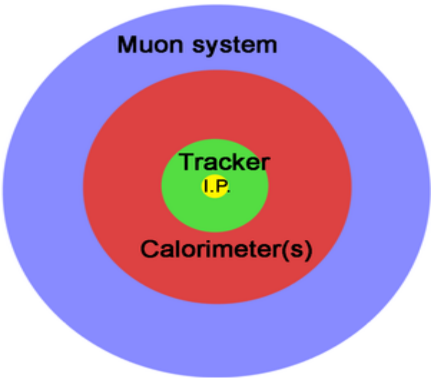

Figure 3.3: Hermetic detector

3.3 The Large Electron Positron Collider : LEP

The Large Electron Positron Collider (LEP) was an e^+e^- accelerator with storage ring of 26.7 km in circumference. It was operated at the range of 80 to 209 GeV center of mass energies from 1989 to 2000 [6]. The LEP accelerator ring, as shown in figure 3.4, was situated in an underground tunnel with an average diameter of 4m and of varying depth, from minimum 50 m to maximum of 150 m and had an inclination angle 1.4°. The LEP collider was operated in two phases, LEP1 from 1989 to 1995 at center of mass energy around 91 GeV and second phase, LEP2, from 1995 to 2000. LEP2 was the phase in which center of mass energy was increased steadily form 130 GeV to 209 GeV.

The LEP storage ring was the final accelerator in a chain of five accelerators, as shown in figure 3.4. The task of each accelerator was to accelerate the electrons and positrons which were generated by an electron gun and the positron converter

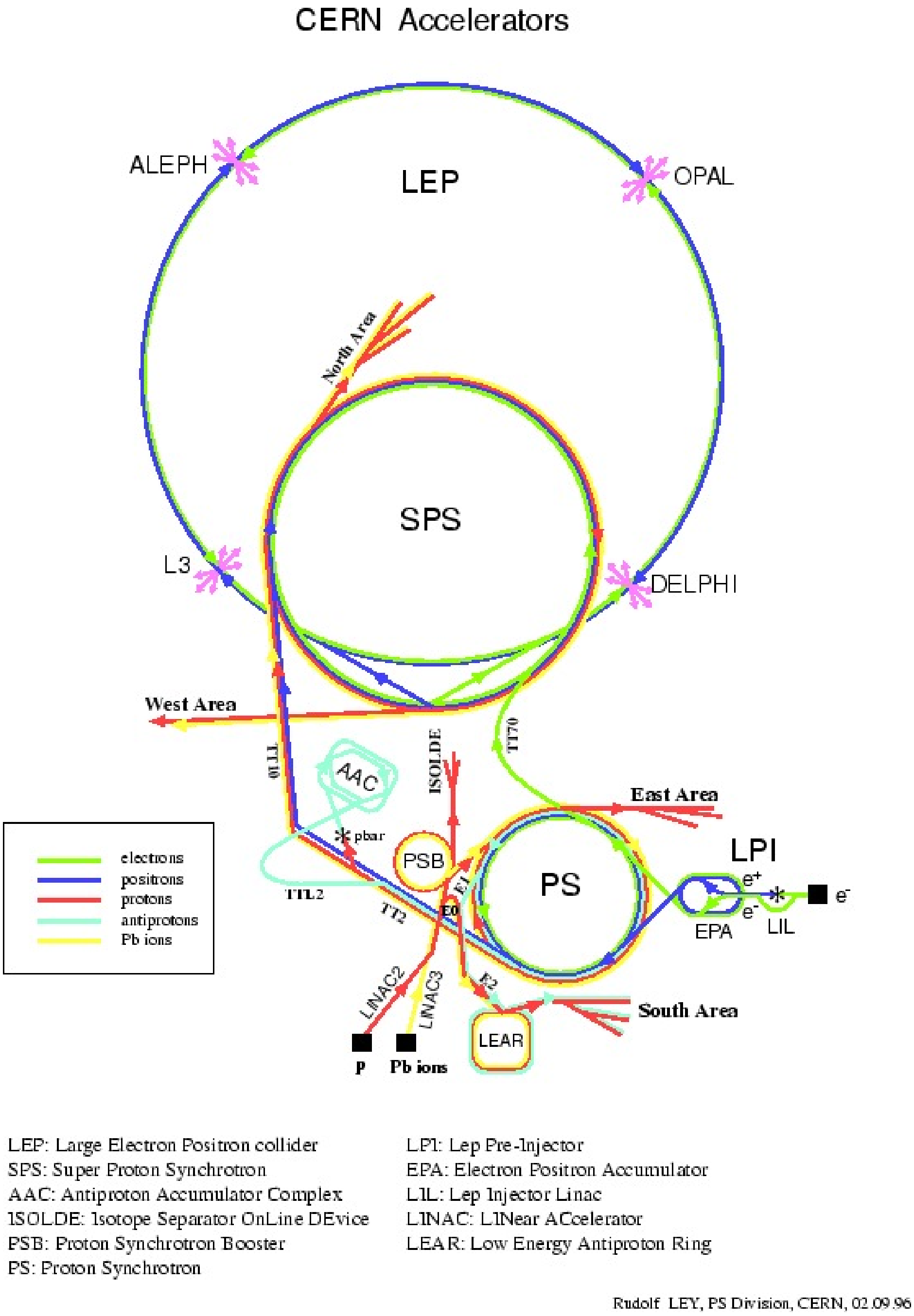

LEP: Large Electron Positron collider
SPS: Super Proton Synchrotron
AAC: Antiproton Accumulator Complex
ISOLDE: Isotope Separator OnLine DEvice
PSB: Proton Synchrotron Booster
PS: Proton Synchrotron

LPI: Lep Pre-Injector
EPA: Electron Positron Accumulator
LIL: Lep Injector Linac
LINAC: LINear ACcelerator
LEAR: Low Energy Antiproton Ring

Rudolf LEY, PS Division, CERN, 02.09.96

Figure 3.4: The Large Electron Positron (LEP) Collider. Image source: http://www.hep.ucl.ac.uk/ jpc/all/ulthesis/img94.gif

respectively. Electrons generated from the gun were accelerated upto 200 MeV energy through LINAC. Positrons were produced using the bremsstrahlung followed by pair production, when part of beam was deviated towards the tungsten target. To accelerate them up to 600 MeV second LINAC was used and then they were accumulated in an Electron-Positron Accumulator (EPA). EPA condensed the beam in to bunches via synchrotron radiation damping. The CERN Proton Synchrotron (PS) accelerated them up to 3.5 GeV and then they were injected into CERN Super Proton Synchrotron (SPS) to achieve the energy of 22 GeV. After this both the electrons and positrons were injected into the LEP in order to get the desired energy.

The Luminosity, $\mathcal{L}$ and the beam energy are the two fundamental parameters for designing any particle collider. Beam energy depends upon the physics processes of interest and its observation and for this, luminosity must be high enough to allow such observations at a good rate. Experimentally, Luminosity is the rate of collisions towards the interaction point and is given by

$$\mathcal{L} = \frac{N_e N_p n_b f_{rev}}{4\pi\sigma_x\sigma_y}$$

where $N_e(N_p)$ is the number of electrons (positrons) per bunch, n_b is the number of bunches per beam, f_{rev} is the revolution frequency and $\sigma_x(\sigma_y)$ is the bunch cross section in transverse plane. The designed Luminosity of LEP was 1.6 x 10^{31} $cm^{-2}s^{-1}$ for $E_{CM} \approx 91GeV$ and 2.7 x 10^{31} $cm^{-2}s^{-1}$ for $E_{CM} > 91GeV$ when LEP was upgraded to LEP-II

3.3.1 Experiments at the LEP

To study the different aspects of particle collisions at the LEP, the four different multipurpose detectors ALEPH, DELPHI, L3 and OPAL were built around four intersection points as shown in figure 3.4 where collisions between e^+ and e^- took place. All these four detectors are briefly described in the following section

- **ALEPH**: Apparatus for LEp PHysics (ALEPH) detector [7] was designed to explore the physics related to SM and also to search for physics beyond the

Standard Model. The ALEPH detector was constructed in cylindrical layers around a beam pipe which was made up of beryllium, with collision point between the e^+ and e^- at the middle. Moving in outwards directions from the beam pipe, ALEPH held a two layered double-sided silicon microstrips vertex detector. For each track, it measured two pairs of coordinates, 6.3 cm and 11 cm away from the beam axis over a length of 40 cm along the beam line; a time projection chamber(TPC) which was 4.4 metres long and had a diameter of 3.6 metres surrounded the inner track chamber. Its main purpose was to detect charged particles. An electromagnetic calorimeter, ECAL , to identify electrons and photons; a hadron calorimeter, HCAL, to detect hadrons; and a superconducting coil, 6.3 metres in length and 5.3 metres in diameter, to provide the 1.5 Tesla magnetic field necessary to work out a particle's charge and for the measurements of particle's momentum. The whole system was placed inside a 12-sided cylinder and surrounded by a muon-detection system. First events at ALEPH detector in LEP were measured in July 1989. Figure 3.5 represents the layout of ALEPH detector. Details of the detector can be found in reference [7].

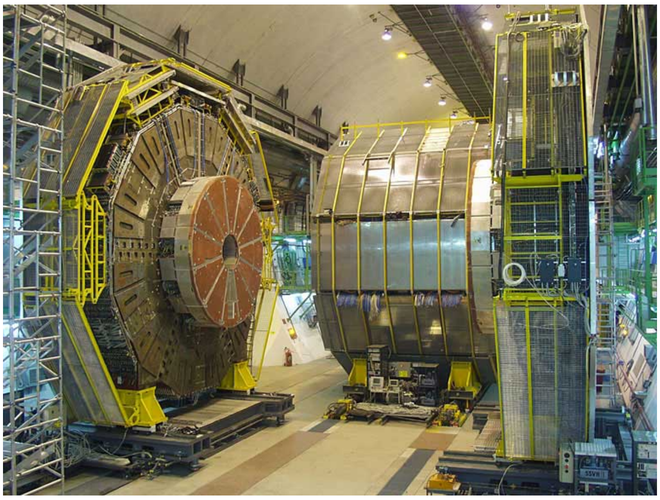

Figure 3.5: Layout of the ALEPH detector at the Large Electron Positron Collider. Image source: https://cds.cern.ch/record/1997342

- **DELPHI**: DEtector with Lepton, Photon and Hadron Identification (DEL-

PHI) detector [8] was composed of a central cylinder filled with subdetectors, with two end-caps , with length and diameter of 10 metres and weighed 3500 tonnes. A large superconducting magnet placed between an electromagnetic calorimeter and a hadronic calorimeter. The magnet produced a field to deflect charged particles, and to enable the measurements of their charge and momenta . The DELPHI detector used the ring imaging Cherenkov technique to individualized secondary charged particles and used an advanced silicon detector to detect short-lived particles by anticipating the tracks back towards the collision point.

- **OPAL**: The Omni-Purpose Apparatus at LEP (OPAL) detector [9] was about 12 m in length with height and width of 12 m. Detector components were arranged around the beam pipe, in a layered structure. OPAL's central tracking system consisted of a silicon microvertex detector, a vertex detector, a jet chamber, and z-chambers. In order to get the location of decay vertices of short-lived particles along with improvement in momentum resolution was the purpose of the silicon microvertex detector and the vertex chamber. Using the amount of ionization created by a particle and curvature of its track due to magnetic field, the central jet chamber was able to identify the particle. These chambers worked to identify tracks in the plane which are perpendicular to the beam axis. They were accompanied by "z-chambers" at the outside edge of the jet chamber. Further out from the beam pipe, OPAL's calorimeter system was subdivided into electromagnetic calorimeters, hadron calorimeters and forward calorimeters placed around, and close to the beam pipe at the two ends of the detector to catch particles sent forward by collisions in LEP. The end caps of the detector were formed by the Muon detectors.
- **L3**: L3 (It was named L3 due to the third Letter of Intent to be submitted for approval in 1982) detector [10] consisted of various subdetectors around the central beamline as shown in figure 3.6. The silicon strip microvertex detector and a time-expansion chamber were the first subdetectors out from the

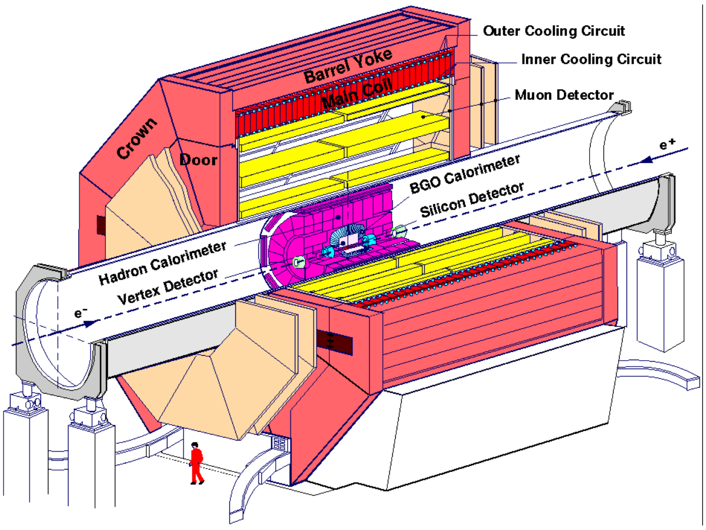

Figure 3.6: Schematic view of the L3 detector at the Large Electron Positron Collider. Image source: http://l3.web.cern.ch/l3/PR/index.html

beamline. Purpose of both the detectors was to trace the paths of charged particles from the collision. The three main outer layers of the L3 detector were an electromagnetic calorimeter, a hadronic calorimeter and a muon detector. Calorimeters, made up of dense material, measure the energy deposited by the particles. In between the electromagnetic and hadronic calorimeters, set of scintillation counters were placed to recognize and reject signals from energetic particles from space and cosmic ray muons that could disturb the measurements. The outermost layer of the detector was the magnet. It generated a magnetic field 10,000 times stronger than the average field on the Earth's surface. Magnetic fields are generally used in detectors to deflect charged particles and curvature of the deflection is used to calculate the momentum of particle .

The LEP accelerator was commissioned in July 1989 and the first beam in the collider was circulated on July, 14. For seven years the accelerator was operated at around 100 GeV and produced millions of uncharged carriers of the weak force, Z particles. For second operational phase, accelerator was upgraded with addition of 288 superconducting accelerating cavities to double the energy that led to the production of W bosons [11]. Energy in the LEP collider finally topped in the year 2000 with centre of mass energy 209 GeV. In the 11 years of its research the LEP experiments have provided the detailed study of electroweak interactions. Studies done using the LEP also proved the existence of three and only three generations of particles of matter. LEP experiments were shut down in November 2000 in order to make way for the construction of the LHC in the same tunnel.

3.4 The Tevatron

Tevatron was the proton-antiproton ($\bar{p}p$) particle accelerator and collider at Fermi National Accelerator Laboratory (Fermilab) in United States. It was world's highest energy collider until the Large Hadron collider (LHC) took over in 2010. The figure 3.7 shows the schematic view of the acceleration. The Tevatron was a synchrotron which accelerated antiprotons and protons in a 6.28 km circular ring to energies upto 900 GeV making centre of mass energy of 1.8 TeV. The collider was operated at centre of mass energy of 1.96 TeV until it was shut down on September 30^{th}, 2011.

In the Tevatron [12], particle beams travelling through a vacuum pipe were surrounded by superconducting electromagnets. The more than 1,000 superconducting magnets were used to bend the beam in a large circle and operated at 4° K. The acceleration occurred in a number of stages. In first stage, 750 KeV Cockcroft-Walton pre-accelerator ionized the hydrogen gas and then accelerated using a positive voltage. The ions then passed into the 150 meter long linear accelerator, LINAC, which used oscillating electrical fields for the acceleration of the ions upto 400 MeV. Ions were then passed through a carbon foil to remove the electrons and the charged protons then moved into the Booster, a small circular synchrotron where protons were passed up to 20,000 times in order to achieve $\sim$ 0.8 GeV of energy. Particles from the booster were passed to the main injector which accelerated the protons up to 120 GeV. The antiprotons were created by the antiproton Source. 120 GeV protons were collided with a nickel target which led to the production of antipro-

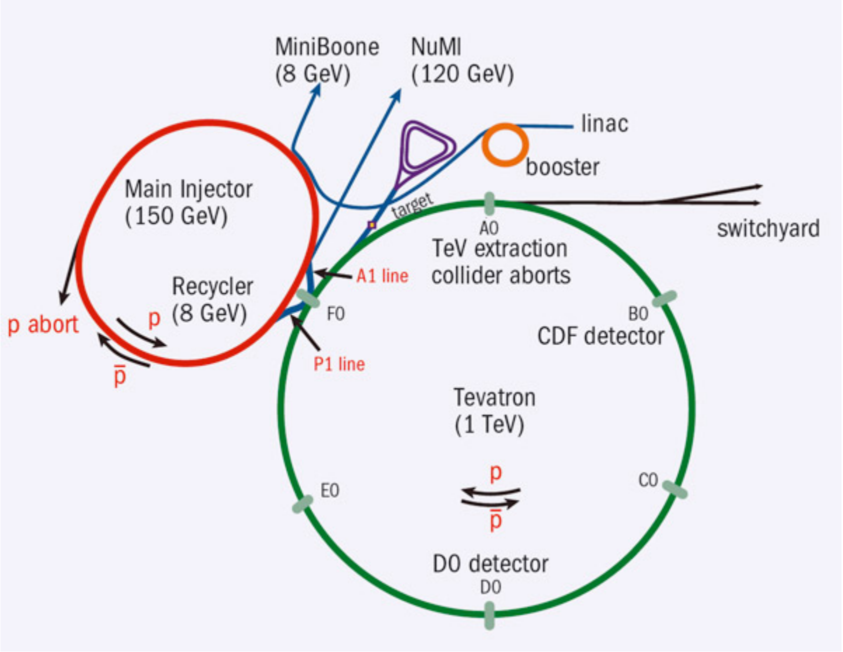

Figure 3.7: Schematic view of the Tevatron at Fermilab. Image source: http://images.iop.org/objects/ccr/cern/51/9/22/CCtev2_09_11.jpg

tons which were collected and stored in the accumulator ring. The accumulator ring then passed the antiprotons into the Main Injector. The particles from the Main Injector were accelerated by the Tevatron up to energy of 980 GeV. The protons and antiprotons were accelerated in opposite directions which were made to collide at $\sqrt{s} = 1.96$ TeV with their paths crossed in the CDF and DZero detectors.

3.4.1 CDF and DZero: Experiments at the Tevatron

CDF [13] and DZero [14]were the two detectors of the Tevatron which were built to register the collisions between protons and antiprotons. Each detector contained various subsystems for the detection of different types of particles coming out from collisions with the speed of particle approaching the speed of light c. Particle collisions created showers of new particles at the center of both the detectors. These detectors recorded each particle's flight path, electric charge, energy and momentum. In 1995, physicists from both the experiments announced the discovery of first top quark [15] ever produced at an accelerator, making it the major achievement of the collider.

3.5 The Large Hadron Collider : LHC

World's largest and the highest particle energy accelerator and collider, Large Hadron Collider (LHC), is located at CERN, Geneva where it spreads between the Swiss and French borders. The LHC [16] is built after disassembling the LEP collider in 2000, using the same old tunnel which was used in the LEP collider. It is installed in circular tunnel of 3.8 m in diameter with circumference of 27 Km, buried 50 to 175 m below the ground. It is designed to collide the oppositely moving proton beams with 7 TeV on 7 TeV energy producing a total of 14 TeV of energy in the center of mass system. It is in operation since 2012. The LHC has been built to answer key unresolved questions in particle physics including extension of the Standard Model and nature of Dark Matter.

Inside the accelerator, two proton beams travel at the speed close to the speed of light (0.99998c) with very high momentum and energies before colliding with each other. The beams rotate in opposite directions in two different beam pipes (tubes) which are kept at ultra high vacuum. They are surrounded around the accelerator ring by strong magnetic field. This strong field is achieved using the superconducting state which efficiently conducts electricity with almost zero resistance and zero energy loss. To achieve this state, magnets are required to be cooled at around 2° K, a temperature colder than outer space. Due to this reason, superconducting magnets of the accelerator are attached to a distribution system of liquid helium. Thousands of magnets of different sizes and varieties are used to keep the beams around the accelerator. It includes 1232 dipole magnets, with the length of 15 m each, to bend the beams, and 392 quadrupole magnets, each having length of 5 to 7 m, to focus the beams. Just prior to collision, another different kind of magnet is used to 'congesting' the particles closer together in order to increase the chance of collisions/interactions. The proton beams are bunched together in 2808 bunches

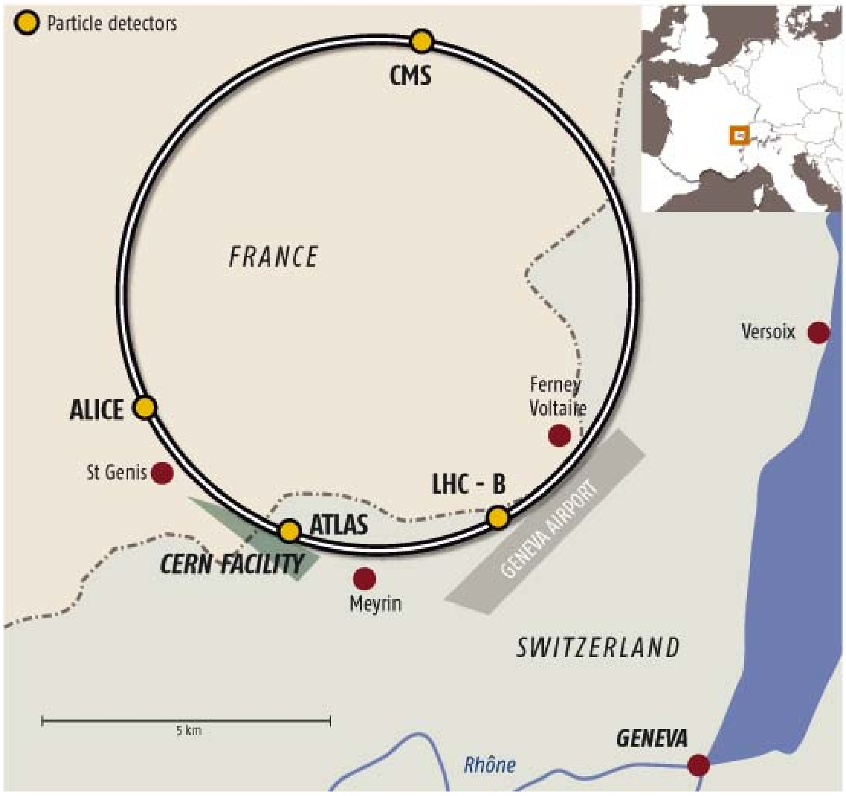

Figure 3.8: Overview of the Large Hadron Collider and its experiments. Image source: https://pure.uva.nl/ws/files/1084558/69147_06.pdf

spread in 27 km beam pipe, with bunch spacing of 25 ns. This means there will be discrete interactions at the interval of 25 ns. Other technical details of the LHC accelerator scheme can be found at [16]. The Luminosity of a collider is

$$\mathcal{L} = \frac{N^2 k f_{rev} \gamma}{4\pi \epsilon_n \beta^\star}$$

Where, N is the number of particles in each of the k circulating bunches, f is the revolution frequency, $\beta^\star$ is the value of the betatron function at the crossing point, ϵ_n is the emittance corresponding to one σ contour of the beam (nominal value 3.75 μm), γ is the Lorentz factor,

The LHC is just one part of the overall CERN particle accelerator facility. Protons or ions before entering the LHC have to go through a series of accelerating stages. First, the electrons are stripped from hydrogen atoms to produce protons.

Then, the protons enter the Linear Particle accelerator (LINAC-2), that fires beams of protons into the Proton Synchrotron Booster (PSB) to 50 MeV. The PSB uses radio frequency cavities to accelerate the protons up to 1.4 GeV. The cavities contain a radio-frequency electric field that pushes the proton beams to higher speeds and inject the beam to Proton Synchrotron (PS). Gigantic magnets generate the magnetic fields necessary to keep the proton beam on the circular track. When proton beam reaches at the appropriate energy level, the PS injects it into Super Proton Synchrotron (SPS) accelerator. The beams are divided into bunches and each bunch contains 1.1 x 10^{11} protons, with 2808 bunches per beam. The SPS injects beam into the LHC, with one beam travelling clockwise and another traveling counter clockwise. Inside the LHC, the beam continues to accelerate for around 20 minutes. At top speed, the beam makes 11,245 trips around the LHC every second. The two beams converge at one of the four detector sites positioned along the LHC and produce 600 million collisions per second. The layout scheme of the LHC accelerators is shown in figure 3.8 and its injection scheme is shown in figure 3.9. When particles collide at such high energies, they break down into smaller constituent particles, called quarks and gluons which further undergo fragmentation to produce subatomic particles such as pions, protons, kaons etc. The detectors collect the information by recording the paths of subatomic particles or information on the energy deposited in the subdetectors. These detectors are very complex in terms of their geometry and various components are discussed below.

3.5.1 Experiments at the LHC

Different aspects of particle physics are under study using the LHC. To achieve these physics goals, detectors have been installed at four main interaction points. The various interaction points at the LHC are shown in figure 3.10. These four main experiments are :

- **A Toroidal LHC Apparatus (ATLAS)** : ATLAS [17] is one of the two general-purpose detectors at the LHC. It is investigating a broad area of

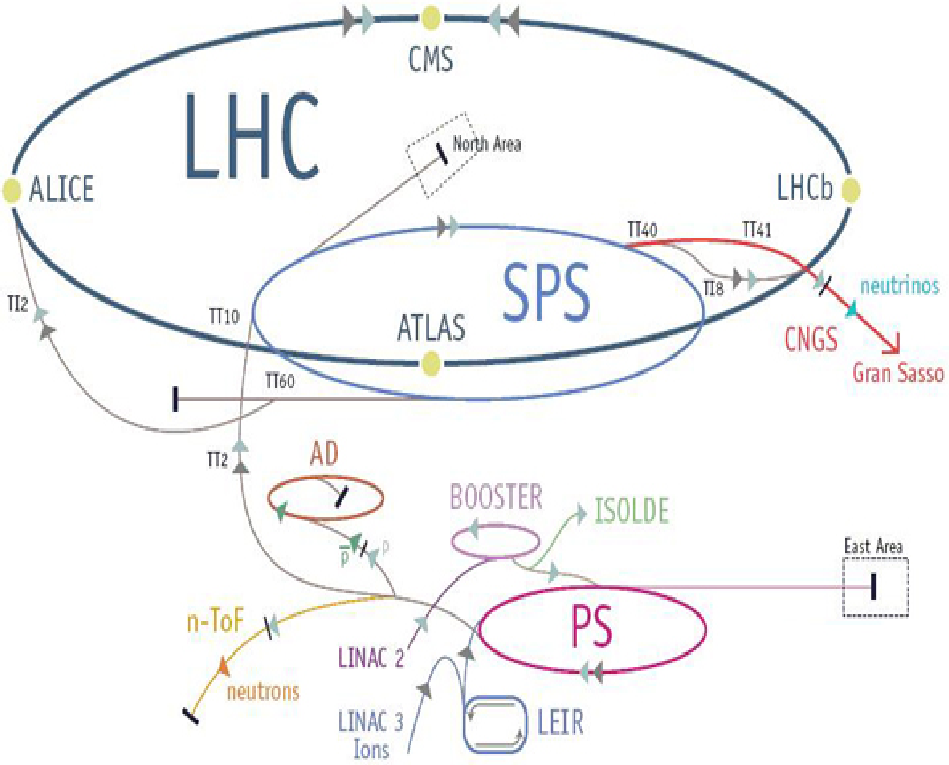

Figure 3.9: Injection scheme at the Large Hadron Collider. Image source: http://a403.idata.over-blog.com/2/66/75/34/20-mai/LHC.jpg

physics which includes search for possible candidates of dark matter and extra dimensions. ATLAS is recording set of measurements on the particles created in collisions; particle's path, identities, and their energies. This is carried out in the ATLAS using six different detecting subsystems which identify particles and measure their energy and momentum. One of the important elements of the ATLAS is it's huge magnet system which bends the paths of charged particles for the measurement of momentum. To digest these data, the ATLAS made a very advanced trigger and data acquisition system, and a large computing system. More than 3000 physicists from over 175 institutes in 38 countries work on this experiment.

- **A Large Ion Collide Experiment (ALICE)**: For the ALICE experiment

[18], the LHC collides lead ions to regenerate the conditions prevailing soon after the the Big Bang when the Universe was extremely dense and hot. Data from the experiment allows scientists to study a state of matter, quark-gluon plasma, believed to have existed soon after the Big Bang. Ordinary matter of the Universe is made up of atoms, each atom containing a nucleus comprised of neutrons and protons, surrounded by an electron cloud. Protons, neutrons are composed of quarks which are bound together by the gluons. Collisions at high energies generate the temperatures more than 100,000 times hotter than the core of the Sun. It is believed that at such high temperatures, the proton and neutron will 'melt', thus freeing the quarks from the gluon bonds and creating a state of matter called quark-gluon plasma. The ALICE collaboration studies this quark-gluon plasma as it expands and cools, investigating how progressively it gives rise to the particles that constitute the matter of our Universe today.

- **Compact Muon Solenoid (CMS) Experiment**: The CMS experiment [19] is a general purpose detector. It has a broad physics programme ranging from studying the SM physics including the discovery of the Higgs Boson, to searching for extra dimensions and the dark matter. Although it has very similar scientific goals as the ATLAS experiment, however it uses different technical solutions and design of its detector magnet system to achieve the goals. The CMS detector is built around a huge solenoid magnet while the ATLAS uses toroidal magnet. This takes the form of a cylindrical coil of superconducting cable that generates a magnetic field of 4 T, about 100000 times that of the Earth. The magnetic field is confined by a steel 'yoke' that forms the bulk of the detector's weight of 14000 tonnes. An unusual feature of the CMS detector is that instead of being built underground, like other giant detectors of the LHC experiment, it was constructed on surface, before being lowered underground in 15 sections and reassembled.
- **LHC-beauty (LHCb)**: The LHCb [20] is the specialized experiment to study

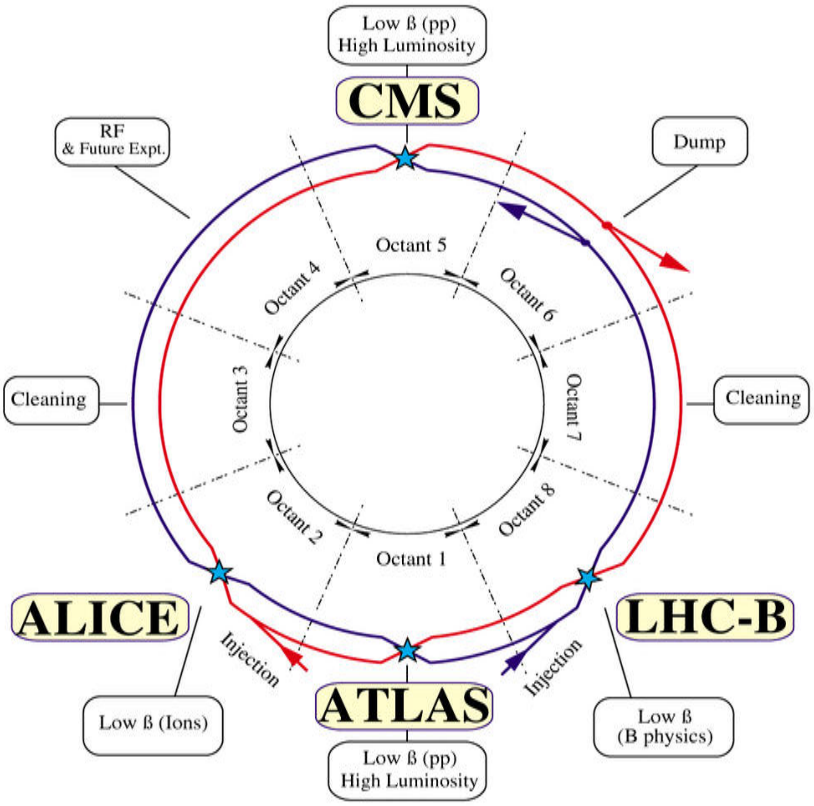

Figure 3.10: Various detector systems at the Large Hadron Collider. Image source: https://cds.cern.ch/record/841573

the b-physics and to understand why we live in a Universe that appears to be composed almost of matter, but no antimatter. It specializes in investigating the difference between matter and antimatter by studying the ‘beauty quark’, or ‘b quark’. Instead of surrounding the entire collision point with an enclosed detector, the LHCb experiment uses a chain of sub-detectors to detect forward particles. The first sub-detector is placed close to collision point, while the next one stands one behind the other, over a length of 20 m. An abundance of different types of quarks will be created by the LHC before they decay quickly into other forms. To catch the b-quarks, LHCb has developed sophisticated movable tracking detectors close to the path of the beams circling in the LHC.

3.6 The CMS Detector

The Compact Muon Solenoid (CMS) is one of the two multi-purpose detectors at the LHC which is designed to establish the SM predictions including discovery of Higgs boson [21,22], as well as for the study of the new sectors of physics beyond Standard Model (BSM) like SUSY particles and candidates for Dark Matter. Discovery of Higgs boson, in 2012 is one of the major achievements of the CMS experiment. Higgs is a particle which is responsible for the masses of quarks. The CMS detector has a cylindrical symmetry around the beam pipe in the radial direction and is placed at the Point 5 (P5) interaction point of the LHC, inside an underground cavern at Cessy in France. The detector is placed in such a way that it coincides with the pp collision point. It has a cylindrical symmetry about the center of the detector along the beam pipe. The central part covers the big barrel region and the structure is closed with the endcaps on both the sides. The CMS detector is used not only to study the pp collisions, but also the heavy ion (Pb) collisions.

The CMS detector is a hermetic detector of length 21.5 m with diameter of 15 m and total weight of 14000 tons. It is designed with a 3.8 T solenoidal magnetic field provided by the largest superconducting magnet ever built. The solenoid is 13 meters long with an inner diameter of 5.9 meters. Inside the solenoid, inner tracker and calorimeters are located and layers of muon stations are placed outside the solenoid on both the barrel and endcap sides. The structure of the CMS detector is shown in figure 3.11.

3.6.1 The CMS Co-ordinate System

The CMS experiment uses a right-handed coordinate system, with the origin at the nominal interaction point, the x-axis pointing to the centre of the LHC ring, the y-axis pointing up (perpendicular to the plane of the LHC ring), and the z-axis along the anticlockwise-beam direction. The azimuthal angle, ϕ is measured from the x-axis in xy-plane and the radial coordinate in this plane is represented by r.

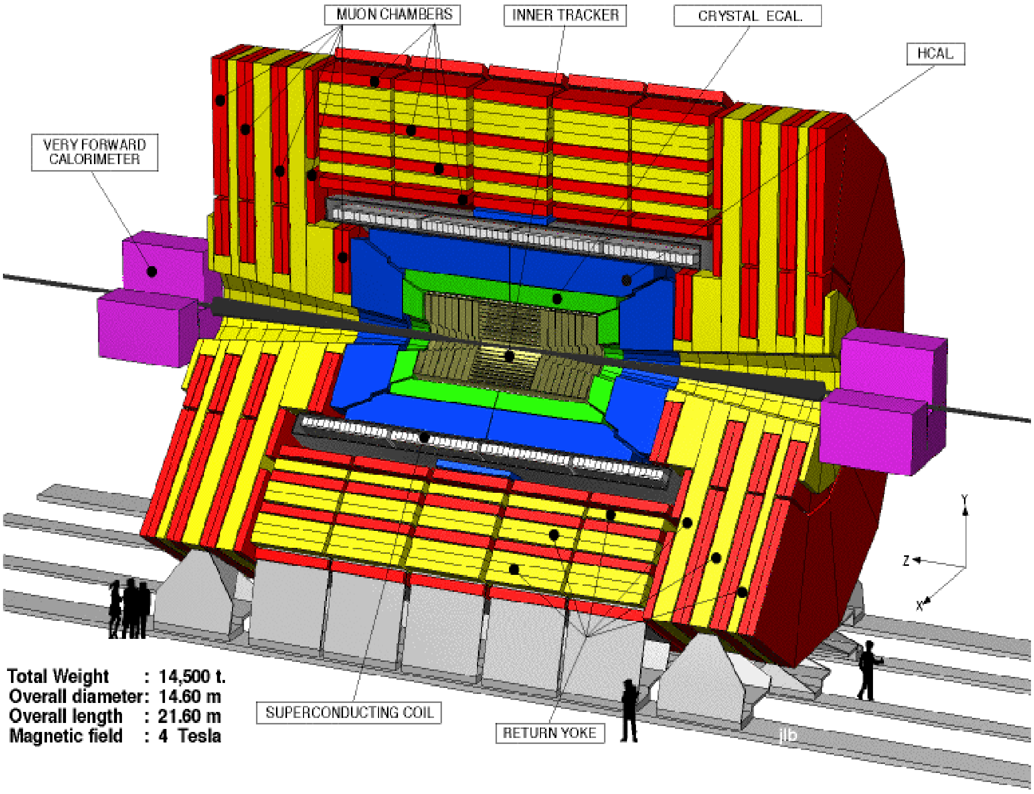

Figure 3.11: Overview of the Compact Muon Solenoid detector. Image source: http://www.phys.ufl.edu/hee/cms/images/CMSdetc3D.gif

The polar angle θ is measured from the positive z-axis. It is preferred to use a quantity, pseudorapidity, in place of θ, because the pseudorapidities are Lorentz invariant under the boost along the z-axis. The pseudorapidity is defined as:

$$\eta = -ln\left(tan\frac{\theta}{2}\right) \tag{3.3}$$

The region within pseudorapidity range, $|\eta| < 2.5$, is known as central region, whereas the region with $|\eta| > 2.5$ is known as forward region. The longitudinal view of one quadrant of the CMS is shown in figure 3.12.

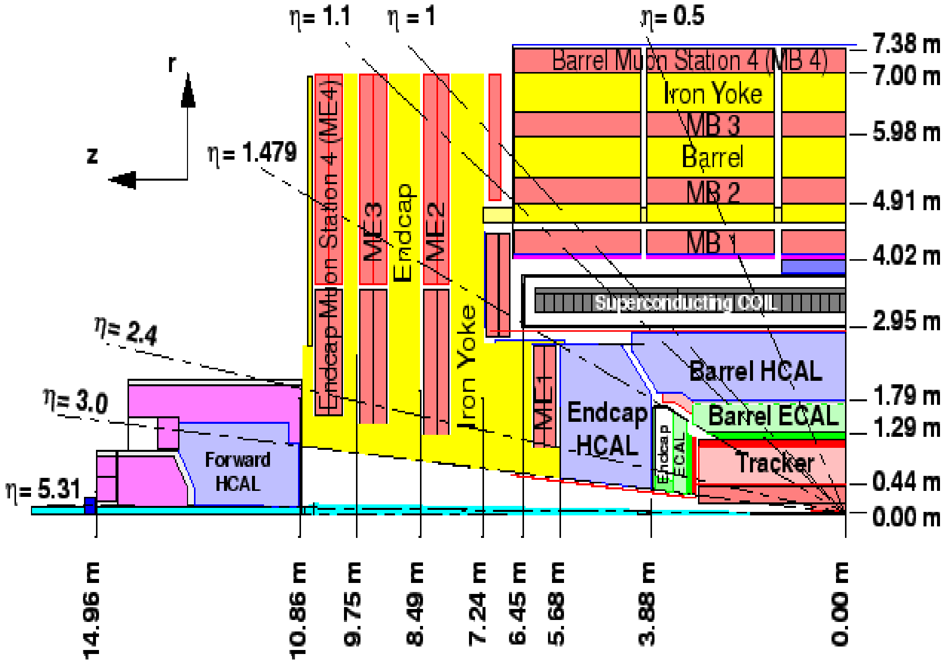

Figure 3.12: One quadrant of the CMS detector in Longitudinal mode. Image source: http://www.hephy.at/user/friedl/diss/html/node8.html

3.6.2 The CMS Tracking System

To get efficient measurement of charged particles produced during pp collisions, the tracking system [23, 24] of the CMS tracker is designed. It has a length of 5.8 m and a diameter of 2.5 m. The tracker system is located inside the superconducting magnet and surrounds the interaction region. The CMS solenoid is designed to provide a homogeneous magnetic field of 3.8 T over the full volume of the tracker. Since a large number of tracks are required to be processed using the information from the tracker. the CMS tracking system is required to have high granularity and fast response. The two dimensional layout diagram of the CMS tracking system is shown in figure 3.13.

The CMS tracking system has an active surface area of 200 m^2. The charged particle reconstruction efficiency, provided by the CMS tracking system is higher than 95% for the particles with p_T larger than 1 GeV/c within absolute pseudorapidity range of 2.5. The information from the CMS tracker is used for the High

Level Triggering, which reduces the event collection rate and the amount of storage to great extent. The CMS tracking system is entirely based on the Silicon sensors and is composed of pixel and strip detectors which are described below

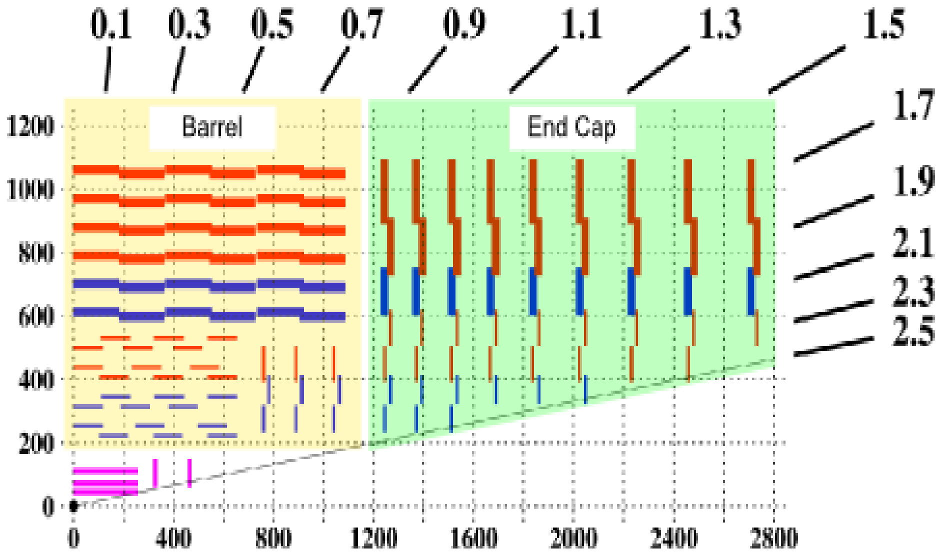

Figure 3.13: Layout diagram of the CMS Tracking system. Image source: http://cms.desy.de/e53612/e155175/e155179/

- **Silicon Pixel detector** : The innermost part of the CMS detector is covered by the pixel detector, which consists of 1440 pixel modules [24]. These pixel modules are arranged in three barrel layers, known as BPIX, of radii of 4.4 cm, 7.3 cm and 10.2 cm with a length of 53 cm. In addition to BPIX, there are four disks (FPIX), two at each side of the BPIX, i.e., in the forward region. The FPIX disks are at a distance of 34.5 cm and 46.5 cm on both sides of the interaction point. The tracker includes around 66 million pixels, each with dimensions of 100 x 150 μm. The resolution of the measurement from high precision points is obtained in the pixel detector from the trajectory of the charged particle within the pseudorapidity range of 2.5. The resolution of measurement by a pixel module is 13 μm, 30 μm and 20 μm along x-direction, y-direction and longitudinal z-direction, respectively.
- **Silicon Strip detector**: The intermediate radial region ($20 < r < 116$ cm) is

covered by the silicon strip tracker, where the particle flux is relatively small as compared to the region of pixel detector. This enables the use of bigger sized detectors. The dimensions of a silicon strip detector are 10 cm x 180 μm, for the inner part of the detector and 25 cm x 180 μm, for the outer part of the detector, which covers the surface area of around 200 m^2. There are around 9.3 million read-out channels for the strip detector.

3.6.3 Electromagnetic Calorimeter

Electromagnetic Calorimeter (ECAL) [25] is designed to measure the energy of particles like electrons, positrons and photons, which interact via electromagnetic interactions. The ECAL is a hermetic homogeneous calorimeter, which is based on the production of a shower initiated by an electron/positron or a photon inside an absorber. The photons, in particular, get converted into electron-positron pairs by the phenomenon of the pair production. The electrons and positrons undergo the phenomenon of bremsstrahlung, in which a photon is emitted. Such kind of successive conversions continue until the energy of the photon falls below the threshold limit of pair production. Actually the energy of the initial particle is shared equally by the final state particles. The average length, traversed by a particle in order to produce the aforementioned emissions, is known as 'radiation length' (X_0) [1]. An electromagnetic shower also gets developed in the transverse plane. A term 'Moliere radius' is associated with the shape of the shower in the transverse plane. It represents the radius of the cylinder in which 90 % of the total energy of the shower is deposited. Moliere radius, as well as radiation length are specific to the choice of material.

The ECAL of the CMS detector is composed of 61,200 lead tungstate (PbWO4) crystals in the central barrel region and about 7,234 crystals in each of the two endcaps on both sides of the barrel region. The lead tungstate material is of high density (8.28 g/cm^3) with small Moliere radius (2.2 cm) and small radiation length

---

[1] It is the average distance travelled by an electron/positron or photon over which its energy reduces by a factor of 1/e.

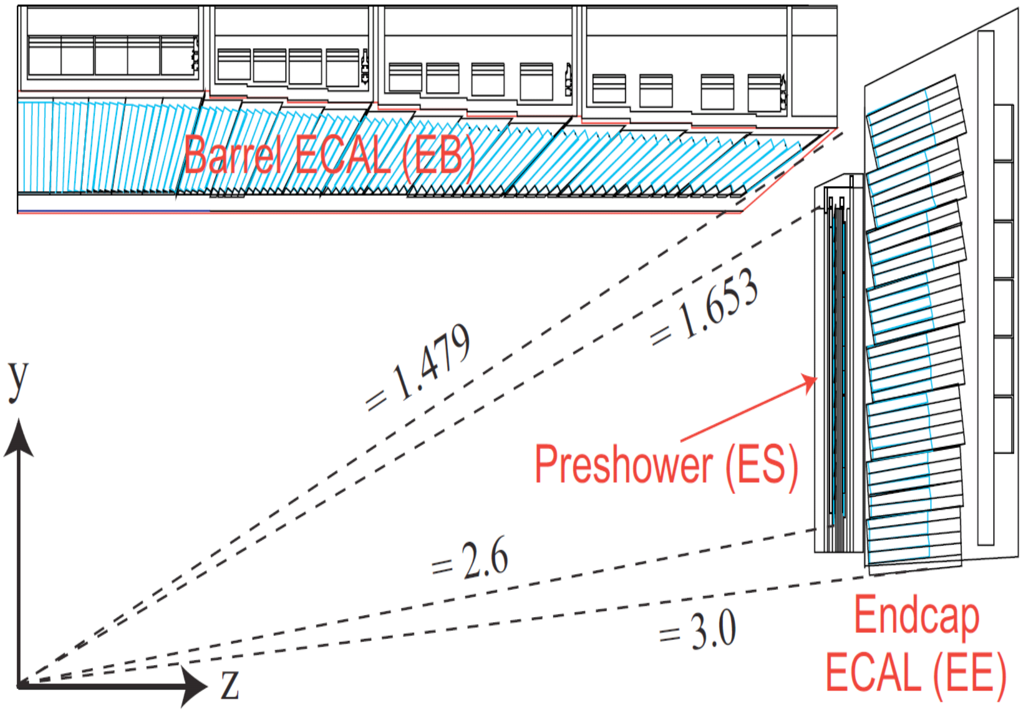

Figure 3.14: ECAL system used in the CMS detector at the LHC. Image source: http://www.t2.ucsd.edu/twiki2/pub/UCSDTier2/ParticlePhysics2013/ecal-presentation.pdf

(0.89 cm). It is the best material for the ECAL of CMS detector, due to its good radiation tolerance power and fast response time. The phenomenon of total internal reflection is used to transmit the light signal produced by electrons, positrons, photons and charged particles due to the scintillation process. To detect the light signals produced by scintillation, avalanche photo-diodes (APDs), Silicon sensor based photodetector, and vacuum photo triodes (VPTs) are employed in the barrel and endcaps, respectively. This light signal is converted to electrical signal by these devices. A scintillation photon knocks out an electron out of Silicon atom on striking it. The electron thus produced, gets accelerated in the applied electric field and strikes other atoms to produce an avalanche of electrons. Thus a very high current is produced in a short time with the use of the APDs even with the relatively low yield of light produced by the lead tungstate crystals for each incident particle. The signal is then amplified, digitized and immediately transported away by fibre optic cables to perform the analysis.

The schematic view of the ECAL system of the CMS detector is shown in figure 3.14. The inner radius of the barrel section (EB) of the ECAL sub-detector is 129 cm and is organized with 36° supermodule covering the pseudorapidity region, $|\eta| < 1.479$. A supermodule is constructed using four modules and each module is equipped with five pairs of crystals. The length of each crystal is 230 mm which corresponds to radiation length of 25.8X0. The front-face cross section of the crystal is 22 mm x 22 mm. The endcaps (EE) of the ECAL are at a distance of 3.14 m from the interaction point covering the pseudorapidity region, $1.479 < |\eta| <3.0$. Each endcap is composed of the semi-circular aluminium plates, where 25 crystals are arranged in an array of 5 x 5 super-crystals. Each crystal has a front face cross-section of 28.6 mm x 28.6 mm with a length of 0.22 m, which corresponds to the radiation length of $25X_0$.

3.6.4 Hadronic Calorimeter

To measure the energy of a hadronic jet, the CMS hadronic calorimeter (HCAL) [26] which is a sampling calorimeter, is used. The HCAL plays a crucial role in identification of the particles produced during proton collisions. The particles like neutrinos do not interact with the detector material but they may also be detected indirectly using conservation of the momentum in transverse plane, i.e., missing transverse energy. Hadron shower in the HCAL is produced by inelastic interactions of hadrons with the material of the detector. Energy of the incident hadrons is released by the nuclear excitation and hadron production along with the production of other additional particles. As compared to the term radiation length used for the ECAL, the term interaction length (λ_t) is used for the hadron showers [2]. A hadronic shower is wider and longer as compared to the electromagnetic shower. Since the radiation length of the electromagnetic shower is smaller than that of the interaction length of the hadronic shower, ECAL is placed in front of the HCAL.

---

[2] It is defined as the distance traversed by a hadron to lose energy by a factor of 1/e

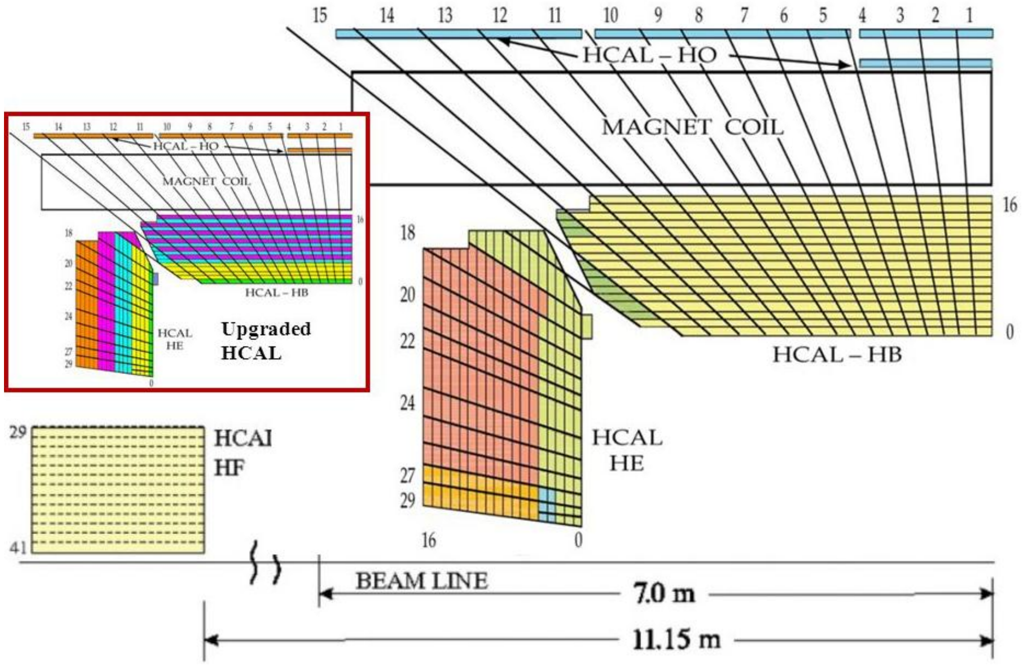

Figure 3.15: Layout diagram of the HCAL system of the CMS detector. Image source: http://images.slideplayer.com/35/10426478/slides/slide_13.jpg

The HCAL is not completely immersed in the magnet coil, due to the shortage of space between the solenoid and the ECAL. The layout diagram of the HCAL subsystem of the CMS detector is shown in figure 3.15. The HCAL has four sections, an inner hadron barrel (HB), an outer detector (HO), an endcap part (HE) and a forward calorimeter (HF)

The HCAL is made up of repeating layers of dense absorber and tiles of plastic scintillator. The hadronic shower produced by the particles passing through HCAL causes the scintillator tiles to emit blue-violet light. The optical signals are converted into fast electronic signals by photosensors called Hybrid Photodiodes (HPDs). HPDs are photodetectors configured especially for the CMS that can operate in a high magnetic field and give highly amplified response, in proportion to the original signal, for a large range of particle energies. The HPDs are housed in special readout boxes within the calorimeter volume. The light signals from the calorimeter are delivered to the HPDs by special fibre-optic waveguides and then sent to data acquisition system (DAQ system) for purposes of event triggering and event reconstruction. When the HCAL was initially proposed, HPD was the only viable solution for the detection of scintillation light in the high magnetic field environment. A new technology for the Photo-sensors has emerged. It uses the Silicon Photomultiplier (SiPM), which offers higher photon-detection efficiency and signal gain. To improve the performance of the HCAL subsystem, the HPDs have been replaced by SiPMs during 2013-14 when the LHC was shut down for long duration.

3.6.5 Superconducting Magnet

Magnetic field plays very significant role in any collider experiment for the identification of charged particles. A very strong magnet [27] is required in order to induce the sufficient bending of the charged particles and help to measure the charge and momentum of each of these particles. The superconducting magnet for the CMS detector has been designed to reach a 4 T field in a free bore of 6 m in diameter and 12.5 m length with a stored energy of 2.6 GJ at full current. However, due to technical reasons, it is being operated at 3.8 T. The flux is returned through a 10,000 ton yoke comprising of 5 wheels and 2 endcaps, composed of three disks. Figure 3.16 shows artistic view of the CMS solenoidal magnet. The strong magnetic field provides a very compact layout to the CMS detector along with the efficient particle detection.

3.6.6 The CMS Muon System

One of the most important tasks of the CMS detector is detection of the muons. As the name suggests, precise and robust measurement of muons is the central theme of the CMS detector. Muons can penetrate several meters of iron without interacting, whereas the other particles can be stopped by the time they cross the Calorimeter. Therefore, the muon system is situated at the edge of the CMS detector. It is a very powerful tool for recognizing the signature of interesting physics processes, e.g., decay of Higgs boson into four muons, which is also considered as the golden channel

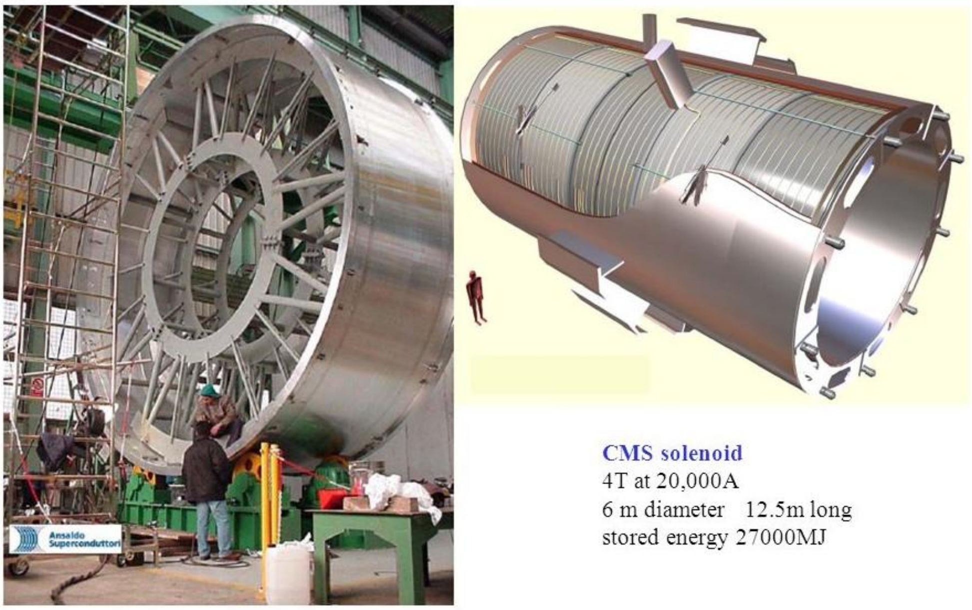

Figure 3.16: View of Superconducting magnet used in the CMS detector. Image source: https://images.slideplayer.com/36/10648021/slides/slide_21.jpg

for the Higgs studies. The functions of the muon system [28] include identification of the muons, their charge and momentum measurements and triggering.

The muon system of the CMS detector provides good momentum resolution and triggering capability, with the help of high field solenoidal magnet and its flux-return yoke. The muon system of the CMS is designed to measure the muons with momentum over a large range. The layout diagram of the muon system of the CMS detector is shown in figure 3.17. The CMS detector uses following three types of gaseous particle detectors for muon identification:

- **Drift tubes (DTs)** : The drift tubes (DTs) of the muon subsystem, covers pseudorapidity range, $|\eta| < 1.2$. It consists of five wheels each wheel is divided into 12 sectors, each of the sectors consists of four chambers, one chamber resides inside the magnet return yoke and one chamber is outside the magnet return yoke. The remaining two chambers are sandwiched in between the magnet return yoke. Each DT chamber consists of either two or three superlayers

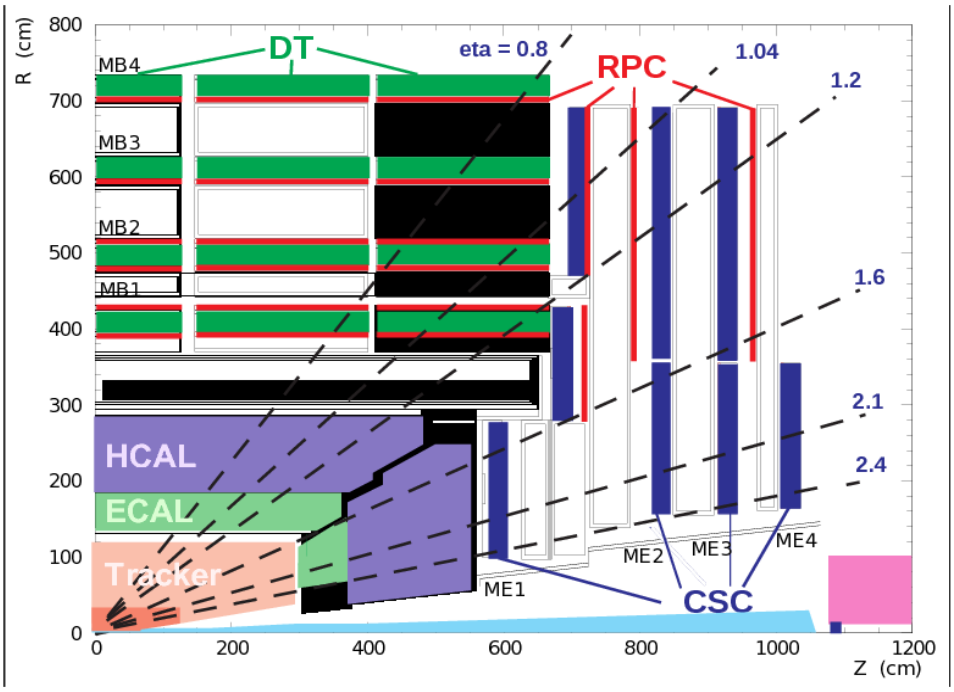

Figure 3.17: Layout diagram of the Muon System of the CMS detector. Image source: https://cds.cern.ch/record/1456510

(SL); each SL, which is a combination of four consecutive layers of thin tubes staggered by half a tube, gives excellent time-tagging capability, with a time resolution of a few nanoseconds. This capability provides local, stand-alone and efficient bunch crossing identification. The design and the precise mechanical construction of the DT chamber allows to achieve 100 pm precision in global r-ϕ position measurement.

- **The Cathode strip chambers (CSCs)**: The CSCs provide precise tracking and triggering of muons in the endcaps and hence constitute an essential component of the CMS muon system. The performance of the CSCs is critical to many physics measurements based on muons. The pseudorapidity region, $0.9 < |\eta| < 1.2$, is covered by both the DT chambers and CSC. There are 468 CSCs in the two muon endcaps. Each endcap consists of 4 stations of chambers, labelled ME1 to ME4 in order of increasing distance from the interaction point, which are mounted on the disks enclosing the CMS magnet, perpendicular to the beam direction. In each disk, the chambers are divided into two concentric rings around the beam axis (3 for ME1 chambers). Each CSC, trapezoidal in shape, consists of six gas gaps. For each of the gas gaps, there is a plane of radial cathode strips and a plane of anode wires perpendicular to the strips. To avoid the gaps in muon acceptance, the CSC chambers are overlapped except for the ME1/3 section. There are 36 chambers in each ring of the muon station, except for the innermost (high 77) rings of ME2-ME4, which have 18 chambers. A CSC consists of arrays of positively-charged anode wires crossed with negatively-charged copper cathode strips within a gas volume.

- **Resistive plate chambers (RPCs)** : RPCs are gaseous parallel-plate detectors that combine adequate spatial resolution with a time resolution comparable to that of scintillators. RPC is capable of tagging the time of an ionizing particle in a much shorter time as compared to the 25 ns between the LHC bunch crossings (BX). Therefore, a fast dedicated muon trigger device based on RPCs can identify unambiguously the relevant BX to which a muon track is associated with, even in the presence of the high particle rate and background expected at the LHC. Signals from such a device directly provide the time and position of a muon hit with the required accuracy. The RPC detectors are employed in the CMS as a dedicated trigger system in both the barrel as well as in the endcap regions. They complement the muon tracking system: DTs in the barrel and CSCs in the endcaps. From the geometrical point of view, the muon system is divided into five wheels in the barrel and four disks in each endcap. Each barrel wheel is divided into 12 sectors, covering the full azimuthal dimension. Each sector consists of four layers of DTs and six layers of RPCs, a total of 480 RPC stations covering average area of 12 m^2. The two innermost DT layers are sandwiched between RPC layer (RBlin and RB 1 out for the innermost RB 2in and RB 2out for the second one). The third and the fourth DT layers are complemented with a single RPC layer, placed on their inner side (RB3 and RB4).

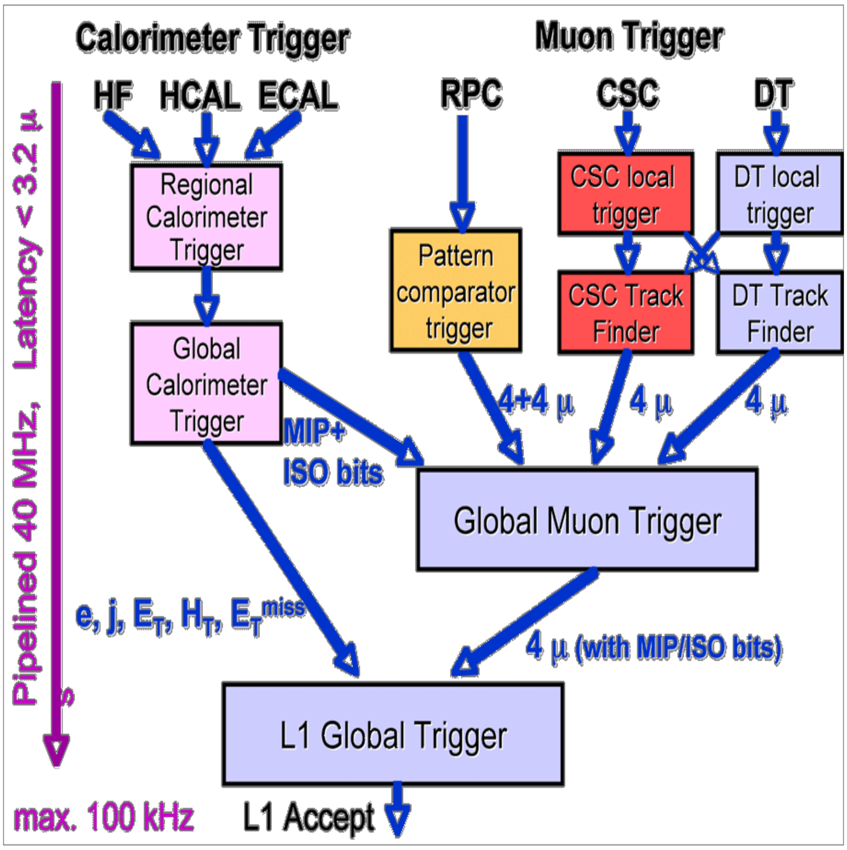

Figure 3.18: Flow diagram of Level 1 trigger system of the CMS detector. Image source: http://cms-global-muon-trigger.web.cern.ch/cms-global-muon-trigger

3.6.7 The CMS Trigger System

The interaction rate of pp collisions at the LHC is very high. The beam crossing interval for protons is 25 ns, which corresponds to a crossing frequency of 40 MHz. A number of collisions occur at each crossing of the proton bunches but it is not possible to store and process the large amount of data associated with these events. The number of events needs to be reduced in order to be processed and stored. The CMS trigger system performs this task, in two steps known as: Level-1 (L1) Trigger [29] and High-Level Trigger (HLT) [30].

The L1 Trigger consists of custom designed, largely hardware based programmable electronics, whereas the HLT is a software based system implemented using about one thousand commercial computer processors. The design output rate limit of the L1 Trigger is 100 kHz, which uses coarsely segmented data from the Calorimeters and the muon system, while holding the high-resolution data in pipelined memories in the front-end electronics. The L1 Trigger System is organized into three major subsystems: the L1 Global Calorimeter trigger (GCT), the L1 Global Muon trigger (GMT) and the L1 Global trigger (GT). The muon trigger is further organized into subsystems representing the three different muon detector systems. The L1 muon trigger also has a global muon trigger that combines the trigger information from the DT, CSC and RPC subdetectors. The Global trigger takes the decision to reject an event or to accept it for further evaluation by the HLT. The decision is based on algorithm calculations and on the readiness of the sub-detectors and the DAQ system, which is determined by the Trigger Control System (TCS). The Level-1 Accept (L1A) decision is communicated to the sub-detectors through the Timing, Trigger and Control (TTC) system. The architecture of the L1 Trigger is depicted in figure 3.18. The L1 Trigger has to analyze event information for every bunch crossing. The allowed Ll Trigger latency, between a given bunch crossing and the distribution of the trigger decision to the detector front-end electronics, is 3.2 μs. The processing must therefore be pipelined in order to enable a quasi-deadtime free operation. The L1 Trigger electronics is housed partly on the detectors, partly in the underground control room located at a distance of approximately 90 m from the experimental cavern.

The architecture of the CMS detector DAQ system is shown schematically in figure 3.19. The CMS Trigger and DAQ system is designed to collect and analyze the detector information at the LHC bunch crossing frequency of 40 MHz. The DAQ system must sustain a maximum input rate of 100 kHz and must provide enough computing power for a software filter system, the HLT, to reduce the rate of stored events by a factor of 1000. Thus, the main purpose of the DAQ and HLT system is to read the CMS detector event information for those events that are selected by the Ll Trigger and to select, from amongst those events, the most interesting ones for output to mass storage. The proper functioning of the DAQ at the desired performance is a key element in reaching the physics potential of the CMS experiment. To summarize, the online event filtering process in the CMS experiment will be carried out in two steps:

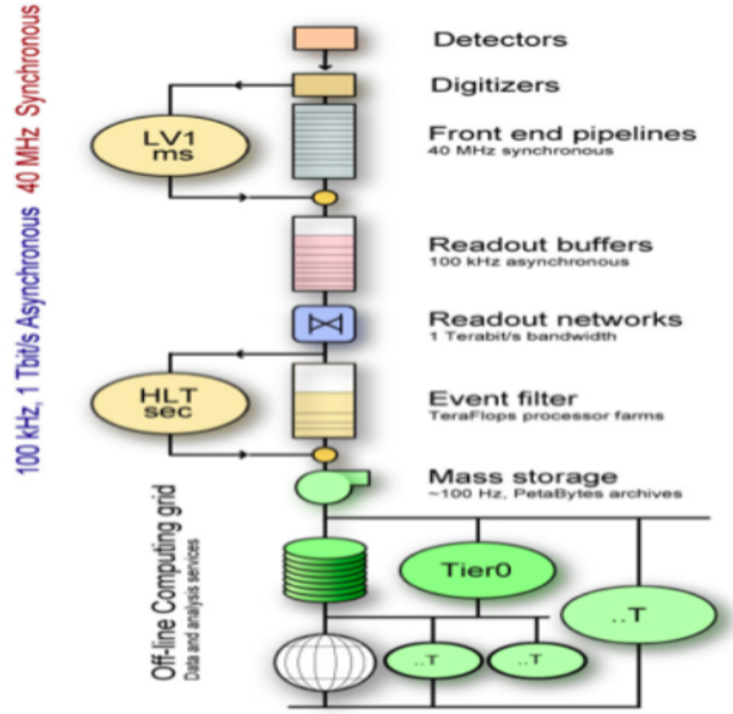

Figure 3.19: Structure of the trigger system used in the CMS detector. Image source: http://andreyoon.com/images/cmstrigger.png

- The L1 Trigger, with a total processing time of 3 μs, including the latencies for the transport of the data and control signals. During this time interval, the data is stored in the pipeline memories in the front-end electronics. The L1 Trigger is designed to accept a maximum rate of 100 kHz.

- The HLT, with a total processing time of up to $\sim$ 1s. During this time interval, the data are stored in random-access memories. The HLT is designed to provide maximum output of mean event rate of $\sim$ 100 Hz.

3.7 Detection of Particles in the CMS Detector

The detectors, designed to discover new particles, must be designed to observe all possible decay products and should be capable of measuring their position and energy very accurately. A transverse view of the CMS detector in the form of a slice is shown in figure 3.20. The detection of particles in the CMS detector, upon interaction with the detector material is explained below:

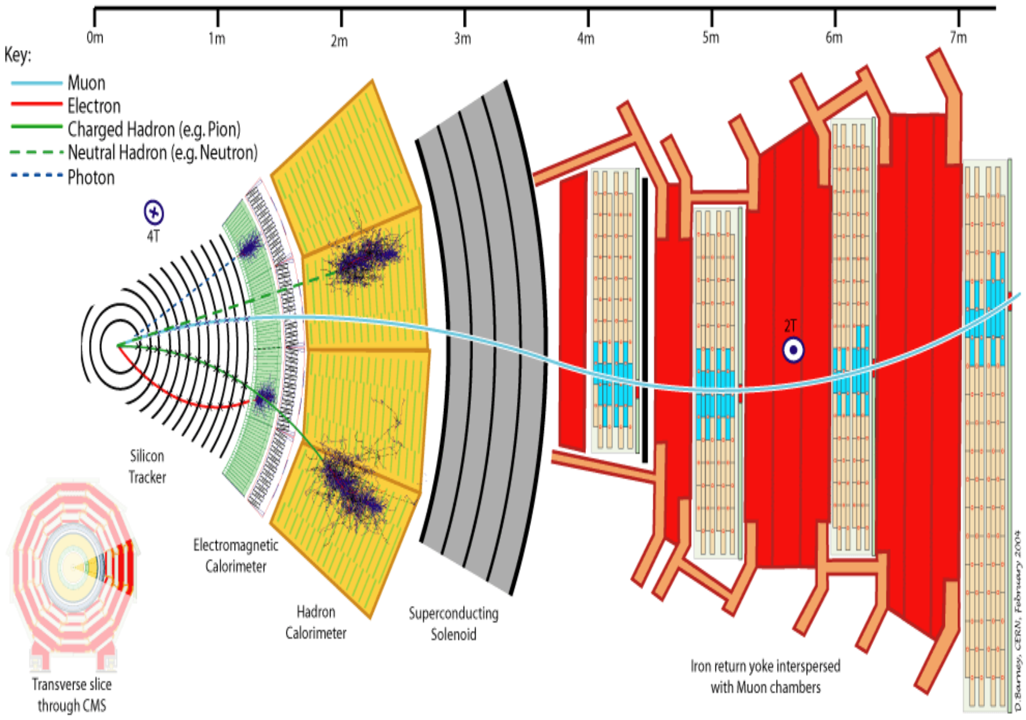

Figure 3.20: Particle detection in the CMS detector at the LHC. Image source: https://cds.cern.ch/record/2205172/files/CMS Slice.gif

- The particles produced at the interaction point have to first pass through the CMS tracker system, which is purely Silicon based. A charged particle, upon passing through the tracker, creates the electron-hole pairs, which are collected by the electrodes to provide the signal. The signals from different silicon pixels and strips are combined to form the track of the charged particles.
- The particles, after passing the tracker region, enter the ECAL, where the electrons and photons deposit most of their energy by electromagnetic interactions,

e.g. ionization, bremsstrahlung, pair production, Compton scattering, etc. An energetic electron, while passing through the ECAL, radiates photons through bremsstrahlung. If the energy of the bremsstrahlung photon is sufficiently high, it will produce an electron-positron pair through pair-production. Each of the partners of pair production will then radiate photons. The processes of bremsstrahlung and pair-production will then result into an "electromagnetic shower". The growth of this shower will continue until the secondary particles are no longer capable of multiplying. The energy loss by an electron is characterized in terms of radiation length, which is defined as the distance over which the electron loses (1/e) fraction of its energy by radiation loss only.

- After passing through the ECAL, the particles enter the HCAL, where the charged and neutral hadrons deposit their energy. A hadron, upon passing through the HCAL material, builds up a shower through multiple strong interactions, resulting in the production of a large number of particles in each secondary interaction. This process results into hadron shower development.
- The next layer in the CMS detector is of muon chambers. At the end of the HCAL, only muons and neutrinos survive. The neutrinos do not interact with detector material, at all. The muons, being weakly interacting massive charged particles, also interact with the ECAL and the HCAL
- In the muon chamber, the muons are detected by the information obtained from the DT, CSC and RPCs

Bibliography

[1] M. Conte and W. W. MacKay, “An Introduction to the Physics of Particle Accelerators ”, World Scientific Publishing Co. Pvt. Ltd. (2008)

[2] J. D. Cockcroft and E. T. S. Walton, “Experiments with High Velocity Positive Ions.-(I) Further Developments in the method of obtaining High Velocity Positive Ions”, Proceedings of the Royal Society A **136**, 619 (1932)

[3] R. J. Van de Graaf et. al., “The Electrostatic Production of High Voltage for Nuclear Investigations”, Phys. Rev. **43 (3)**, 149 (1933)

[4] R. B. Neal, “ The Stanford Two-Mile Accelerator”, W. A. Benjamin, Inc., New York (1968)

[5] O. E. Lawrence and M. S. Livingston, ”The Production of High Speed Light Ions Without the Use of High Voltages”. Phys. Rev. **40 (1)**, 19 (1932)

[6] S. Myers and E. Picasso, “The Design, construction and commissioning of the CERN Large Electron Positron collider”, Contemp. Phys. **31**, 387 (1990)

[7] M. De Palma et al., “ALEPH: Technical Report”, (1983)

[8] W. Bart et al., “DELPHI: Technical Proposal”, (1983)

[9] M. Decamp, “The Opal Detector Technical Proposal”, (1983)

[10] C. Von Dardel et al., “L3 Technical Proposal”, (1983)

[11] C. Rubbia, “The Discovery of the W and Z bosons”, Phys. Rept. **239**, 241 (1994)

[12] http://www.fnal.gov/pub/tevatron/tevatron-accelerator.html

[13] R. Blair et al.,"The CDF detector: Technical design report", (1996)

[14] S. Abachi et al.,"The D0 detector", Nucl. Inst. method A **338**, 185 (1994)

[15] C. Campagnari and M. Franklin, "The Discovery of the top quark", Rev. Mod. Phys. **69**, 137 (1999)

[16] 0. S. Bruning et al., "LHC Design Report Vol. 1: The LHC Main Ring", (2004)

[17] G. Aad et al., "The ATLAS Experiment at the CERN Large Hadron Collider", JINST **3**, S08003 (2008)

[18] K. Aamodt et al., "Thc ALICE experiment at the CERN LHC", JINST **3**, 508002 (2008)

[19] S. Chatrchyan et al., "The CMS experiment at the CERN LHC", JINST **3**, 508004 (2008)

[20] Jr. A. A. Alves et al., "The LHCb Detector at the LHC," JINST **3**, 508005 (2008)

[21] F. Englert and R. Brout, "Broken Symmetry and the Mass of Gauge Vector Mesons", Phys. Rev. Lett. **13**, 321 (1964)

[22] P. W. Higgs, "Broken Symmetries and the Masses of Gauge Bosons", Phys. Rev. Lett. **13**, 508 (1964)

[23] CMS Collaboration, "Tracker technical design report", (1998)

[24] V. Khachatryan et al., "CMS Tracking Performance Results from early LHC Operation", Eur. Phys. C **70**, 1165-1192 (2010)

[25] CMS Collaboration, "CMS: The electromagnetic calorimeter. Technical design report", CERN-MICC-97-33, CMS-TDR-4 (1997)

[26] CMS Collaboration, "CMS: The hadron calorimeter technical design report", CERN-LHCC-97-31 (1997)

[27] G. Acquistapace et al., "CMS, the magnet project: Technical design report", (1997)

[28] CMS Collaboration, "CMS, Muon technical design report", CERN-LHCC-97-32, (1997)

[29] CMS Collaboration, "CMS TriDAS project: Technical design report, The Trigger Systems: Technical Design Report CMS", (1997)

[30] CMS Collaboration, "CMS TriDAS project: Technical design report, Data Acquisition and High Level Trigger", CERN (2002)

Chapter 4

Data Quality Monitoring at the CMS

The CMS detector at the Large Hadron Collider at CERN is one of the multipurpose general detector. At the LHC, millions of proton-proton collisions take place each second which are recorded by the CMS detector. These millions of proton-proton interactions generate huge amount of data for the physics analyses. All the sub-detectors of the CMS need to perform in accurate and optimal conditions to record these data for analyses. After 2012, the LHC is colliding more proton bunches in a narrower beam of particles. Under such conditions, the CMS has to make sure that both the hardware and software can handle these challenges and record the data of high quality. To accomplish this task a group of physicists has been constituted, which is responsible to scrutinize the quality of the data. The group is named as Physics Performance and Data-set (PPD) group.

The key role of PPD [1] group is to ensure the quality of data at the time of collisions as well as after the collisions. After monitoring the quality of data from collisions it is then provided to the different physics analysis groups for the various physics analyses. The organization of the PPD group along with the coordinators of its various subgroups for the year 2017-18 is shown in figure 4.1. In this chapter the validation work done for 2015 and 2016 data for the Physics data and MC validations

(PdmV) group and certification of collision data taken by the CMS detector during 2017 for DQM-DC group at centre of mass energy 13 TeV is presented. The PPD group has further 3 subgroups for specific purposes. These groups are;

- **Alignment, Calibration and Database (AlCaDB)**
- **Data Quality Monitoring and Certification (DQM-DC)**
- **Physics Data and MC Validation (PdmV)**

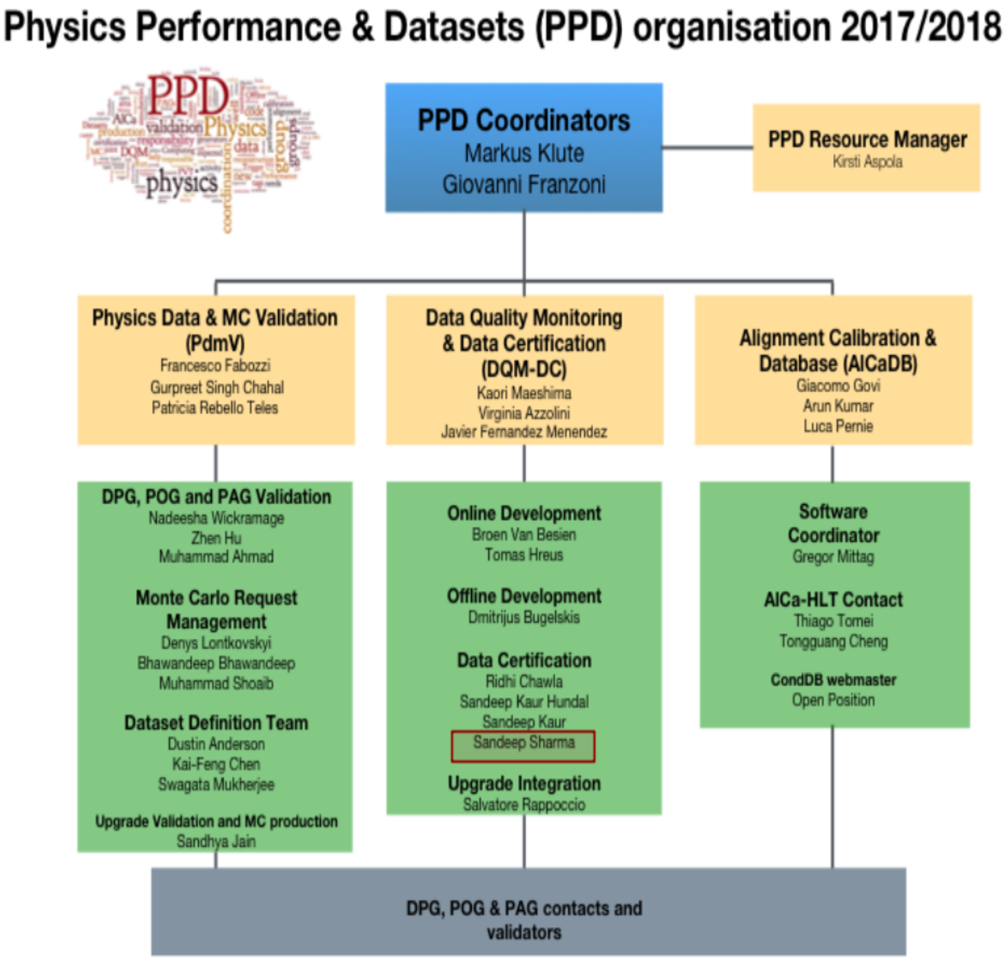

Figure 4.1: The Layout of subgroups in Physics Performance and Data-set group

4.1 Data Quality Monitoring (DQM)

The Data Quality Monitoring, DQM, of Compact Muon Solenoid detector is a crucial resource for delivering data of very high quality for various physics studies. Major Goal of DQM system [2] is to ensure the high quality of data taken during the particle collisions. So, DQM plays an important role in providing the true and reliable certification of collision data.

4.1.1 Responsibilities of DQM Group

The key responsibilities of the DQM [3] group to support, employ and handle this framework are broadly classified in to four areas.

- **DQM shift operations**: The Shift operations is the basic but crucial responsibility for the CMS collaboration. Effective shift operations are mandatory for efficient handling of the data from collisions. Large number of shifters perform the monitoring task for both Online and Offline chains. It is the responsibility of the DQM group to coordinate shift allocations and training of shifters. All the important instructions from various Detector performance Groups, DPGs and Physics Object Groups, POGs need to be propagated well to these shifters.
- **Development**: Each subsystem of detector has specific monitorables which are required for good data quality monitoring. Development of the tools required in DQM process is accomplished by the experts and specialists of DQM team. The experts from all the DPGs and POGs contribute in the DQM development. The CMSSW code which is provided to all the DPGs requires to be analyzed and reviewed so that all desired changes can be implemented in the main release. The analysis includes understanding of the code, changes implemented in it and interaction with the developers regarding the changes. The various subsystems also support by providing all the necessary configuration required for DQM GUI to include in the testing procedures.

- **Data Certification**: Certification [4] is another important liability of DQM group. DQM group needs to release and provide the Golden Java Script Object Notation (JSON) files which contain the valuable information regarding runs in terms of their meaningful lumisections. These JSON files are used by all analysers in the collaboration to perform the various physics analyses. In order to provide the correct JSON file, DQM team needs to collect all the valuable and correct information from the certification experts of various DPGs and POGs. It is the responsibility of the DQM-DC group to keep a close watch on each run which is flagged BAD by any of the DPG or POG and to retrieve the best possible information even from the bad runs so that the most part of lumisections can be made available to the JSON file for further analyses.
- **System Operations and maintenance**: Several production systems have been used to run the DQM software. Particularly for the online world, DQM group itself is responsible for its own infrastructure. Production systems test, maintain and support the infrastructure at point 5 with the help of P5 system administrators, which is provided to different subsystems. DQM group also needs to provide on-call DQM experts for 24/7 during data taking process and report their findings daily to run coordination meeting. This helps the Run coordination team to monitor the ongoing data taking process. Providing support to the users, coordination with http group, managing data and regular up-gradation of the documentation are among the significant sectors of system operation and maintenance which are looked after by the group. Operations and maintenance of tools like DQM GUI for Monitoring, scripts used for validations and certifications are done by the DQM group. These tools play key role in the entire process of data quality monitoring.

The role of DQM group can be summarized [5] as a process which begins from online world at the interaction point, P5 to monitor the live data and finishes off in offline world with the announcement of Golden JSON file after the certification of prompt-reco data.

4.1.2 DQM: Tiers and Layers

The CMS collaboration has approved sole and steady framework which covers all the possible uses of this DQM framework. It is used to accomplish the live follow up on the status of various sub-detectors used in data taking, to carry out the prompt reconstruction of data offline, performing the certification of runs and to determine the goodness of physics objects using the CMS software release framework, known as the CMSSW. To get the better understanding of the DQM on the basis of above usage, Data Quality Monitoring process [3] is divided in to 3 tiers and 4 layers. These tiers and layers are briefly described below;

- **3 Tiers are:**

  Release Validation : Validation Code of DQM is accountable for the production of plots which are exhibited in the RelVal DQMGUI, DQM graphical user interface, as shown in figure 4.2. Various Data and Monte Carlo validators use these plots to approve the various newer releases or versions of CMS software framework, CMSSW. The validated software, which is the end product of this process, is used by the whole collaboration. This global process of release validation is managed by PdmV subgroup of PPD organization.

  Online DQM: After passing the High Level trigger, a part of data is handled at Point 5 using the online DQM cluster. This process produces the live plots to follow up the status of running sub-detectors. These plots are checked by shifters (24/7) using the Online DQM GUI, to ensure the good performance of the detector and to spot problems of any kind during the Run. All the information is then propagated to online runregistry as shown in figure 4.3, by the shifters. This process is managed by the DQM-DC team and results in the online follow up of the detector as its end product.

  Offline DQM: Data coming from the detector is sent to Tier0 for the immediate reconstruction, which is known as express reconstruction along with the reconstruction of data with 48 hours delay, called as Prompt-reconstruction. The efficiency plots of every sub-detector from various DPG

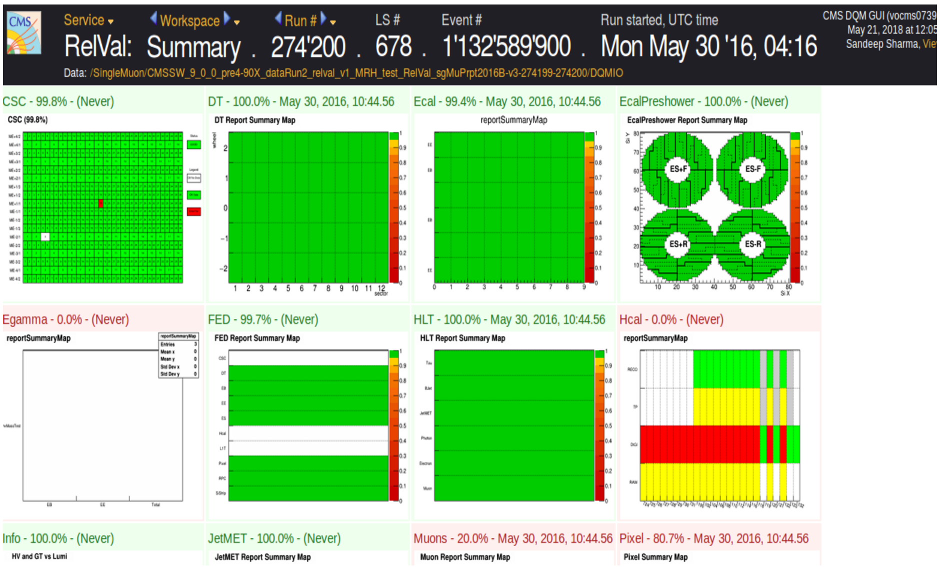

Figure 4.2: Extract of the RelVal DQM GUI showing the plots which are used to validate the versions of CMSSW. CMSSW 900pre4 in this case

groups and physics variables like number of charged tracks, transverse momentum, eta distribution of the produced particles etc., of all POG groups are analyzed by the Prompt feedback groups and certification experts. The results of the analyses are then conveyed by the certification experts to the central Data Certification team using offline runregistry, documented as in figure 4.4. The end product of this process is in the form of Golden JSON file, which contains all the meaningful data (runs along with their lumisections) to be used for the analysis of collisions. The DQM-DC team looks in to this entire process [6] of offline monitoring.

- **4 Layers**: The four layers of DQM are mentioned below. These layers are basically four important tools to perform the DQM process.

  Production of DQM plots: The production of DQM plots tool is of extreme importance for the DQM process. Data Acquisition system, DAQ coordinates with Tier0 in order to define the right input data and also ensures that correct DQM plots are produced. Production of plots for Release Validation and Online monitoring are governed by PdmV and DQM DC respectively.

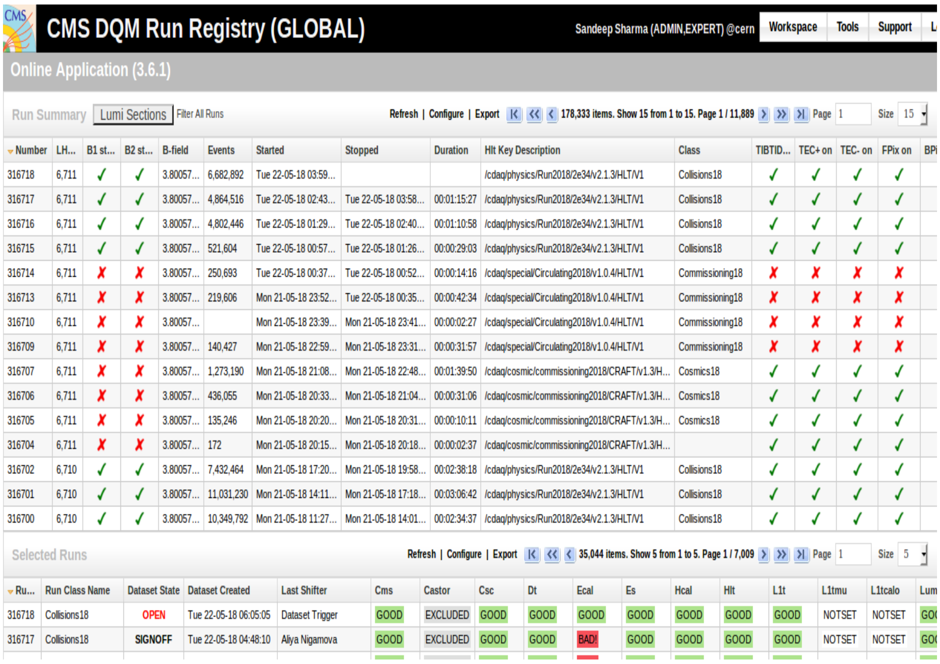

CMS DQM Run Registry (GLOBAL)

Sandeep Sharma (ADMIN,EXPERT) @cern

Online Application (3.6.1)

Run Summary | Lumi Sections | Filter All Runs

Refresh | Configure | Export 178,333 items. Show 15 from 1 to 15. Page 1 / 11,889 Page 1 Size 15

Number	LH...	B1 st...	B2 st...	B-field	Events	Started	Stopped	Duration	Hlt Key Description	Class	TIBTID...	TEC+ on	TEC- on	FPix on	BPi
316718	6,711	✓	✓	3.80057...	6,682,892	Tue 22-05-18 03:59...			/cdaq/physics/Run2018/2e34/v2.1.3/HLT/V1	Collisions18	✓	✓	✓	✓	
316717	6,711	✓	✓	3.80057...	4,864,516	Tue 22-05-18 02:43...	Tue 22-05-18 03:58...	00:01:15:27	/cdaq/physics/Run2018/2e34/v2.1.3/HLT/V1	Collisions18	✓	✓	✓	✓	
316716	6,711	✓	✓	3.80057...	4,802,446	Tue 22-05-18 01:29...	Tue 22-05-18 02:40...	00:01:10:58	/cdaq/physics/Run2018/2e34/v2.1.3/HLT/V1	Collisions18	✓	✓	✓	✓	
316715	6,711	✓	✓	3.80057...	521,604	Tue 22-05-18 00:57...	Tue 22-05-18 01:26...	00:00:29:03	/cdaq/physics/Run2018/2e34/v2.1.3/HLT/V1	Collisions18	✓	✓	✓	✓	
316714	6,711	✗	✗	3.80057...	250,693	Tue 22-05-18 00:37...	Tue 22-05-18 00:52...	00:00:14:16	/cdaq/special/Circulating2018/v1.0.4/HLT/V1	Commissioning18	✗	✗	✗	✗	
316713	6,711	✗	✗	3.80057...	219,606	Mon 21-05-18 23:52...	Tue 22-05-18 00:35...	00:00:42:34	/cdaq/special/Circulating2018/v1.0.4/HLT/V1	Commissioning18	✗	✗	✗	✗	
316710	6,711	✗	✗	3.80057...		Mon 21-05-18 23:39...	Mon 21-05-18 23:41...	00:00:02:27	/cdaq/special/Circulating2018/v1.0.4/HLT/V1	Commissioning18	✗	✗	✗	✗	
316709	6,711	✗	✗	3.80057...	140,427	Mon 21-05-18 22:59...	Mon 21-05-18 23:31...	00:00:31:57	/cdaq/special/Circulating2018/v1.0.4/HLT/V1	Commissioning18	✗	✗	✗	✗	
316707	6,711	✗	✗	3.80057...	1,273,190	Mon 21-05-18 21:08...	Mon 21-05-18 22:48...	00:01:39:50	/cdaq/cosmic/commissioning2018/CRAFT/v1.3/H...	Cosmics18	✓	✓	✓	✓	
316706	6,711	✗	✗	3.80057...	436,055	Mon 21-05-18 20:33...	Mon 21-05-18 21:04...	00:00:31:06	/cdaq/cosmic/commissioning2018/CRAFT/v1.3/H...	Cosmics18	✓	✓	✓	✓	
316705	6,711	✗	✗	3.80057...	135,246	Mon 21-05-18 20:20...	Mon 21-05-18 20:31...	00:00:10:11	/cdaq/cosmic/commissioning2018/CRAFT/v1.3/H...	Cosmics18	✓	✓	✓	✓	
316704	6,711	✗	✗	3.80057...	172	Mon 21-05-18 20:15...	Mon 21-05-18 20:18...	00:00:02:37	/cdaq/cosmic/commissioning2018/CRAFT/v1.3/H...		✓	✓	✓	✓	
316702	6,710	✓	✓	3.80057...	7,432,464	Mon 21-05-18 17:20...	Mon 21-05-18 19:58...	00:02:38:18	/cdaq/physics/Run2018/2e34/v2.1.3/HLT/V1	Collisions18	✓	✓	✓	✓	
316701	6,710	✓	✓	3.80057...	11,031,230	Mon 21-05-18 14:11...	Mon 21-05-18 17:18...	00:03:06:42	/cdaq/physics/Run2018/2e34/v2.1.3/HLT/V1	Collisions18	✓	✓	✓	✓	
316700	6,710	✓	✓	3.80057...	10,349,792	Mon 21-05-18 11:27...	Mon 21-05-18 14:01...	00:02:34:37	/cdaq/physics/Run2018/2e34/v2.1.3/HLT/V1	Collisions18	✓	✓	✓	✓	

Selected Runs

Refresh | Configure | Export 35,044 items. Show 5 from 1 to 5. Page 1 / 7,009 Page 1 Size 5

Ru...	Run Class Name	Dataset State	Dataset Created	Last Shifter	Cms	Castor	Csc	Dt	Ecal	Es	Hcal	Hlt	L1t	L1tmu	L1tcalo	Lum
316718	Collisions18	OPEN	Tue 22-05-18 06:05:05	Dataset Trigger	GOOD	EXCLUDED	GOOD	GOOD	GOOD	GOOD	GOOD	GOOD	GOOD	NOTSET	NOTSET	GO
316717	Collisions18	SIGNOFF	Tue 22-05-18 04:48:10	Aliya Nigamova	GOOD	EXCLUDED	GOOD	GOOD	BAD!	GOOD	GOOD	GOOD	GOOD	NOTSET	NOTSET	GO

Figure 4.3: Online runregistry

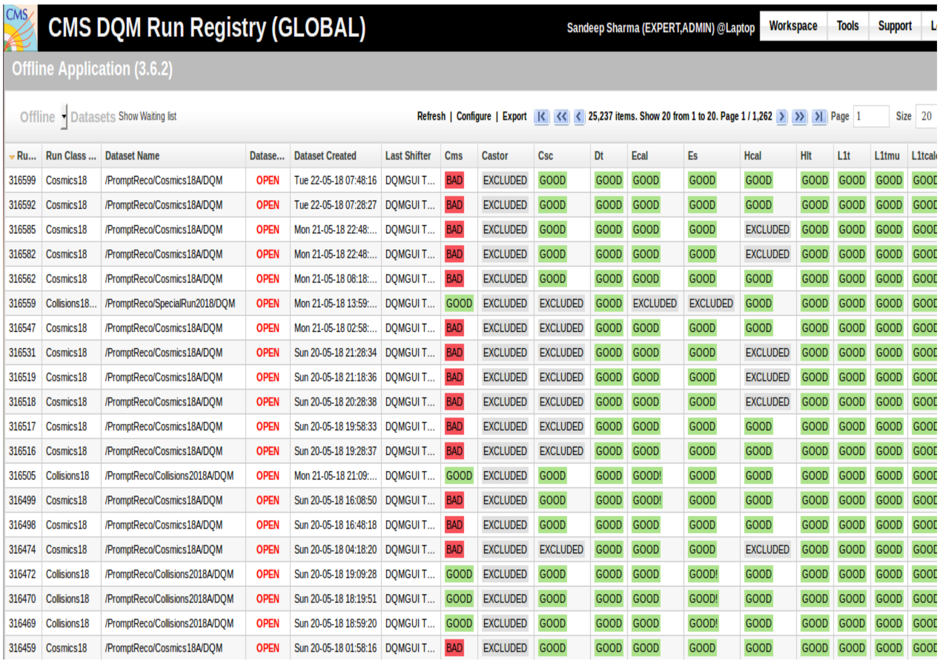

CMS DQM Run Registry (GLOBAL)

Sandeep Sharma (EXPERT,ADMIN) @Laptop

Offline Application (3.6.2)

Offline Datasets Show Waiting list

Refresh | Configure | Export 25,237 items. Show 20 from 1 to 20. Page 1 / 1,262 Page 1 Size 20

Ru...	Run Class ...	Dataset Name	Datase...	Dataset Created	Last Shifter	Cms	Castor	Csc	Dt	Ecal	Es	Hcal	Hlt	L1t	L1tmu	L1tcal
316599	Cosmics18	/PromptReco/Cosmics18A/DQM	OPEN	Tue 22-05-18 07:48:16	DQMGUI T...	BAD	EXCLUDED	GOOD	GOOD	GOOD	GOOD	GOOD	GOOD	GOOD	GOOD	GOOD
316592	Cosmics18	/PromptReco/Cosmics18A/DQM	OPEN	Tue 22-05-18 07:28:27	DQMGUI T...	BAD	EXCLUDED	GOOD	GOOD	GOOD	GOOD	GOOD	GOOD	GOOD	GOOD	GOOD
316585	Cosmics18	/PromptReco/Cosmics18A/DQM	OPEN	Mon 21-05-18 22:48:...	DQMGUI T...	BAD	EXCLUDED	GOOD	GOOD	GOOD	GOOD	EXCLUDED	GOOD	GOOD	GOOD	GOOD
316582	Cosmics18	/PromptReco/Cosmics18A/DQM	OPEN	Mon 21-05-18 22:48:...	DQMGUI T...	BAD	EXCLUDED	GOOD	GOOD	GOOD	GOOD	EXCLUDED	GOOD	GOOD	GOOD	GOOD
316562	Cosmics18	/PromptReco/Cosmics18A/DQM	OPEN	Mon 21-05-18 08:18:...	DQMGUI T...	BAD	EXCLUDED	GOOD	GOOD	GOOD	GOOD	GOOD	GOOD	GOOD	GOOD	GOOD
316559	Collisions18...	/PromptReco/SpecialRun2018/DQM	OPEN	Mon 21-05-18 13:59:...	DQMGUI T...	GOOD	EXCLUDED	EXCLUDED	GOOD	EXCLUDED	EXCLUDED	GOOD	GOOD	GOOD	GOOD	GOOD
316547	Cosmics18	/PromptReco/Cosmics18A/DQM	OPEN	Mon 21-05-18 02:58:...	DQMGUI T...	BAD	EXCLUDED	EXCLUDED	GOOD	GOOD	GOOD	GOOD	GOOD	GOOD	GOOD	GOOD
316531	Cosmics18	/PromptReco/Cosmics18A/DQM	OPEN	Sun 20-05-18 21:28:34	DQMGUI T...	BAD	EXCLUDED	EXCLUDED	GOOD	GOOD	GOOD	EXCLUDED	GOOD	GOOD	GOOD	GOOD
316519	Cosmics18	/PromptReco/Cosmics18A/DQM	OPEN	Sun 20-05-18 21:18:36	DQMGUI T...	BAD	EXCLUDED	EXCLUDED	GOOD	GOOD	GOOD	EXCLUDED	GOOD	GOOD	GOOD	GOOD
316518	Cosmics18	/PromptReco/Cosmics18A/DQM	OPEN	Sun 20-05-18 20:28:38	DQMGUI T...	BAD	EXCLUDED	EXCLUDED	GOOD	GOOD	GOOD	EXCLUDED	GOOD	GOOD	GOOD	GOOD
316517	Cosmics18	/PromptReco/Cosmics18A/DQM	OPEN	Sun 20-05-18 19:58:33	DQMGUI T...	BAD	EXCLUDED	EXCLUDED	GOOD	GOOD	GOOD	GOOD	GOOD	GOOD	GOOD	GOOD
316516	Cosmics18	/PromptReco/Cosmics18A/DQM	OPEN	Sun 20-05-18 19:28:37	DQMGUI T...	BAD	EXCLUDED	EXCLUDED	GOOD	GOOD	GOOD	GOOD	GOOD	GOOD	GOOD	GOOD
316505	Collisions18	/PromptReco/Collisions2018A/DQM	OPEN	Mon 21-05-18 21:09:...	DQMGUI T...	GOOD	EXCLUDED	GOOD	GOOD	GOOD!	GOOD	GOOD	GOOD	GOOD	GOOD	GOOD
316499	Cosmics18	/PromptReco/Cosmics18A/DQM	OPEN	Sun 20-05-18 16:08:50	DQMGUI T...	BAD	EXCLUDED	GOOD	GOOD	GOOD!	GOOD	GOOD	GOOD	GOOD	GOOD	GOOD
316498	Cosmics18	/PromptReco/Cosmics18A/DQM	OPEN	Sun 20-05-18 16:48:18	DQMGUI T...	BAD	EXCLUDED	GOOD	GOOD	GOOD	GOOD	GOOD	GOOD	GOOD	GOOD	GOOD
316474	Cosmics18	/PromptReco/Cosmics18A/DQM	OPEN	Sun 20-05-18 04:18:20	DQMGUI T...	BAD	EXCLUDED	EXCLUDED	GOOD	GOOD	GOOD	EXCLUDED	GOOD	GOOD	GOOD	GOOD
316472	Collisions18	/PromptReco/Collisions2018A/DQM	OPEN	Sun 20-05-18 19:09:28	DQMGUI T...	GOOD	EXCLUDED	GOOD	GOOD	GOOD	GOOD!	GOOD	GOOD	GOOD	GOOD	GOOD
316470	Collisions18	/PromptReco/Collisions2018A/DQM	OPEN	Sun 20-05-18 18:19:51	DQMGUI T...	GOOD	EXCLUDED	GOOD	GOOD	GOOD	GOOD!	GOOD	GOOD	GOOD	GOOD	GOOD
316469	Collisions18	/PromptReco/Collisions2018A/DQM	OPEN	Sun 20-05-18 18:59:20	DQMGUI T...	GOOD	EXCLUDED	GOOD	GOOD	GOOD	GOOD!	GOOD	GOOD	GOOD	GOOD	GOOD
316459	Cosmics18	/PromptReco/Cosmics18A/DQM	OPEN	Sun 20-05-18 01:58:16	DQMGUI T...	BAD	EXCLUDED	GOOD	GOOD	GOOD	GOOD	GOOD	GOOD	GOOD	GOOD	GOOD

Figure 4.4: Offline runregistry

But production of plots for Offline Monitoring is done by Tier0 and sequences are managed by DQM Team.

Envisioning of the Plots using DQM-GUI: The DQM-DC team manages this tool and provides all the required support and documentation to the subsystems by developing specific plugins. Different server occurrences of the tool running at several different locations make the tool difficult to manage. Online DQMGUI servers are controlled by the DQM-DC team whereas RelVal and offline servers are governed by the CMSWEB HTTP group.

Validation and certification : Validations of the CMSSW releases and certification of Runs are performed by the shifters and experts with the help of CMSSW code and GUI plugins. DQM DC team interacts and provides all the basic training to the code developers, PFGs and certification experts to make sure that this validation and certification task is done efficiently.

Recording the results using runregistry: In order to follow the correct information about quality flags with respect to data collected from the CMS detector, runregistry is used by the Data Certification team. This whole class of information is used by the DQM DC team to deliver the final Golden JSON file to the collaboration.

The entire process [7] of DQM which is described above using 3 Tiers and 4 layers is shown in the schematic way using figure 4.5.

4.2 Release Monitoring: RelMon

Release monitoring, RelMon [8], is another significant tool of Data Quality Monitoring process. To analyze the data from the CMS detector a software framework, CMSSW, is required. This CMSSW is upgraded and maintained by releasing the newer versions by the Physics data and Monte-Carlo Validation group (PdmV). RelMon is a tool used to achieve the comparison between the two CMSSW releases using root files consist of various DQM histograms. This task of comparison is known as

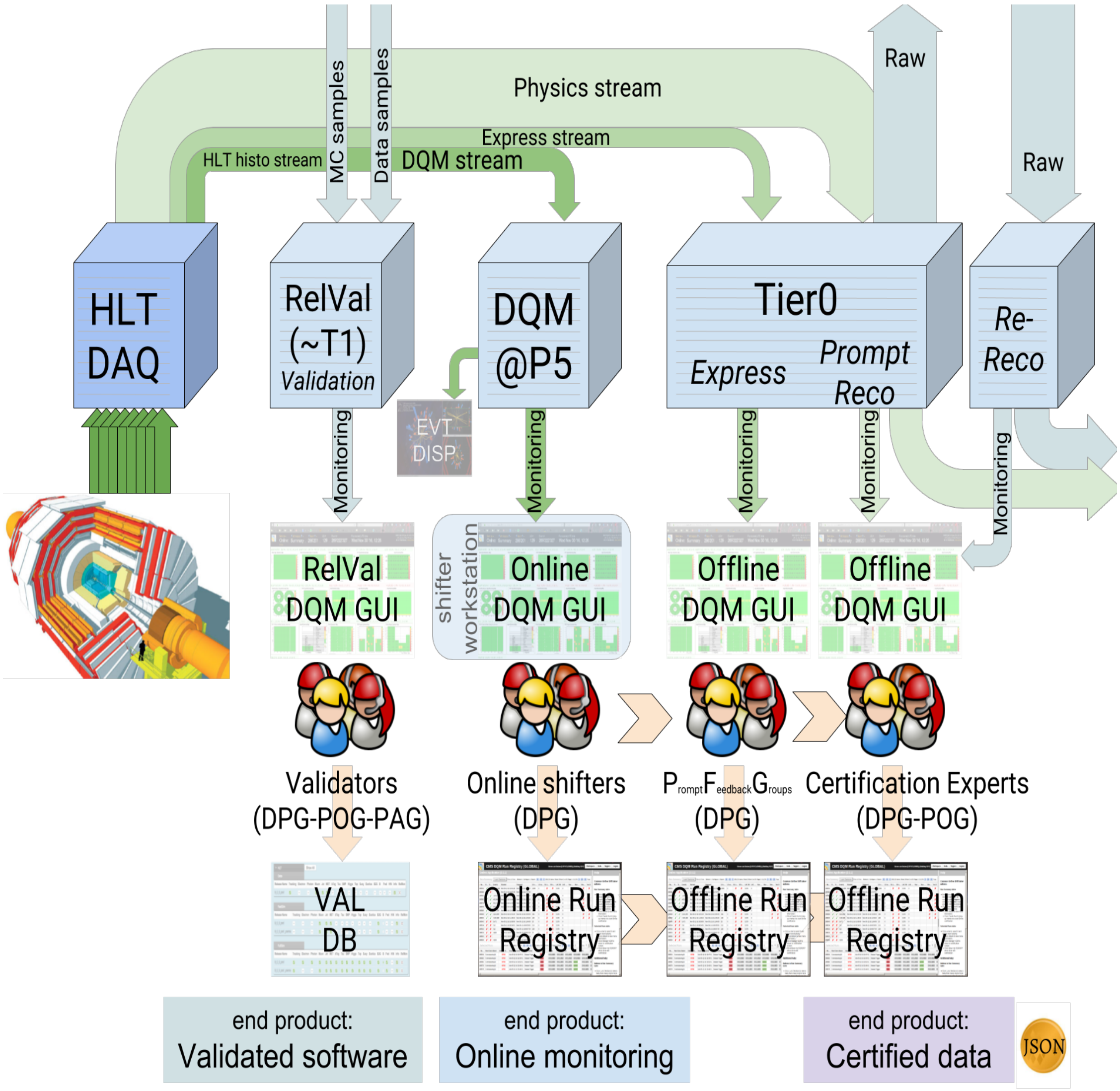

Figure 4.5: Flow chart describing the complete DQM process at the CMS. Image source: https://twiki.cern.ch/twiki/pub/CMS/DQMPositions/

validation in which ‘test CMSSW release’ is validated against the ‘reference CMSSW release’. All the Detector performance Groups, DPGs, Physics Object Group, POGs and Physics Analysis Groups, PAGs [9] generate the important set of histograms on a group of data and Monte-Carlo samples. Details about the method, Validation group and samples used along with results are described in following sections.

4.2.1 Method to Perform Validation

The main task of PdmV group is to give approval or to validate the release of newer version of the CMSSW. Validators from various PAGs and POGs examine the new developments from newer version(s) of the CMSSW releases and the software infrastructure, Data quality monitoring (DQM) package for the validation group needs to be maintained by them. Validation is performed using Data and Monte-Carlo (full simulation, fast simulation) work flows. When two CMSSW releases are compared there can be differences in the results and these differences, their origin and consequences need to be addressed and fixed. Comparisons between the releases are made by analyzing the DQM histograms of various PAGs, DPGs and POGs from both the releases. This comparison of histograms are based on the statistical Chi-Square test where the threshold of p value[1] (1e-05) determines if comparison has passed the test or not. Results due to differences are marked as *Ok*, *Expected* or *Failure* depending upon the development of the new CMSSW release. Report is prepared to highlight in particular the salient features of the comparison, based on the validation which involves a manual, visual inspection of physical quantities of interest, reconstructed in the two CMSSW releases, which is then uploaded to validation database (ValDB) page [10]. Once the developments are verified to be valid, they are used in CMSSW for data taking at Tier-0, data-processing and Monte Carlo production. It is only after analyzing the reports and level of discrepancies from all the PAGs, POGs and DPGs, PdmV group approves or disapproves the CMSSW versions. If the versions are found to be compatible then PdmV group

---

[1] The p value is defined as the level of marginal relevance within a statistical hypothesis test which represents the probability of the occurrence of a given event

makes them public, to be used by all the users of the CMS collaboration for various analyses processes. Figure 4.6 shows the official page where comparison campaigns for the CMSSW are announced.

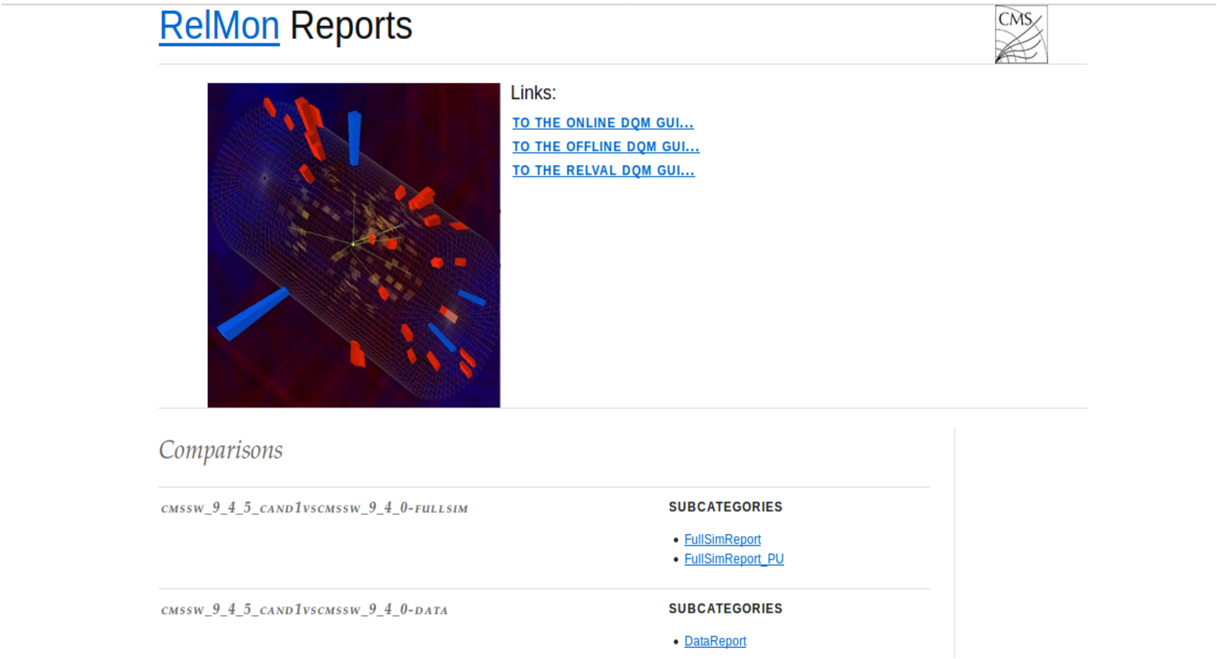

RelMon Reports

Links:

TO THE ONLINE DQM GUI...
TO THE OFFLINE DQM GUI...
TO THE RELVAL DQM GUI...

Comparisons

CMSSW_9_4_5_CAND1VSCMSSW_9_4_0-FULLSIM

SUBCATEGORIES

- FullSimReport
- FullSimReport_PU

CMSSW_9_4_5_CAND1VSCMSSW_9_4_0-DATA

SUBCATEGORIES

- DataReport

Figure 4.6: The Official RelMon comparison page where test and reference CMSSW releases are mentioned.

4.2.2 The Standard Model Physics Validation

Various Physics analysis groups, PAGs, like Standard Model, Susy, TOP, B Physics and Higgs play very important role to study and analyze the physics processes. Standard model is one of the most important physics groups amongst all the PAGs. In SMP-PAG validation is performed using electroweak muon dqm (EwkMuDQM)and electroweak electron dqm (EwkElecDQM) modules. To perform the validation, compatibility check of new version of the CMSSW is made w.r.t to older version and these comparisons are chosen in such a way that Monte-Carlo is checked against Monte-Carlo and data work-flow against data work-flow only, as shown in figures

4.7 and 4.8. For the Data, Single electron, Single muon, Double muon, Double electron samples have been used for the validations.

4.2.2.1 Samples used for Validation

- **ZEE, Double electron sample**: Reconstruction of Z boson using electron and positron, Z → e^+ e^-
- **ZMM, Double muon sample**: Reconstruction of Z boson using muon and antimuon, Z → μ^+ μ^-
- **WE, Single electron sample**: Reconstruction of W boson using electron and neutrino/antineutrino, $W^+ \to e^+ \ \nu_e$, $W^- \to e^- \ \bar{\nu_e}$
- **WM, Single muon sample**: Reconstruction of W boson using muon and anti-neutrino/antineutrino, $W^+ \to \mu^+ \ \nu_\mu$, $W^- \to \mu^- \ \bar{\nu_\mu}$

4.2.2.2 Workflow used for Validation

- Data validation which consists of electron and muon data samples.
- Monte-Carlo validation which consists of full Simulation with and without PileUp , fast Simulation with PileUp only

4.2.3 Analysis of DQM Plots

To validate the test release in comparison to the reference release, consistency study of some significant variables for electron and muon sample, like dilepton mass, dilepton transverse momentum, leading, sub-leading jet's momentum, pseudorapidity, of the samples become very important. These variables are being analyzed using DQM codes (EwkElecDQM and EwkMuDQM codes) of SMP-PAG group, which are run locally and resulting output distributions are studied. Some of the variables which were considered for the present study are listed and defined in the following sections.

4.2.3.1 List of Variables

- **Kinematics**: Transverse momentum (p_T), pseudorapidity (η), charge, difference of transverse momentum between the positive and negative muons/electrons (Δp_T)
- **Muon ID variables**: To identify the real muon and rejecting the reconstructed muons from other sources muon identification variables are used. e.g. d_{xy}, which measure's the transverse distance of muon to the primary vertex of an interaction.
- **Electron ID variables**: To differentiate the real electron from the fake ones, shower shape variable is used. These variables are called as electron identification variable which is a measure of the shape of showers, e.g. $\sigma_{i\eta i\eta}$ [2]
- **Electron ISO variables**: Separation between the reconstructed hits around the electron in ECAL (Ecaliso), in HCAL (Hcaliso) and separation of tracks from the electron track (Trackiso) both in Barrel and Endcap.
- **Muon ISO variables** : Muons are required to be well isolated from energy deposits and other charged particles in its vicinity to reduce the fake muon contributions from other sources. Tracker relative isolation is one of the variables used for isolation of muons.
- **Jet variables**: Number of Jets, transverse momentum (p_T) and pseudorapidity (η) of leading and sub-leading jet, Opening angle between leading and sub-leading jet ($\Delta\phi$)
- **Photon variables**: Number of photons, transverse momentum, p_T and pseudorapidity, η of photons
- **Z boson variables**: Dilepton invariant Mass, transverse momentum
- **Trigger variable**: whether fired or not
- Number of muons/electrons, Number of good muons/electrons, Primary Vertex distribution

---

[2] It is defined as the width of the ECAL cluster along the η direction computed for all the crystals in the 5 x 5 block of crystals centered on the highest energy crystal of the seed cluster

All the above mentioned variables are very important to understand the reconstructed objects (W and Z boson in this case). The other important variable which is of key importance is phi star, ϕ^* [11].

4.2.3.2 Phi star (ϕ^*) Variable

At the energy of TeV scale, large amount of the photons, W and Z bosons are produced during the hadronic collisions. The dilepton system is boosted in the transverse direction due to the QCD radiation in the initial state of the hard scattering. This leads to non zero component of transverse momentum q_T for the dilepton system. The correct modeling of the vector boson q_T distribution is important in many physics analyses at the LHC for which the production of W or Z bosons constitutes a significant background. At High q_T values, perturbative calculations are used where as for low q_T soft gluon re-summation technique is used. The Z boson production cross section is dominated by the low q_T spectrum which is explained by transverse-momentum re-summation formalism. The measurements of low q_T at high energy experiments like at the LHC and at the Tevatron, were dominated by uncertainties in experimental resolutions and event selection efficiency, which had direct impact on the precision of q_T measurement by constraining the bin width selection for the measurements. So the investigation for additional observable(s) with lesser sensitivity to experimental uncertainties and with refined experimental resolution was required. The optimal experimental observables to probe the low q_T domain of Z production were found to be the a_T, the transverse momentum of dilepton pair [12] and phi-star variable ϕ^* [12]. a_T is less sensitive to the lepton p_T resolution than q_T and also the selection cut efficiencies for lepton isolation are less related with a_T as compared to q_T. If a_T is divided by dilepton invariant mass, q, it becomes even less susceptible to lepton p_T resolution than the a_T. This results in to the new variable named as phi star variable ϕ^*. So studying of $\phi^* = a_T/$q in low q_T non perturbative region leads to an improved understanding.

$$a_T = 2\frac{p_T^1 p_T^2}{p_T^1 + p_T^2} sin\Delta\phi \tag{4.1}$$

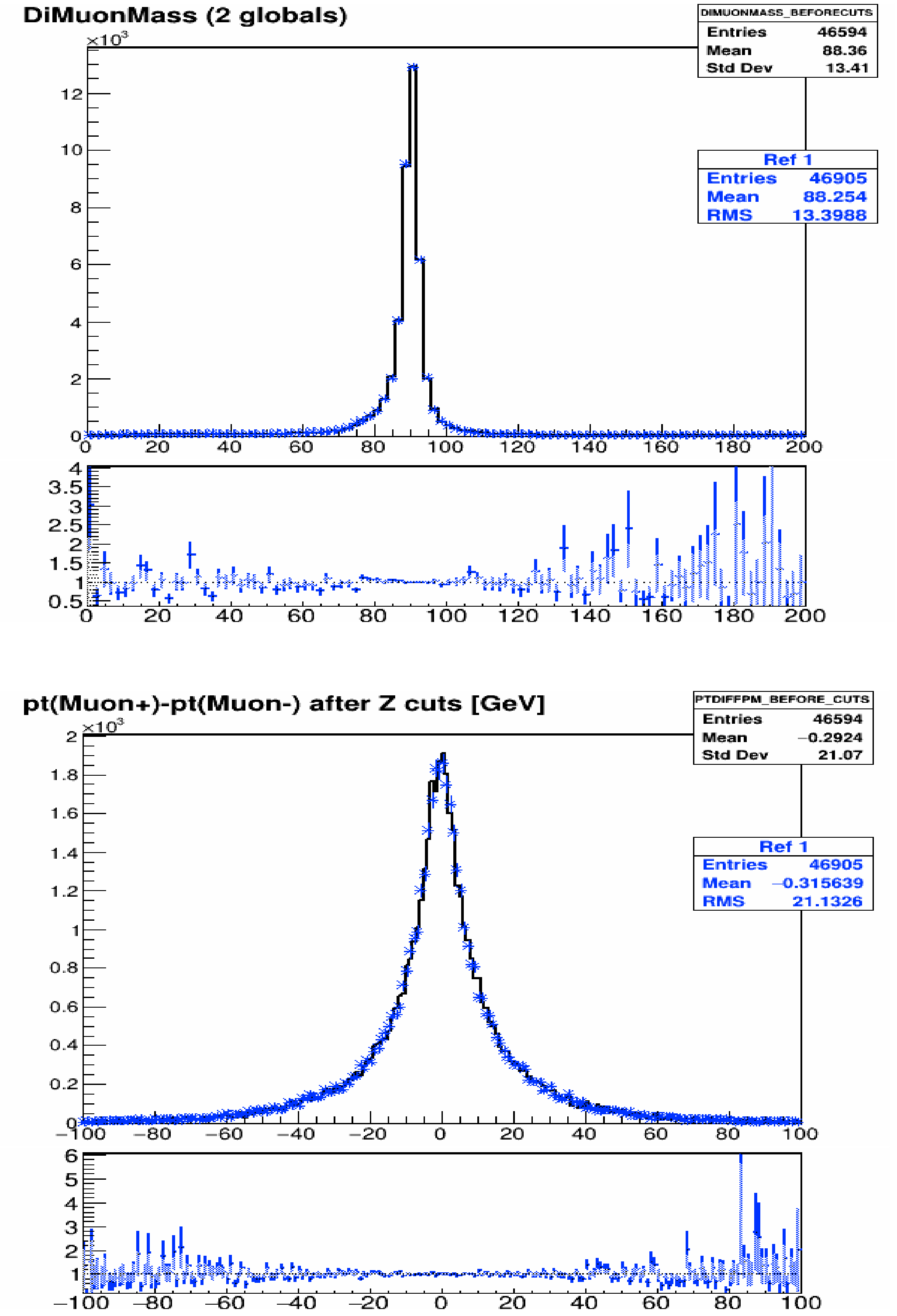

Figure 4.7: Distributions comparing the `CMSSW_8_1_0_pre5` (blue) and `CMSSW_8_1_0_pre4` (black) releases using Double Muon sample for 2015 data, a) Z reconstructed from two muons: Invariant Mass distribution (top) and p_T difference between positive and negative muon after implementing the Z selection cuts (bottom). Both the distributions show the good agreement between the two releases exhibiting the success.

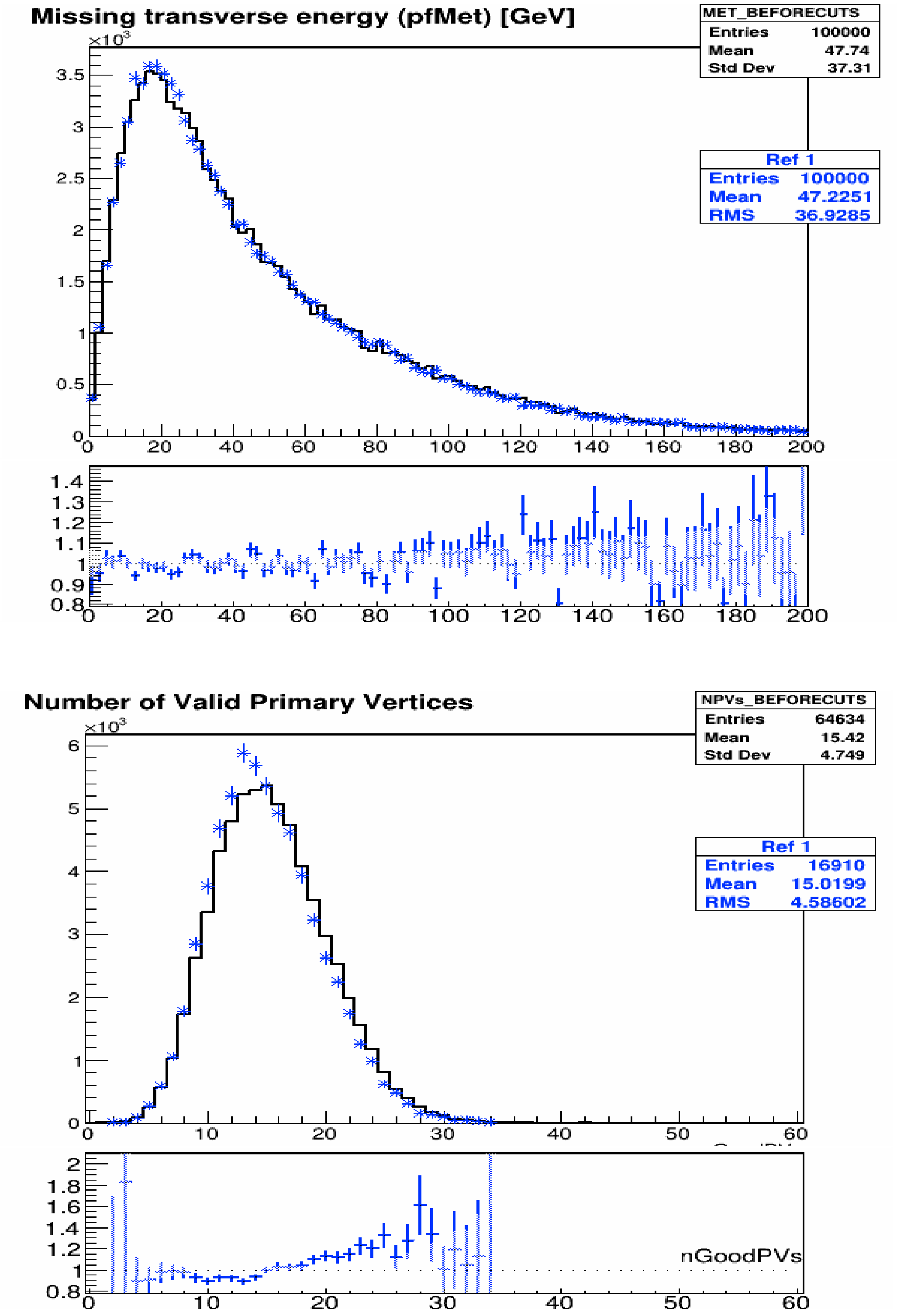

Figure 4.8: Distributions comparing the `CMSSW_8_1_0_pre3` (blue target) and `CMSSW_8_1_0_pre2` (black reference) releases using ZEE sample for full simulation, a) Missing transverse energy distribution (top) and Number of good primary vertices (bottom) before applying Z selection cuts. Distribution shows the good agreement between the two releases but the NPVs distributions showing the failure `CMSSW_8_1_0_pre3` against `CMSSW_8_1_0_pre2` release.

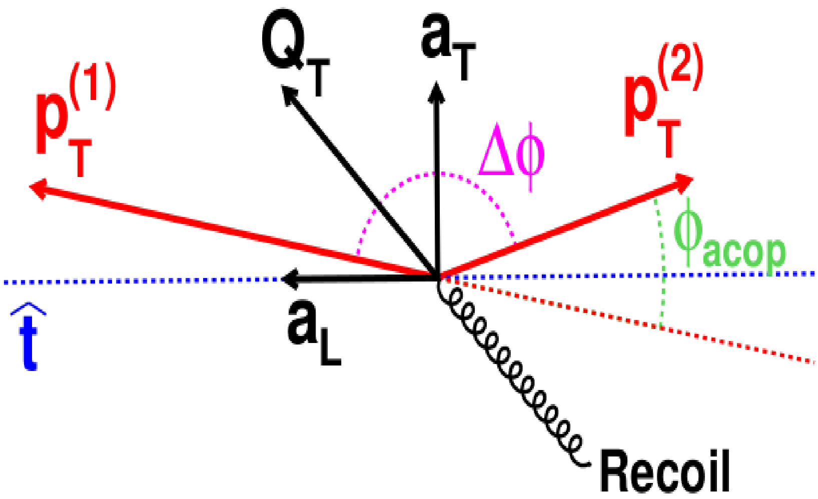

Figure 4.9: Figure describing the acoplanarity, azimuthal opening angle between leptons and the transverse momentum of dilepton pair. Image source: https://slideplayer.com/slide/3948429/

$$q = \sqrt{2p^1p^2(1 - cos(\Delta\theta)} \tag{4.2}$$

where, q is the dilepton invariant mass , $\Delta\phi$ is the azimuthal opening angle of lepton pair having momenta p^1 and p^2 with $\Delta\theta$ is the angle between the two leptons as shown in figure 4.9.

$$\phi^* = \frac{a_T}{q} \approx tan(\frac{\phi_{acop}}{2})sin(\theta^*_\eta) \tag{4.3}$$

where, $\phi_{acop} = \pi - \Delta\phi$ and θ^*_η is the scattering angle of the leptons with respect to the proton beam direction in the rest frame of the dilepton system. θ^*_η can be defined in the terms of lepton variables.

$$cos(\theta^*_\eta) = tanh(\frac{\eta^- - \eta^+}{2}) \tag{4.4}$$

where, η^- (η^+) is the pseudorapidity of the negatively (positively) charged lepton, respectively. The ϕ^* variable has certain dominance over the q_T. Some of the major advantages of this variable are as follows;

- As ϕ_{acop} and θ_η^* depend absolutely on the directions of the two leptons, which are measured with a precision of a milliradian or better, ϕ^* is experimentally very well measured as compared to any other quantity that relies on the momenta of the leptons
- The experimental resolution for ϕ^* is significantly better than the one for q_T, which enables the possibility to better test theoretical ideas and constrain non-perturbative effects [13]
- ϕ^* is correlated to the quantity a_T/q , where q is the invariant mass of the lepton pair and a_T represents the transverse momentum of dilepton pair, and therefore probes the same physics as with the transverse momentum, q_T
- Values of ϕ^* ranging from 0 to 1 probe the q_T distribution mainly up to $\sim$ 100 GeV/c

4.2.4 Selection Cuts

Specific set of selection cuts have been used to validate and analyze the DQM plots of certain set of variables like transverse momenta, p_T, pseudorapidity, η-distribution, invariant mass of di-bosons for WM, WE, ZMM and ZEE samples for 2015-16 data. Selection cuts which are used in the analyses are optimized from time to time depending upon the beam and bunch spacing. Selection cuts used here to select the leptons (electrons and muons) in all of the above samples for 2015 and 2016 data are medium identification cuts [14, 15]. These cuts are recommended by the Muon and Electron POGs after examining all the situations. Details of these cuts are below:

4.2.4.1 For Muons

- Each muon is required to possess transverse momentum more than 25 GeV and lie with in pseudorapidity range of 2.1 ($p_T >$ 25 GeV and $\eta <$ 2.1)

- The ratio of the sum of transverse momenta of all the tracks [3] to the muon track transverse momentum should be less than 0.1 (IsoCut < 0.1)
- To reconstruct the Z boson from the two muons, one of the muon needs to have transverse momentum more than 20 GeV and other muon is required to have transverse momentum more than 10 GeV ($p_{T_{\mu_1}} > 20$ GeV, $p_{T_{\mu_2}} > 10$ GeV)
- The invariant mass of the chosen pair ($M_{\mu\mu}$) should lie in the range 60 to 120 GeV/c^2 .
- Triggers : HLT IsoMu, HLT IsoTkMu, HLT Mu (recommended by MUON POG).

4.2.4.2 For Electrons

- Each electron is required to possess transverse momentum more than 25 GeV and lie within pseudorapidity range of 2.4 ($p_T > 25$ GeV and $\eta < 2.4$)
- To reconstruct the Z boson from the two electrons, one of the electron needs to have transverse momentum more than 25 GeV and other electron is required to have transverse momentum more than 15 GeV ($p_{T_{e1}} > 25$ GeV and $p_{T_{e2}} >$ 15 GeV)
- One out of the two electrons involved in the reconstruction of Z needs to lie with in pseudorapidity range of 2.4 and other in 2.5 ($\eta < 2.4$ (2.5))
- The invariant mass of the chosen pair (M_{ee}) should lie in the range 60 to 120 GeV/c^2 .
- Triggers : HLT Ele, HLT DoubleEle.

After implementing the above selection cuts, the distributions of certain important variables as described above are shown in figures 4.10 and 4.11.

---

[3] These are the tracks which are centred around a muon track and lie within a cone of radius less than 0.3

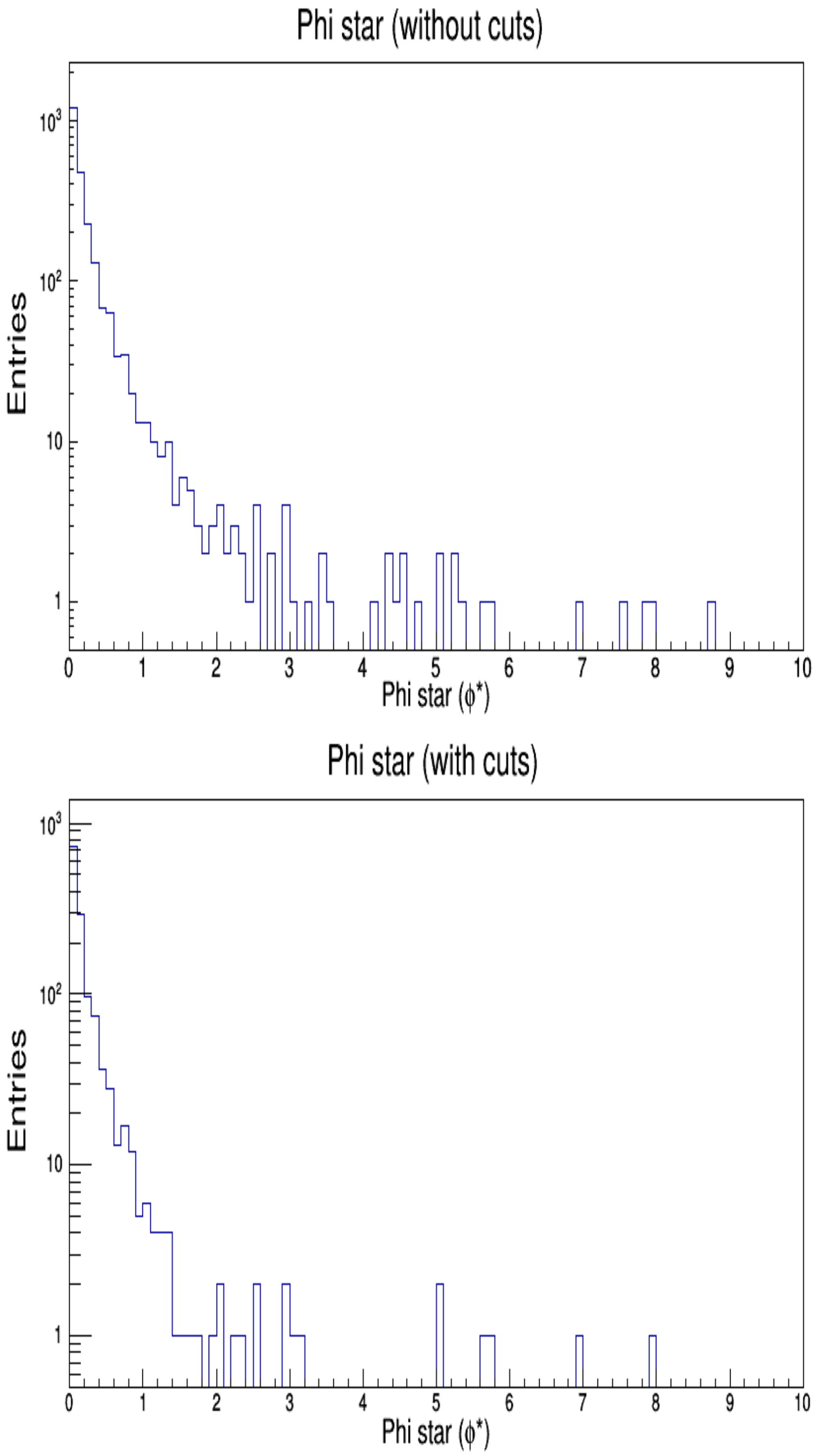

Figure 4.10: Phi star (ϕ^*) distribution before (top) and after (bottom) applying the Z selection cuts using the Double electron sample. This variable was introduced to the EwkElecDQM code and then obtained distribution was sent to SMP group where it was approved for inclusion in the CMSSW releases.

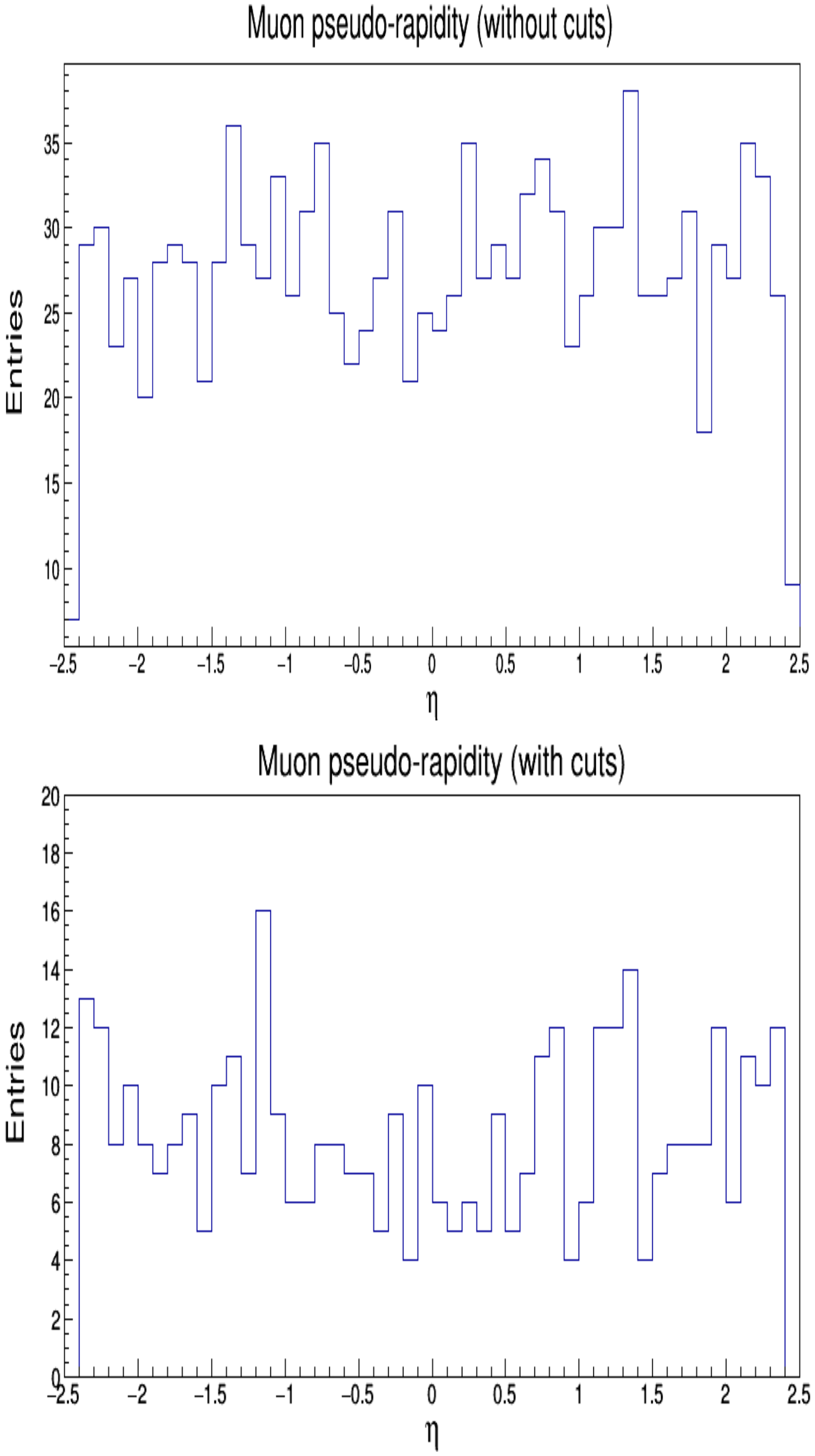

Figure 4.11: Pseudorapidity distribution before (top) and after (bottom) applying the W selection cuts using the Single muon sample.

4.3 Data Certification: DQM-DC

Data certification is another major subgroup of PPD which takes part in online monitoring and offline monitoring along with the certification of data coming out of collisions in the CMS detector. The principle goal of DQM-DC [4] team is to organise, monitor and maintain the various live monitoring applications and visualization tools of both online and offline DQM modules. Along with this, DC team is also responsible for central certification process in which it is needed to prepare the list of runs and lumisections (LS) good for physics analysis performed by the various groups and users of the CMS collaboration.

4.3.1 Data Taking and Data Flow Process at the CMS

The process of certification begins with the start of data taking, when collisions of proton proton beams at the five main interaction points, among which the CMS is located at one interaction point of the LHC, occur. In the beam, proton bunches have bunch spacing of 25 ns. Each proton beam carries 2808 bunches and within each bunch there are 10^{11} number of protons which leads to about 600 million collisions per second. But it is not possible that every proton of beam 1 collides with another proton from beam 2. A number is assigned to every single collision of protons in order to give the identity, this assigned identity is called as 'run number'. Particles resulting from the collisions are detected by various subsystems of the CMS detector which include the Silicon tracker, Calorimeters ECAL, HCAL and muon chambers.

During collisions, particles interact with each other and the detector records information about energy and momenta of incoming and outgoing particles in the form of electrical signals. Entire data processing is connected to the computing system of the LHC. In order to study physics it is important to understand the kind of particles (physics objects) produced and the process in which these particles are produced. To extract all this information, reconstruction of the events need to be done. The process of reconstruction is performed via tracking, in which particle trajectories are reconstructed using the tracks, vertexing, in which extrapolation of tracks is done using certain selection criteria in order to find the originating point of these tracks, and particle identification is done by classifying each track. All the extracted information is stored in the form of histograms. If the process of reconstruction is done immediately after collision event without any delay it is called as 'Express Stream', if it is performed after the delay of 48 hours it is called as 'Prompt Reconstruction' and further delay leads to 'Re Reconstruction'. All the live information about every collision event with all the required details of all the sub-detectors is sent to Online DQM GUI for monitoring and then propagated to online runregistery for book keeping. It is the responsibility of online shifter to check whether all the subsytems of the detector are present in data acquisition system, DAQ and included in data taking process or not. It is the online shifter which provides the very first information about the detector and run to the DQM team during the collisions/data taking. All of raw data from DAQ and trigger system is propagated to Tier0 [16] where processing of raw data in to primary data set takes place (Prompt Reconstruction). Once the data is completely processed all the information is propagated to the offline GUI for the visualization of physics objects and then this information is passed to offline runregistery for book keeping. All the information in this way flows from the online world to offline world before certification of these data/events can happen.

4.3.2 Run Classes at the CMS

It is not only proton collision runs that are recorded or detected by the CMS detector and certified by the DQM-DC team, the runs are also classified in to different classes based on the detector and trigger conditions. Certification is not performed on all of the run classes but only on classes which can provide the good and meaningful physics objects. Runs are classified in to:

- **CruZeT runs**: CruZeT stands for cosmic runs at zero tesla. This implies that the cosmic runs are recorded when the CMS has magnetic field of zero tesla. Cosmic runs are for the high energy particles (mostly protons) coming from the universe which hit the earth's atmosphere and produce hundreds of secondary particles on reaching its surface as shown in figure 4.12

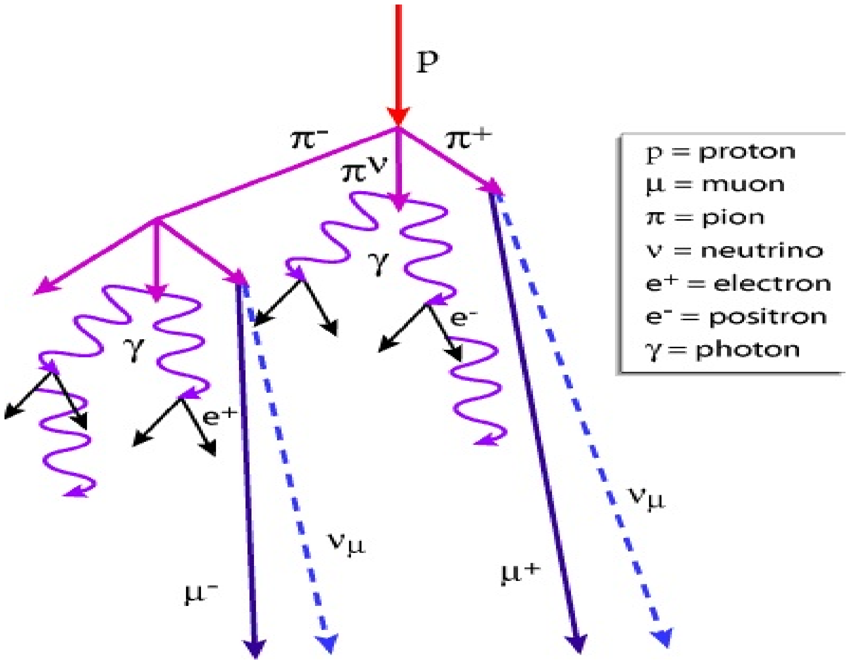

Figure 4.12: Cosmic rays producing the secondary particles including muons. Source: http://physicsopenlab.org/2017/08/29/cosmic-rays-composition/

These particles may have the energy as large as 100 times the energy of particles colliding at the LHC. These cosmic ray particles interact with matter to produce the secondary charged particles including muons, named as cosmic muons. Muons can travel hundreds of metres without interacting with the matter and hence can be detected at the earth's surface and even at deep underground. This penetrating nature of muons helps the muon subsytem of the CMS detector to detect them.

Cosmic run in DQM is defined only if both the proton beams are absent, tracker subsytem is present in the DAQ while recording these runs and with atleast one out of three muon subsystems (CSC, DT and RPC) should be on, while taking the cosmic data.

- **CRAFT runs**: CRAFT stands for Cosmic Runs at Four Tesla. In this class the above mentioned criterion for cosmic runs remains the same except the magnetic field. These runs are taken after switching on the CMS magnet system which provides a magnetic field of 4 Tesla.

- **Commissioning runs**: These are the runs which are taken when both the beams are present in the LHC beam-pipe and are stable ones but HLT menu is not good from the physics point of view. There is also a possibility of having non stable beam with HLT menu good for physics, even in such cases runs will be considered as commissioning runs. So it is the beam stability and HLT menu for physics which decides this class of runs. Also the magnetic field should be equal to 4 Tesla while recording this kind of data.

- **Standard Collision runs**:These are the runs which are taken when both the beams are present in the LHC beam-pipe and are stable ones having required centre of mass energy with the magnetic field of 4 Tesla and good HLT menu from the physics point of view. All the subsytems should be included in DAQ during the data taking.

- **Short Collision runs**: These are the runs which have the detector and the trigger conditions same as of standard collision runs but have run length of very few minutes. Runs which have very less number of lumisections, hardly 3 or 4, with total luminosity of run $< 80\ nb^{-1}$ are considered as short runs. In these runs statistics is so small that no useful physics information from them can be extracted to study the relevant physics part. So these runs are not considered for the certification.

DQM-DC team certifies all the above data/runs classes except commissioning, which does not have any kind of meaningful physics in it and short collision runs as it lacks the required statistics to extract the important and useful physics information from them. Also for the cosmic runs (CruZeT and CRAFT) if number of tracks are less than 100 then such runs are not considered for the certification because of insufficient statistics.

4.3.3 Tools for Certification

DQM-DC team constantly monitors the flow of the runs from Online RR to Offline RR. To have all the required information for the process of certification certain tools are required to propagate the information in proper channel. Tools required are

- **Online runregistry**: For monitoring the live status of all sub-detectors of the CMS and to store all the information of collision events like run number, energy, run start time, stop time and magnetic field.
- **Primary Datasets**: These are the datasets required for the certification of runs. These datasets cover almost all possible types of physics processes which are under study by various sub groups. Name of these primary datasets are
    i) **Single Muon**
    ii) **Single Photon**
    iii) **JetHT**
    iv) **Zero Bias**
- **Tier 0**: To perform the task of prompt reconstruction of the primary datasets described above from the raw data.
- **Offline DQM GUI**: For monitoring all the physics objects created using the above datasets and analyze them in the form of DQM histograms.
- **Offline runregistry**: To store all the information from all DPGs and POGs about the detector parts and physics objects for each collision event/run

4.3.4 Workflow of the Data Certification

Many subsystems (DPGs and POGs) take part in the process of central data certification. The detector performance groups which participate include CSC, DT, RPC, Tracker, Pixel, SiStrip, ECAL and HCAL whereas the physics object groups which participate are JetMet, Muon, Lumi and Egamma. The online shifters from each DPG and POG provide their initial feedback of each event/run to their respective experts. After getting the feedback from shifters, experts analyze the DQM plots related to detector performance and physics object which is reconstructed during the PromptReconstruction. Then this information about the goodness or badness of run for the various DPGs and POGs is saved and stored in the respective workspace of subsystem using offline RR. For example Muon experts check all the DQM distributions related to the reconstructed muon for every run which needs to be certified and mention their findings about the run whether it is good or bad in the muon workspace of offline run-registry.

Certification is a process which is carried out weekly. It starts immediately with data taking and stops only when detector stops taking data. DQM-DC team, every week, makes a call for list of runs which propagate and become available from online RR to offline RR for the certification. This list is sent to all the DPGs and POGs which are involved in the certification. Experts of every subsystem feed their findings to their respective workspace from which DQM-DC team extracts the information and puts all the certified runs, whether good or bad, in complete state. Based on the information DC team separates the good run from the list and creates a JSON file for Golden channel physics and Muon channel physics which consists of the lumisection wise information of each and every good run. These JSON files are used to plot the luminosity plot of data, which compares how much data is recorded by the CMS out of data delivered by the LHC. Also only the data which is marked good is compared with the data recorded by the CMS. This comparison gives the direct view about performance of the detector. The difference between the CMS recorded data and the CMS validated good data is because of the losses suffered by the DPG or reconstructed physics objects. These losses are also studied in detail by the DQM-DC group to see whether it is possible to recover any single bit of lumisection of bad runs or not. In such cases experts are asked to review their findings about the run and change the flag of data from bad to good. Once bad data is recovered by the subsystem, central DC team again performs the entire process to gain the lumisection and luminosity of that run. Also few bad data is recovered during the process of re-reconstruction. Once whole year data taking and certification of the data finishes, all the results are made public and every CMS user can use these JSON files for their analyses purposes.

4.3.5 Certification during 2017

During the year 2017, DQM-DC team certified the cosmic and proton-proton Collision data taken at the centre of mass energy of 13 TeV. In collision data not only proton proton collision data was certified but also a special class of Xe-Xe collision data. The LHC operations resumed in the end of May 2017 after a technical stop of 4 months. In order to calibrate the sub-detectors, CMS started taking Commissioning and CruZeT runs to have the correct idea about the performance of the detector.

4.3.5.1 Certification of Cosmic Runs

The process of certification in 2017 started with the CruZeT campaign on 10-04-2017. First cosmic run which was recorded with 0 Tesla magnetic field of detector was 290129, taken on 27-03-17. During the whole year DC team has certified 348 CruZeT runs and 591 Cosmic runs taken with 4 Tesla magnetic field, which are called as ‘CRAFT’. 293491 was the first CRAFT run which was taken on 07-05-17 and call for first CRAFT was given on 15-05-17. Central DC team does not provide the JSON files for the cosmic runs. But if any user wants to use this certified cosmic data the user can generate its own JSON file using the instructions to produce JSON file, which is provided by the DC team.

4.3.5.2 Certification of Collision17 Runs

The first collision run ‘294927’ with the centre of mass energy of 13 TeV and magnetic field of 3.799 Tesla took place on 23-05-17 having the LHC fill number 5698. The HLT menu was not good for the physics during this period so runs which were taken with this HLT menu during the period called Era A, was named as 'Commissioning runs'. There were 311 commissioning runs that were taken before the HLT menu for physics became good and collision runs made available for the certification. Era A comprised of runs ranging from 294927-297019, with last run taken on 16-06-17. Dataset name was changed from the Era A to Era B with the change in the HLT menu key. During the entire 2017, a total of 1026 collision runs were recorded with 13 TeV centre of mass energy, out of which 43 runs were special ones which were taken with HLT menu not good for physics, so these runs were not considered for the certification. 399 runs from these collision data had insufficient statistics that could hardly be certified so they were also excluded from the certification process. Also 3 runs were taken with the bunch crossing of 50 ns instead of 25 ns and 7 low PU runs along with 3 Xe-Xe collision runs were also taken. So all these runs together were not considered for the certification. The LHC has delivered 49.98 fb^{-1} of luminosity for these 1026 collision runs and the CMS has recorded 45.14 fb^{-1} out of the delivered luminosity. The loss of 4.84 fb^{-1} of luminosity corresponds to the dead time and down time of the detector. Among these 1026 runs, only 571 runs were certified which corresponds to the 44.10 fb^{-1} luminosity, the loss of 1.04 fb^{-1} is due to the above mentioned runs (signoff, special runs, 50 ns, low PU) which were not considered for the certification process. The Luminosity plots corresponding to these values are shown in figures 4.13 and 4.14 [17]. The details about the runs recorded by the CMS and certified by the DQM-DC team in year 2017 at $\sqrt{s} = 13$ TeV are listed in table 4.1.

44.10 fb^{-1} luminosity corresponding to collision runs were available for the certification and all runs amounting this luminosity were certified by the DQM-DC team giving 100 % efficiency for the certification procedure. Out of this luminosity the data which corresponds to the good runs containing all the information of good lumisections of these runs has luminosity of 41.86 fb^{-1}. The only good runs which were certified are known as the CMS validated runs or Golden validated runs. The luminosity difference between the CMS validated and the CMS recorded for physics(runs considered for certification) is attributed to the losses either due to complete bad runs or bad lumisections of the good runs. The losses are discussed briefly in next section.

ERA	From Run	To Run	Dataset Name	Golden Certified Luminosity (in fb^{-1})
Run2017A	294927	297019	/PromptReco /Collisions2017A/DQM	0
Run2017B	297046	299329	/PromptReco /Collisions2017B/DQM	4.823
Run2017C	299368	302029	/PromptReco /Collisions2017C/DQM	9.664
Run2017D	302030	303434	/PromptReco /Collisions2017D/DQM	4.252
Run2017E	303824	304797	/PromptReco /Collisions2017E/DQM	9.278
Run2017F	305040	306462	/PromptReco /Collisions2017F/DQM	13.540
Run2017G	306546	306657	/PromptReco /Collisions2017G/DQM	0.09
Run2017H	306896	307082	/PromptReco /Collisions2017H/DQM	0.22

Table 4.1: List of runs certified during 2017

4.3.5.3 The Data Losses

During the year 2017 there was data loss of 2.20 fb^{-1} luminosity. This loss is due to various DPG and POG losses related to bad runs or few bad lumi sections of the overall good runs. Losses are classified in to two categories: the inclusive loss and the exclusive losses. Inclusive losses are those losses in which two or more than two detector groups contribute in the losses. e.g. Inclusive loss due to Pixel detector is more than 500 pb^{-1} and similarly for the Silicon Strip same amount of inclusive loss is recorded as shown in figure 4.15. The same amount of loss due to these

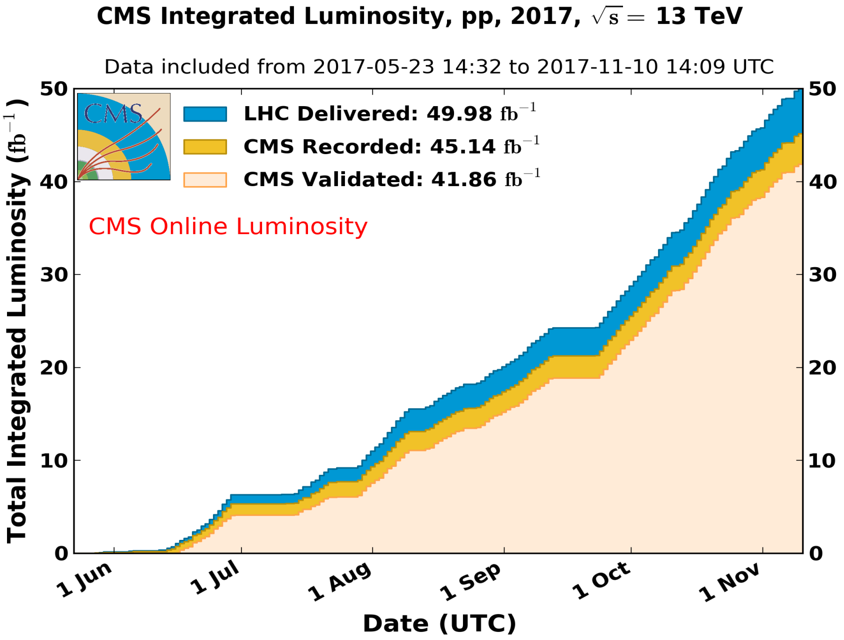

Figure 4.13: Graph representing the LHC delivered luminosity (azure), the CMS recorded (orange) and certified as good for all kind of physics analysis (Golden Physics) while having the stable beam (light orange).

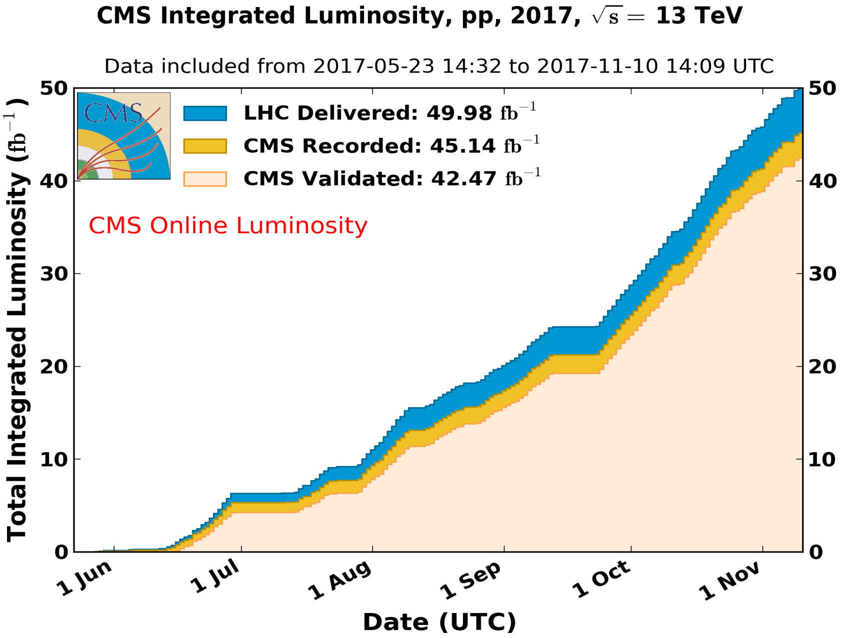

Figure 4.14: Graph representing the LHC delivered luminosity (azure), the CMS recorded (orange) and certified as good for the Muon physics analysis only (Muon Physics) while having the stable beam (light orange).

two subsytems implies that few runs which are marked bad by Pixel detector is also marked bad separately by the Silicon Strip detector so therefore the same runs which are contributing in the losses of these two systems. The exclusive losses correspond to the losses explicitly by the specific DPG or POG e.g. the exclusive loss due to RPC detector is around 48 pb^{-1} as shown in figure 4.16. This loss is solely due to few runs which do not pass the desired quality test of RPC detector only for the rest of subsystems these runs are marked good and pass the quality test for other subsystems. Losses can also be classified in to detector control system, DCS loss or data quality flags loss. Total luminosity loss of 2.20 fb^{-1} for 2017 run contains 1.28 fb^{-1} loss due to DCS and 0.93 fb^{-1} loss because of data quality flags and are shown in figures 4.17 and 4.18 respectively. HCAL, CSC and Strip were the DPG which contributed majorly in the DCS loss. The losses due to only these three DPGs valued around 1.0 fb^{-1} (975 pb^{-1}). Major loss of quality flags were due to pixel and HLT subsytem, they both together counted the loss of around 500 pb^{-1}. The details about the losses of each DPG and POG can be found in the reference [18] for entire 2017 and in the references [19, 20] for losses in terms of the detector control system and quality flags respectively.

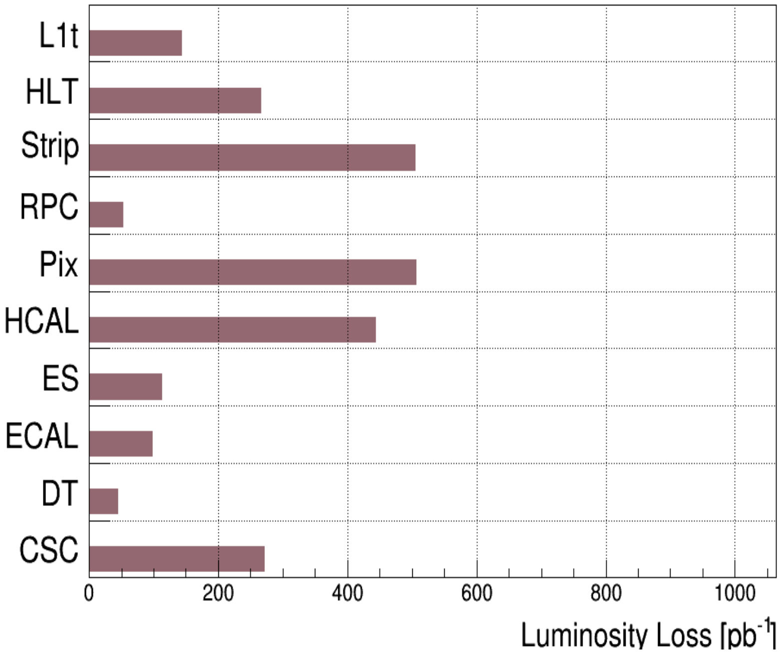

Figure 4.15: Total inclusive losses for 2017 data. Luminosity losses are in pb^{-1}

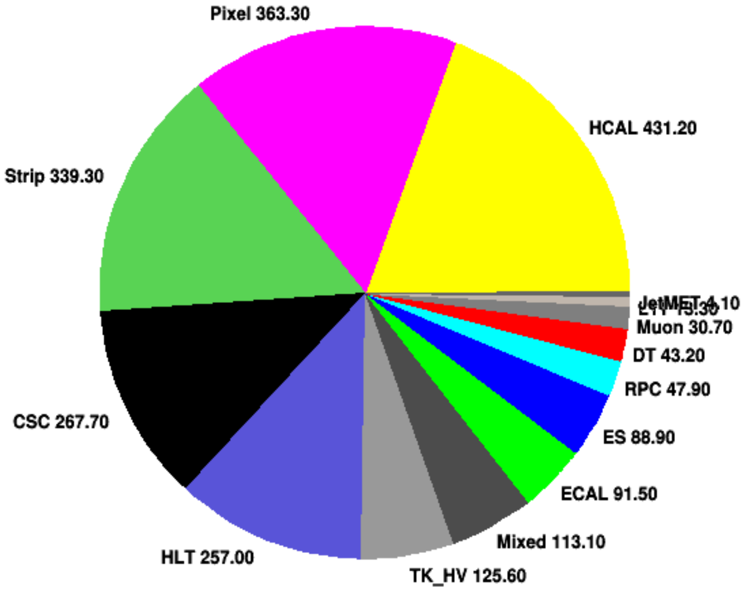

Figure 4.16: Total exclusive losses for 2017 data. Luminosity losses are in pb^{-1}

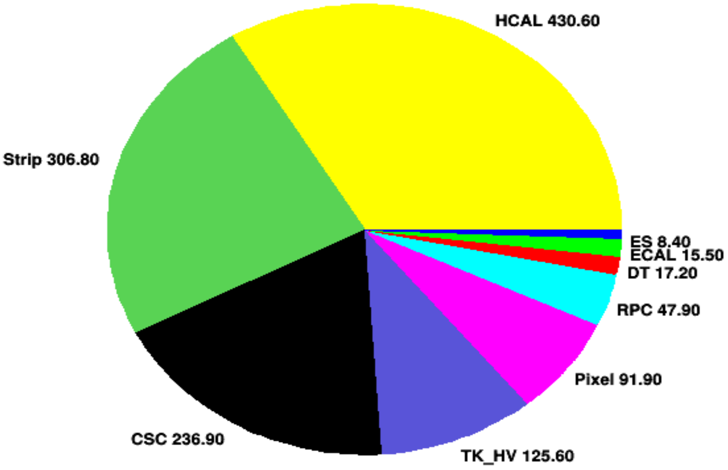

Figure 4.17: Exclusive losses in terms of the DCS loss for 2017 data. Luminosity losses are in pb^{-1}

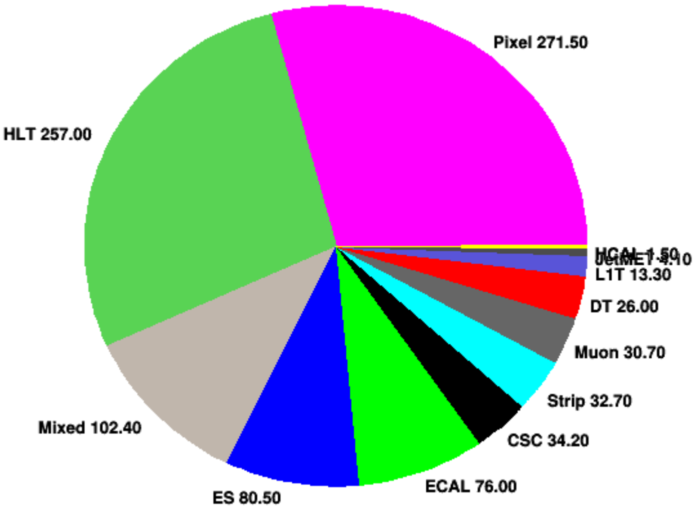

Figure 4.18: Exclusive losses in terms of quality flags loss for 2017 data. Luminosity losses are in pb^{-1}

Bibliography

[1] http://cms.web.cern.ch/news/new-physics-performance-and-dataset-group-cms

[2] S. Lindner, “CMS Data Quality Monitoring: Offline Workflow and Physics”, Austria (2011)

[3] https://twiki.cern.ch/twiki/bin/view/CMS/DQMPositions

[4] https://twiki.cern.ch/twiki/bin/view/CMS/DQM

[5] A. Cimmino, “Data Quality Monitoring and Performance Studies of the Resistive Plate Chamber Detector at the CMS Experiment at LHC”, Austria (2010)

[6] A. Aghabayli, “Data Quality Monitoring at CMS with Machine Learning”, CERN openlab Summer Student Report, CERN (2016)

[7] https://twiki.cern.ch/twiki/bin/view/CMSPublic/WorkBookDQM

[8] https://twiki.cern.ch/twiki/bin/view/CMSPublic/RelMon

[9] https://twiki.cern.ch/twiki/bin/view/CMSPublic/PhysicsResultsConveners

[10] https://cms-conddb.cern.ch/PdmV/valdb

[11] A. Banfi et al., “Predictions for Drell-Yan ϕ^* and Q_T observables at the LHC, Phys. Lett. B **715**, 152 (2011)

[12] A. Banfi et al., “Optimisation of variables for studying dilepton transverse momentum distributions at hadron colliders”, Eur. Phys. J. C **71**, 1600 (2011)

[13] A. Banfi et al., "Probing the low transverse momentum domain of Z production with novel variables", JHEP **1**, 1 (2012)

[14] https://twiki.cern.ch/twiki/bin/viewauth/CMS/CutBasedElectronIdentificationRun2

[15] https://twiki.cern.ch/twiki/bin/viewauth/CMS/SWGuideMuonIdRun2

[16] https://twiki.cern.ch/twiki/bin/view/CMSPublic/WorkBookComputingModel

[17] https://twiki.cern.ch/twiki/bin/viewauth/CMS/DataQuality

[18] https://cms-service-dqm.web.cern.ch/cms-service-dqm/CAF/certification/scripts/CMSSW_9_0_0/LumiWeb/Losses/2017/Loss−Final2017_total/LossSummary.html

[19] https://cms-service-dqm.web.cern.ch/cms-service-dqm/CAF/certification/scripts/CMSSW_9_0_0/LumiWeb/Losses/2017/Loss−Final2017_HVonly/LossSummary.html

[20] https://cms-service-dqm.web.cern.ch/cms-service-dqm/CAF/certification/scripts/CMSSW_9_0_0/LumiWeb/Losses/2017/Loss−Final2017_flagonly/LossSummary.html

Chapter 5

Phenomenology of Multi-Particle Production

Collisions of particles at relativistic high energies lead to the production of various new elementary particles. These particles are produced due to the gluon-gluon, quark-quark and quark-gluon interactions between the constituent quarks and gluons of the colliding particles. The produced particles can be the baryons (qqq state), mesons ($\bar{q}q$ state) or leptons. Simplest but the most significant observation to describe the mechanism of particle production is charged particle multiplicity and the distribution of number of particles produced, known as multiplicity distribution [1]. Multiplicity distribution, MD, carries important information about the correlations of particles produced, thus providing a very fine way to inquest the dynamics of the quark-quark, gluon-gluon and quark-gluon interactions. Particle production mechanism [2] can be described in terms of several phenomenological models which use the laws of statistical mechanics, thermodynamics, fluid mechanics, hydrodynamics and statistics etc. Ensemble theory approach from statistical mechanics has been applied to establish the statistical models which incorporate statistical fluctuations as a vital information source. Various phenomenological models have been very successful in describing the mechanism of particle production in high energy interactions.

Current high energy experiments for studying particle collisions use high precision sophisticated detectors which have several distinct layers of sub-detectors, adequate in detecting the neutral and charged particles produced during the particle collisions very accurately. In order to understand the particle production mechanism, predictions of the theoretical and phenomenological models are compared with the experimentally observed distributions of particles resulting from high energy collisions. One of the most readily measured quantities is the number of particles produced. The following sections of this chapter give a brief overview of multiplicity measurements, some basic definitions of probability distribution, moments and their notations. Also several statistical distributions, various phenomenological approaches and models which have been successful in describing the multiplicity distributions are described in this chapter.

5.1 Overview of Multiplicity Distributions

Collision or interaction of two particles is generally described in terms of cross-section which is calculated by measuring the number of particles produced. The cross section essentially gives the measure of the probability of production of particular number of particles. The multiplicity distribution is generally defined in terms of probability by the formula

$$P_n = \frac{\sigma_n}{\sum_{n=0}^{\infty} \sigma_n} = \frac{\sigma_n}{\sigma_{total}} \tag{5.1}$$

where σ_n is the cross section for production of 'n' number of particles and σ_{total} represents the total cross section of interaction at center of mass energy $\sqrt{s}$. Experimentally this probability, P_n, is obtained from the number of charged particles produced at specific multiplicity, n_{ch} and the total number of particles produced during the collisions, N_{total}. The probability is defined as in equation (5.1) with n is replaced by n_{ch}. The production probability of n charged particles in the final state resulting from the particle collisions is associated with particle production mechanism. The multiplicity distribution, MD, obeys conventional Poisson distribution if there is no correlation between the particles produced i.e. particles produced in the high energy interactions are exclusive and independent of each other. The interaction in this case follows '$a + b \rightarrow c + d +$ ....', where a and b are colliding particles and c, d are the particles produced after collision. In such cases dispersion, which is defined by $D = \sqrt{< n^2 > - < n >^2}$, is related with the average multiplicity $< n >$. The presence of any kind of correlation amongst the particles leads to the deviation from Poissonian form. The measurement of charged multiplicity distributions provide notable constraints for models of multiparticle production. Few of these models are derived from the Quantum Chromodynamics, in which particle formation involves soft scale based on the non perturbative techniques of QCD.

Multiplicity distributions at low energies, of order of $\sim$ 10 GeV for leptonic and hadronic collisions such as e^+e^- or pp, could be described very well using Poisson distribution [3,4]. The multiplicity distributions exhibited a broader width at higher energies showing the significant deviation from the Poissonian form. The correlation in the particles produced during the collisions was found to be responsible for the deviations. In 1972 Koba, Nielsen and Olesen [5] brought forward the theory of universal scaling for multiplicity distributions at high energies which is known as KNO scaling. The energy dependence of the dispersion defined by relation $D \propto < n >$ implied the compliance of KNO scaling. But 13 years later violation of KNO scaling was observed by UA5 collaboration while analysing the multiplicity data at $\sqrt{s}$ = 540 GeV [6] obtained from $\bar{p}p$ collisions. Later on it was revealed by the collaboration that KNO scaling was violated even at $\sqrt{s}$ = 200 GeV [7]. The data at these energies were well described by the negative binomial distribution NBD [8] with k and $< n >$ as its two important parameters. The parameter k describes the width of distribution. But the failure of NBD in describing the MDs was observed at $\sqrt{s}$ = 900 GeV and $\sqrt{s}$ = 1.8 TeV [9] at Tevatron. The failure of NBD led Giovannini and Ugoccioni to put forward a two component model [10, 11] in 1999. This model was based on the combination of two NBDs, one as soft component of interactions and other as semi-hard component and was successful in describing the data at $\sqrt{s}$ = 1.8 TeV. This combination model clearly explained the experimental results in favour of multi-partonic interactions. The overlap of various interactions has effect on the distributions and illustrates the deviations from KNO scaling at lower energies. Few years later in 2002 Kodama and Aguiar used the concept of non-extensive entropy based on Tsallis model [12] to describe the multiplicity data at lower energies [13] for *pp* collisions (at 27 and 44 GeV). Recently another statistical distribution named, Weibull distribution, is used to describe the multiplicity data at higher energies. The advantage of using this distribution is that it can be fitted to the non-symmetrical data. Though Weibull distribution failed to describe the data at lower energies at $\sqrt{s} \sim 91$ GeV but its implementation and success on multiplicity data at higher energies (LHC energies) is investigated and presented in the thesis.

All the existing distributions and models which describe the data at lower and intermediate energies fail to explain the experimental data of multiplicity at LHC energies, $\sqrt{s} = 0.9$ TeV to 7 TeV. This motivated us to work on the problem of charged particle multiplicity data at highest available energy. The analysis has been done for energies ranging between 14 GeV to 7 TeV and published by us. However the work reported in this thesis is focused on the study of multiplicity for energies ranging from 91 GeV to 7 TeV. In the following sections scaling properties like Feynman scaling and KNO scaling etc. are discussed along with several statistical and phenomenological distributions which are successful in describing the data.

5.2 Basic Theoretical Concepts

Particle production in high energy interactions can be described by the uncorrelated emissions i.e. the particle produced is independent of each other. In such cases multiplicity distribution is governed by Poissonian form. Discrepancies to this form indicate the correlations between the particles produced. Over the last 20 years the multiplicity distributions at various center of mass energies, $\sqrt{s}$, have been studied by using different analytical and phenomenological approaches. Some of these are described in the following section.

5.2.1 Feynman Scaling

Fields radiated in an inclusive process, like $a+b \rightarrow c+anything$, at high energies are Lorentz contracted in the longitudinal z-direction and makes field energy a δ function in z [14]. This field energy is distributed uniformly in longitudinal momentum space using Fourier transformation in order to have equal average amount of energy in any element dp_z. Using the phenomenological concept of quantum number exchange between the colliding particles, Feynman explained that the number of particles with a given mass, m and transverse momentum, p_T per dp_z interval depends on the energy, E = E(p_z) [15] as;

$$\frac{dn}{dp_z} \sim \frac{1}{E} \tag{5.2}$$

This can be used further to find the probability of particle type i, having mass m, transverse momentum p_T and longitudinal momentum p_z as;

$$\frac{d\sigma^c_{ab}}{\sigma_{total}} \quad = \quad f_i(p_T, \frac{p_z}{W})\frac{dp_z}{E}d^2p_T \quad = \quad f_i(p_T, \frac{p_z}{W})d^2p_T\, dy \tag{5.3}$$

with W = $\frac{\sqrt{s}}{2}$ and particle energy, E is defined as;

$$E = \sqrt{m^2 + p_T^2 + p_z^2} \tag{5.4}$$

where Function, $f_i(p_T, x = \frac{p_z}{W})$, which is called as scaling function or Feynman function [16], describes the distribution of particles. Feynman put forward the hypothesis that scaling function, f_i becomes independent of W at high energies and is known as *Feynman scaling*. x, which is known as *Feynman* variable is the fraction of particle's longitudinal momentum, p_z to incident particle's total energy W ($x = \frac{p_z}{W}$). By integrating the equation (5.3) [1], the mean multiplicity as a function of $\sqrt{s}$ can be derived giving the expression in equation (5.6). This shows the falling of exclusive cross sections with the increasing energy $\sqrt{s}$ as;

---

[1] $\int_{x=-1}^{1}\int f_i(p_T, \frac{p_z}{W})\frac{dp_z}{E}d^2p_T \;=\; f_i(p_T, \frac{p_z}{W})ln(\frac{\sqrt{s}}{m^2})$

$$< n > \propto\ lnW\ \propto\ ln\sqrt{s} \quad with\, W = \frac{\sqrt{s}}{2} \tag{5.5}$$

$$e^{-<n>} \sim \frac{1}{\sqrt{s}} \tag{5.6}$$

Using the relation of rapidity [2] and integrating the equation (5.3) gives the dependence of rapidity on energy as, $|y_{max}| \sim ln\,(\frac{\sqrt{s}}{m^2})$, where $|y_{max}|$ is total phase space available to particles, implying that the maximum rapidity also increases with $ln\,\sqrt{s}$ in a collision. Considering the assumption of uniform distribution of particles in rapidity, the numbers of particles produced in unit rapidity interval is given by;

$$\frac{dn}{dy} = const. \tag{5.7}$$

The scaling function, $f_i(p_T, x)$ has a limit that as $s \to \infty$ then $x \to 0$ i.e. it becomes independent of s at high energies. $f_i(p_T, x)$ reaches to a constant value at smaller x [3]. Height of rapidity distribution near mid-rapidity ($y = 0$), which is called as plateau, is defined by $\bar{f}_i(x)$ at $x = 0$. The function $\bar{f}_i$ represents the integration over p_T^2. As $\bar{f}_i(0)$ has constant value which means height of distribution is independent of energy $\sqrt{s}$. Similarly, the pseudorapidity at mid rapidity ($\frac{dn}{d\eta}$) is nearly constant on applying the Feynman scaling. The transfer from y to η depends on average transverse mass m_T ($= \sqrt{p_T^2 + m^2}$). Under the condition $m^2 <<< p_T^2$, pseudorapidity approximates the rapidity. This average transverse mass square, m_T^2 is weakly dependent on the energy i.e. transformation factor changes only by 1 % with change in the energy from $\sqrt{s} = 100$ GeV to 1 TeV. Also this transformation is responsible for dip in the distribution near $\eta \sim 0$ which is not present in the rapidity distribution. The dip in η distribution depends on ratio p_T/m and η value. This behaviour is shown in figure 5.1 where ratio $\frac{p_T}{m} = 1$.

---

[2] Rapidity is given by, $y = \frac{1}{2}\, ln\frac{E+p_z}{E-p_z}$ and $\frac{dy}{dp_z} \sim \frac{1}{E}$

[3] Integrating by parts $\frac{dx}{\sqrt{4m_T^2/s+x^2}} = d\, ln(x + \sqrt{4m_T^2/s + x^2})$ and that integral $\int_0^1 \bar{f}_i(x)\, ln\, x\, dx$ converges for finite $\bar{f}_i(0)$

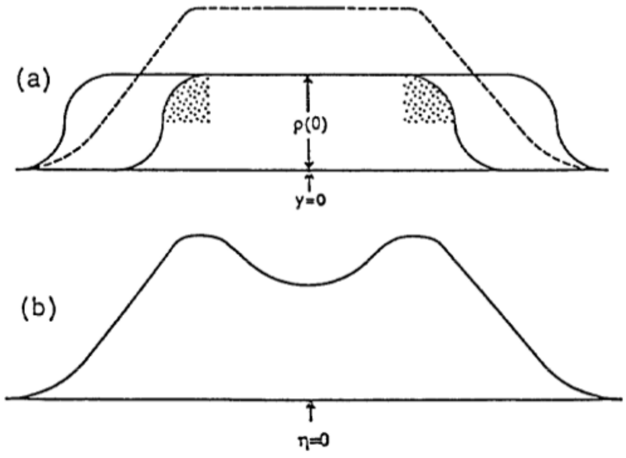

Figure 5.1: Figure describing the (a) Rapidity distributions for two energies: (solid lines) assuming Feynman Scaling, (dashed line) a more realistic situation at the higher energy (b) Pseudorapidity distribution for p_T =m

5.2.2 Koba-Nielsen-Olesen (KNO) Scaling

In 1972 Koba, Nielsen and Olesen [5] proposed the scaling relation for multiplicity distributions, known as KNO scaling, which was derived from the Feynman scaling. The shape of multiplicity distribution can be described well using the assumption that energy dependence of multiplicity distribution at higher energies could be formulated using the average multiplicity. They established this scaling behaviour to explain the issue of energy dependence of multiplicity.

Number of particles in the final state is scaled by defining a variable $z = \frac{n}{<n>}$, where $< n >$ represents the average multiplicity at energy, $\sqrt{s}$. The probability is given by, $P_n = \frac{\sigma_n}{\sigma_{total}} \;=\; \frac{1}{<n>}\,\Psi(z)$. KNO scaling is generally believed to have an asymptotic property i.e. validity in the limit $< n > \to \infty$ and was derived by using the extended form of the Feynman function expression, equation (5.3) KNO scaling is derived by calculating,

$$< n(n-1).....(n-q+1) > \;=\; \int f^{(q)}(x_1, p_{T,1}; .....; x_q, p_{T,q}) \frac{dp_{z,1}}{E_1} d^2p_{T,1} ..... \frac{dp_{z,q}}{E_q} d^2p_{T,q} \tag{5.8}$$

The function $f^{(q)}$ is used to describe the correlation of q particles i.e. q particles having energy E_q, transverse momentum $p_{T,q}$, longitudinal momentum $p_{z,q}$ and *Feynman* variable-x_q. Integrating the equation (5.8) for all x_i leads to polynomial in the form of $ln\sqrt{s}$ i.e.

$$P_n = \Big(\frac{1}{ln\sqrt{s}}\Big)\Psi\Big(\frac{n}{ln\sqrt{s}}\Big) + O\Big(\frac{1}{ln\sqrt{s}^2}\Big) \tag{5.9}$$

Since $< n > = \sum_n P_n(s)\, n$, substituting the equation (5.9) in the expression of $< n >$ leads to the relation ' $< n > \propto ln\sqrt{s}$ [4]. This means the probability, P_n, of the distribution can be scaled in terms of $ln\sqrt{s}$ as;

$$P_n = \frac{1}{< n >}\Psi\Big(\frac{n}{< n >}\Big) + O\Big(\frac{1}{< n >^2}\Big) \tag{5.10}$$

From the above equations it is found that the first term is due to the leading term in $ln\sqrt{s}$, i.e. $ln(\sqrt{s})^q$ where as second term consists of all other terms in $ln\sqrt{s}$, i.e. $(ln\sqrt{s})^{q'}$ for $q' < q$. Ψ $(z = \frac{n}{<n>})$ is a universal function which is energy-independent. This implies that multiplicity distribution at all the energies plotted as function of z would fall on one curve. KNO scaling predicts the increase in width of the multiplicity distribution with the increase in average multiplicity. KNO scaling is an immediate outcome of the observation that rapidity plateau remains constant with the increase in energy [17]. The increase of multiplicity results from the stretching of the available rapidity space. The field radiates the particles uniformly in y, so that the entire distribution fluctuates up and down with the total field energy, in a manner that it remains independent of $\sqrt{s}$. Therefore, the multiplicity distribution, and the ratio of the width of the distribution to the mean of distribution, remain the same. Experimentally, it is known that KNO scaling holds for energies up to $\sqrt{s} \sim 60$ GeV. The rise of the rapidity plateau with increase in energy was the perfect scenario to show the violation of Feynman scaling (so is the violation of KNO scaling). KNO scaling was found to be violated logarithmically with increasing energy $\sqrt{s}$ and first violation was observed in $\bar{p}p$ collision in UA5 experiment at centre of mass energy, $\sqrt{s} = 540$ GeV.

---

[4] $< n > = \sum_n P_n(s)\, n = \int_0^\infty n\, P_n(s)\; \mathrm{d}n = \int_0^\infty z\Psi(z)\; \mathrm{d}z \approx ln\sqrt{s}$

5.3 Statistical and Thermal Distributions

To characterize the multiplicity distribution, several statistical distributions based on probability theory and models have been used in the past. The statistical and probability distributions play key role in defining the multiplicity at various energies. These probability distributions are described in the following section.

5.3.1 Poisson Distribution

Poisson distribution, named after French mathematician S. Poisson [18], is a method to measure the number of events for a specific outcome of a discrete variable in a destined time or space for which an average number of events can be determined. Poisson distribution follows the situation where there are lesser successful events against failure or vice-verse and also the events with in any interval should be independent of another. If particles produced in the high energy interactions are independent of each other i.e. absence of any kind of correlation amongst them, then multiplicity follows the Poisson distribution. The probability distribution of n particles is then given by;

$$P_n = \frac{< n >^n}{n!} e^{-<n>} \tag{5.11}$$

It has only single free parameter, $< n >$, which is the mean of the distribution. Any correlation between the particles will lead to the deviation from this poissonian form. Poisson distribution exhibits the asymptotic KNO scaling. Probability distribution function can be defined separately for even and odd number of particles in order to take care of 'even-odd' effect which implies that the total number of charged particles produced should be even to obey the charge conservation principle. Probability in this situation is defined as

$$P_n = \frac{< n >^n}{n!} e^{-<n>}, \qquad for\, n = even \tag{5.12}$$

$$P_n = 0, \qquad for\, n = odd \tag{5.13}$$

Poisson distribution was used to describe the exclusive distribution of particles produced in an interaction; '$a + b \rightarrow c + d + ...$'. Experimentally at higher energies ($\sqrt{s} \sim 30$ GeV) Poisson distribution failed to define the particle multiplicity suggesting the existence of correlation between the particles produced.

5.3.2 Gamma Distribution

Thermal models like Boltzmann-Gibbs (BG) model [19, 20] (or its generalizations) are based on the canonical distributions. These models describe only the particles which are uncorrelated and non-interacting. But in high energy interactions, particles stemming out are characterized by correlations and interactions amongst themselves. For intermediate and high momenta ($p_T > 3$ GeV/c) BG distribution fails to define the multiplicity spectra as well as transverse momentum spectra. At the lower and intermediate energies, where BG distribution fails, Gamma distribution provides the successful explanation of experimental multiplicity data.

In statistics the Gamma distribution is a continuous probability distribution and member of the distributions which have two parameters given by;

$$f(x;\alpha;\beta) = \begin{cases} \frac{\beta^{\alpha}}{\Gamma(\alpha)}\ (x-\mu)^{(\alpha-1)} e^{-\beta\,(x-\mu)} & \text{if } x > 0 \\ 0 & \text{otherwise} \end{cases} \tag{5.14}$$

The probability function of the Gamma distribution for variable x can be written in the form;

$$P_x = A_m\ (x-\mu)^{(\alpha-1)} e^{-\beta\,(x-\mu)} \tag{5.15}$$

where A_m ($= \frac{\beta^{\alpha}}{\Gamma(\alpha)}$) is a normalization constant of the distribution. α: the shape parameter, β: the inverse scale parameter or rate parameter [5] and μ: the location parameter, are the fit parameters of the Gamma distribution. In general location parameter, μ is taken as 0 to have standard Gamma distribution which has the form,

---

[5] Rate parameter is defined as the reciprocal of the scale parameter

$$P_x = A_m \; x^{(\alpha-1)} e^{-\beta\, x} \tag{5.16}$$

The parameters α and β of the distribution are normally greater than 1 but under condition $\alpha = 1$, the Gamma distribution becomes the exponential distribution. Both the parameters α and β define the shape of the graph but change in β shows an intense effect on the shape of distribution as shown in figure 5.2. When the shape parameter, α is increased and scale parameter, β is kept constant then the distribution shifts towards right side of zero. If α approaches infinity, then distribution takes the form of normal distribution. The mean of Gamma distribution is simply the ratio of its two parameters and defined as

$$< x > \; = \; \frac{\alpha}{\beta} \tag{5.17}$$

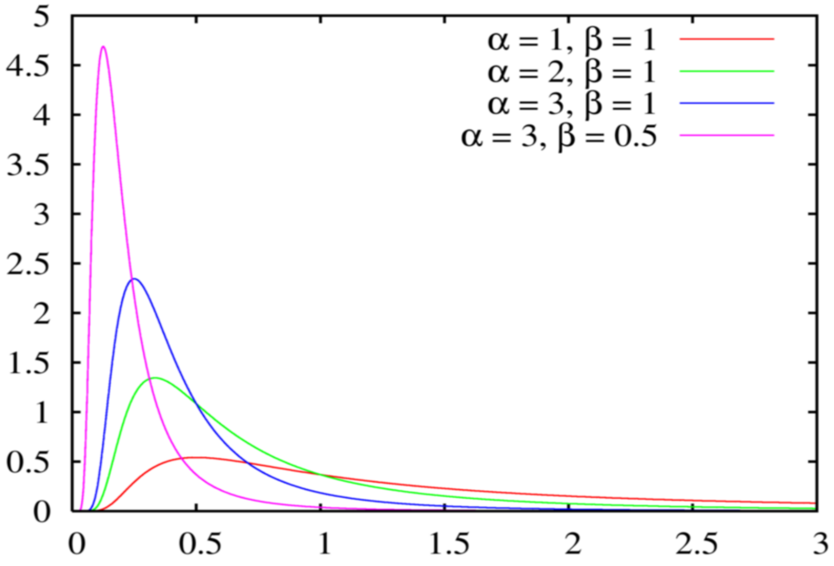

Figure 5.2: Figure showing the Gamma distribution for few alpha and beta values to show the change in the shape of the Gamma distribution. Image source: https://en.wikipedia.org/wiki/Inverse-gamma_distribution

In high energy collider experiments, emitted particles have a tendency to bunch together in a narrow cone known as a jet. Hadrons in a jet have a very confined distribution around the axis of jet in momentum space. Due to this narrow distribution they might be considered as one dimensional ensemble. If the momentum-energy conservation is considered ($\sum \epsilon_i$ = E and considering all the hadrons going in the same direction with $\epsilon_i = |p_i|$) during hadronization then the particles produced evolve into one dimensional micro-canonical ensemble[6]. If the momentum distribution in events with fixed multiplicity is defined by Boltzmann Gibbs distribution[7] then the normalized single particle distribution of particles in events with n multiplicity is defined as;

$$f_n(\epsilon) = A_c \, e^{-\beta_n \epsilon} \tag{5.18}$$

where $A_c = \beta_n^D \;/\; (k_D \; \Gamma(D))$ is a constant, $k_D = (\int d\Omega_p)$, the angular part of the momentum space integral, D the dimension of the phase space and β_n is related to the inverse temperature of the system and is given by equation (5.21). Ω represents the momentum space volume of a microcanonical state and ϵ represents the energy of a particle produced. Total energy E in then $= \sum \epsilon_i$. $k_D = \int d\Omega_p$ follows from the conditions

$$1 \;=\; \int d\Omega_p \int dp \, p^{D-1} f_n(\epsilon) \tag{5.19}$$

$$\frac{E}{n} \;=\; \int d\Omega_p \int dp \, p^{D-1} \epsilon f_n(\epsilon) \tag{5.20}$$

By substituting the equation (5.18) in to the equation (5.20) and integrating it gives the dependence of β_n on multiplicity n and energy E. It is found that inverse temperature, β_n [21], in every event is proportional to the multiplicity n, as;

$$\beta_n \;= \frac{D\, n}{E} \tag{5.21}$$

Multiplicity distribution in this case follows Gamma distribution [21,22] whose probability distribution function is the same as defined in equation (5.16).

---

[6] Microcanonical system is defined as a system contained in constant volume V having fix energy E with a constant number of particles N and is completely isolated from its surroundings

[7] The Boltzmann distribution is a probability distribution of the particles in a system over several possible states. It defines the probability of a certain state as a function of energy of the state and temperature of the system on which it is applied. It is given by; $p_i = \frac{e^{-\epsilon_i/k_B T}}{\sum_{j=1}^{M} \epsilon_i/k_B T}$. Where p_i is the probability of state i having energy ϵ_i, k_B is the Boltzmann constant, T is the system temperature and M is the total number of states accessible to the system.

In case the average momentum distribution follows a micro-canonical behaviour then the shifted multiplicity (n-n_0) follows Gamma distribution. n_0 is a constant which gives the shift in the multiplicity and is defined as $n_0 = 1 + \frac{2}{D}$, where D is the dimension of phase space. This shift in multiplicity from $n \rightarrow (n\text{-}n_0)$ can be made without violating KNO scaling. In this case the normalized single particle distribution in events with n multiplicity is defined as;

$$f_n(\epsilon) \;\propto\; \frac{\Omega_{n-1}(E-\epsilon)}{\Omega_n(E)} \tag{5.22}$$

where above equation is in accordance with micro-canonical momentum space volume at fixed energy and multiplicity, and given by;

$$\Omega_n(E) = \frac{k_D^n\ \Gamma(D)}{n!}\ E^{nD-1} \tag{5.23}$$

The probability distribution function in this case is given by,

$$P_n = A_m\ (n-n_0)^{(\alpha'-1)} e^{-\beta'\,(n-n_0)} \tag{5.24}$$

Where α' is the shape parameter and β' is the inverse scale parameter of the Shifted Gamma distribution

5.3.3 Negative Binomial Distribution

Negative Binomial distribution plays a key role in describing the multiplicity spectrum. NBD has been applied on experimental measurements of multiplicity to characterize the process of multi particle production over broad range of energy for several interaction processes. NBD describes well the multiplicity distributions for nearly all the inelastic high energy processes except for data from the highest available energies ($\sim$ TeV). The probability distribution function of NBD is derived by considering an infinite series of Bernoulli trials [23] with probability of success p of an event on each single trial. It is defined as

$$P_n^{NBD}(p,k) = \begin{pmatrix} n+k-1 \\ n \end{pmatrix} (1-p)^n p^k \tag{5.25}$$

It provides the probability of n failures before k successes, having success probability p. Using the equation $\Gamma(x+1) = x\Gamma(x)$ the above equation can be simplified. Thus,

$$\binom{n+k-1}{n} = \frac{(n+k-1)!}{n!(k-1)!} = \frac{\Gamma(n+k)}{\Gamma(n+1)\Gamma(k)} = \frac{(n+k-1)(n+k-2).....k}{\Gamma(n+1)} \tag{5.26}$$

$$P_n^{NBD}(p,k) = \frac{\Gamma(n+k)}{\Gamma(n+1)\Gamma(k)}(1-p)^n p^k \tag{5.27}$$

The mean $< n >$ of the distribution is related with the probability, p by

$$\frac{1}{p} = 1 + \frac{< n >}{k} \tag{5.28}$$

Using the above equation probability function of NBD gets simplified in to

$$P_n^{NBD}(p,k) = \frac{\Gamma(n+k)}{\Gamma(n+1)\Gamma(k)} \left(\frac{< n > /k}{1+ < n > /k}\right)^n \frac{1}{(1+ < n > /k)^k} \tag{5.29}$$

Under the condition of large k, $k \to \infty$ ($k^{-1} \to 0$), NBD approaches back to Poissonian form and for $k = 1$, NBD reduces to the geometrical distribution[8].

Where as for negative values of k binomial distribution can be formed from NBD. Figure 5.3 shows the NBDs with different set of parameters. $P_{p,k}^{NBD}(n)$ function obeys KNO scaling only if parameter k of NBD function is constant and independent of energy. Probability of NBD function can be written in the KNO form as,

$$\Psi_{NBD}(z) = \frac{k^k}{\Gamma(k)} z^{k-1} e^{-kz} \tag{5.30}$$

with limit $< n >$/k >> 1 and z = $n/ < n >$ being fixed. Analysis of k as a function of energy, $\sqrt{s}$, for multiplicity distribution directly exhibits whether KNO

---

[8] The geometric distribution is a special case of the negative binomial distribution with the number of successes (k) equal to 1. It is a discrete distribution for n =0, 1, 2, ... having probability density function, $P_n = (1-p)^n p$ with p as the probability of success.

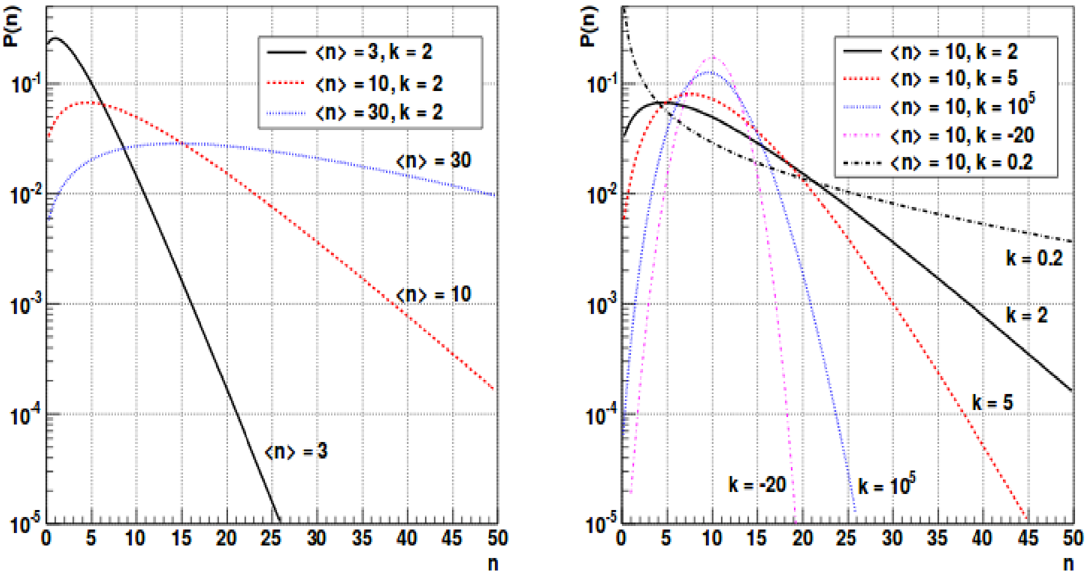

Figure 5.3: Example of Negative binomial distributions with a) constant value of parameters k at different set of parameter $< n >$ and b) with constant value of parameters $< n >$ at different set of parameter k. Plot taken from [16]

scaling is violated or not. Multiplicity distribution following the NBD originates from the fact that particles emitted in the interaction process are correlated. This correlation is exhibited by the recurrence relation $g(n)$ [16];

$$g(n) = \frac{(n)P(n)}{P(n-1)} \tag{5.31}$$

This is constant in case of uncorrelated emission. Any divergence from the constant value of recurrence relation reflects the existence of correlations. For Poisson distribution, $P(n) = \frac{<n>^n}{n!} e^{-<n>}$ the uncorrelated emission of particles, $g(n) = < n >$ is a constant. The particles which are distinguishable (by means of their momenta) are represented by the term (n) of equation (5.31). In terms of NBD, recurrence relation is written as,

$$g(n) = a + bn \qquad k = a/b \;\; and < n > = \;\; a/(1-b) \tag{5.32}$$

where $a =< n > \;\; k/(< n > +k)$ and $b =< n > /(< n > +k)$, which makes

$g(n) = a(1 + n/k)$. Experimentally it is found that parameter k increases with increase in rapidity range and decreases with increase in $\sqrt{s}$ for a fixed rapidity interval. At higher energies the relation of k with energy $\sqrt{s}$ is found to be,

$$k^{-1} = \alpha + \ \beta \, ln\sqrt{s} \tag{5.33}$$

with α and β as constants.

5.3.4 Krasznovszky-Wagner Distribution

Krasznovszky-Wagner distribution is named after physicists S. Krasznovszky and I. Wagner. The Generalized geometrical optical model is the basis of KW distribution [24]. This probability distribution was found very fruitful in describing the multiplicity distributions of inelastic and non diffractive processes at energies ranging from $\sqrt{s}$ = 14 GeV - 900 GeV [25, 26]. It is a three parameter function whose probability distribution function is defined as,

$$P(< n >, m, A) = \frac{2\, m\, F(A)^{A}\, z^{mA-1}\, e^{-F(A)\, z^{m}}}{< n > \ F(A)} \tag{5.34}$$

where $z = \frac{n}{<n>}$ and $F(A) = \frac{\Gamma^{m}(A+1/m)}{\Gamma^{m}(A)}$. Parameter A is a scaling violation parameter which depends upon the energy $\sqrt{s}$ and m is a constant, a real positive number, depending upon the collision type. The probability distribution obeys KNO scaling if the value parameter A remains constant in the limit $\sqrt{s} \to \infty$. From the analysis of data with KW distribution it was found that the parameter A decreases with increase in energy [26]. At higher energies ($\sqrt{s} > 546$ GeV), KW distribution shows departure from the experimental data.

5.3.5 Lognormal Distribution

Lognormal (or log-normal) distribution [27, 28] is a continuous probability distribution of a random variable with its normally distributed logarithm. This implies if a variable x is distributed lognormally then function dependent on x i.e. $y = ln(x)$ will have normal distribution. The probability function is given by,

$$P_n(\mu, \sigma, m) = \frac{1}{\sigma\sqrt{2\pi}} \frac{1}{x-\mu} e^{-\frac{ln((x-\mu)/m)^2}{2\sigma^2}} \tag{5.35}$$

where σ is the shape parameter, μ, the location parameter and m, the scale parameter which is also the median of the distribution.

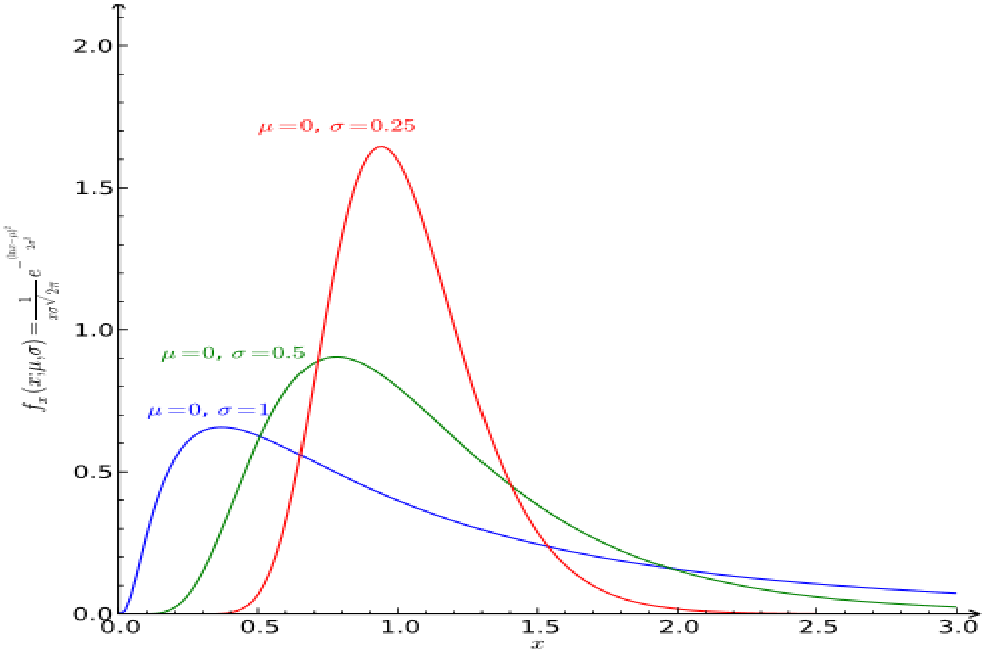

Figure 5.4: Plot showing the effect of σ on the log-normal probability density function and its consequence on the shape of the distribution with Location parameter, $\mu = 0$. Image source: https://en.wikipedia.org/wiki/Log-normal_distribution

The shape parameter, σ does not change the location of the graph, it just influences the overall shape as shown in figure 5.4. Scale parameter m, makes the graph to shrink or stretch while the location parameter μ tells the position of graph on x-axis. In standard conditions μ is taken as 0 and m is considered as 1, so the resulting distribution has only shape parameter, σ. Log-normal successfully describes the data at lower energies i.e. from $\sqrt{s} = 14$ GeV to 34.8 GeV [28] but it fails to justify the experimental multiplicity data beyond 40 GeV.

5.4 Weibull Model

Weibull distribution [29] was named after its inventor, Waloddi Weibull, a Swedish mathematician in 1937. It is a continuous probability distribution which can take numerous shapes and can be fitted to the data which is non-symmetrical in nature. Weibull distribution is the most practiced distribution for the analyses of data and fitting. The basic advantage in analyses done by using Weibull method is that it determines the precise failure or success rate even with very small sample size. The standard Weibull distribution has only two parameters, characteristic value or scale factor (λ) and slope value which is also known as shape parameter (k). As the name suggests, shape parameter is responsible for the shape of the Weibull distribution where as scale factor gives the approximation to the expected measurements. Figure 5.5 shows various shapes of the Weibull distribution at different values of shape parameter but with constant scale factor, λ. The probability function for a Weibull random variable is given by;

$$P_n(n, \lambda, k) = \frac{k}{\lambda}\Big(\frac{n-\mu}{\lambda}\Big)^{(k-1)} exp^{-(\frac{n-\mu}{\lambda})^k}, \qquad where\ n \geq 0. \tag{5.36}$$

Under standard conditions μ, the location parameter, is considered as 0, thus probability is defined as,

$$P_n(n, \lambda, k) = \frac{k}{\lambda}\Big(\frac{n}{\lambda}\Big)^{(k-1)} exp^{-(\frac{n}{\lambda})^k}, \qquad where\ n \geq 0. \tag{5.37}$$

$$P_n(n, \lambda, k) = 0, \qquad where\ n < 0. \tag{5.38}$$

While $\lambda > 0$ is the scale parameter and $k > 0$ is the shape parameter. These two parameters for the distribution are related to the mean of the function, as

$$\bar{n} = \lambda\Gamma(1 + 1/k) \tag{5.39}$$

If the scale parameter λ, is increased and shape parameter k, is kept constant then the distribution extends towards the right and its height decreases [30]. If it is decreased then the distribution extends towards the left (i.e., towards its beginning or towards 0) and its height increases, where as its shape remains unchanged in both the cases. The value of shape parameter $k < 1$ implies the reduction in the failure rate where as $k > 1$ implies the increase in the failure rate over time. Consistency in failure rates is illustrated by the value $k = 1$. Standard Weibull distribution which has two parameters does not produce negative values [31] which is very important feature for the data analysis where actual measurements, like charged particle multiplicity, can not be negative.

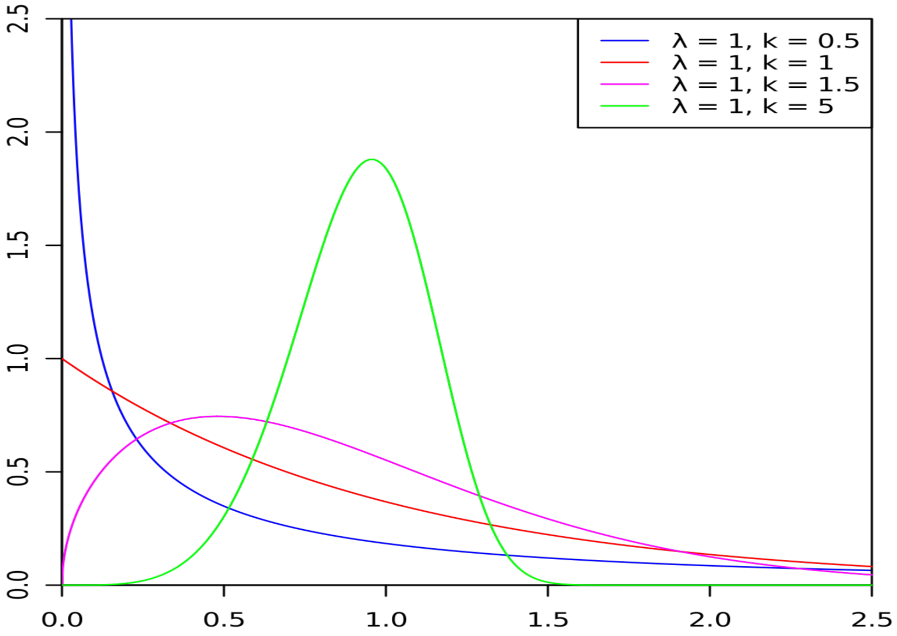

Figure 5.5: Weibull probability distribution exhibiting the various shapes with constant value of scale factor, λ with different slope values, k. Plot taken from [29]

5.5 Tsallis Non-extensive Statistics

All models and distributions defined and elaborated in previous sections can be used to make predictions for charged particle multiplicity and use the basic concepts of probability and statistics. Another distribution which is derived from the concepts of statistical mechanics and a non-extensive behaviour of entropy, has also been used to study the multiplicities in high energy interactions. Entropy has the most acceptably an extensive nature. However, this is normally acceptable when we study and analyse the short range interactions, at least for lower energies. But when we analyse the long range interactions like quark-quark, gluon-quark and gluon-gluon interactions this assumption no longer stands valid. In such interactions the standard statistical mechanics which is extensive, becomes non-extensive in nature. Therefore, it becomes very crucial to take care of the non-extensive nature during the study of important observables like multiplicity and transverse momentum.

Constantino Tsallis [12] introduced a possible and desirable solution for this problem. He brought forward the concept of replacing the regular Gibbs entropy[9] with a new Tsallis entropy which is non-extensive in nature. This Tsallis entropy is indexed by a parameter q, a real-valued parameter, which measures the extent of deviation from extensivity. Most of the results from statistical mechanics can be transformed into this new concept. In study of production of quark-gluon plasma in heavy-ion collisions at higher energies, thermostatistics is notably significant. In very high energy collisions, statistical equilibrium is supposed to be achieved which leads to the non exponential form of transverse energy distribution of the hadrons produced during the collisions. This non exponential behaviour has been observed not only in heavy ion collisions but also in the leptonic collisions, $e^+e^- \rightarrow hadrons$ [32] as well as in hadronic collisions, $pp\,(\bar{p}p) \rightarrow hadrons$ [16] and can be described very well by adopting non-extensive equilibrium as ascribed to the Tsallis non-extensive thermodynamics. In above mentioned scenarios, Tsallis statistics is the best possible solution and technique available to describe the multiplicity distributions and transverse momentum distributions for a broad range of energies from lower energies (GeV scale) up to the highest available energies at the LHC. Thus Tsallis non-extensive phenomenon plays a key role in the high energy collisions. In the following sections generalized form of statistical mechanics of Tsallis statistics is discussed.

---

[9] The macroscopic state of a system is characterized by the distribution on the microstates. Entropy function of such system can be represented in the form of probability as $S = -\, k_B \sum_i p_i \, ln \, p_i$, where p_i is the probability of microstate i and k_B is Boltzmann constant.

5.5.1 Tsallis Gas Model

C. Tsallis proposed the concept of "q-entropy" and the conventional Gibbs entropy in view of this new concept is altered as;

$$S = \frac{1 - \sum_a P_a^q}{q-1}, \tag{5.40}$$

with P_a being the probability related with microstate[10] a and sum of the probabilities of all micro-states should be one for normalization; $\sum_a P_a = 1$.

Tsallis redefined the q biased averages of observables [13] as;

$$< O > = \frac{1}{l_q} \sum O_a \, P_a^q, \tag{5.41}$$

The observable, O, here can be rapidity y, transverse momentum p_T or multiplicity for the analysis of high energy interactions. The normalization factor, $l_q = \sum_a P_a^q$

The probability of a microstate for q-biased microstate is defined as;

$$\tilde{P}_a = \frac{P_a^q}{l_q}. \tag{5.42}$$

This q biased micro-state probability is adopted for the estimation and analysis of physical quantities. The entropic index q, a real number, in the limit $q \to 1$ gives back the usual form of extensive entropy. The equilibrium probabilities are driven from P_a by maximizing the entropy under suitable constraints. The fixed value (average) of the energy and conserved charge are the two important and relevant conserved quantities in particle collisions. In Grand canonical system[11], the first law of thermodynamics [12], can be written in terms of charge, entropy and energy as,

$$\delta S + \alpha \sum_a \delta p_a - \beta_T \delta E + \gamma \delta Q = 0 \tag{5.43}$$

---

[10] A microstate is defined as the arrangement of each particle in the system at a given instant.

[11] It is defined as a system contained in constant volume V having fix temperature T with a constant chemical potential μ and can exchange energy and particles with its surrounding.

[12] 1st law of thermodynamics , $\delta U = T\delta S + \mu\delta Q - dW$, in presence of external mechanical variables (x_i) that can change, generalizes to: $\delta U = T\delta S + \mu\delta Q - X\sum_i dx_i$, where δQ is change in the charge and X are the generalized forces correspond to the external variables x_i which are independent of the size of the system

$$E = \sum_a E_a \tilde{p_a} \qquad and \qquad Q = \sum_a Q_a \tilde{p_a} \tag{5.44}$$

with Q_a, E_a being the charge and energy of the microstate a and constants α, β_T, γ are Lagrange multipliers. Lagrange multipliers are used to find the local maxima and minima of a function which is subject to condition that the given values of the variables should satisfy one or more equations. β_T and γ are related with the temperature T and chemical potential, μ as;

$$\beta_T = \frac{1}{T} = \left(\frac{\partial S}{\partial E}\right)_{Q,V} \qquad and \qquad \gamma = \frac{\mu}{T} = -\left(\frac{\partial S}{\partial Q}\right)_{E,V} \tag{5.45}$$

V in above equation is volume acquired by the grand canonical system. By solving the variation equation (5.43), the Tsallis distribution can be obtained,

$$\tilde{p_a} = \frac{1}{Z_q} \left(\exp_q[-\beta(E_a - \mu Q_a)]\right)^q \tag{5.46}$$

Where Z_q is the Grand Partition function and q-exponential function is defined as,

$$\exp_q(A) \equiv [1 - (q-1)A]^{-\frac{1}{q-1}} \tag{5.47}$$

This q-exponential under condition $q > 1$, can be written in the integral form as;

$$[\exp_q(A)]^q = \int_0^\infty dx G(x) e^{xA}, \qquad where\ G(x) = \frac{(\nu x)^\nu}{\Gamma(\nu)} e^{-\nu x} \tag{5.48}$$

with $\nu = \frac{1}{q-1}$, so $G(x)$ which is considered to be the probability distribution for variable x, can take maximum value at $x = 1$. For $q \to 1$, $G(x)$ tends to Dirac delta function $\delta(x-1)$. Generalized partition function, Z_q using grand canonical approach is given by,

$$Z_q(\beta, \mu, V) = \sum_a \exp_q[-\beta(E_a - \mu Q_a)]^q \tag{5.49}$$

It is to be noted that in the limit $q \to 1$, $\exp_q$(A) reduces to the exp(A) and in the context of this limit equations (5.46) and (5.49) reduce to the quantities consistent with the normal Boltzmann-Gibbs statistical mechanics. The parameter

β in equation (5.49) is not the Lagrange multiplier β_T which is the inverse of the temperature but β is associated with the temperature as;

$$T = \frac{\beta^{-1} + (q-1)(E - \mu Q)}{1 + (1-q)S} = \frac{\tilde{T}}{1 + (1-q)S} \tag{5.50}$$

$\tilde{T}$ known as "physical" temperature gives the better explanation of thermal equilibrium than the Tsallis non-extensive temperature, T because of the constraints while dealing with zeroth law of thermodynamics. In case of grand canonical approach where chemical potential is constant charge can be conserved by controlling the average charge but in canonical approach chemical potential is not constant so it becomes important to apply the charge conservation directly. Direct charge conservation becomes important because of the fluctuations around average Q which plays a significant role even at smaller values of Q. This modifies the partition function as;

$$Z_q(\beta, Q, V) \;=\; \sum_a \delta(Q - Q_a) \exp_q[-\beta(E_a)]^q \tag{5.51}$$

where $\delta(Q - Q_a)$ is a Kronecker delta. The canonical probability in this case is then defined by,

$$\tilde{p_a} = \frac{\delta(Q - Q_a)}{Z_q} \; (\exp_q[-\beta(E_a)])^q \tag{5.52}$$

5.5.1.1 Tsallis Multiplicity Distribution

Tsallis multiplicity distribution is the particle multiplicity distribution obtained from Tsallis non-extensive statistics. Using the probability of a microstate for q-biased microstate [13], the probability for system having exactly n number of particles is given by,

$$P_n \;=\; \sum_a \delta(n - n_a)\tilde{p_a} \tag{5.53}$$

n_a is the number of particles in state a. Partition function constrained to n particles is defined as;

$$Z_q^{(n)}(\beta,\mu,V) \;=\; \sum_a \delta(n-n_a)(\exp_q[-\beta(E_a-\mu Q_a)])^q \tag{5.54}$$

Then probability function for multiplicity distribution is; $P_n = \frac{Z_q^{(n)}}{Z_q}$. q-exponential function can be represented in the integral form and written as;

$$Z_q^{(n)}(\beta,\mu,V) = \int_0^\infty dx G(x) Z^{(n)}(x\beta,\mu,V) \tag{5.55}$$

Generating function for multiplicity distribution related to the probability defined above is;

$$F(t) \;=\; \sum_{n=0}^{\infty} P_n t^n \;=\; \frac{1}{Z_q}\sum_n Z_q^{(n)} t^n \tag{5.56}$$

The generalized partition function, $Z^{(n)}$ with $q = 1$, for n particles for the ideal gas can be described in terms of Boltzmann Gibbs function as

$$Z^n(\beta,\mu,V) = \frac{1}{n!}[V\sum_{i=1}^{h}\phi_i(\beta)\exp(\beta\mu q_i)]^n \tag{5.57}$$

with limit $n < \frac{1}{3q-1}$, here it is considered that h different species of particles are produced in the collisions, with mass m_i and charges q_i, $i = 1, ..., h$. where as function $\phi_i(\beta)$ is defined as;

$$\phi_i(\beta) = \frac{g_i m_i^2}{2\pi^2\beta} K_2(\beta m_i) \tag{5.58}$$

with $K_2(\beta m_i)$ being the modified Bessel function and g_i is statistical factor of a particle. If number of particles produced exceeds the limit described above ($n < \frac{1}{3q-1}$) then it causes the deviation (inconsistency) in the partition function of Tsallis ideal gas. In ideal gas, parameter β approaches to zero, which is responsible for this divergence. To escape this disparity, a Vander Waal's hard core interaction is introduced. This is done by including the concept of excluded volume [13] which

---

[13] The excluded volume is that volume of the particle that is inaccessible to other particles i.e. volume which do not participate in the interaction process and is given by 4 times the volume of particle produced (meson or baryon). $v_0 = 4$ x $\frac{4\pi r^3}{3}$, r is the radius of the particle

imitates this effect. The partition function for n particles is attained by replacing the volume, V with the V - nv_0, new partition function has form,

$$Z^n(\beta,\mu,V) \rightarrow \; Z^n(\beta,\mu,V-nv_0)\;\Theta(V-nv_0) \tag{5.59}$$

Θ is the Heaviside function which restricts numbers of particles in volume V to $n < \frac{V}{v_0}$. By substituting the partition function (equation (5.57)) in the expression of generating function (equation (5.56)), the generating function of Tsallis probability can be obtained and is given by;

$$\begin{aligned} F(t) \approx \exp(t-1)Vn_d[1+(q-1)\lambda(Vn_d\lambda-1)-2v_0n_d] \\ +(t-1)^2(Vn_d)^2[(q-1)\frac{\lambda^2}{2}-\frac{v_0}{V}] \end{aligned} \tag{5.60}$$

$$\lambda(\beta,\mu) = -\frac{\beta}{n_d}\frac{\partial n_d}{\partial\beta} \tag{5.61}$$

n_d is the density of particles for several particle species and related to the average number of particles $< n >$ by,

$$n_d(\beta,\mu) \;=\; \frac{< n >}{V} \;=\; \sum_{i=1}^{h}\phi_i(\beta)\exp(\beta\mu q_i) \tag{5.62}$$

Where ϕ_i represents the density of particle i and is given by equation (5.58). Tsallis probability generating function has the same form as that of Negative Binomial distribution ($F_{NBD} = [1-\frac{<n>}{k}(t-1)]^{-k} = \exp[< n > (t-1)]$) with average of number of particles $< n >$ for Tsallis probability as;

$$< n > \;=\; Vn_d[1+(q-1)\lambda(Vn_d\lambda-1)-2v_0n_d] \tag{5.63}$$

The parameter k of NBD is related to the Tsallis entropic index, q as,

$$\frac{1}{k} = (q-1)\lambda^2 - 2\frac{v_0}{V} \tag{5.64}$$

This leads to the limit on q as $q > 1 + \frac{2v_0}{\lambda^2 V}$. If q is found to have a value below the limit then MD would be of Binomial form. This situation is analogous to the condition if parameter k of NBD is negative then we have binomial form of MD.

Tsallis distribution having entropic index, $q > 1$ makes the width of multiplicity distribution wider than the conventional distributions like Poisson and NBD. The entropic index, q plays vital role in determining the width of multiplicity distribution. If we have small value of limit q-1 then multiplicity data from experiments can be approximated by NBD, in this situation parameter k of NBD is related to entropic index, q as $k \propto (q-1)^{-1}$. Reasonable increase in value q from the unity makes the Tsallis distribution wider and comparable to the experimental data.

We have used this concept of non-extensive entropy to describe and analyse the multiplicity spectrum at high energies which could not be explained by the models as described in previous sections of this chapter. The analysis aims to determine the success of Tsallis statistics on multi particle production in high energy interactions.

5.6 Two Component Model

Experimental data of charged particle multiplicity distributions in leptonic collisions at high energies ($\sqrt{s} \geq 91$ GeV) exhibit the existence of shoulder structure (dip-bump in the MD) in the region of intermediate multiplicity. This shoulder structure is related with the emission of hard gluons which results in the appearance of one or more than one additional jets in the final state. These jets act as footprints of QCD partons and carry the kinematic properties of the partons (quarks and gluons). Even NBD, which is the most successful distribution in defining the multiplicity data at lower and intermediate energies ($\sqrt{s} < 91$ GeV), fails at these energies. Giavonnini et al. proposed a two component approach [10] to study the shoulder structure in e^+e^- annihilation. In this two component approach the multiplicity distrubtions were assumed to be a weighted superposition of two NBDs associated to two-jet and multi-jet (≥ 3 jets) production. Probability in this case have five parameters weight factor α, $< n_1 >$, k_1 of one NBD and $< n_2 >$, k_2 of second NBD and given by,

$$P_n(\alpha; < n_1 >, k_1; < n_2 >, k_2) = \alpha P_n^{NB}(< n_1 >, k_1) + (1-\alpha) P_n^{NB}(< n_2 >, k_2) \quad (5.65)$$

The weight factor, α, gives the 2-jet events fraction and can be obtained by using a jet finder algorithm [33] at various energies. The same characteristic was observed by UA5 collaboration for energy, $\sqrt{s} = 540$ and 900 GeV in $\bar{p}p$ interactions. The multiplicity distrubtions at these energies can be described by using two NBD-shaped components. To understand this Giavonnini and Ugoccioni performed the systematic investigation and found that these components can be described in terms of soft and semi-hard events [11]. Though the superimposed physical sub-structure in leptonic and hadronic collisions are different but the weighted superposition mechanism is the same in two cases. These soft and semi-hard events can be understood in terms of events with and with out minijets. The UA1 collaboration defined the minijets as group of particles having a total transverse energy more than 5 GeV. The contribution due to soft events represent the events which do not have mini-jets and the semi-hard events are the events having mini-jets [34, 35]. The multiplicity distributions are then defined as a weighted superposition of the two components, soft and semi-hard. The weight α_{soft} represents the fraction of events with no mini-jets. In this case the probability of multiplicity distribution is given as;

$$P_n = \alpha_{soft} P_n^{MD} + (1 - \alpha_{soft}) P_n^{MD} \tag{5.66}$$

The multiplicity distribution (MD) of each component can be any of the distributions described earlier. Analyses of experimental data at higher energies using this approach reflects how the contribution of the events with mini-jets grows with energy, $\sqrt{s}$.

5.7 Moments

Moments play crucial role in investigating the characteristics of charged particle multiplicity in high energy interactions. Higher order moments and its cumulants are the precise tools to study the correlation between the particles produced in these interactions [36]. The departure from the independent and uncorrelated production of particles can be measured well using the factorial moments, F_q. Not only the correlation between the particles but the violation or holding of KNO scaling at higher energies can also be studied and understood correctly by using the normalized moments of order q, C_q. These moments are defined as;

$$C_q = \frac{< n^q >}{< n >^q} \tag{5.67}$$

$$F_q = \frac{< (n(n-1)....(n-q+1)) >}{< n >^q} \tag{5.68}$$

The factorial moments and their cumulants, K_q, are near to precise in defining the tail part of distribution where events with multitude of particles give a meaningful contribution. The factorial moments and cumulants are related to each other and given by relation;

$$F_q = \sum_{m=0}^{q-1} C_{q-1}^{m} K_{q-m} F_m \tag{5.69}$$

The relations between the factorial moments and cumulants for the first five ranks are given below;

$$\begin{aligned}
F_1 &= K_1 = 1 \\
F_2 &= K_2 + 1 \\
F_3 &= K_3 + 3K_2 + 1 \\
F_4 &= K_4 + 4K_3 + 3K_2^2 + 6K_2 + 1 \\
F_5 &= K_5 + 5K_4 + 10K_3K_2 + 10K_3 + 15K_2^2 + 10K_2 + 1
\end{aligned} \tag{5.70}$$

Factorial moments exhibit the features of any kind of correlation present between the particles and cumulants of order q illustrate absolute q-particle correlation which can not be brought down to the lower order correlation. In other words, if all q particles are related to each other in q^{th} order of cumulants then it can not be divided in to disconnected groups i.e. q particle cluster can not be split in to smaller clusters. The ratio of cumulants to factorial moment is known as H_q $(= \frac{K_q}{F_q})$ variable. It is easy to study the features of cumulants and factorial moments in the form of ratio than the absolute cumulants and moments [37]. These moments and their dependence on energy $\sqrt{s}$ helps in improving, redefining and rejecting various Monte-Carlo or statistical models which can be used in describing the production of particles at high energies.

5.8 Average Charged Multiplicity

The energy dependence of mean charged multiplicity $< n >$ is expected to reflect the underlying particle production process. A number of phenomenological models have been proposed to describe the behaviour of mean charged multiplicity with energy. Enrico Fermi [38] was the first to suggest the evolution of mean multiplicity with energy using the phase space model which was based on the fireball and hydrodynamical models for hadron-hadron interactions [39]. He suggested the form;

$$< n >= a\sqrt{s}^{b} \tag{5.71}$$

In another different approach [40] it was found that all the models were predicting the power law dependence of energy on mean multiplicity. It was found that using this approach the relation of multiplicity with energy describing by equation (5.71) can be obtained in the limit of a continuous distribution. For the discrete distributions the above equation (5.71) is modified as;

$$< n >= a\sqrt{s}^{b} - 1 \tag{5.72}$$

To describe the data at higher energies a fit corresponds to the empirical relation was proposed [41]. This emiprical relation is the most widely accepted relation which describes the multiplicity as a function of energy $\sqrt{s}$ as;

$$< n >= a + b\, ln(\sqrt{s}) + c\, ln^{2}(\sqrt{s}) \tag{5.73}$$

Bibliography

[1] I. M. Dremin and J. W. Gary, "Hadron multiplicities", Phys. Rep. **349**, 301 (2001)

[2] W. Kittel and E. A. De Wolf, "Soft Multihadron Dynamics", World Scientific Publishing Co. Pvt. Ltd., (2005)

[3] M. Althoff et al., "Jet production and fragmentation in e^+e^- annihilation at 12-43 GeV", Z. Phys. C **22**, 307 (1984)

[4] M. Derrick et al., "Study of quark fragmentation in e^+e^- annihilation at 29 GeV: Charged-particle multiplicity and single-particle rapidity distributions", Phys. Rev. D **34**, 3304 (1986)

[5] Z. Koba, H. B. Nielsen, P. Olesen, "Scaling of multiplicity distributions in high-energy hadron collisions", Nucl. Phys. B **40**, 317 (1972)

[6] G.J. Alner et al., "A new empirical regularity for multiplicity distributions in place of KNO scaling", Phys. Lett. B **160**, 199 (1985)

[7] R.E. Ansorge et al., "Charged particle multiplicity distributions at 200 and 900 GeV c.m. energy", Z. Phys. C **43**, 357 (1989)

[8] A. Papoulis, "Probability, Random Variables, and Stochastic Processes", 2nd edition, New York: McGraw-Hill, 57 (1984)

[9] F. Rimondi et al., "Aspen Multipart. Dyn. 1993", 400 (1993)

[10] A. Giovanninni, S. Lupia and R. Ugoccioni, "Common origin of the shoulder in multiplicity distributions and of oscillations in the factorial cumulants to factorial moments ratio", Phys. Lett. B **374**, 231 (1996)

[11] A. Giovanninni and R. Ugoccioni, "Soft and Semi-Hard Components Structure in Multiparticle Production in High Energy Collisions", Nucl. Phys. Proc. Suppl. **71**, 201 (1999)

[12] C. Tsallis, "Possible generalization of Boltzmann-Gibbs statistics", J. Stat. Phys. **52**, 479 (1988)

[13] C.E. Aguiar and T. Kodama, "Non-extensive statistics and multiplicity distribution in hadronic collisions", Physica A **320**, 371 (2003)

[14] K. Goulianos, "Universality of Particle Multiplicities", Gleb Wataghin School on High Energy Phenomenology, Campinas, Brazil (1994)

[15] R. P. Feynman, "Very High-Energy Collisions of Hadrons", Phys. Rev. Lett. **23**, 1415 (1969)

[16] J. F. Grosse-Oetringhaus, K. Reygers, "Charged-Particle Multiplicity in Proton-Proton Collisions", J. Phys. G **37**, 083001 (2010)

[17] T. Uematsu, "Scaling of Multiplicity Distributions and Statistical Mechanics Analogy of Multiparticle Production", Prog. Theor. Phys. **51**, 3, (1974) of KNO Scaling , Phys. Lett. B **160**, 199 (1985)

[18] T. Takao and K. Yokoyama, "On a Scaling Parameter for the Multiplicity Distribution in High Energy Interactions", Prog. Theor. Phys. **49**, 3 (1979)

[19] L. Boltzmann (current form by M. Planck), "Boltzmann equation", Eric Weisstein's World of Physics, (1872)

[20] P. Perrot, "A to Z of Thermodynamics", Oxford University Press, ISBN 0-19-856552-6, (1985)

[21] K. Urmossy, G. G. Barnafoldi and T. S. Biro, "Generalized Tsallis Statistics in Electron-Positron Collisions ", Phys. Lett. B **701**, 111 (2011)

[22] K. Urmossy, G.G. Barnafoldi and T. S. Biro,"Microcanonical jet-fragmentation in protonproton collisions at LHC energy", Phys. Lett. B **718**, 125 (2012)

[23] J. F. Lawless, "Negative binomial and mixed Poisson regression", CJS **15**, 209 (1987)

[24] S. Krasznovszky, I. Wagner, "Universal Description of Inelastic and Non (single)-Diffractive Multiplicity Distributions in pp Collisions at 250, 360 and 800 GeV/c", Nuovo Cimento A **41**, 539 (1983)

[25] S. Krasznovszky, I. Wagner, "Description of charged-particle multiplicity distributions in e^+e^- annihilation at TRISTAN and LEP1 energies from AMY, ALEPH, OPAL and DELPHI collaborations", Phys. Lett. B **295**, 320 (1992)

[26] S. Krasznovszky, I. Wagner, "Description of inelastic and nondiffractive multiplicity distributions in pp and $\bar{p}p$ collisions at ISR and SppS energies", Phys. Lett. B **306**, 403 (1993)

[27] S. Carius, G. Ingelman, "The log-normal distribution for cascade multiplicities in hadron collisions", Phys. Lett. B **252**, 647 (1990)

[28] U. P. Sukhamte, "Log-normal multiplicity distributions and the dual parton model", 22^{nd} International Symposium on Multiparticle Dynamics, Santiago de Compostela, Spain, UICHEP-TH/92-14, 201 (1992)

[29] A. Papoulis and S.U. Pillai, "Probability, Random Variables, and Stochastic Processes", 4th edition, Boston: McGraw-Hill, ISBN 0-07-366011-6, (2002)

[30] http://www.weibull.com/hotwire/issue14/relbasics14.html

[31] S. Dash, B.K. Nandi and P. Sett, "Multiplicity distributions in e^+e^- collisions using Weibull distribution", Phys. Rev. D **94**, 074044 (2016)

[32] I. Bediaga, E.M.F. Curado and J.M. de Miranda, “A non-extensive thermodynamical equilibrium approach in $e^+e^- \to$ hadrons”, Physica A **286**, 156 (2000)

[33] S. Dahiya, M. Kaur and S. Dhamija, “Analysis of multiplicities in e^+e^- interactions using 2-jet rates from different jet algorithms”, J. Phys. G: Nucl. Part. Phys. **28**, 2169 (2002)

[34] A. Giovanninni and R. Ugoccioni, “Possible scenarios for soft and semi-hard component structure in central hadron-hadron collisions in the TeV region”, Phys. Rev. D **59**, 094020 (1999)

[35] C. Fglesang, “Multiparticle Dynamics”, edited by A. Giovannini and W. Kittel, World Scientific, Singapore, 193 (1997)

[36] M. Praszalowicz, “Negative Binomial Distribution and the multiplicity moments at LHC”, Phys. Lett. B **704**, 566 (2011)

[37] A. Capella, I. M. Dremin, V. A. Nechitailo and J. Tran Thanh Van, “Moment Analysis of Multiplicity Distributions”, Z.Phys. C **75**, 89 (1997)

[38] E. Fermi et al., “High-energy nuclear events”, Prog. Theor. Phys. **5**, 570 (1950)

[39] H. Satz, “On the phenomenology of multihadron production in e^+e annihilation”, Current Induced Reactions **56**, 49 (1975)

[40] R. Szwed, “New AMY and DELPHI Multiplicity Data and the Lognormal Distribution”, Mod. Phys. Lett. A **6**, 245 (1990)

[41] W. Thome et al., “Charged Particle Multiplicity Distributions in p p Collisions at ISR Energies”, Nucl. Phys. B **129**, 365 (1977)

Chapter 6

Results and Discussion

6.1 Introduction

The study of charged multiplicity in the final state of high energy interactions can unveil information about the series of events that occur at the early stage of interaction. Analysis of the charged particle multiplicity gives an understanding about the dynamics of formation of hadrons as a combination of quarks (anti-quarks) and gluons, collectively known as partons. Charged particle production in final state exhibits the footprints of this evolution of hadrons from the partons, embedded in the form of correlations among the particles. Production of multitude of particles [1] at high energies originates from the interactions amongst partons quarks and gluons. The partons which are coloured, fragment together to form colourless hadrons (baryons: qqq or mesons: $\bar{q}q$). Sometimes the hadrons produced are unstable in nature and decay into the lighter stable particles. The stable particles are the final state particles which are observed in the particle detectors. The formation of hadrons from the partons is known as hadronization. This process of hadronization occurs nonperturbatively where the coupling constant, α_S of strong interaction becomes very large. The production of final state particles is understood theoretically and also through phenomenological models. In the present work various phenomenological models, as described in the previous chapter, have been used to study the multiparticle production. The results from these models are compared with the experimental data at various energies obtained from different experiments. Detailed analyses on charged particle multiplicities have been done using the different particle collisions. The study presented in the thesis is categorized in the following categories:

- Hadronic (h-h) collisions at various energies
- Leptonic (e^+e^-) collisions at various energies
- Hadron-Nucleus (h-A) collisions at various energies

6.2 Analysis of Hadronic Interactions

In high energy collisions, the particles colliding with each other have a total relativistic mass and energy much higher than their rest mass and energy because of the high velocity they achieve during the process of acceleration. The dynamical properties of quarks and gluons which constitute hadrons can be well understood using hadronic interactions [2]. In these interactions the distribution of the number of produced hadrons provides a basic means to characterize the events. A conventional case of two colliding hadrons can lead to the production of several particles due to different interaction processes such as quark-quark, gluon-gluon and quark-gluon interactions. To study the characteristics and detailed features of multiparticle production during the hadronic interactions, we have analysed the data of pp collisions from the CMS detector [3] at the LHC at CERN and $\bar{p}p$ data from the UA5 experiment [4, 5] at the SPS at CERN.

6.2.1 Study of pp Interactions using the CMS Data

In the present study multiplicity distributions of charged particles for proton proton collisions at centre of mass energies $\sqrt{s}$ = 0.9, 2.36 and 7 TeV [6] and in different restricted pseudorapidity intervals using the CMS detector at the LHC are analysed and presented in this chapter. Full phase space multiplicity data get influenced by energy-momentum conservation but data at restricted pseudorapidity intervals is likely to have less impact due to the constraints of energy-momentum conservation [7]. This behaviour helps in exploring the fundamental dynamics of strong interaction in QCD in a more prominent way. The data samples analysed here were recorded at the CMS detector and consist of inelastic and non single diffractive events produced in the final state of the interactions. Events at these energies were selected using minimum bias trigger [8] which includes mostly soft interactions with particles having small transverse momenta. Multiplicity spectrum up to pseudorapidity region $|\eta| < 2.4$ was accepted as there was considerable drop [9, 10] in the reconstruction of data for region $|\eta| > 2.4$. After applying all the appropriate selection cuts total sample of 132294, 11674 and 441924 NSD events were selected at energy $\sqrt{s} = 0.9$, 2.36 and 7 TeV respectively.

6.2.1.1 Analysis of Multiplicities

Multiplicity data at pseudorapidity intervals $|\eta| < 0.5$, 1.0, 1.5, 2.0 and 2.4 have been analysed at $\sqrt{s} = 0.9$, 2.36 and 7 TeV. Also the multiplicity data with larger transverse momenta, $p_T > 500$ MeV have been analysed. As experimental data is available only at the highest interval for $p_T > 500$ MeV, so analysis is performed only at $|\eta| < 2.4$. We have used the NBD, Gamma, Shifted Gamma, the Tsallis and the Weibull models to obtain the multiplicity distributions at these energies. The results from these distributions from different models are then compared with the experimental data. Detailed description about the probability distribution functions, PDF, of these models has been given in chapter 5. The best fits of these functions have been obtained by using the fit procedure of ROOT version 6.08/00 [11] from CERN to minimize the χ^2 using the library MINUIT 2. During the fitting we have considered the probability distribution for 7 TeV extending up to continuous range of number of produced particles. Probability beyond these values falls below 0.01 ($<$ 0.1 %) which is due to the very low statistics at each of these points. Consideration of these points lead to the very large errors in the fit parameters of the distributions. Figures 6.1 - 6.3 show the results of these models fitted on experimental data for 0.9 TeV, figures 6.4 - 6.6 show the various distributions fitted to the 2.36 TeV data and 6.7 - 6.9 for the 7 TeV data. Multiplicity analysis of the data having p_T greater than the 500 MeV in pseudorapidity window $|\eta| < 2.4$ at energies, $\sqrt{s} = 0.9$, 2.36 and 7 TeV are shown in figures 6.10 - 6.12. A comparison of chi-square and p values of these fits are given in table 6.1 and the parameters of these fits at various pseudorapidity intervals at energies 0.9, 2.36 and 7 TeV are shown in table 6.2. Confidence Level, CL or probability values, generally known as p values [12], are calculated for each χ^2/ndf value to determine the statistical significance of the results obtained from various models used in the analyses. These p values for different models are shown in table 6.1. The p value is used to test the hypothesis i.e. it measures how much evident we are against the null hypothesis (to nullify the hypothesis). This null hypothesis here implies that the models being used for determining multiplicity distributions, successfully define the experimental data. The p values can vary from 0 to 1, p value ≤ 0.001 (0.1 %) indicates the strong evidence to reject the null hypothesis where as for values ≥ 0.001 we can not reject the null hypothesis. So p value or CL value becomes significant in accepting or rejecting these models statistically. Confidence level, $CL > 0.1$ % implements the less than 1 in 1000 chances of being wrong. All the results having $CL > 0.1$ % are statistically acceptable for these models.

6.2.1.2 Results and Discussion

The probability distributions calculated from the NBD, Gamma, Shifted Gamma, the Weibull and the Tsallis models are implemented on *pp* collision data for several pseudorapidity intervals at energies, $\sqrt{s} = 0.9$, 2.36 and 7 TeV from the CMS experiment. It is observed that the Weibull, Shifted Gamma and the Tsallis models could reproduce the experimental data well for most of the pseudorapidity intervals with few exceptions. A comparison of the χ^2/ndf and p values at several pseudorapidity intervals at above mentioned energies for these distributions are given in table 6.1 and fit parameters of these distributions are shown in table 6.2. It is found that for most of the data, χ^2/ndf values for all these fits are comparable with p values corresponding to $CL > 0.1$ %

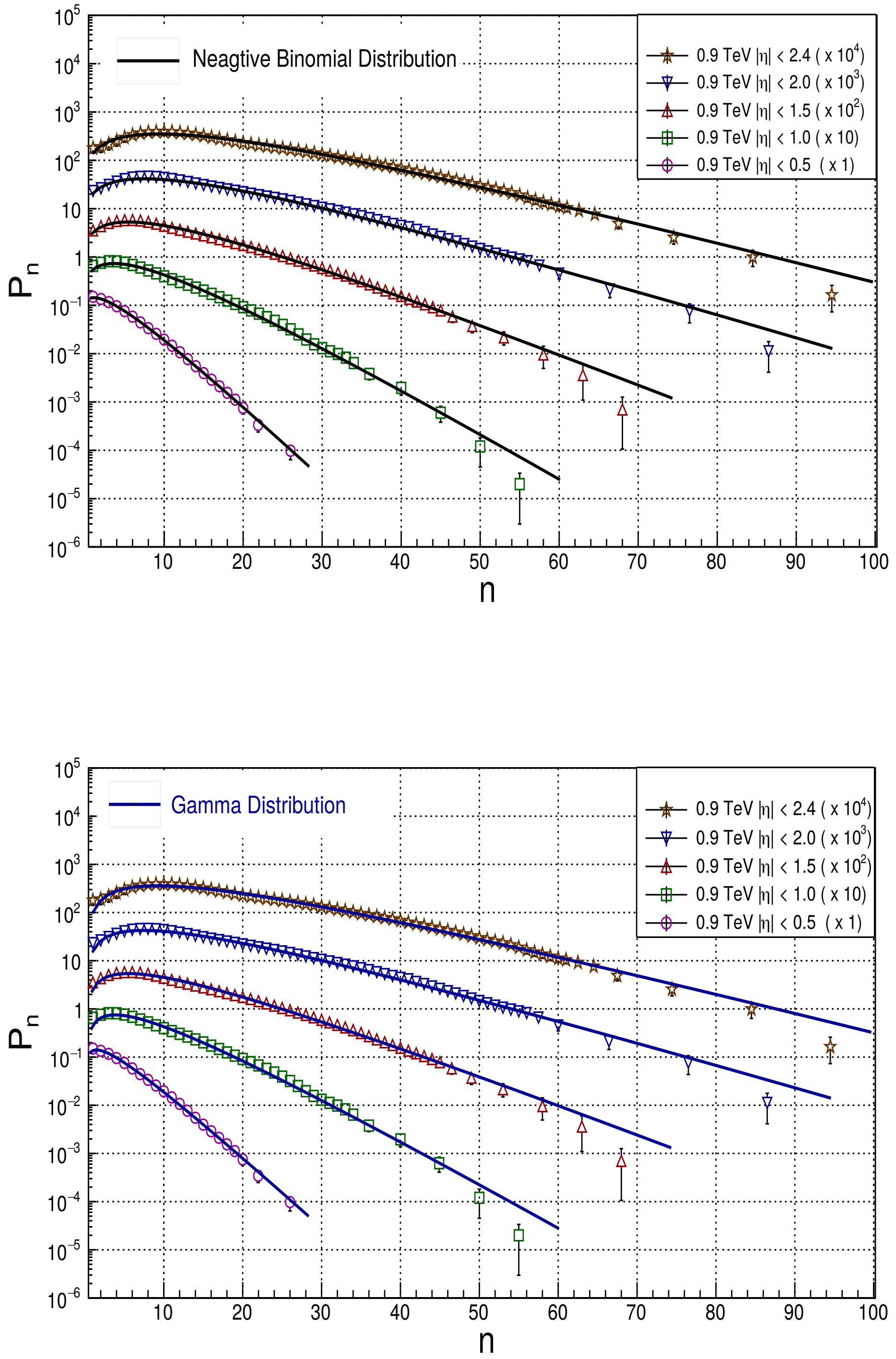

Figure 6.1: The charged particle multiplicity distributions in *pp* collisions by the CMS experiment at 0.9 TeV and comparison of the experimental data with the NBD and the Gamma distributions.

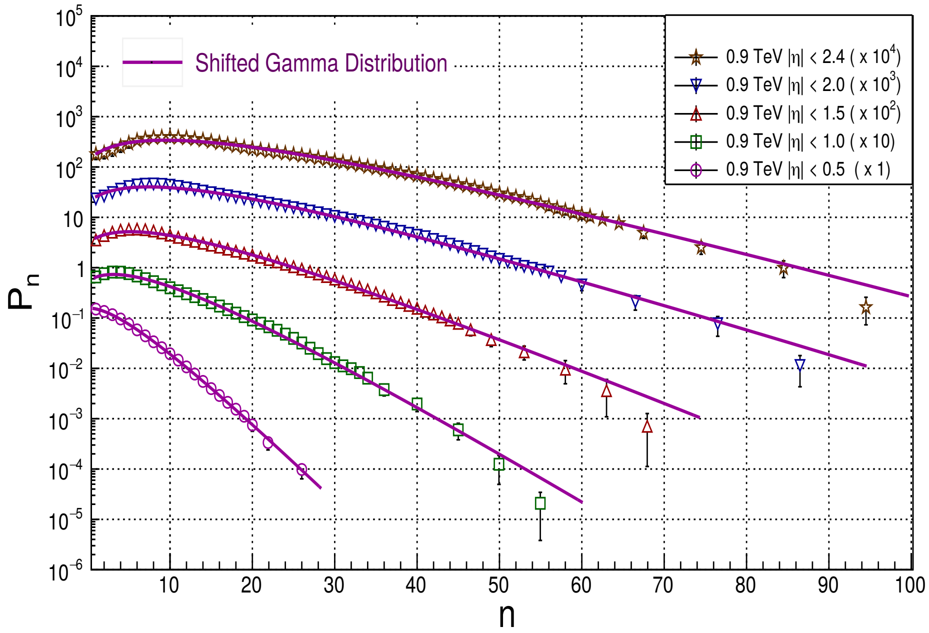

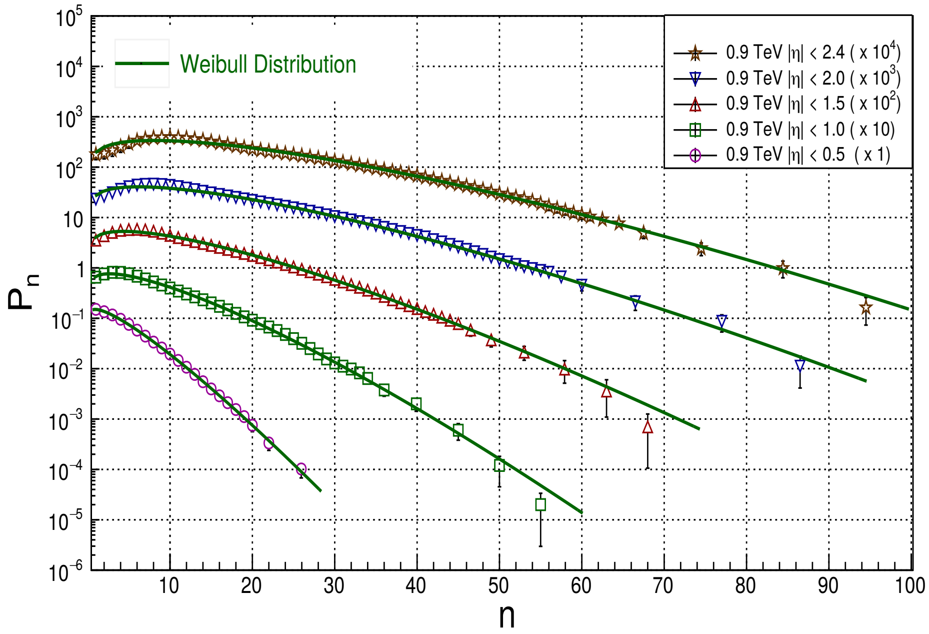

Figure 6.2: The charged particle multiplicity distributions in *pp* collisions by the CMS experiment at 0.9 TeV and comparison of the experimental data with the Shifted Gamma and the Weibull distributions.

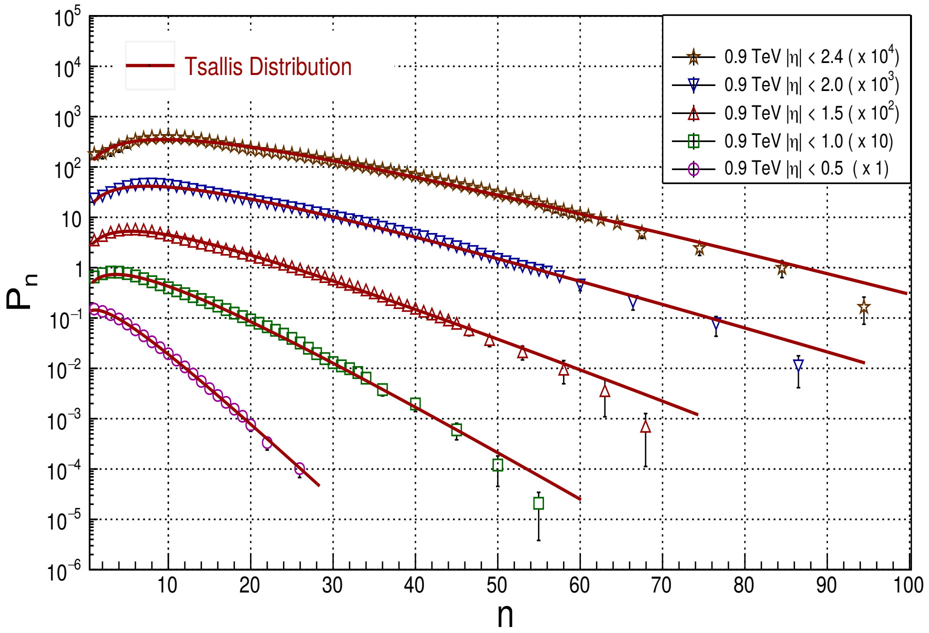

Figure 6.3: The charged particle multiplicity distributions in *pp* collisions by the CMS experiment at 0.9 TeV and comparison of the experimental data with the Tsallis distribution.

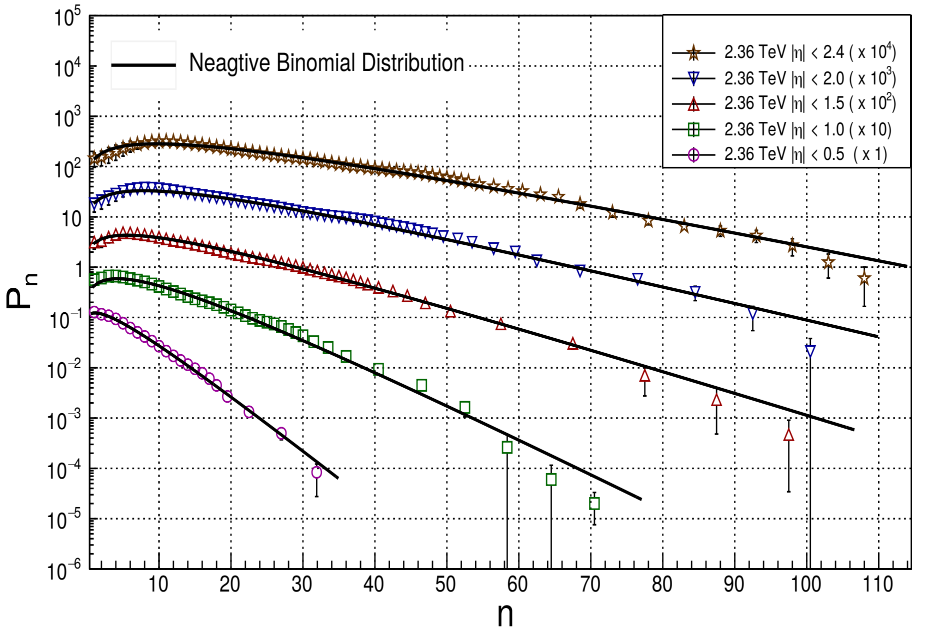

Figure 6.4: The charged particle multiplicity distributions in *pp* collisions by the CMS experiment at 2.36 TeV and comparison of the experimental data with the NBD distribution.

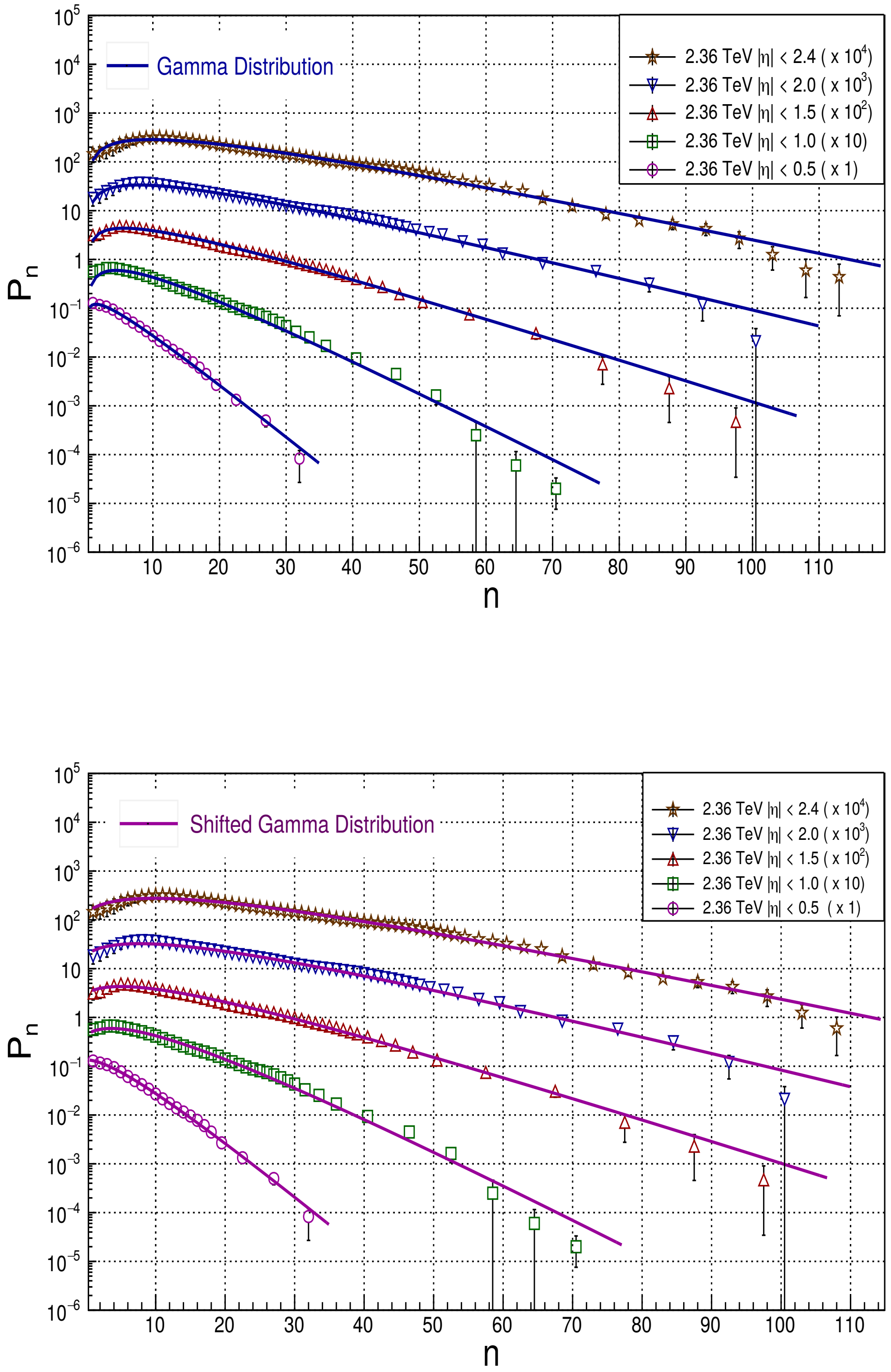

Figure 6.5: The charged particle multiplicity distributions in *pp* collisions by the CMS experiment at 2.36 TeV and comparison of the experimental data with the Gamma and Shifted Gamma distributions.

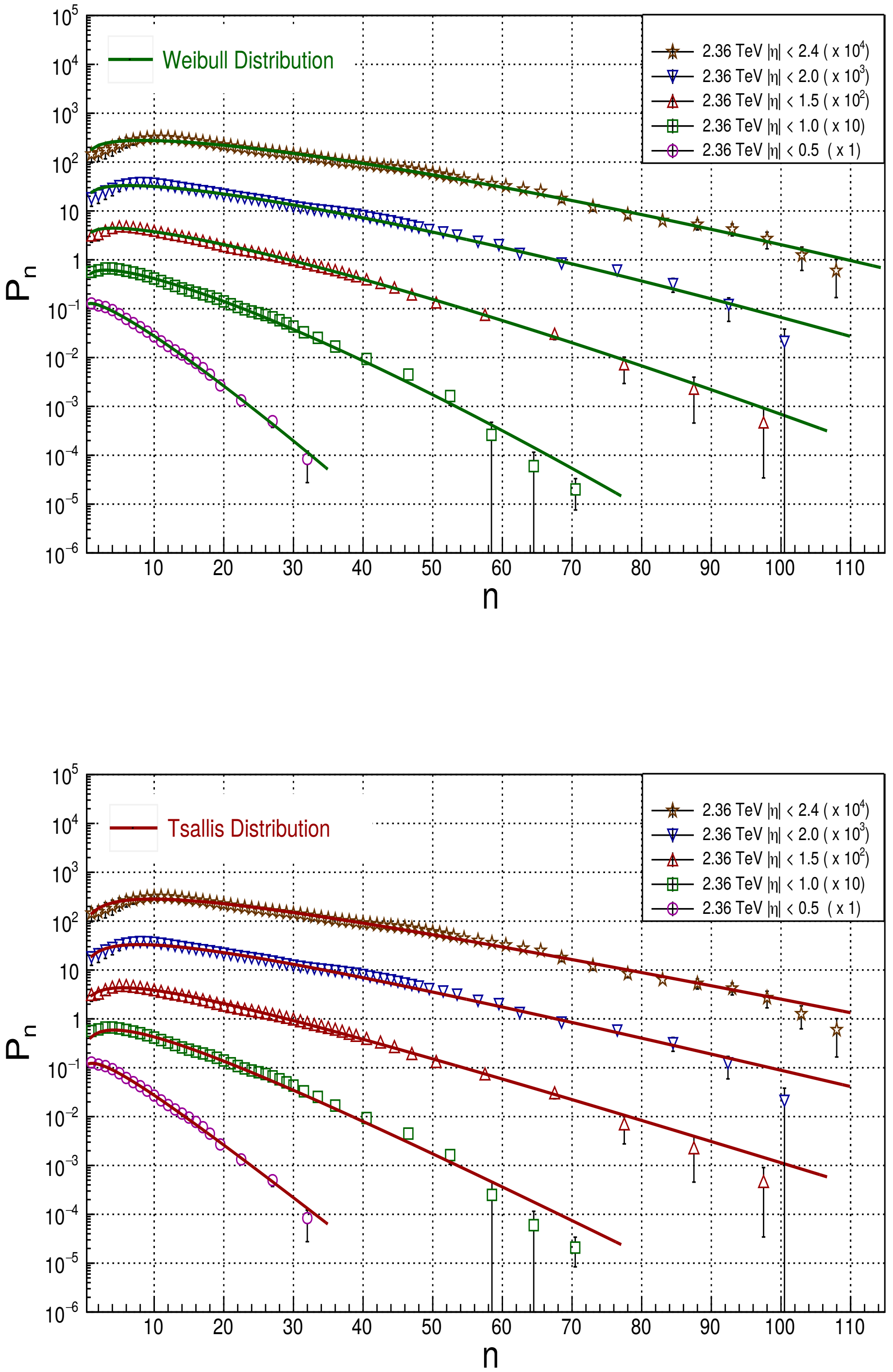

Figure 6.6: The charged particle multiplicity distributions in *pp* collisions by the CMS experiment at 2.36 TeV and comparison of the experimental data with the Weibull and the Tsallis distributions.

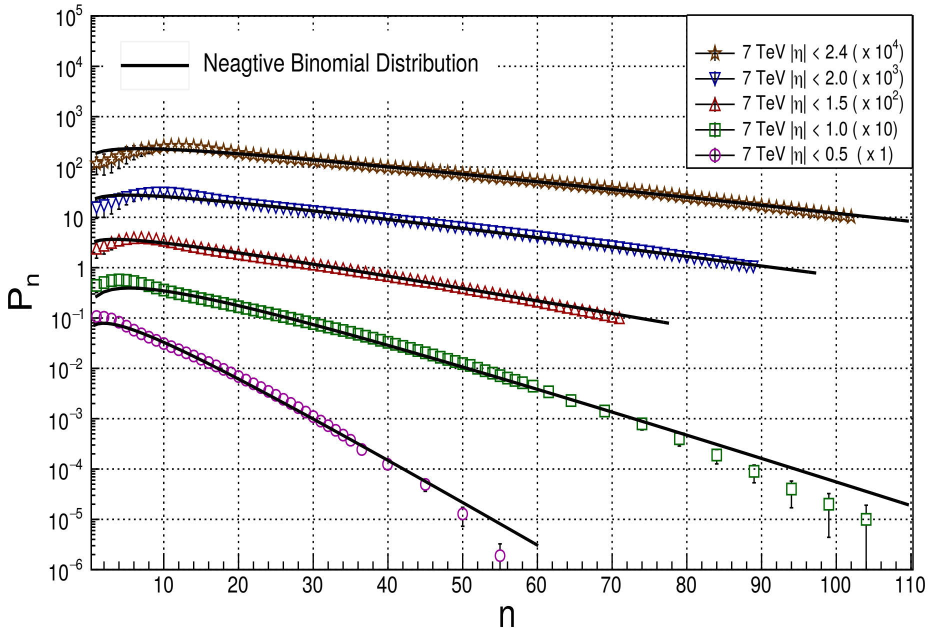

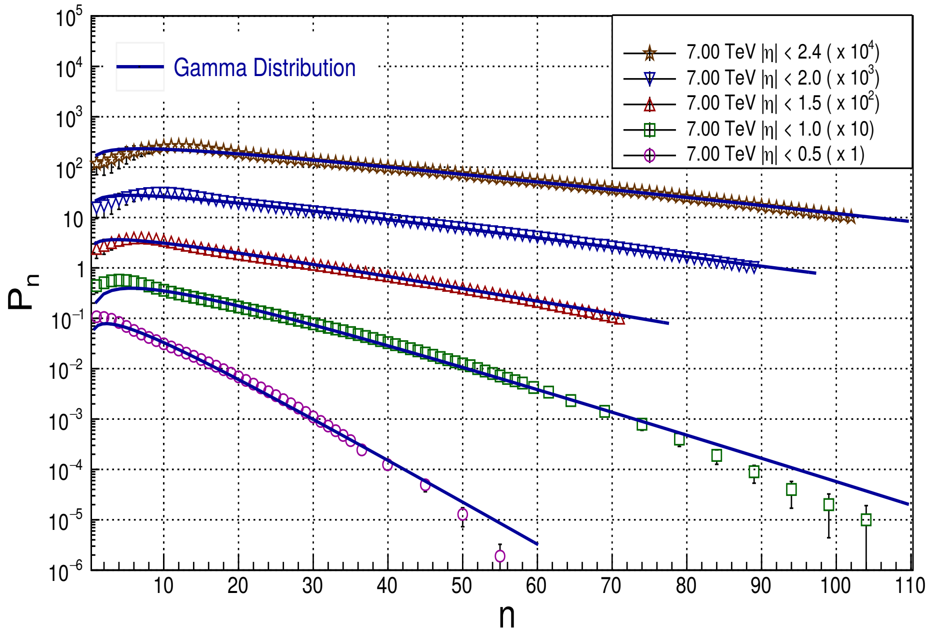

Figure 6.7: The charged particle multiplicity distributions in *pp* collisions by the CMS experiment at 7 TeV and comparison of the experimental data with the NBD and the Gamma distributions.

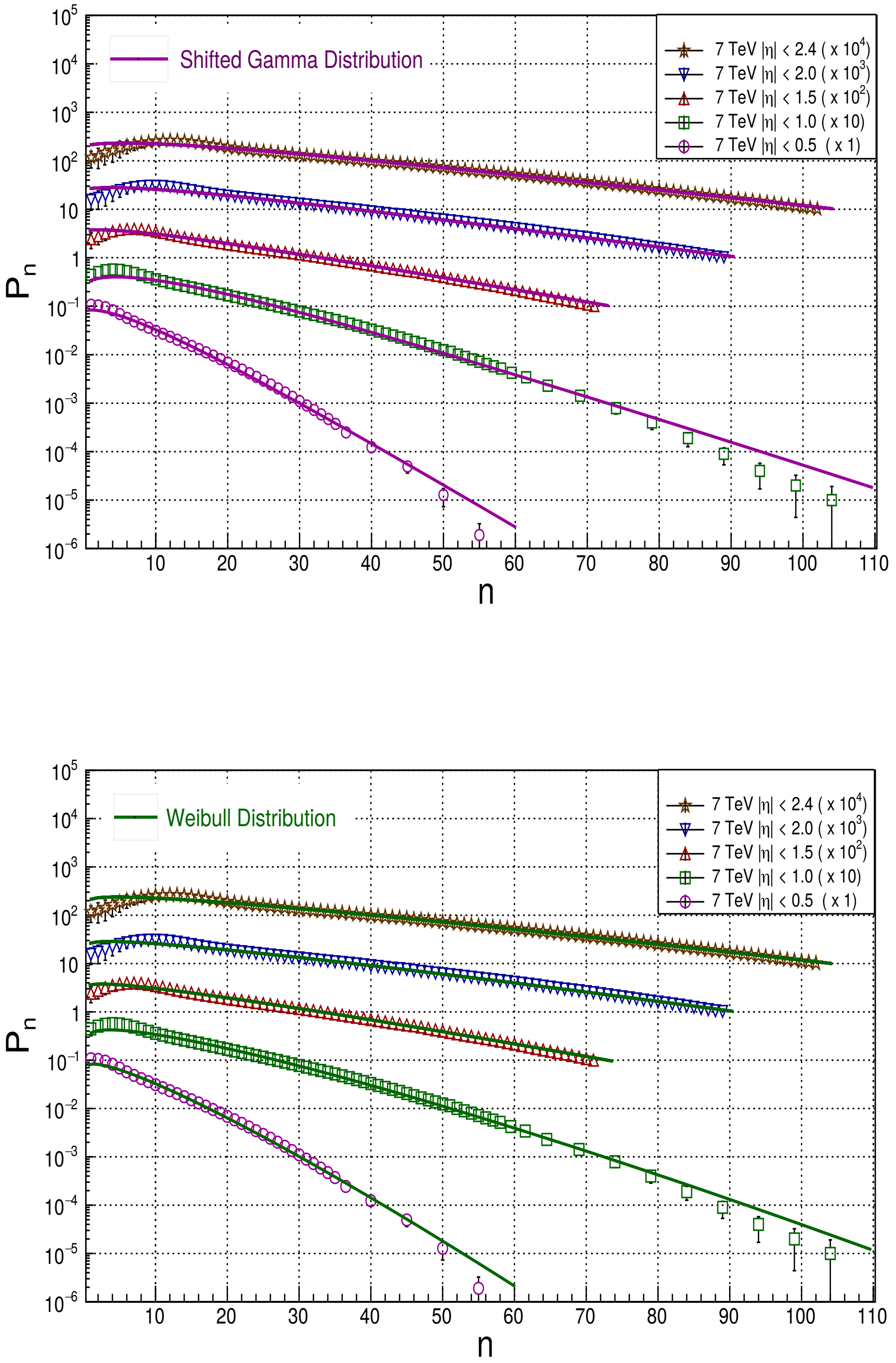

Figure 6.8: The charged particle multiplicity distributions in *pp* collisions by the CMS experiment at 7 TeV and comparison of the experimental data with the Shifted Gamma and the Weibull distributions.

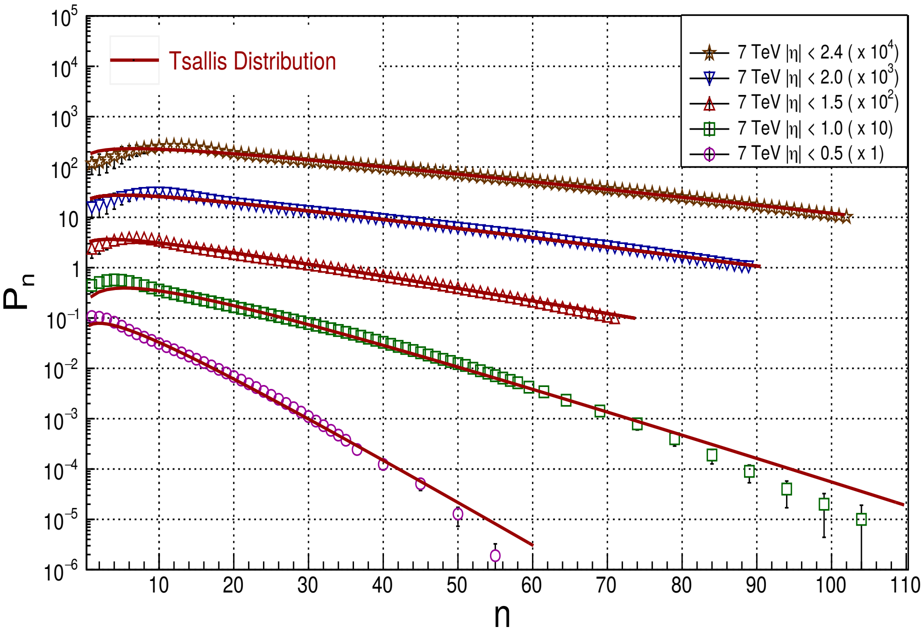

Figure 6.9: The charged particle multiplicity distributions in *pp* collisions by the CMS experiment at 7 TeV and comparison of the experimental data with the Tsallis distribution.

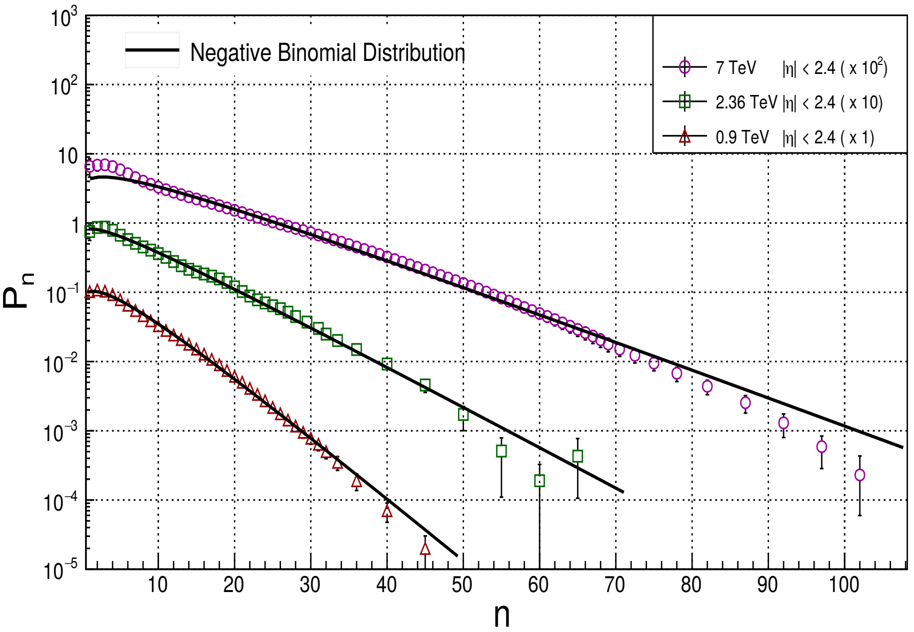

Figure 6.10: The charged particle multiplicity distributions in *pp* collisions by the CMS experiment at $|\eta| < 2.4$ with $p_T > 500$ MeV and comparison of the experimental data with the NBD distribution.

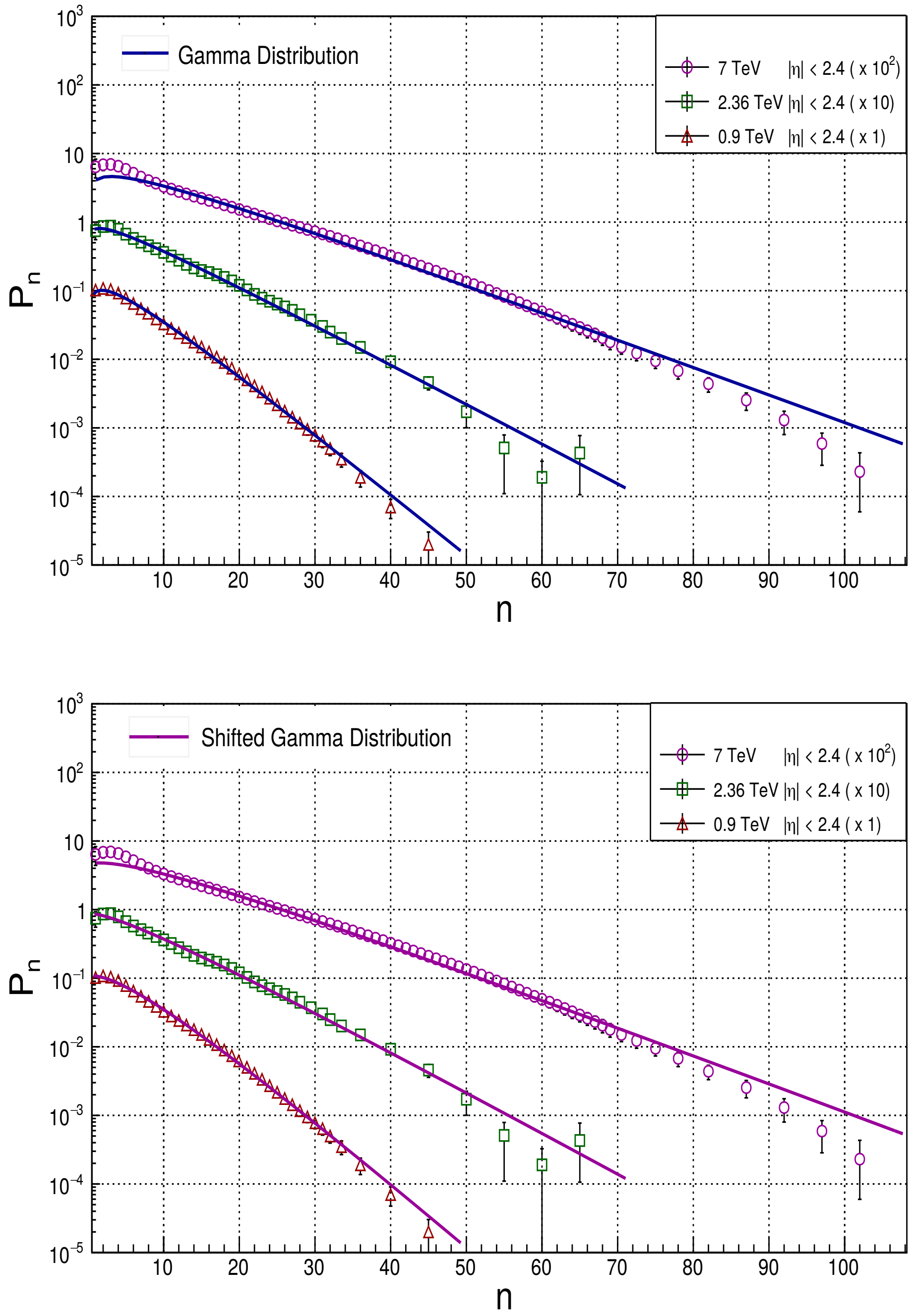

Figure 6.11: The charged particle multiplicity distributions in *pp* collisions by the CMS experiment at $|\eta| < 2.4$ with $p_T > 500$ MeV and comparison of the experimental data with the Gamma and Shifted Gamma distributions.

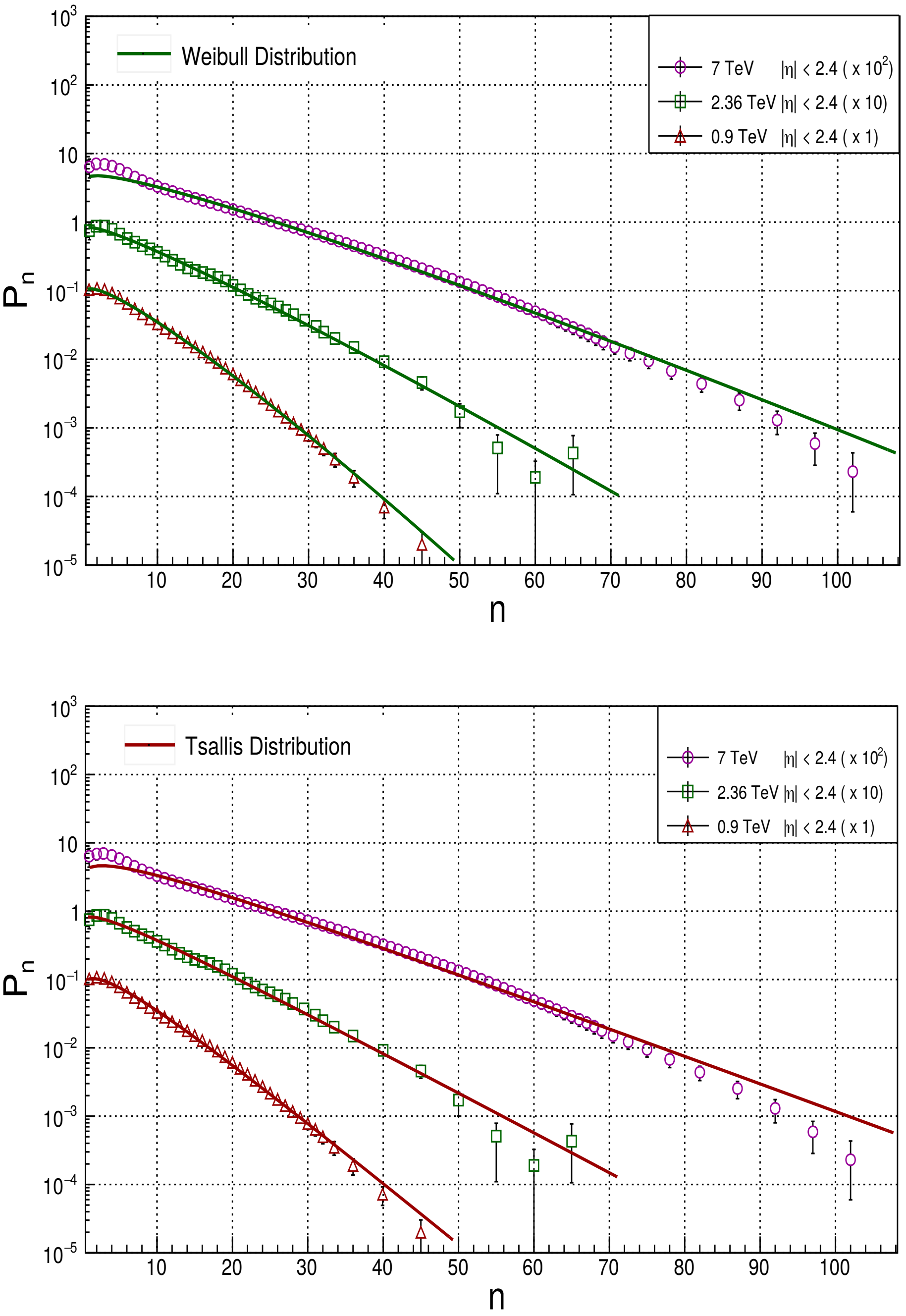

Figure 6.12: The charged particle multiplicity distributions in *pp* collisions by the CMS experiment at $|\eta| < 2.4$ with $p_T > 500$ MeV and comparison of the experimental data with the Weibull and the Tsallis distributions.

Energy (TeV)	$\|\eta\|$ Interval	NBD Distribution		Gamma Distribution		Shifted Gamma Distribution		Tsallis Distribution		Weibull Distribution	
Particles with all available p_T in all $\|\eta\|$ regions											
		χ^2/ndf	p value	χ^2/ndf	p value	χ^2/ndf	p value	χ^2/ndf	p value	χ^2/ndf	p value
0.9	0.5	1.57/19	1.0000	3.21/19	1.0000	0.98/19	1.0000	1.58/17	1.0000	0.81/19	1.0000
	1.0	43.77/36	0.1750	54.50/36	0.0247	33.66/36	0.5804	43.64/34	0.1244	16.03/36	0.9984
	1.5	42.07/48	0.7134	48.49/48	0.4531	35.41/48	0.9113	41.32/46	0.6683	18.89/48	0.9999
	2.0	33.18/58	0.9964	38.11/58	0.9798	31.21/58	0.9985	33.06/56	0.9938	22.51/58	1.0000
	2.4	46.79/64	0.9478	52.93/64	0.8368	44.02/64	0.9733	46.82/62	0.9240	32.83/64	0.9996
2.36	0.5	6.61/19	0.9960	7.41/19	0.9917	5.94/19	1.0000	6.60/17	0.9882	5.21/19	0.9992
	1.0	60.09/36	0.0071	67.79/36	0.0011	50.59/36	0.0541	59.99/34	0.0039	29.70/36	0.7614
	1.5	27.36/46	0.9868	30.10/46	0.9662	25.24/46	0.9945	27.28/44	0.9774	17.53/46	1.000
	2.0	45.39/56	0.8437	46.44/56	0.8162	45.25/56	0.8473	45.31/54	0.7941	35.57/56	0.9848
	2.4	40.95/65	0.9915	44.91/65	0.9729	44.98/65	0.9778	40.94/63	0.9859	37.61/65	0.9974
7	0.5	91.85/37	0.0001	101.40/37	0.0001	75.86/37	0.0002	91.74/35	0.0001	55.5/37	0.0259
	1.0	171.26/66	0.0001	183.71/66	0.0001	149.11/66	0.0001	170.93/64	0.0001	86.72/66	0.0446
	1.5	35.34/68	0.9996	34.93/68	0.9997	35.89/68	0.9995	35.38/66	0.9991	31.83/ 68	0.9999
	2.0	41.73/86	1.0000	40.41/86	1.0000	44.27/86	0.9999	41.69/84	1.0000	40.58/86	1.0000
	2.4	50.06/99	1.0000	47.91/99	1.0000	54.67/99	0.9999	49.96/97	1.0000	51.92/99	1.0000
Particles with $p_T > 500$ MeV and $\|\eta\| < 2.4$											
0.9	2.4	21.26/34	0.9565	32.84/34	0.5244	17.86/34	0.9896	21.26/32	0.9177	23.14/34	0.9204
2.36	2.4	35.61/36	0.4870	36.37/36	0.4514	33.43/36	0.5914	35.61/34	0.3195	29.58/36	0.7664
7	2.4	172.04/75	0.0001	178.07/75	0.0001	157.02/75	0.0001	172.01/73	0.0001	122.35/75	0.0005

Table 6.1: Comparison of χ^2/ndf values and p values at all pseudorapidity intervals for the NBD, the Gamma, Shifted Gamma, the Tsallis and the Weibull distributions for charged hadron multiplicity spectra.

$\|\eta\|$ Interval	Gamma		Shifted Gamma		Tsallis		Weibull	
$\sqrt{s} = 0.9$ TeV								
	α	β	α'	β'	K_{TS}	q	k	λ
0.5	1.515 ± 0.068	0.352 ± 0.010	2.265 ± 0.156	0.395 ± 0.015	1.726 ± 0.098	1.431 ± 0.004	1.183 ± 0.024	4.386 ± 0.112
1.0	1.848 ± 0.061	0.223 ± 0.004	2.498 ± 0.098	0.244 ± 0.005	2.084 ± 0.080	1.356 ± 0.033	1.282 ± 0.017	8.622 ± 0.158
1.5	1.844 ± 0.058	0.153 ± 0.003	2.371 ± 0.081	0.167 ± 0.004	2.028 ± 0.070	1.201 ± 0.046	1.316 ± 0.017	12.740 ± 0.195
2.0	1.865 ± 0.053	0.117 ± 0.002	2.331 ± 0.067	0.128 ± 0.002	2.025 ± 0.055	1.111 ± 0.003	1.345 ± 0.016	16.970 ± 0.220
2.4	1.944 ± 0.054	0.102 ± 0.002	2.382 ± 0.062	0.111 ± 0.002	2.101 ± 0.058	1.055 ± 0.008	1.383 ± 0.016	20.440 ± 0.241
$\sqrt{s} = 2.36$ TeV								
0.5	1.379 ± 0.068	0.260 ± 0.009	1.855 ± 0.141	0.284 ± 0.012	1.501 ± 0.088	1.546 ± 0.030	1.147 ± 0.024	5.414 ± 0.141
1.0	1.743 ± 0.060	0.168 ± 0.003	2.187 ± 0.089	0.179 ± 0.004	1.892 ± 0.073	1.475 ± 0.029	1.234 ± 0.017	10.840 ± 0.218
1.5	1.595 ± 0.057	0.105 ± 0.003	1.892 ± 0.081	0.112 ± 0.003	1.682 ± 0.066	1.284 ± 0.026	1.252 ± 0.020	15.830 ± 0.299
2.0	1.644 ± 0.057	0.082 ± 0.002	1.931 ± 0.075	0.087 ± 0.002	1.731 ± 0.063	1.183 ± 0.021	1.272 ± 0.020	21.240 ± 0.365
2.4	1.684 ± 0.057	0.070 ± 0.002	1.959 ± 0.071	0.075 ± 0.002	1.751 ± 0.059	1.136 ± 0.031	1.299 ± 0.020	25.530 ± 0.408
$\sqrt{s} = 7$ TeV								
0.5	1.461 ± 0.050	0.201 ± 0.007	1.841 ± 0.083	0.214 ± 0.004	1.571 ± 0.062	1.674 ± 0.010	1.066 ± 0.014	7.473 ± 0.150
1.0	1.645 ± 0.044	0.113 ± 0.003	1.897 ± 0.059	0.118 ± 0.002	1.725 ± 0.043	1.593 ± 0.004	1.099 ± 0.012	14.820 ± 0.218
1.5	1.767 ± 0.041	0.081 ± 0.001	1.317 ± 0.059	0.063 ± 0.002	1.247 ± 0.035	1.401 ± 0.026	1.107 ± 0.017	20.451 ± 0.338
2.0	1.738 ± 0.039	0.061 ± 0.002	1.325 ± 0.050	0.048 ± 0.001	1.265 ± 0.040	1.303 ± 0.007	1.116 ± 0.016	27.320 ± 0.388
2.4	1.506 ± 0.031	0.046 ± 0.001	1.344 ± 0.047	0.040 ± 0.001	1.284 ± 0.035	1.228 ± 0.055	1.127 ± 0.015	32.789 ± 0.422

Table 6.2: Parameters of the Gamma, Shifted Gamma, the Tsallis and the Weibull distributions for charged hadron multiplicity spectra for all pseudorapidity intervals at 0.9, 2.36 and 7 TeV

Gamma, Shifted Gamma and the Tsallis fits though provide the clear justification of experimental data but these distributions fail at pseudorapidity intervals $|\eta| < 0.5$ and $|\eta| < 1.0$ at 7 TeV with $CL < 0.1\%$. The Weibull model explains the experimental data very well for all $|\eta|$ regions at every energy. For multiplicity with transverse momenta, $p_T > 500$ MeV all the fits fail to reproduce the experimental data at $\sqrt{s} = 7$ TeV for pseudorapidity region, $|\eta| < 2.4$.

For the Weibull model shape parameter, k increases with increase in pseudorapidity interval at given energy and do not vary significantly with energy for a given pseudorapidity interval. Though one can observe the minute decrease in the k values with increase in energy as shown in table 6.2, this decrease is insignificant owing to the large errors. The shape parameter is associated with the nature of the fragmentation process. In *h*-*h* interactions the dynamics of the fragmentation process does not vary much with the energy in given pseudorapidity interval. The scale parameter λ, which determines the width of the distribution, increases with the energy for particular set of pseudorapidity intervals as well as with increase in pseudorapidity interval at a given energy. This behaviour of scale parameter is expected as it is associated to the mean multiplicity, which increases with the centre of mass energy as well as with the pseudorapidity intervals and can be described using empirical relation [13]. In figure 6.13 the variation of parameter λ with the energy, $\sqrt{s}$ for extreme pseudorapidity intervals, $|\eta| < 0.5$ and $|\eta| < 2.4$ is plotted. The dependence of parameters of the Weibull distribution on energy shown by the solid lines in the figure 6.13 can be described using relation;

$$\lambda = a + b(ln\sqrt{s}) + c\,(ln\sqrt{s})^2 \tag{6.1}$$

The fit parameters a, b and c for the extreme pseudorapidity intervals are given below;

For $|\eta| < 0.5$; $a = 4.462 \pm 0.099$, $b = 0.762 \pm 0.298$ and $c = 0.403 \pm 0.160$

For $|\eta| < 2.4$; $a = 20.931 \pm 0.219$, $b = 4.767 \pm 0.806$ and $c = 0.681 \pm 0.450$

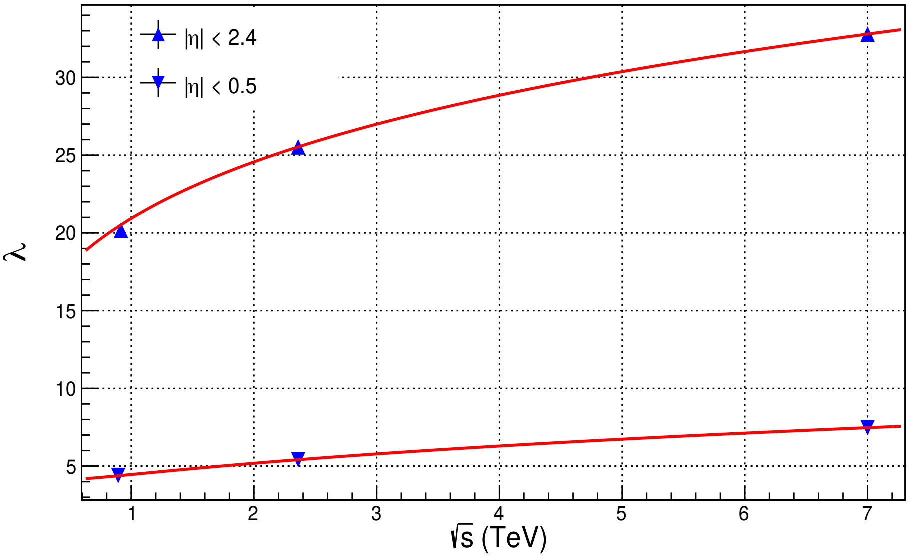

Figure 6.13: Dependence of the Weibull parameter λ on energy, $\sqrt{s}$.

For the Gamma and Shifted Gamma distributions, shape parameters, β and β' show decrease in the values with increasing energy as well as with pseudorapidity intervals. The shape parameter, β (β') is expected to decrease as it is related to the dimension, D which decreases with the energy as, $D \sim \frac{1}{\sqrt{s}}$ [14]. The scale parameter α (α') of the Gamma (Shifted Gamma) distribution is a parameter which affects the shape of the distribution. This parameter varies very minutely and remains almost constant within limit of errors which indicates that the shape of the distribution remains independent of the increase in energy and pseudorapidity.

For the Tsallis statistics, value of entropic index, q, which measures the departure of entropy from its extensive behaviour exceeds unity in every case as observed from table 6.2. For a given pseudorapidity interval $|\eta|$, q value increases with increase in energy but decreases with increase in pseudorapidity interval size at a given energy. This increase in the q value indicates that the non-extensive behaviour of entropy becomes more pronounced at higher energies. The dependence of q on the energy, $\sqrt{s}$, can be defined in terms of power law where $q = A_0 \ \sqrt{s}^{B_0}$ which is inspired by the observation that single particle energy distribution obeys a power law behaviour [15] . Figure 6.14 shows the variation of q values with the energy at several pseudorapidity intervals. The parameters of power law used to describe this variation of q with energy are given in table 6.3. It is observed that value of parameter B_0 of power law remains almost constant within limits of error for each pseudorapidity interval, depicting the weak but constant dependence of q on the centre of mass energy, $\sqrt{s}$.

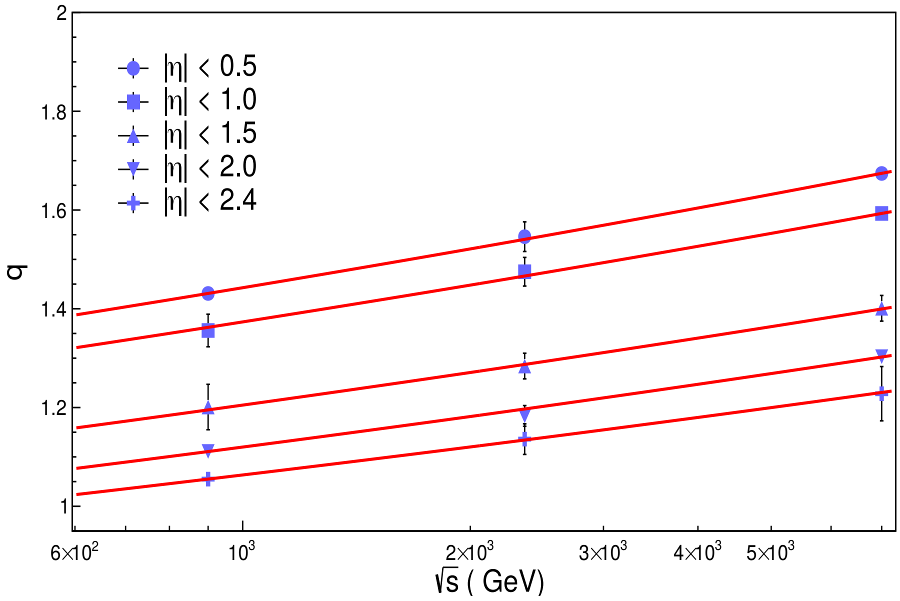

Figure 6.14: The dependence of entropic index, q of the Tsallis statistics on energy, $\sqrt{s}$ fitted with power law, $q = A_0\ \sqrt{s}^{B_0}$

$\lvert\eta\rvert$	q			$q = A_0\ \sqrt{s}^{B_0}$	
	$q_{0.9TeV}$	$q_{2.36TeV}$	q_{7TeV}	A_0	B_0
0.5	1.431 ± 0.004	1.546 ± 0.030	1.674 ± 0.010	0.851 ± 0.020	0.076 ± 0.003
1.0	1.356 ± 0.033	1.475 ± 0.029	1.593 ± 0.004	0.811 ± 0.072	0.076 ± 0.010
1.5	1.201 ± 0.046	1.284 ± 0.026	1.401 ± 0.026	0.706 ± 0.106	0.077 ± 0.018
2.0	1.111 ± 0.003	1.183 ± 0.021	1.303 ± 0.007	0.660 ± 0.014	0.076 ± 0.003
2.4	1.055 ± 0.008	1.136 ± 0.031	1.228 ± 0.055	0.630 ± 0.081	0.075 ± 0.012

Table 6.3: Power law $q = A_0\sqrt{s}^{B_0}$ dependence of entropic index , q on energy $\sqrt{s}$ for different pseudorapidity intervals.

6.2.1.3 Moments

Multiplicity distributions at higher energies become much more broader than at lower energies and the experimental data at these higher energies show the violation of KNO scaling [16]. The correlation between the produced particles and the significant change in the shape of distribution can be studied and understood correctly by using the Moments. The deviation from independent production can be understood if the factorial moments are greater or less than unity. The violation of KNO scaling at higher energies can also be understood correctly by using the normalized moments. Also the energy dependence of these moments implies KNO scaling violation. Analysis of moments on *pp* data using the Weibull model has been done by S.Dash et al. [13]. But no previous study on moments using the Tsallis model has been done. Hence a detailed analysis of the moments using the Tsallis model becomes our obvious choice in an attempt to understand the correlation among the particles produced. The moments C_q and F_q have been calculated by using the Tsallis model and are shown in table 6.4. The dependence of normalised moments, C_q and factorial moments, F_q on the pseudorapidity, $|\eta|$ at a given energy and dependence of C_q and F_q on the energy, $\sqrt{s}$ at a given pseudorapidity interval are shown in figures 6.15 - 6.18. It is found that at each set of pseudorapidity intervals the values of both the moments C_q and F_q increase with increase in centre of mass energy, $\sqrt{s}$. The value of C_q decreases with increase in the pseudorapidity interval at a given energy whereas F_q remains same within limit with increase in pseudorapidity interval as shown in figures 6.17 - 6.18 confirming the KNO scaling violation at higher energies and correlations amongst the produced particles. The values of the moments from the Tsallis models are compared with the CMS experimental values and found to be in good agreement.

6.2.1.4 Average Multiplicity

Dependence of the mean charged multiplicity on centre of mass energy is studied using the empirical relation [17].

Energy (TeV)	$\|\eta\|$	Reduced Moments				Factorial Moments			
		C_2	C_3	C_4	C_5	F_2	F_3	F_4	F_5
0.9	0.5	1.59 ± 0.02	3.49 ± 0.14	9.59 ± 0.83	31.15 ± 4.49	1.37 ± 0.01	2.54 ± 0.01	5.79 ± 0.21	15.27 ± 2.40
	1.0	1.55 ± 0.02	3.21 ± 0.10	8.22 ± 0.35	25.04 ± 0.55	1.42 ± 0.01	2.66 ± 0.06	6.13 ± 0.25	16.56 ± 1.02
	1.5	1.53 ± 0.06	3.12 ± 0.35	7.75 ± 1.52	22.33 ± 5.17	1.45 ± 0.04	2.75 ± 0.24	6.32 ± 1.15	16.65 ± 4.12
	2.0	1.51 ± 0.03	3.06 ± 0.10	7.05 ± 0.44	21.13 ± 1.97	1.46 ± 0.02	2.78 ± 0.08	6.39 ± 0.34	16.81 ± 1.43
	2.4	1.49 ± 0.01	2.92 ± 0.05	6.93 ± 0.22	19.02 ± 0.85	1.44 ± 0.01	2.69 ± 0.05	6.06 ± 0.19	15.67 ± 0.70
2.36	0.5	1.64 ± 0.03	3.71 ± 0.23	10.48 ± 1.29	34.05 ± 6.39	1.45 ± 0.01	2.88 ± 0.09	6.98 ± 0.62	19.26 ± 3.16
	1.0	1.62 ± 0.04	3.59 ± 0.29	9.73 ± 0.93	30.20 ± 2.01	1.48 ± 0.02	2.95 ± 0.07	7.40 ± 0.32	20.90 ± 2.46
	1.5	1.60 ± 0.06	3.46 ± 0.36	9.15 ± 1.78	27.93 ± 8.29	1.53 ± 0.04	3.15 ± 0.29	7.85 ± 1.40	22.37 ± 7.30
	2.0	1.57 ± 0.05	3.27 ± 0.32	8.22 ± 1.49	23.49 ± 6.38	1.52 ± 0.05	3.04 ± 0.27	7.29 ± 1.25	19.71 ± 5.19
	2.4	1.55 ± 0.01	3.12 ±0.31	7.51 ± 1.34	20.30 ± 5.30	1.51 ± 0.06	2.93 ± 0.27	6.74 ± 1.16	17.30 ± 4.42
7	0.5	1.65 ± 0.02	3.84 ± 0.10	11.44 ± 0.48	41.52 ± 2.54	1.52 ± 0.02	3.21 ± 0.08	8.65 ± 0.37	28.32 ± 2.20
	1.0	1.62 ± 0.02	3.59 ± 0.07	10.11 ± 0.34	34.15 ± 1.70	1.52 ± 0.01	3.17 ± 0.05	8.30 ± 0.24	25.98 ± 1.18
	1.5	1.73 ± 0.04	4.14 ± 0.26	12.07 ± 1.35	40.01 ± 6.72	1.68 ± 0.03	3.88 ± 0.22	10.86 ± 1.17	34.28 ± 5.63
	2.0	1.71 ± 0.01	4.08 ± 0.14	11.72 ± 0.51	38.24 ± 2.84	1.69 ± 0.02	3.91 ± 0.14	10.82 ± 0.52	34.01 ± 2.35
	2.4	1.69 ± 0.04	3.87 ± 0.25	10.57 ± 1.22	32.45 ± 5.57	1.67 ± 0.05	3.71 ± 0.23	9.85 ± 1.92	29.21 ± 4.95

Table 6.4: C_q and F_q moments calculated from the Tsallis model for different pseudorapidity intervals at $\sqrt{s} = 0.9$, 2.36 and 7 TeV.

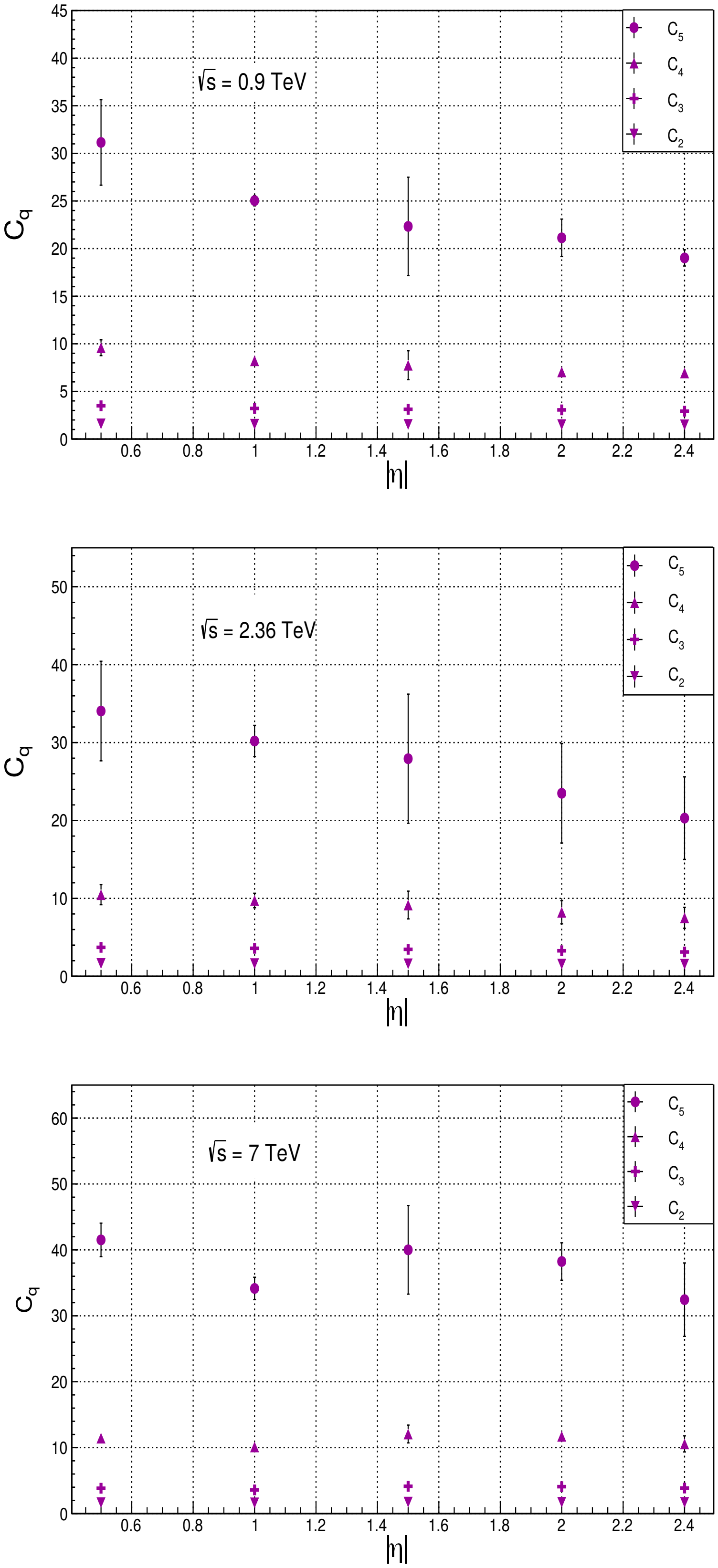

Figure 6.15: C_q moments obtained from the Tsallis model and its dependence on pseudorapidity intervals $|\eta|$ at $\sqrt{s}$ = 0.9, 2.36 and 7 TeV.

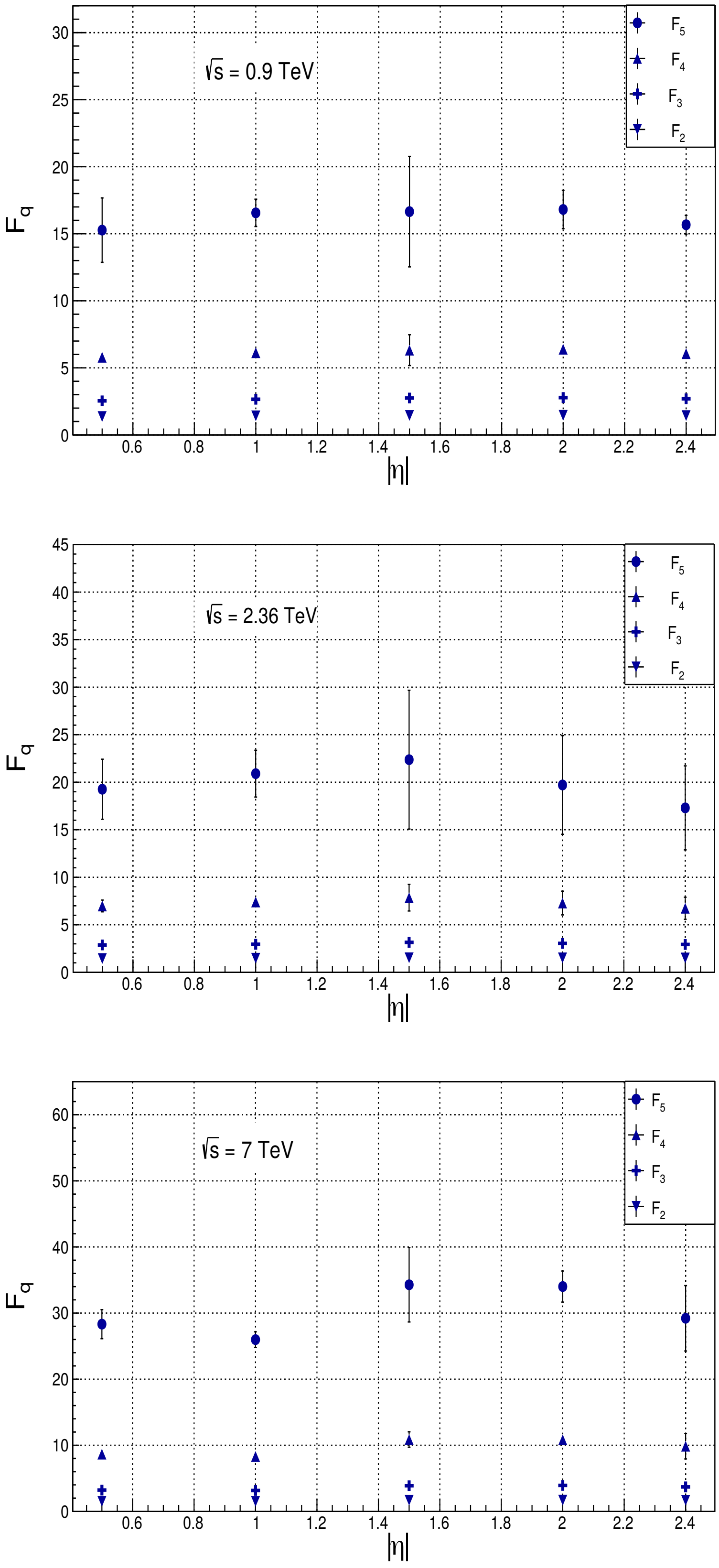

Figure 6.16: F_q moments obtained from the Tsallis model and its dependence on pseudorapidity intervals $|\eta|$ at $\sqrt{s}$ = 0.9, 2.36 and 7 TeV.

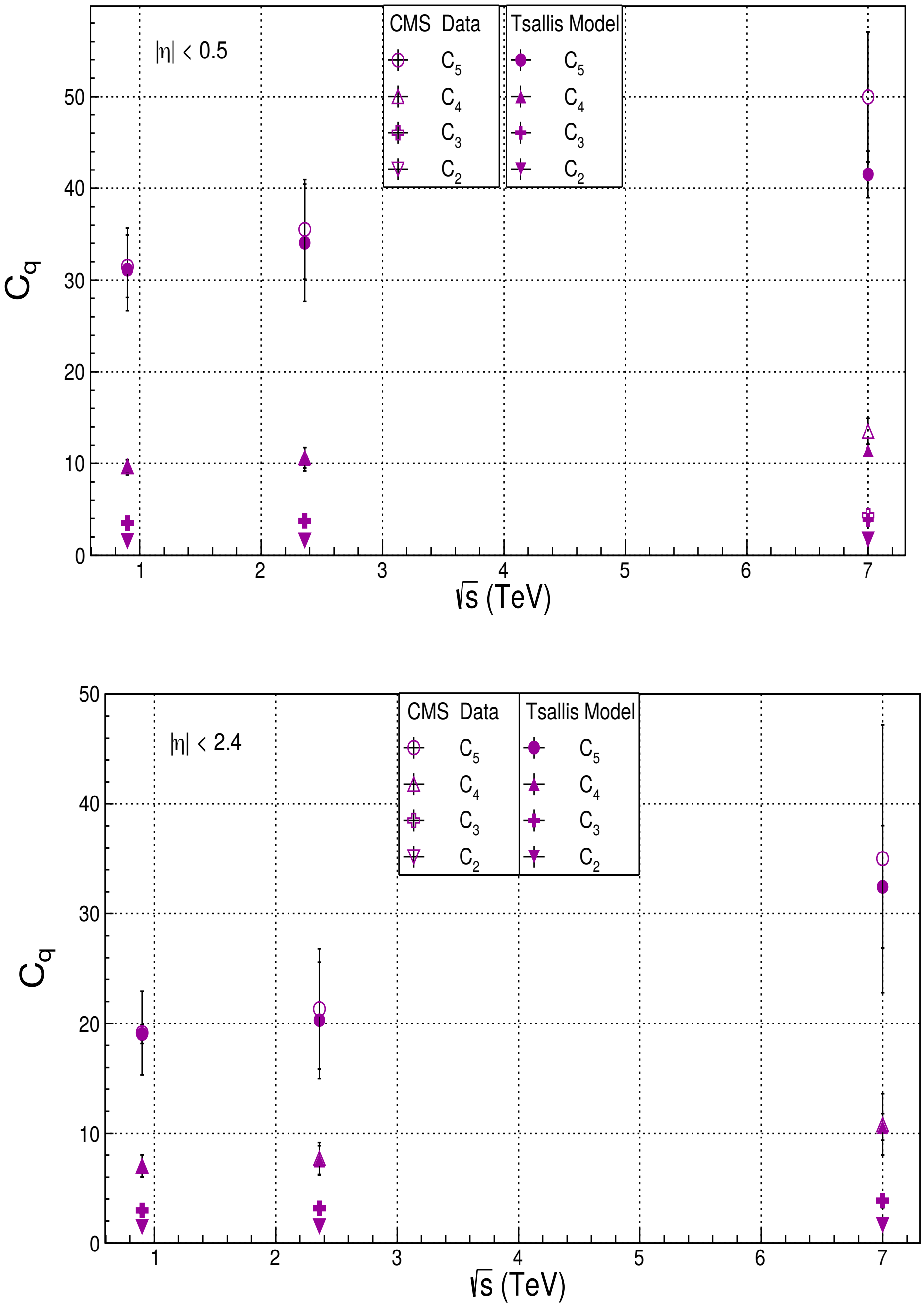

Figure 6.17: The variation of C_q moments with the centre of mass energy at pseudorapidity intervals $|\eta| < 0.5$ and $|\eta| < 2.4$ and comparison of the moments calculated from the Tsallis model with the CMS experimental values [6].

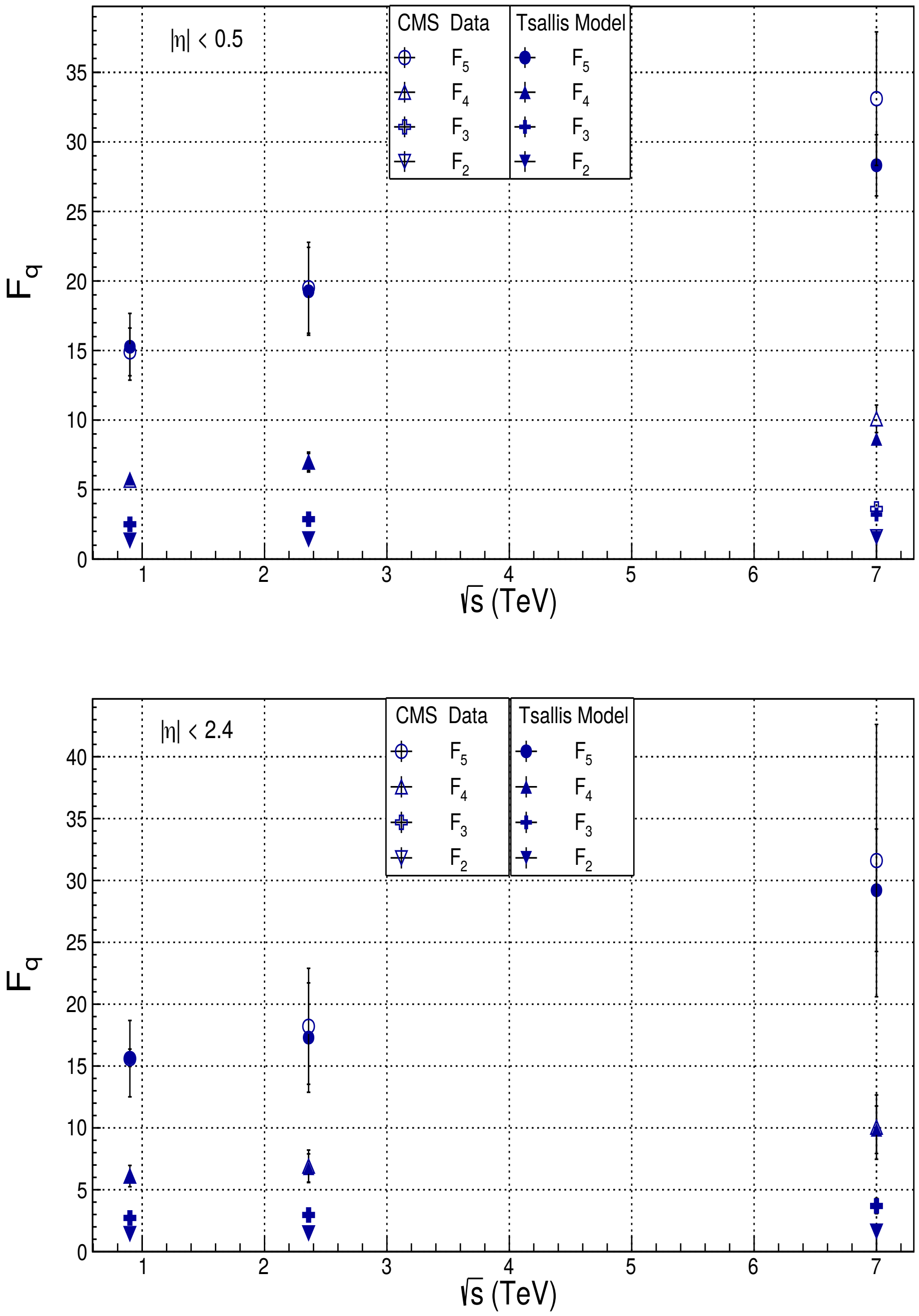

Figure 6.18: The variation of F_q moments with the centre of mass energy at pseudorapidity intervals $|\eta| < 0.5$ and $|\eta| < 2.4$ and comparison of the moments calculated from the Tsallis model with the CMS experimental values [6].

The values of average charged multiplicity calculated from the Tsallis model are compared with the experimental values for *pp* collision data of the CMS experiment. The values are found to be in good agreement taking the errors in account. The extreme pseudorapidities are chosen because of availability of experimental $< n >$ values only at these pseudorapidities. Figure 6.19 shows the comparison of $< n >$ values from the data and model only for $|\eta| < 2.4$. The values of average multiplicity for both model and the experiment are listed in the table 6.5 below.

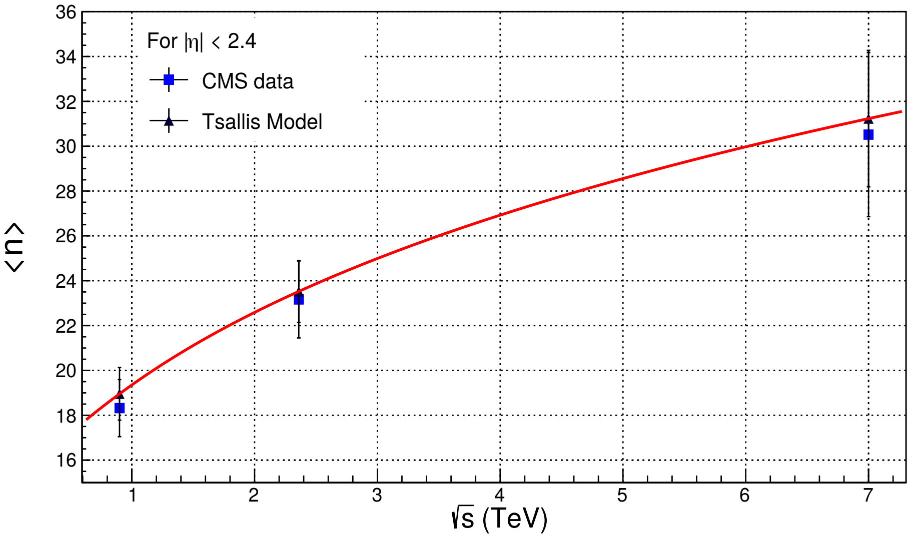

Figure 6.19: Dependence of the average multiplicity on the centre of mass energy. The values from the Tsallis model is compared with the CMS experimental values. The solid line is the fit for the Tsallis model from equation (6.3)

$\|\eta\|$ Interval	Energy (TeV)	Average Charged Multiplicity ($< n >$)	
		CMS Experiment	Tsallis Model
0.5	0.9	4.355 ± 0.207	4.583 ± 0.772
	2.36	5.262 ± 0.250	5.489 ± 0.992
	7.00	6.808 ± 0.335	7.409 ± 1.022
2.4	0.9	18.320 ± 1.273	18.957 ± 1.174
	2.36	23.166 ± 1.716	23.524 ± 1.382
	7.00	30.516 ± 3.660	31.231 ± 3.042

Table 6.5: Average multiplicity $< n >$ at two extreme pseudorapidity intervals, $|\eta| < 0.5$ and $|\eta| < 2.4$ at $\sqrt{s} = 0.9$, 2.36 and 7 TeV

at $|\eta| < 2.4$,

$$For\ CMS\ Data: \quad <n> = 18.77 + 4.39(ln\sqrt{s}) + 0.845(ln\sqrt{s})^2 \tag{6.2}$$

$$For\ Tsallis\ Model: <n> = 19.35 + 3.874(ln\sqrt{s}) + 1.146(ln\sqrt{s})^2 \tag{6.3}$$

At $\sqrt{s} = 7$ TeV, the Tsallis model fails to provide the justification of data for lowest rapidity interval, $|\eta| < 0.5$ which leads to the large difference between the experiment and the model values. However for all other pseudorapidity intervals the agreement is good.

6.2.1.5 Predictions at $\sqrt{s} = 14$ TeV

The energy dependence of entropic index, q of the Tsallis model is described by the power law as discussed in previous section. The parameters of the relation are given in table 6.3 for all pseudorapidity intervals. Using the power law relation, we extrapolate the fit of the Tsallis model to obtain the q-value at $\sqrt{s} = 14$ TeV for different pseudorapidity intervals. Using these q values the multiplicity distributions are derived according to the Tsallis model for each pseudorapidity interval. The mean multiplicity values are then found from the distribution. These q values and the mean multiplicities values for each pseudorapidity interval is given in the table 6.6. The predicted multiplicity distribution for pseudorapidity interval $|\eta| < 1.5$ at $\sqrt{s} = 14$ TeV having entropic index, $q = 1.476 \pm 0.108$ with $<n> = 24.492 \pm 2.571$ is shown in figure 6.20. The multiplicity distributions for other pseudorapidity intervals can be calculated in the same manner. The predicted multiplicity distribution at 14 TeV is also plotted along with multiplicity distributions at 0.9, 2.36 and 7 TeV for $|\eta| < 1.5$ in figure 6.20. The analyses of multiplicities in pp collisions using the CMS data have been published by us and more details can be found in the reference [18].

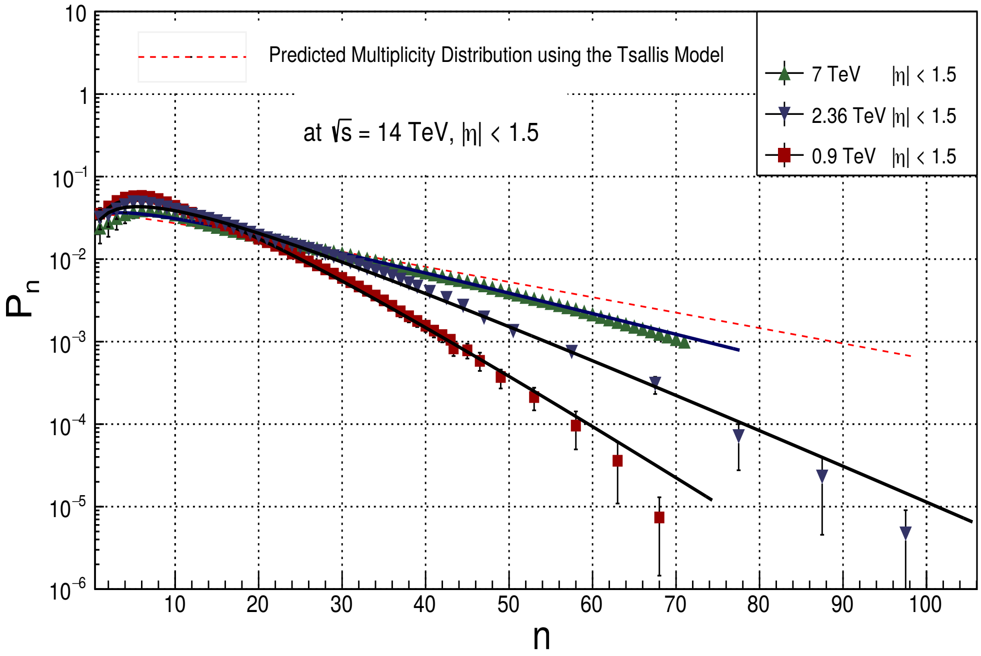

Figure 6.20: The multiplicity spectrum predicted for pp collisions at $\sqrt{s} = 14$ TeV is plotted along with the multiplicity distributions at $\sqrt{s} = 0.9$, 2.36 and 7 TeV at $|\eta| < 1.5$

Pseudorapidity Interval	Tsallis Model	
$\|\eta\|$	q	$< n >$
0.5	1.761 ± 0.004	8.428 ± 1.534
1.0	1.673 ± 0.025	13.027 ± 2.105
1.5	1.476 ± 0.108	24.492 ± 2.571
2.0	1.365 ± 0.002	32.049 ± 2.973
2.4	1.292 ± 0.031	36.176 ± 3.251

Table 6.6: The non-extensive entropic index parameter of the Tsallis fit and average multiplicity predicted at $\sqrt{s} = 14$ TeV at different pseudorapidity intervals for pp collisions.

6.2.2 Study of $\bar{p}p$ Interactions using the UA5 Data

Particles produced during the collisions are emitted with all sort of energies and distributed according to some probability distribution functions. Mean value of the distribution, used in defining the multiplicity spectra, coincides approximately with the average number of particles obtained, called as average multiplicity, from the experiment. Analysis of the experimental multiplicity data on antiproton-proton, $\bar{p}p$, collisions using UA5 streamer chambers [5] at the CERN at different energies, $\sqrt{s}$ = 200, 540 and 900 GeV have been done. The UA5 experiment was performed during 1980s at CERN. Data samples analysed at these energies consist of inelastic and non single diffractive (NSD) events which produced multitude of particles in the final state. The minimum bias trigger [19] was used to select the NSD events at these energies. The trigger excluded almost all the single diffractive events along with other background events and recorded around 95 % of NSD events. This process led to the rejection of around 97 % of hadronic secondary interactions (background) from the sample of events. Data sample analysed here consists of 4156 NSD events at energy, $\sqrt{s}$ = 200 GeV, 7344 events at $\sqrt{s}$ = 540 GeV and 6839 events at $\sqrt{s}$ = 900 GeV. The details of the data collected and of the experiment can be found from [20, 21].

6.2.2.1 Analysis of Multiplicities

Multiplicity data at pseudorapidity intervals $|\eta| < 0.5$, 1.5, 3.0 and 5.0 have been analysed along with the full phase space multiplicity data at centre of mass energies $\sqrt{s}$ = 200, 540 and 900 GeV [20, 21] for $\bar{p}p$ collisions. We have used the NBD, Gamma, the Weibull and the Tsallis models to obtain the multiplicity distributions at these energies. The results are compared with the experimental data. Fitting procedure used here to fit these functions is the same as used in proton-proton analysis described in the previous section. Figures 6.21 - 6.22 show the results of these models fitted on experimental data at 200 GeV, figures 6.23 - 6.24 show the various distributions fitted to the 540 GeV data and figures 6.25 - 6.26 for the

900 GeV data. The χ^2/ndf values have been compared for all the four models and are shown in the table 6.7, where as the parameters of the fitted distributions corresponding to the data are shown in table 6.8.

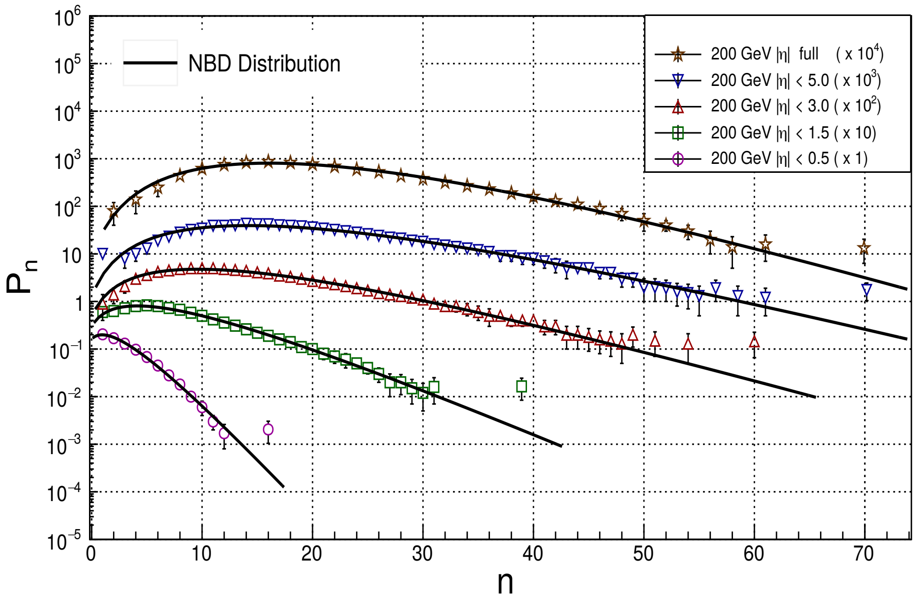

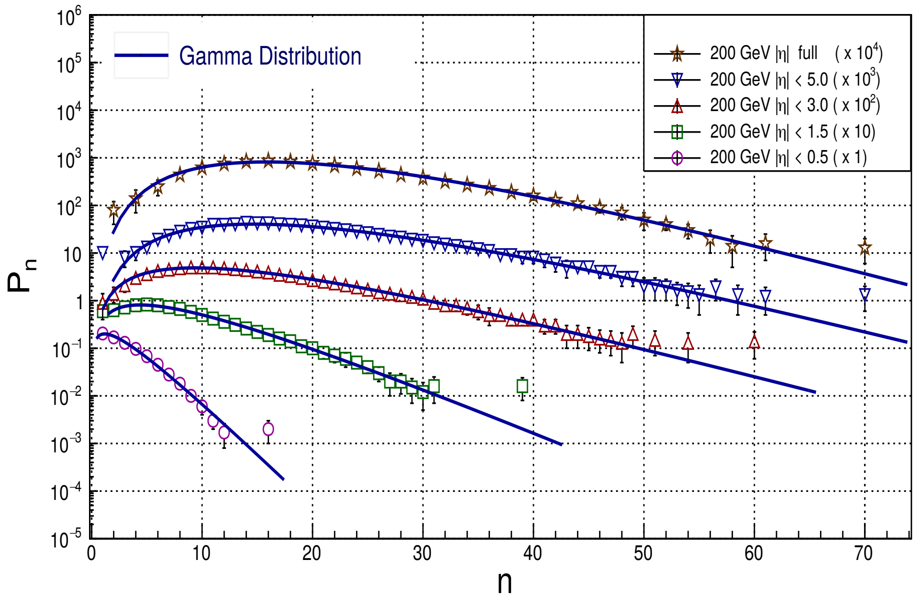

Figure 6.21: The charged particle multiplicity distributions in $\bar{p}p$ collisions by the UA5 experiment at 200 GeV and comparison of the experimental data with the NBD and Gamma distributions.

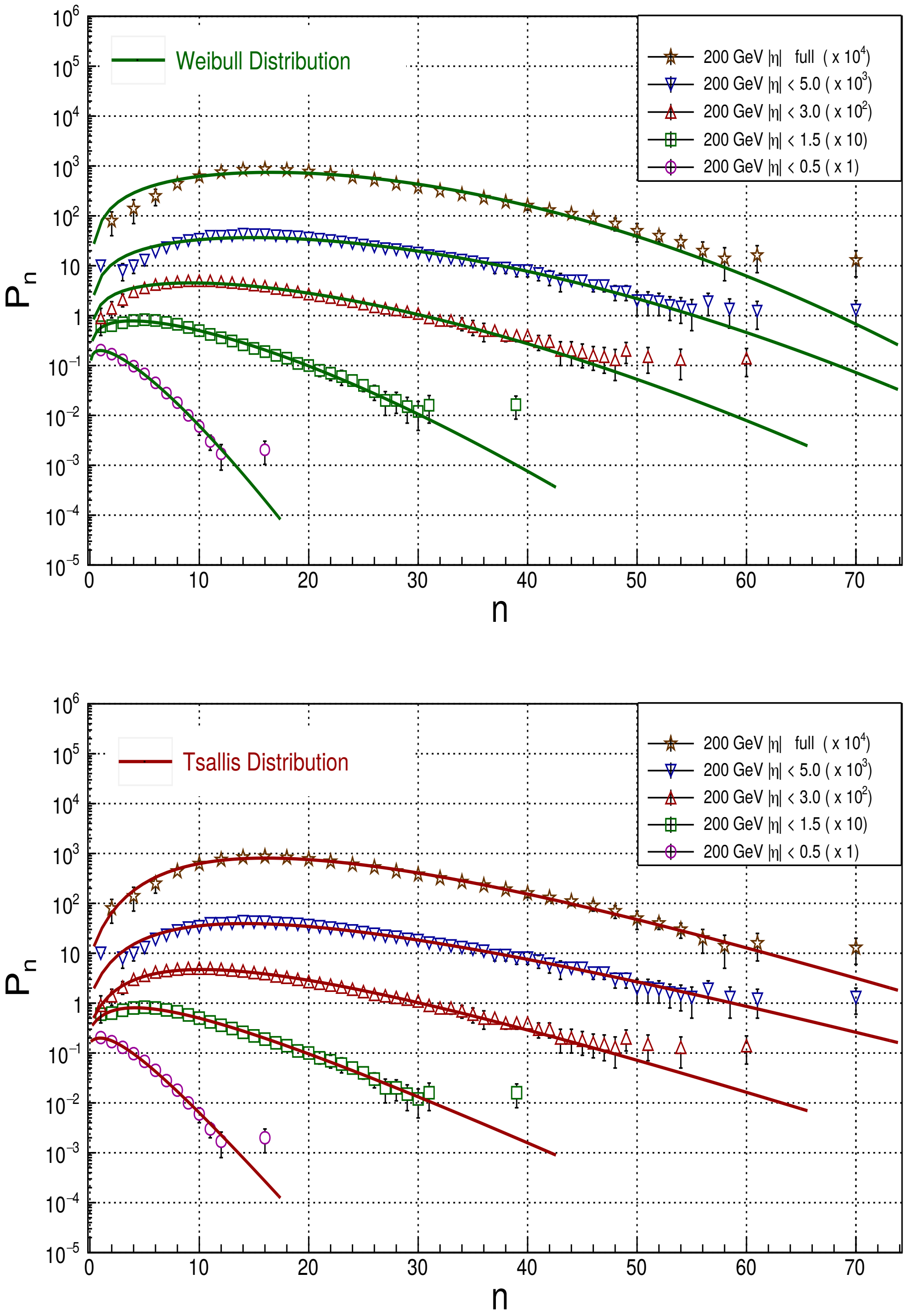

Figure 6.22: The charged particle multiplicity distributions in $\bar{p}p$ collisions by the UA5 experiment at 200 GeV and comparison of the experimental data with the Weibull and the Tsallis distributions.

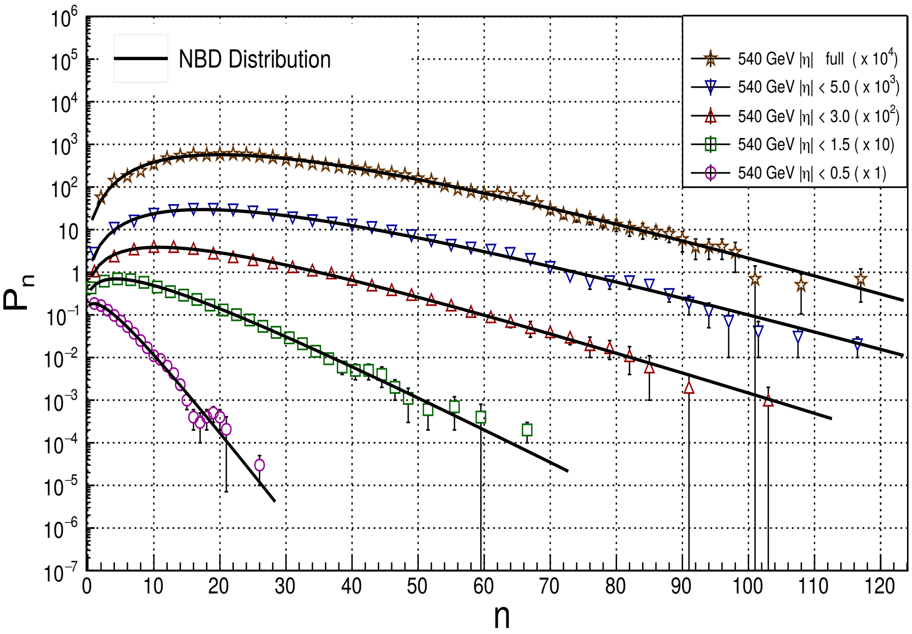

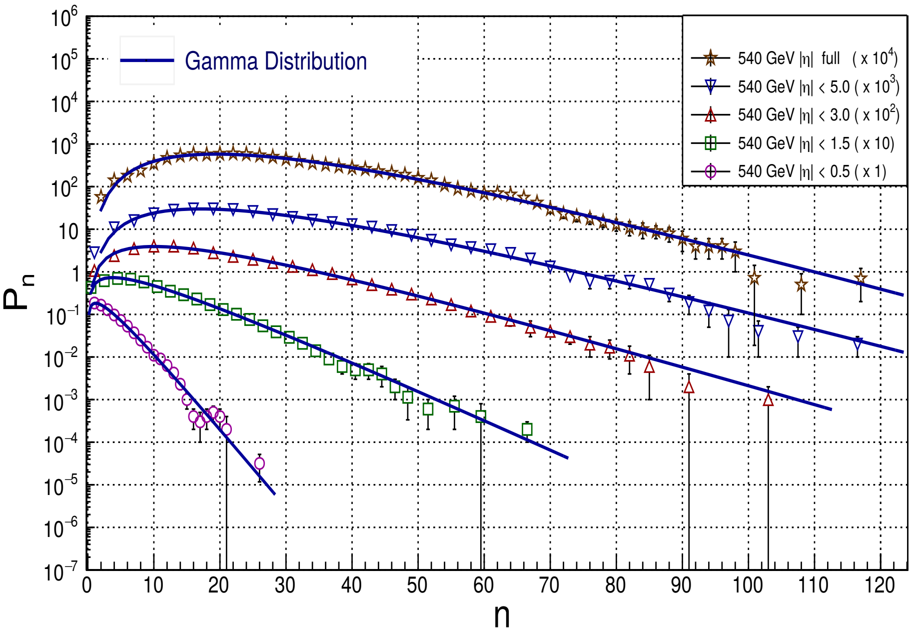

Figure 6.23: The charged particle multiplicity distributions in $\bar{p}p$ collisions by the UA5 experiment at 540 GeV and comparison of the experimental data with the NBD and the Gamma distributions.

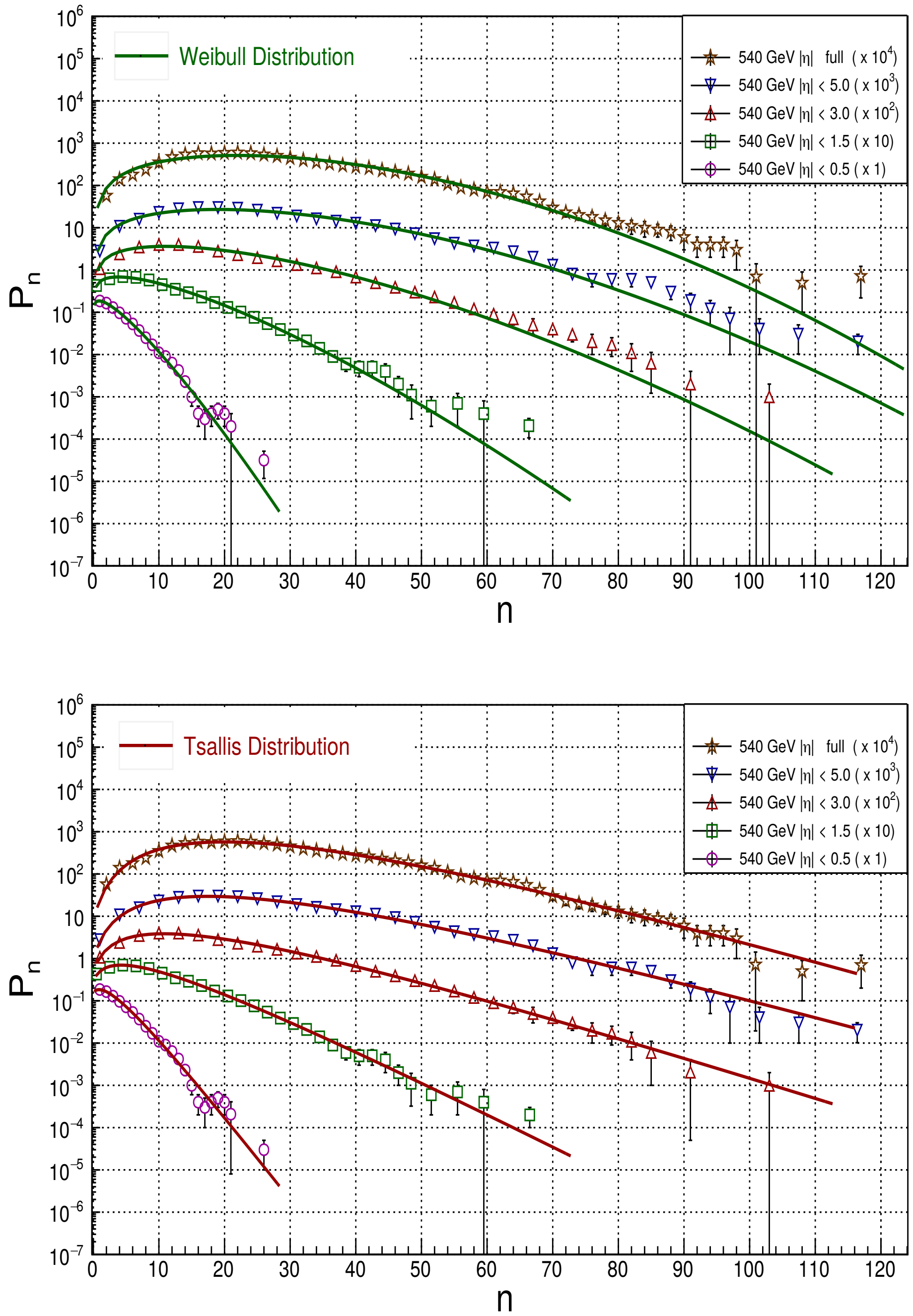

Figure 6.24: The charged particle multiplicity distributions in $\bar{p}p$ collisions by the UA5 experiment at 540 GeV and comparison of the experimental data with the Weibull and the Tsallis distributions.

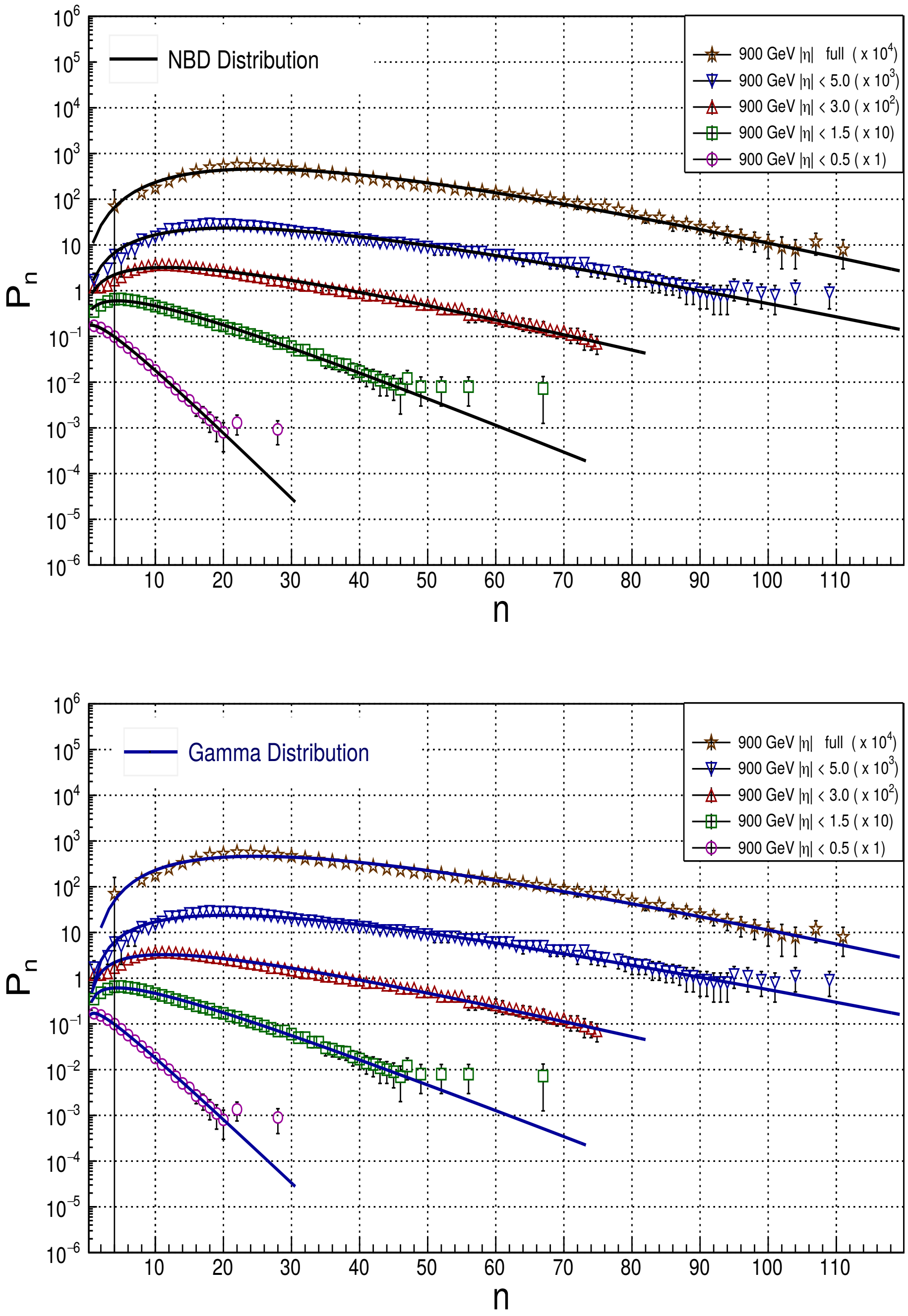

Figure 6.25: The charged particle multiplicity distributions in $\bar{p}p$ collisions by the UA5 experiment at 900 GeV and comparison of the experimental data with the NBD and the Gamma distributions.

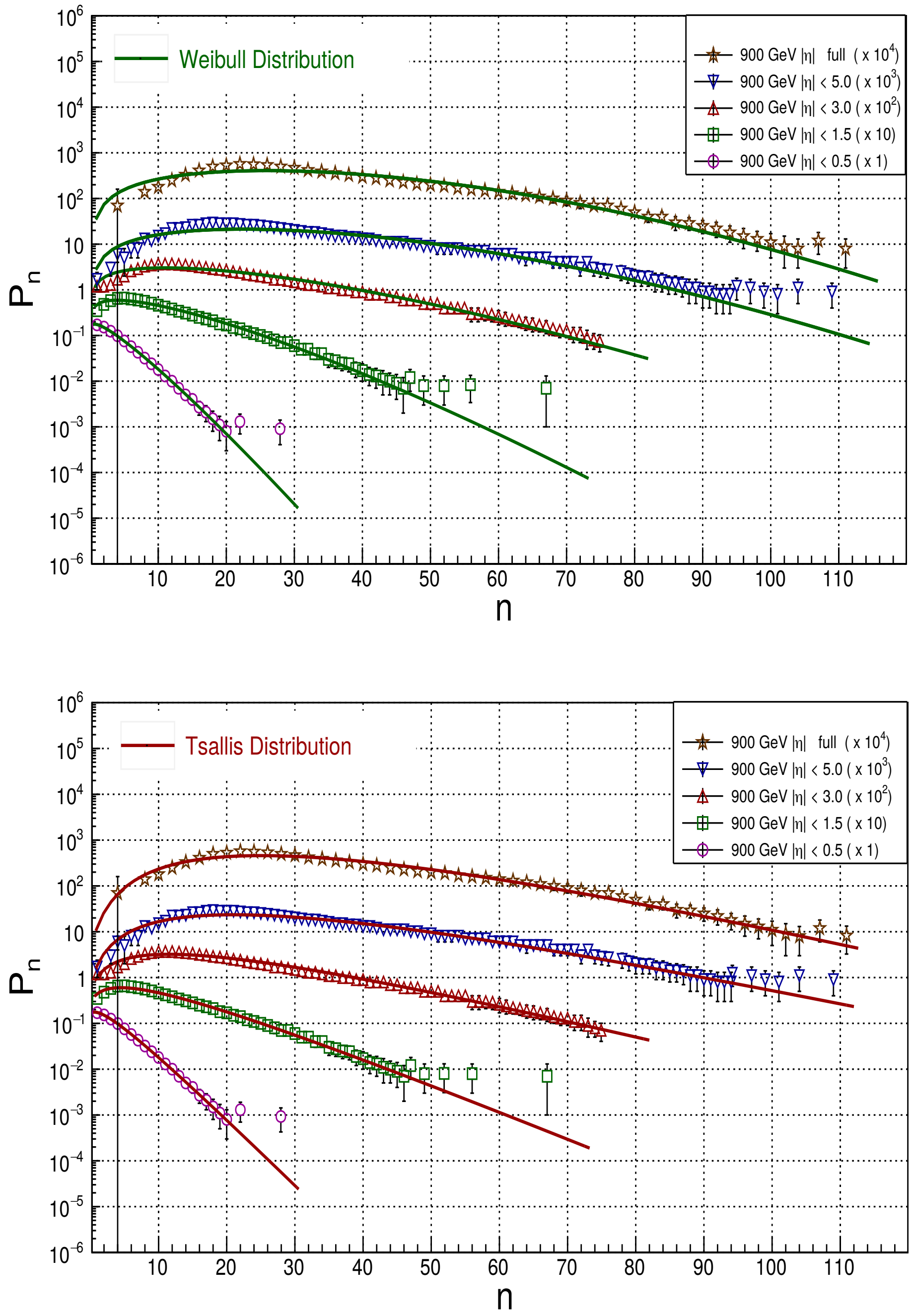

Figure 6.26: The charged particle multiplicity distributions in $\bar{p}p$ collisions by the UA5 experiment at 900 GeV and comparison of the experimental data with the Weibull and the Tsallis distributions.

Energy (GeV)	$\lvert\eta\rvert$	NBD		Gamma Distribution		Weibull Distribution		Tsallis Distribution	
		χ^2/ndf	p value	χ^2/ndf	p value	χ^2/ndf	p value	χ^2/ndf	p value
200	0.5	6.35/10	0.7847	9.05/10	0.5276	5.37/10	0.8651	6.35/8	0.6047
	1.5	11.40/29	0.9986	16.71/29	0.9666	16.61/29	0.9679	11.41/27	0.9963
	3.0	15.54/49	1.0000	11.26/49	1.0000	41.89/49	0.7543	19.78/47	0.9998
	5.0	62.52/55	0.2273	93.26/55	0.0010	69.38/55	0.0919	62.51/53	0.1745
	full	10.73/28	0.9987	9.04/28	0.9997	44.71/28	0.0236	10.72/26	0.9964
540	0.5	21.98/19	0.2853	26.04/19	0.1291	19.84/19	0.4043	29.15/17	0.0332
	1.5	13.41/26	0.9800	49.52/26	0.0036	24.77/26	0.532	13.41/24	0.9589
	3.0	33.86/28	0.2055	53.18/28	0.0028	119.50/28	0.0001	33.86/26	0.1386
	5.0	35.54/33	0.3495	77.15/33	0.0001	127.13/33	0.0001	39.51/31	0.1405
	full	46.41/49	0.5787	65.81/49	0.0547	164.99/49	0.0001	46.41/47	0.4969
900	0.5	5.58/19	0.9987	5.184/19	0.9993	6.49/19	0.9965	5.58/17	0.9938
	1.5	22.88/48	0.9992	15.66/48	1.0000	37.05/48	0.8742	22.88/46	0.9985
	3.0	41.06/72	0.9988	36.08/72	0.9999	77.52/72	0.3071	41.06/70	0.9977
	5.0	66.22/97	0.9929	58.25/97	0.9994	141.81/97	0.0021	63.09/93	0.9952
	full	76.43/49	0.0073	67.85/49	0.0385	162.01/49	0.0001	73.29/47	0.0084

Table 6.7: χ^2/ndf comparison and p values of different distributions at different energies and pseudorapidity intervals

Energy (GeV)	$\|\eta\|$	NBD		Gamma Distribution		Weibull Distribution		Tsallis Distribution	
		K	$< n >$	α	β	k	λ	K_{TS}	q
200	0.5	2.278 ± 0.258	2.663 ± 0.072	1.633 ± 0.096	0.540 ± 0.029	1.278 ± 0.039	3.171 ± 0.076	2.278 ± 0.257	1.310 ± 0.006
	1.5	2.313 ± 0.120	8.181 ± 0.135	1.863 ± 0.068	0.221 ± 0.009	1.420 ± 0.029	9.078 ± 0.147	2.314 ± 0.120	1.138 ± 0.025
	3.0	2.896 ± 0.138	15.441 ± 0.194	2.483 ± 0.103	0.158 ± 0.006	1.618 ± 0.033	16.740 ± 0.208	3.201 ± 0.038	1.021 ± 0.015
	5.0	3.497 ± 0.163	20.530 ± 0.253	3.112 ± 0.150	0.150 ± 0.007	1.843 ± 0.034	22.660 ± 0.271	3.497 ± 0.160	1.008 ± 0.002
	full	4.518 ± 0.234	21.301 ± 0.255	3.799 ± 0.171	0.177 ± 0.008	2.001 ± 0.043	23.410 ± 0.285	4.518 ± 0.230	1.002 ± 0.001
540	0.5	1.882 ± 0.089	3.067 ± 0.045	1.517 ± 0.043	0.441 ± 0.011	1.218 ± 0.018	3.587 ± 0.048	1.697 ± 0.045	1.428 ± 0.021
	1.5	1.995 ± 0.043	9.525 ± 0.083	1.631 ± 0.025	0.169 ± 0.003	1.371 ± 0.002	10.530 ± 0.046	1.995 ± 0.044	1.184 ± 0.019
	3.0	2.482 ± 0.042	18.86 ± 0.140	2.136 ± 0.032	0.113 ± 0.002	1.572 ± 0.013	20.920 ± 0.161	2.482 ± 0.043	1.057 ± 0.005
	5.0	3.116 ± 0.052	26.31 ± 0.171	2.728 ± 0.044	0.104 ± 0.007	1.804 ± 0.015	29.580 ± 0.205	3.115 ± 0.052	1.013 ± 0.004
	full	3.623 ± 0.064	28.31 ± 0.175	3.171 ± 0.051	0.120 ± 0.002	1.938 ± 0.017	31.940 ± 0.206	3.623 ± 0.063	1.009 ± 0.003
900	0.5	1.473 ± 0.100	3.555 ± 0.078	1.314 ± 0.059	0.331 ± 0.014	1.140 ± 0.026	4.075 ± 0.084	1.474 ± 0.100	1.504 ± 0.007
	1.5	1.787 ± 0.068	11.26 ± 0.167	1.622 ± 0.049	0.140 ± 0.005	1.292 ± 0.022	12.260 ± 0.183	1.787 ± 0.067	1.221 ± 0.079
	3.0	2.169 ± 0.071	22.37 ± 0.282	1.998 ± 0.058	0.088 ± 0.003	1.454 ± 0.022	24.460 ± 0.307	2.169 ± 0.071	1.098 ± 0.017
	5.0	2.88 ± 0.086	32.83 ± 0.396	2.616 ± 0.076	0.079 ± 0.003	1.749 ± 0.025	36.370 ± 0.424	2.886 ± 0.086	1.024 ± 0.002
	full	3.548 ± 0.113	35.55 ± 0.370	3.261 ± 0.096	0.091 ± 0.004	1.849 ± 0.030	39.420 ± 0.415	3.562 ± 0.112	1.011 ± 0.003

Table 6.8: Parameters of the NBD, the Gamma, the Weibull and the Tsallis distributions for charged hadron multiplicity spectra for all pseudorapidity intervals at $\sqrt{s}$ = 200, 540 and 900 GeV for $\overline{p}p$ collisions.

6.2.2.2 Results and Discussion

For antiproton-proton collisions, the probability distribution functions calculated from the Tsallis, Weibull, Gamma and NBD models have been implemented on the UA5 experimental data. The χ^2/ndf values have been compared for all the four models and are shown in the table 6.7. The parameters of the distributions fitted to the data are shown in table 6.8. It has been found that all these distributions provide comparative explanation to experimental data of particle production at 200 GeV. Weibull distribution is good to explain the data only at smaller pseudorapidity intervals ($|\eta| < 0.5$ and 1.0) but fails to provide appropriate justification at higher pseudorapidity intervals at $\sqrt{s} = 540$ and at full phase space at $\sqrt{s} = 900$ GeV. At 200 and 540 GeV the Gamma distribution describes the experimental data at all pseudorapidity intervals except at $|\eta| < 5$ whereas for 900 GeV it reproduces the multiplicity data well for restricted pseudorapidity intervals as well as for full phase space. The failure of Gamma distribution at 200 and 540 GeV for higher pseudorapidity interval ($|\eta| < 5$) is attributed to smaller statistics. The Tsallis gas model describes the data at all pseudorapidity intervals of every energy and successfully reproduces the experimental data with p values with a confidence level $CL > 0.1$ %. The shape parameter, β, of the Gamma distribution shows very small decrease in the values with increasing energy as well as with pseudorapidity intervals. This behaviour is expected as the shape parameter is related to the dimension, D which decreases with increase in energy as described in previous sections. α, the scale parameter does not vary significantly with the increase in energy and increase in pseudorapidity intervals at a given energy. It is a numerical parameter which affects only the shape of a distribution. The insignificant change in the values suggests that distribution remains the same with increasing centre of mass energy and pseudorapidity intervals

For the Weibull model scale parameter λ, which determines the width of distribution and is related to the mean multiplicity, increases with the energy for particular set of rapidity interval and also increases with increase in rapidity interval at a given energy, as expected. The shape parameter, k does not vary much with rise in energy at given rapidity intervals as the dynamics of fragmentation process in *h*-*h* interactions remains same and does not change much with the energy and pseudorapidity intervals. Figure 6.27 exhibits the variation of parameters λ of the Weibull fit on the centre of mass energies, $\sqrt{s}$ for full phase space data. The variation trends of λ with the energy can be described using empirical law with $\lambda = a + b(ln\sqrt{s}) + c\ (ln\sqrt{s})^2$

The fit parameters of the relation at full phase space are $a = 112.105 \pm 24.596$, $b = -38.069 \pm 8.341$ and $c = 4.026 \pm 0.702$

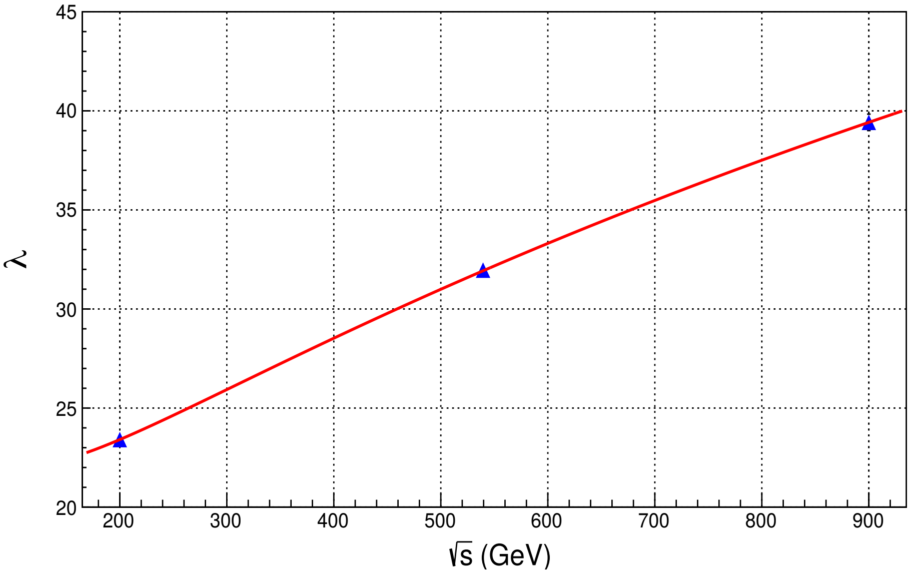

Figure 6.27: Dependence of the Weibull parameter λ on energy at full $|\eta|$.

The Tsallis model provides the comparative description for experimental data. The entropic index, q in each case comes out to be more than unity following the non-extensive nature of entropy in the Tsallis statistics. The increase in q values is very small with increasing energy at given rapidity interval but decrease with rise in rapidity interval at given centre of mass energy, $\sqrt{s}$ implementing the predominance of non-extensive nature of entropy at higher energies. The similar kind of dependence of entropic index on energy was observed in the study of pp collision data indicating the same and uniform behaviour of entropic index in h-h interactions. Figure 6.28 shows the increase in q values with energy $\sqrt{s}$ for full phase space multiplicity at various energies. The dependence of q values on the centre of mass energy can be described using the power law inspired from the observation that single particle energy distribution obeys a power law behaviour. The parameters of power law, $q = A_0\ \sqrt{s}^{B_0}$ defining the dependence of q on the energy at full phase space are, $A_0 = 0.968 \pm 0.010$ and $B_0 = 0.006 \pm 0.001$

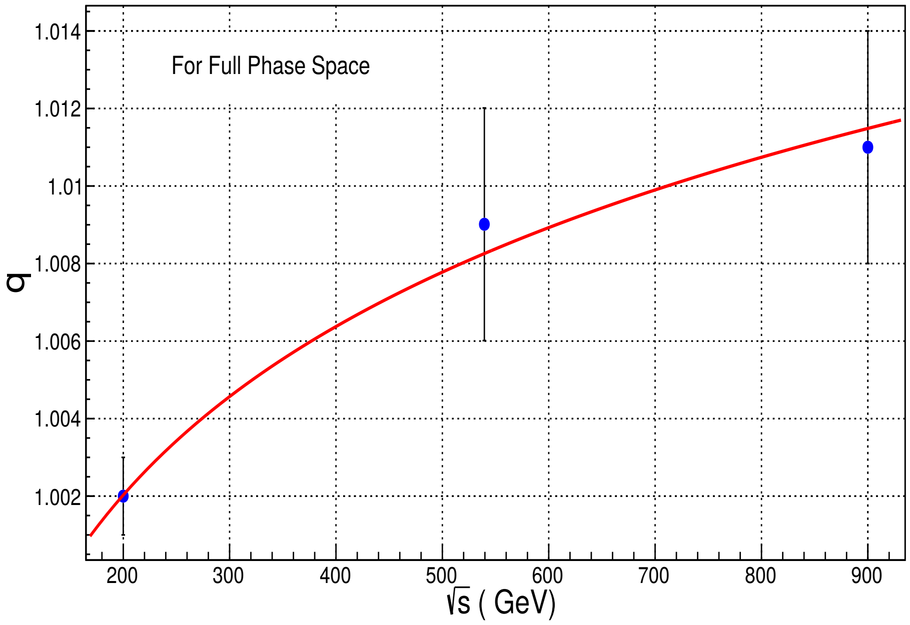

Figure 6.28: The dependence of non-extensive parameter q on the centre of mass energy for full phase space multiplicity. The solid line corresponds to the power law, $q = A_0\ \sqrt{s}^{B_0}$

6.2.2.3 Moments

Detailed analysis of C_q moments has been done using the Tsallis gas model in order to understand the correlation of the particles produced in the final state. The dependence of C_q on the $|\eta|$ at specific energy and dependence of C_q on energy $\sqrt{s}$ at particular rapidity interval for $\bar{p}p$ data are shown in figures 6.29 - 6.31. The first five moments for the experimental data and the values obtained from the Tsallis model are shown in table 6.9. It has been found that at each set of pseudorapidity intervals the value of the moments C_q increases with increase in centre of mass energy, $\sqrt{s}$, but it decreases with increase in the pseudorapidity interval at particular energy. These trends are similar to the one observed in the experiments and are shown in the figures from 6.29 to 6.31. The behaviour of the moments from the Tsallis model clearly shows the correlation between the particles and violation of the KNO scaling at higher energies.

Energy (GeV)	$\|\eta\|$	Experimental values (UA5)				Tsallis Model			
		C_2	C_3	C_4	C_5	C_2	C_3	C_4	C_5
200	0.5	1.90 ± 0.45	4.80 ± 0.40	15.00 ± 1.41	52.00 ± 9.43	1.52 ± 0.01	3.06 ± 0.14	11.86 ± 0.64	44.26 ± 3.09
	1.5	1.56 ± 0.03	3.16 ±0.14	7.70 ± 0.61	22.00 ± 5.00	1.50 ± 0.03	3.00 ± 0.17	7.39 ± 0.83	21.48 ± 4.17
	3.0	1.40 ± 0.03	2.46 ± 0.09	5.10 ± 0.35	12.00 ± 1.41	1.36 ± 0.07	2.30 ± 0.25	4.60 ± 0.67	10.35 ± 1.55
	5.0	1.29 ± 0.03	2.00 ± 0.08	3.80 ± 0.31	7.20 ± 0.85	1.30 ± 0.04	2.03 ± 0.22	3.63 ± 0.53	7.14 ± 1.58
540	0.5	1.93 ± 0.02	5.20 ± 0.20	18.00 ± 1.00	80.00 ± 10.00	1.58 ± 0.01	3.48 ± 0.03	15.87 ± 0.05	69.05 ± 0.10
	1.5	1.62 ± 0.01	3.55 ± 0.08	9.90 ± 0.05	33.00 ± 3.00	1.55 ± 0.02	3.28 ± 0.06	8.69 ± 0.22	27.72 ± 1.05
	3.0	1.46 ± 0.01	2.79 ± 0.05	6.40 ± 0.20	17.00 ± 1.00	1.45 ± 0.01	2.73 ± 0.03	6.31 ± 0.12	17.12 ± 0.53
	5.0	1.35 ± 0.01	2.28 ± 0.03	4.60 ± 0.10	10.30 ± 0.40	1.35 ± 0.01	2.28 ± 0.06	4.59 ± 0.21	10.57 ± 0.81
900	0.5	1.94 ± 0.04	5.40 ± 0.36	19.00 ± 1.41	80.00 ± 14.14	1.64 ± 0.01	3.81 ± 0.08	17.47 ± 0.41	72.41 ± 2.93
	1.5	1.65 ± 0.03	3.70 ± 0.14	10.50 ± 0.11	35.00 ± 5.83	1.59 ± 0.02	3.51 ± 0.11	9.64 ± 0.70	31.81 ± 3.91
	3.0	1.50 ± 0.03	2.93 ± 0.11	7.00 ± 0.58	19.00 ± 2.23	1.47 ± 0.02	2.83 ± 0.06	6.52 ± 0.24	17.21 ± 0.23
	5.0	1.36 ± 0.03	2.33 ± 0.10	4.70 ± 0.45	10.70 ± 0.12	1.36 ± 0.05	2.34 ± 0.20	4.77 ± 0.81	11.04 ± 2.21

Table 6.9: C_q moments calculated from the Tsallis model and comparison with the experimental values for $\overline{p}p$ collisions.

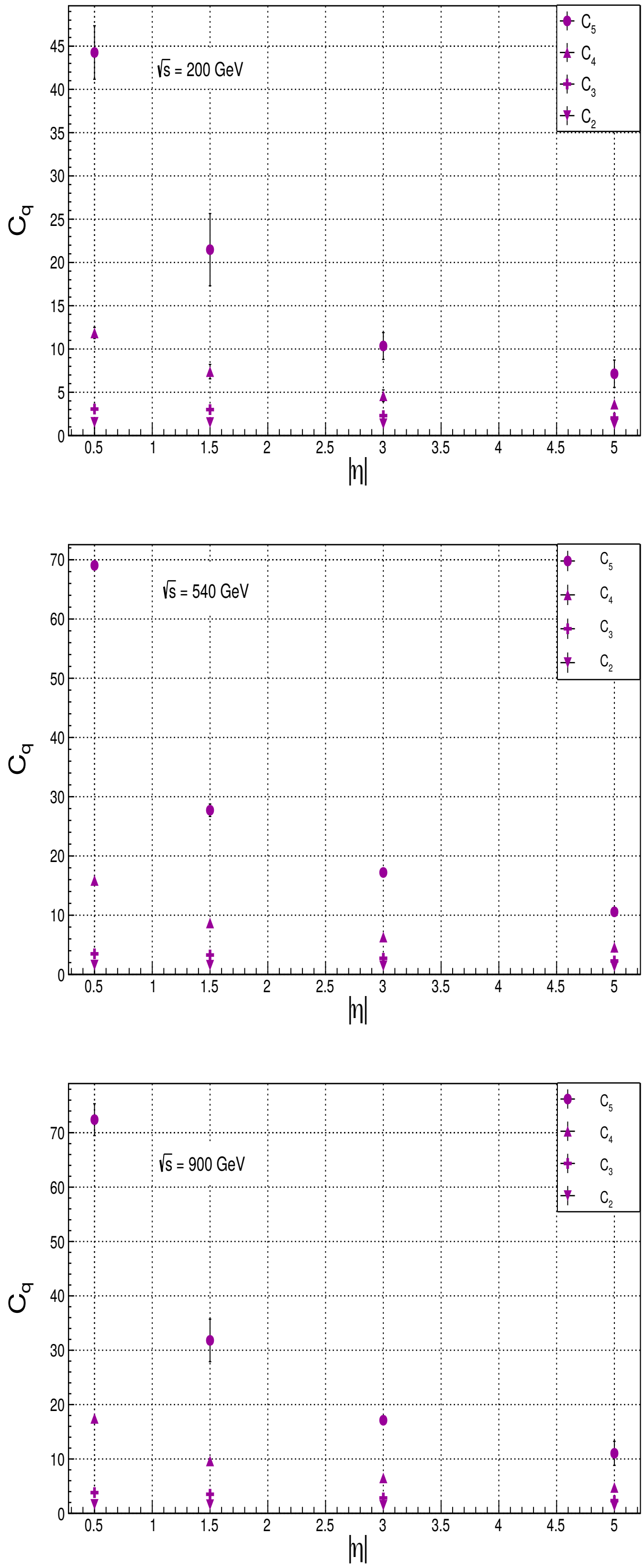

Figure 6.29: C_q moments obtained from the Tsallis model and its dependence on pseudorapidity intervals $|\eta|$ at $\sqrt{s}$ = 200, 540 and 900 GeV.

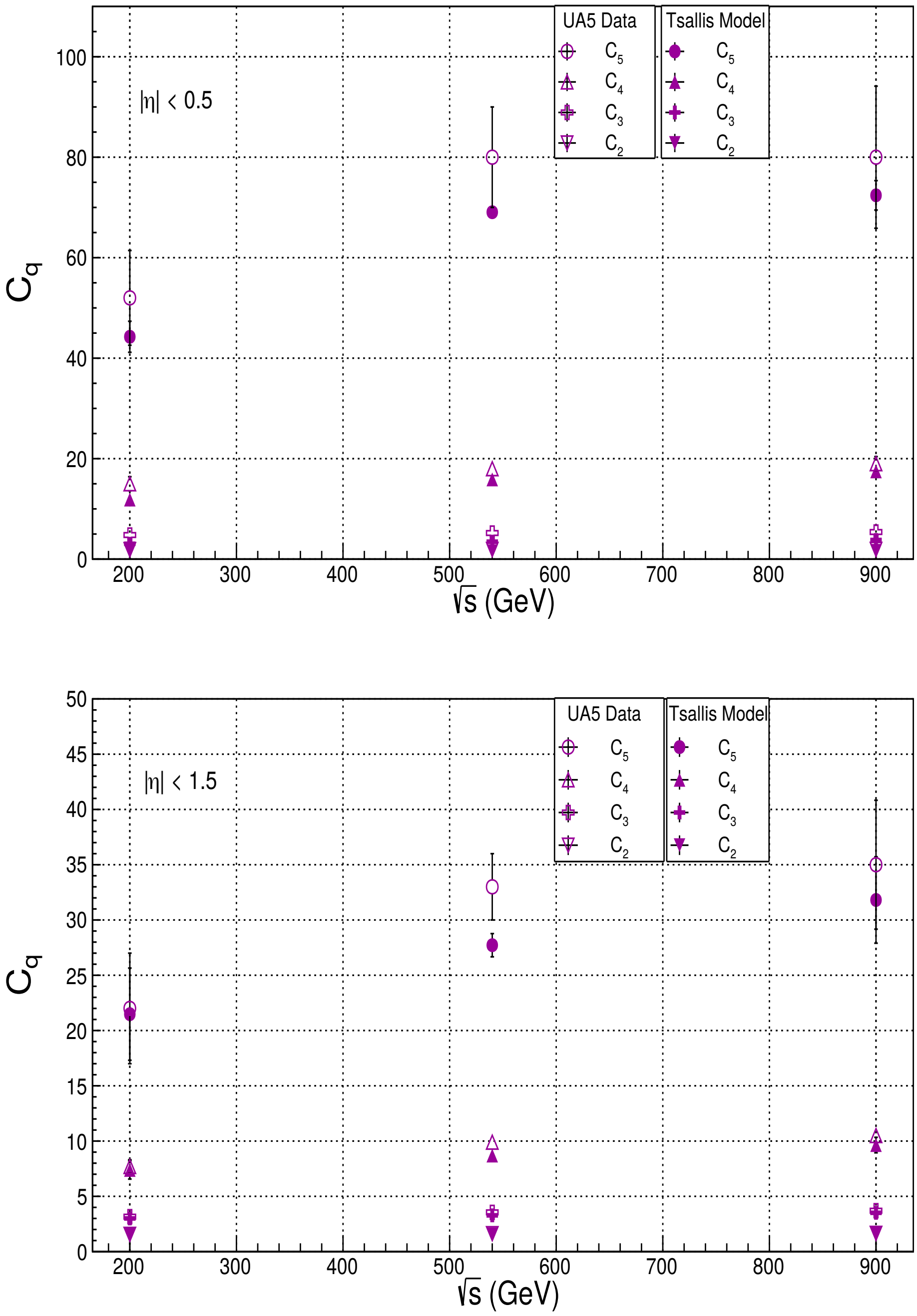

Figure 6.30: The variation of C_q moments with the centre of mass energy at pseudorapidity intervals $|\eta| < 0.5$ and $|\eta| < 1.5$ and comparison of the moments calculated from the Tsallis model with the data.

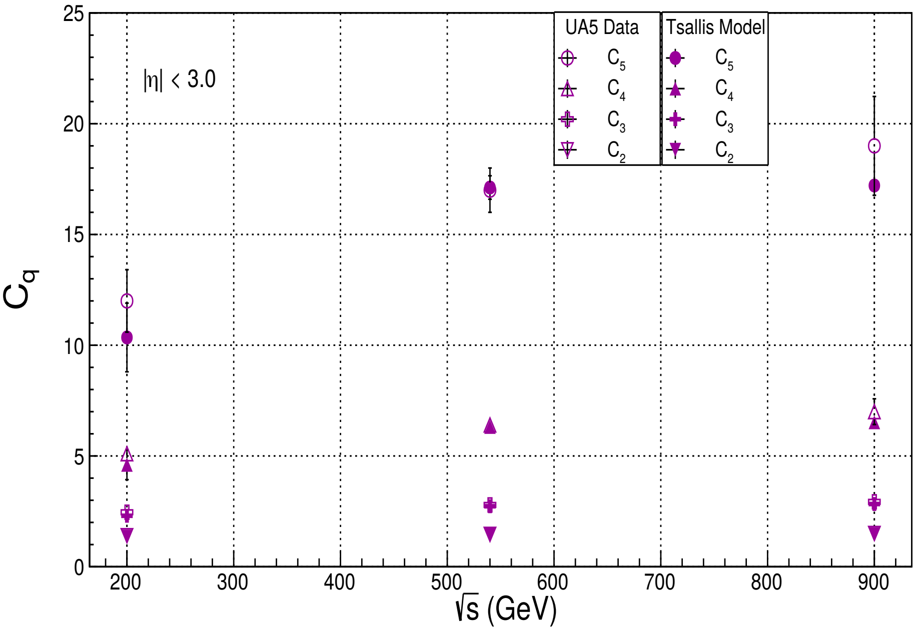

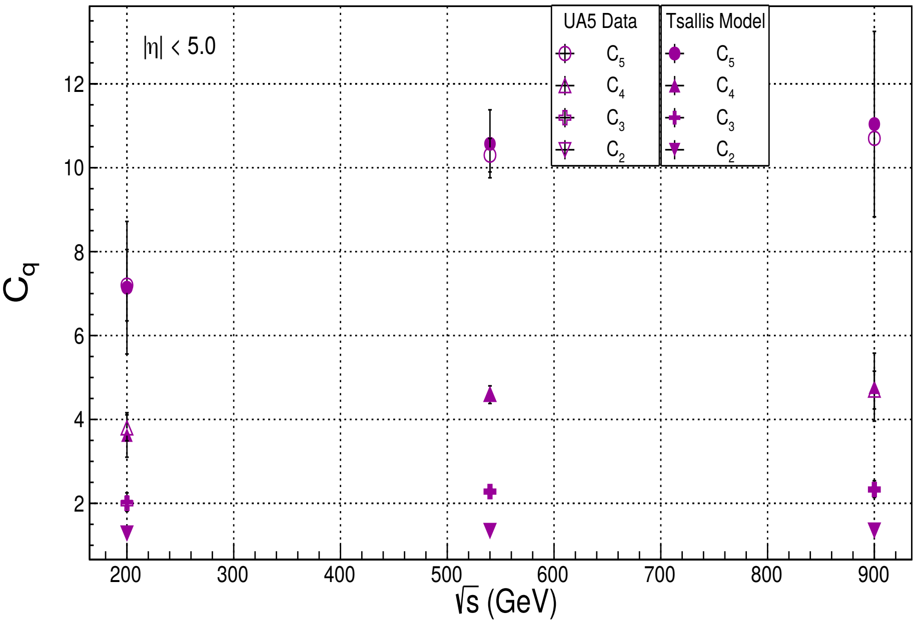

Figure 6.31: The variation of C_q moments with the centre of mass energy at pseudorapidity intervals $|\eta| < 3.0$ and $|\eta| < 5.0$ and comparison of the moments calculated from the Tsallis model with the data

6.2.2.4 Average Multiplicity

The average charged multiplicity values for full phase space are obtained from the Tsallis model and compared with the experimental values for antiproton-proton analysis from the UA5 experiment. The method of calculations is the same as in the case of *pp* collisions. Both the values are listed in the table 6.10 and found to be in good agreement as shown in figure 6.32. This clearly shows the success of the Tsallis model at these energies.

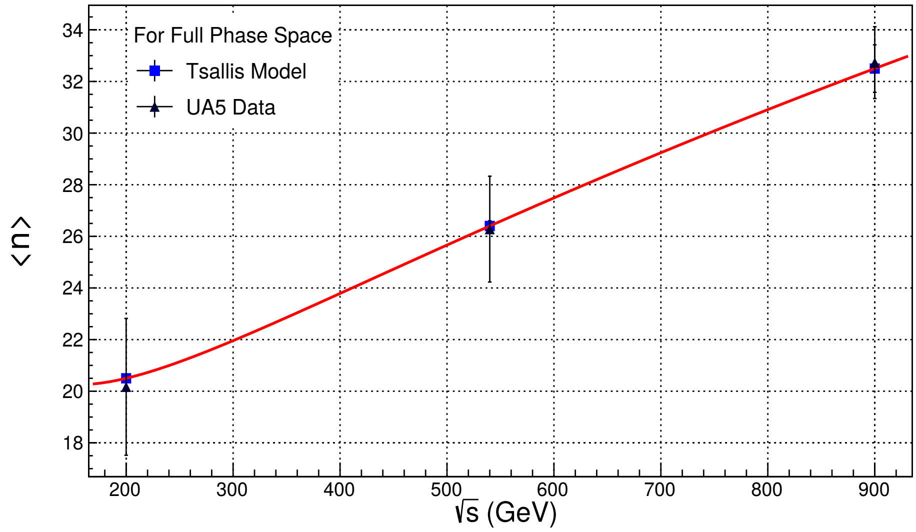

Figure 6.32: Dependence of average multiplicity $< n >$ on the centre of mass energy, $\sqrt{s}$ and comparison with the experimental data. The solid line corresponds to the equation (6.5)

$$For\ \ Data: \qquad < n > = \ 122.01 - 40.33(ln\sqrt{s}) + 3.99(ln\sqrt{s})^2 \tag{6.4}$$

$$For\ \ Tsallis\ \ Model: \ < n > = \ 131.10 - 43.74(ln\sqrt{s}) + 4.30(ln\sqrt{s})^2 \tag{6.5}$$

Energy (GeV)	Average Charged Multiplicity $< n >$	
	UA5 Experiment	Tsallis Model
200	20.17 ± 2.65	20.50 ± 0.14
540	26.28 ± 2.05	26.40 ± 0.20
900	32.73 ± 1.39	32.51 ± 0.92

Table 6.10: Average multiplicity $< n >$ at full phase space at $\sqrt{s} = 200$, 540 and 900 GeV

6.3 Analysis of Leptonic collisions

Multiparticle production has been studied in large variety of processes such as leptonic, hadronic or heavy ion interactions. Out of all the processes, the leptonic interactions provide clear framework for this dedicated study. In leptonic interactions such as e^+e^- collisions, large number of particles are produced, including hadrons [22, 23]. The best advantage of such collisions is that all of the available centre of mass energy is utilized in the particle production. Electrons and positrons are the point like particles which interact via electroweak interaction. The electron-positron pair annihilates to produce a photon or Z^0 boson or a pair of W boson, $W^{\pm}$, via annihilation process, which then decay instantly to form quark-antiquark pair, which subsequently fragment to produce the hadrons; $e^+e^- \rightarrow (Z^0/\gamma)^* \rightarrow W^{\pm} \rightarrow q\bar{q}$. The analyses on multiparticle production in the leptonic collisions have been done for energies ranging from 14 GeV to 206 GeV [24,25]. Multiplicity data from TASSO detector at DESY [26,27], OPAL and L3 detectors of the LEP collider [28] have been used for this study. At lower center of mass energies, $\sqrt{s} = 14$, 22, 34.8 and 43.6 GeV, data in restricted pseudorapidity intervals, $|\eta| < 0.5$, 1.0, 1.5 and 2.0 as well as in full phase space from TASSO experiment [29] have been analysed. In this section, results are presented by using data from the OPAL and the L3 experiments only with $\sqrt{s} \geq 91$ GeV. Details of the leptonic analysis at lower energies, $\sqrt{s} < 91$ GeV, data used, number of events and interpretation of the results can be found at references [24,25] published by us.

6.3.1 Experimental Data

The experimental data used in the analysis of multiplicity distributions of charged particles at different energies are taken from the two experiments, OPAL and L3 at the Large Electron-Positron Collider, LEP at CERN [30]. We have included the results for the data at $\sqrt{s} \geq 91$ GeV from the OPAL and the L3 experiments only in the present study [31]. Data from these two detectors have significant number of events and preferred over the ALEPH and DELPHI detector of LEP, which have lower statistics as compared to the former two experiments. The data have been analysed for energies ranging from $\sqrt{s} =$ 91 GeV to 206 GeV [32–36]. Appropriate selection cuts were implemented on the sample data to collect the final events. The number of hadronic events along with the luminosity at these energies are given in table 6.11.

Experiment	Energy (GeV)	Final selected events	*Luminosity* (pb^{-1})	References
OPAL	91.2	82941	3.5	[32]
	133	766	2.5	[33]
	161	1336	10.0	[34]
	172	228	10.4	[35]
	183	1098	57.2	[35]
	189	3277	186.3	[35]
L3	130.1	556	6.1	[36]
	136.1	414	5.9	[36]
	172.3	325	10.2	[36]
	182.8	1500	55.3	[36]
	188.6	4479	176.8	[36]
	194.4	2403	112.2	[36]
	200.2	2456	117.0	[36]
	206.2	4146	207.6	[36]

Table 6.11: Data samples of e^+e^- collisions used for the analysis at various energies from the OPAL and the L3 experiments.

6.3.2 Multiplicity Analysis

To study the behaviour of multiplicities, the distributions from the NBD, the Weibull, Gamma and the Tsallis models have been implemented. The two component approach to obtain the multiplicity distribution at these energies has also been implemented in each case. Results are compared with the experimental data as shown in figures 6.33 - 6.40. The χ^2/ndf values have been compared for all the four models and are shown in table 6.12. The parameters of the fits corresponding to the figures 6.33 - 6.36 are shown in the table 6.14. To study the data at higher energies where the shoulder structure needs to be considered we have extended the analyses using two component approach for each model. The values of α, which represent the two jet fraction have been taken from the Durham jet finder algorithm. The χ^2/ndf values have been compared for the two component approach implemented on all these models (modified distributions) and the values are shown in table 6.13 along with the p values and the references. The results of MDs using two component approach are shown in figures 6.37 - 6.40 and the parameters of the Modified Weibull and the Modified Tsallis distributions are listed in table 6.15.

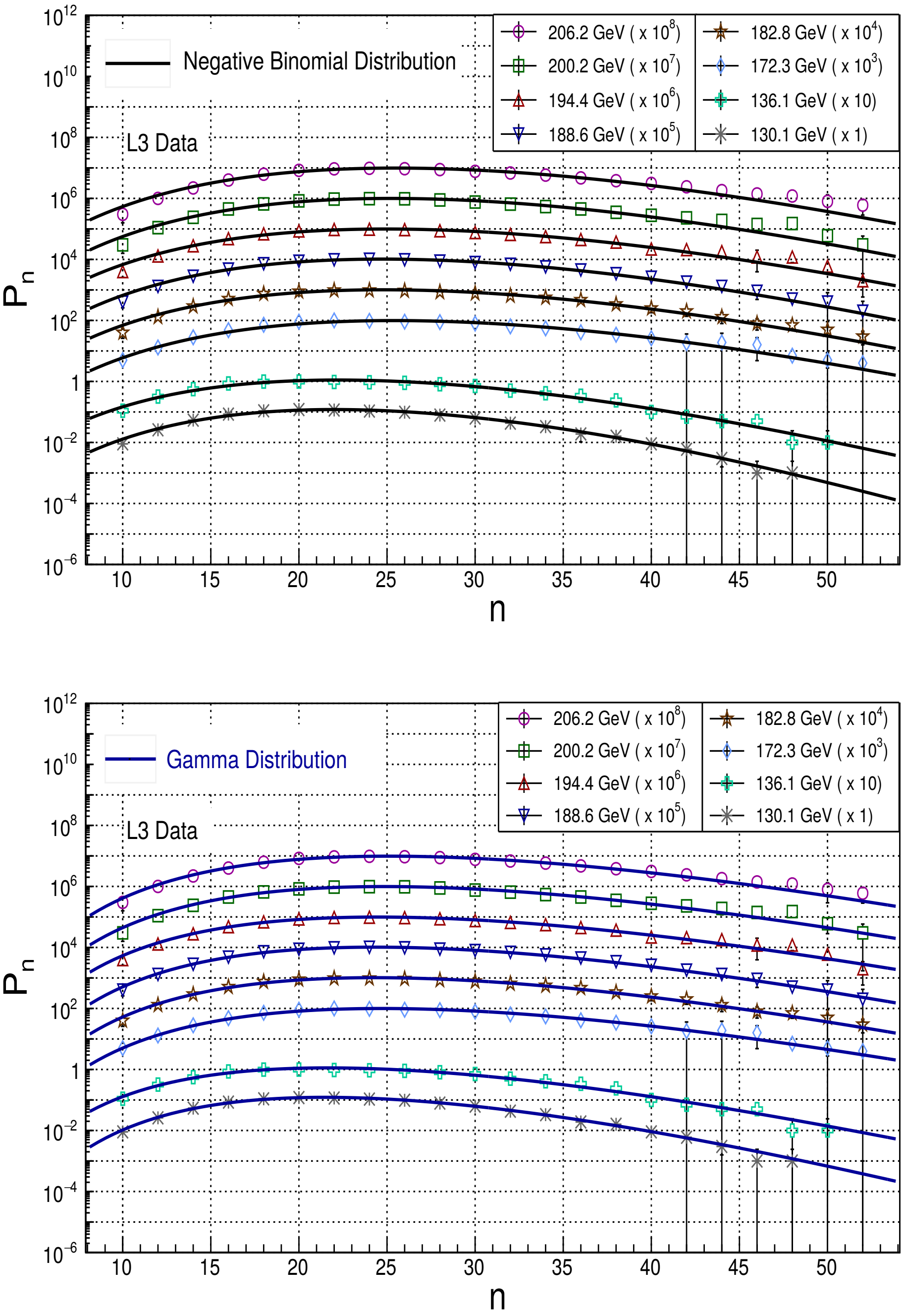

Figure 6.33: The charged particle multiplicity distributions in e^+e^- collisions by the L3 experiment and comparison of the experimental data with the NBD and the Gamma distributions.

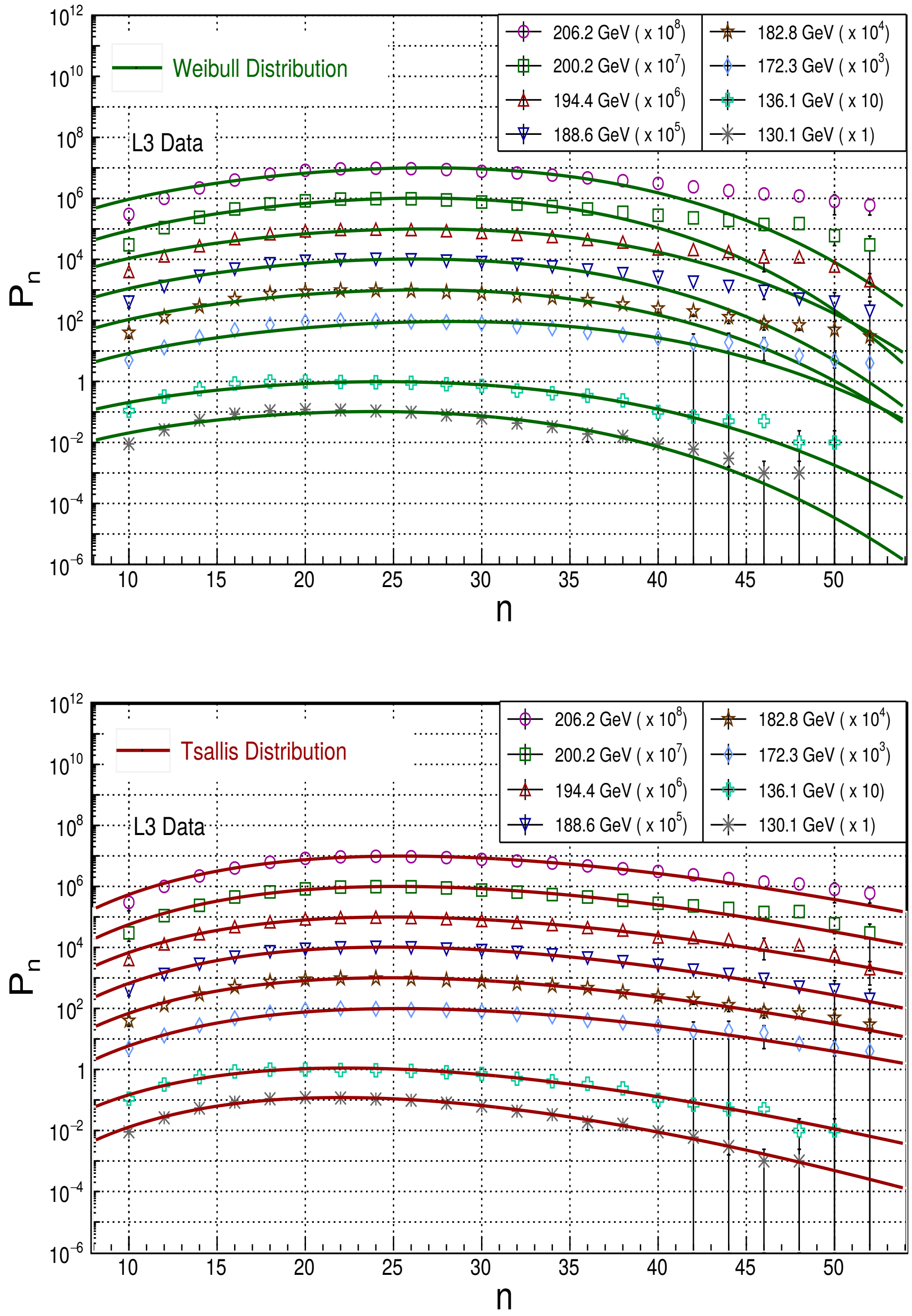

Figure 6.34: The charged particle multiplicity distributions in e^+e^- collisions by the L3 experiment and comparison of the experimental data with the Weibull and the Tsallis distributions.

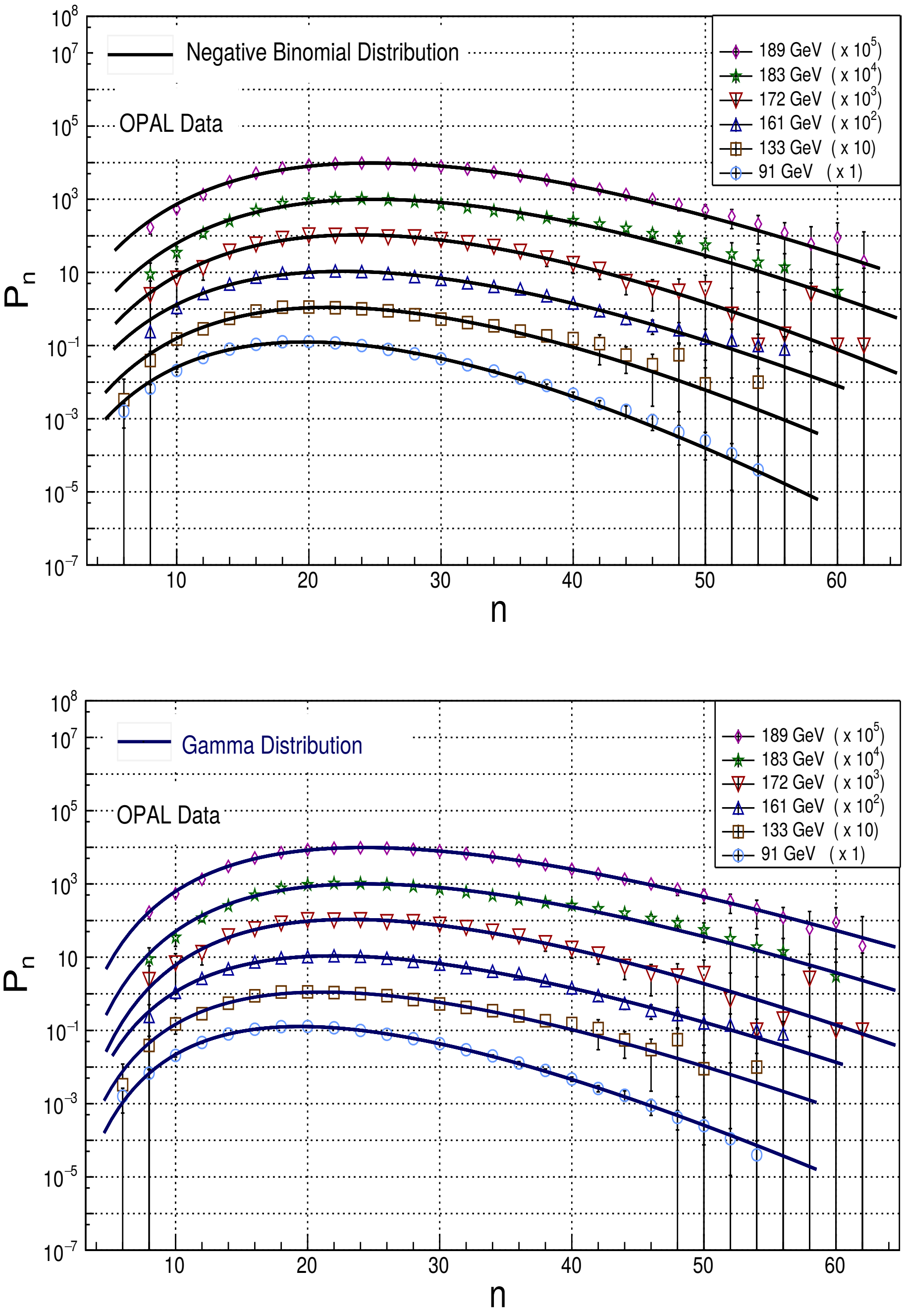

Figure 6.35: The charged particle multiplicity distributions in e^+e^- collisions by the OPAL experiment and comparison of the experimental data with the NBD and the Gamma distributions.

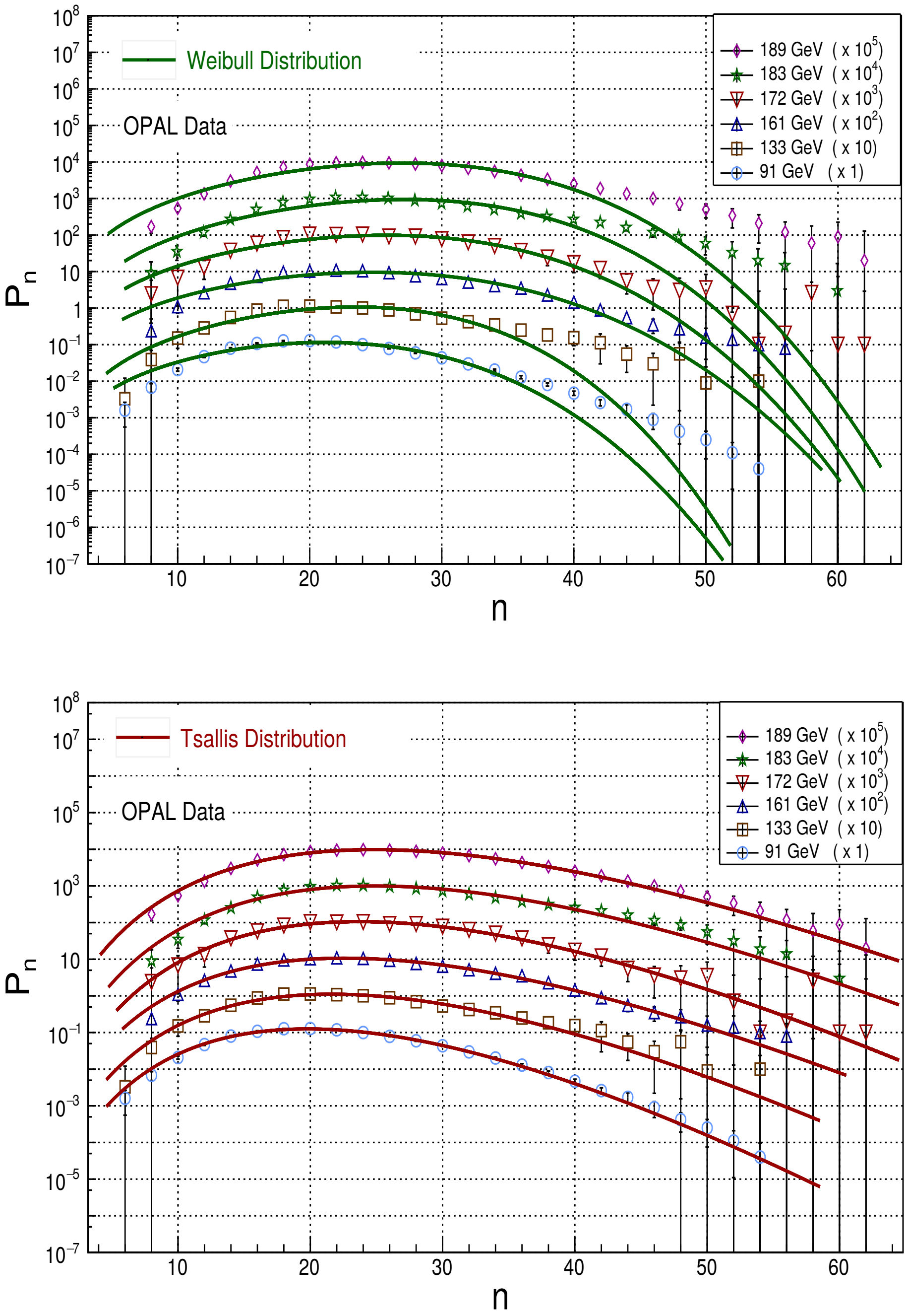

Figure 6.36: The charged particle multiplicity distributions in e^+e^- collisions by the OPAL experiment and comparison of the experimental data with the Weibull and the Tsallis distributions.

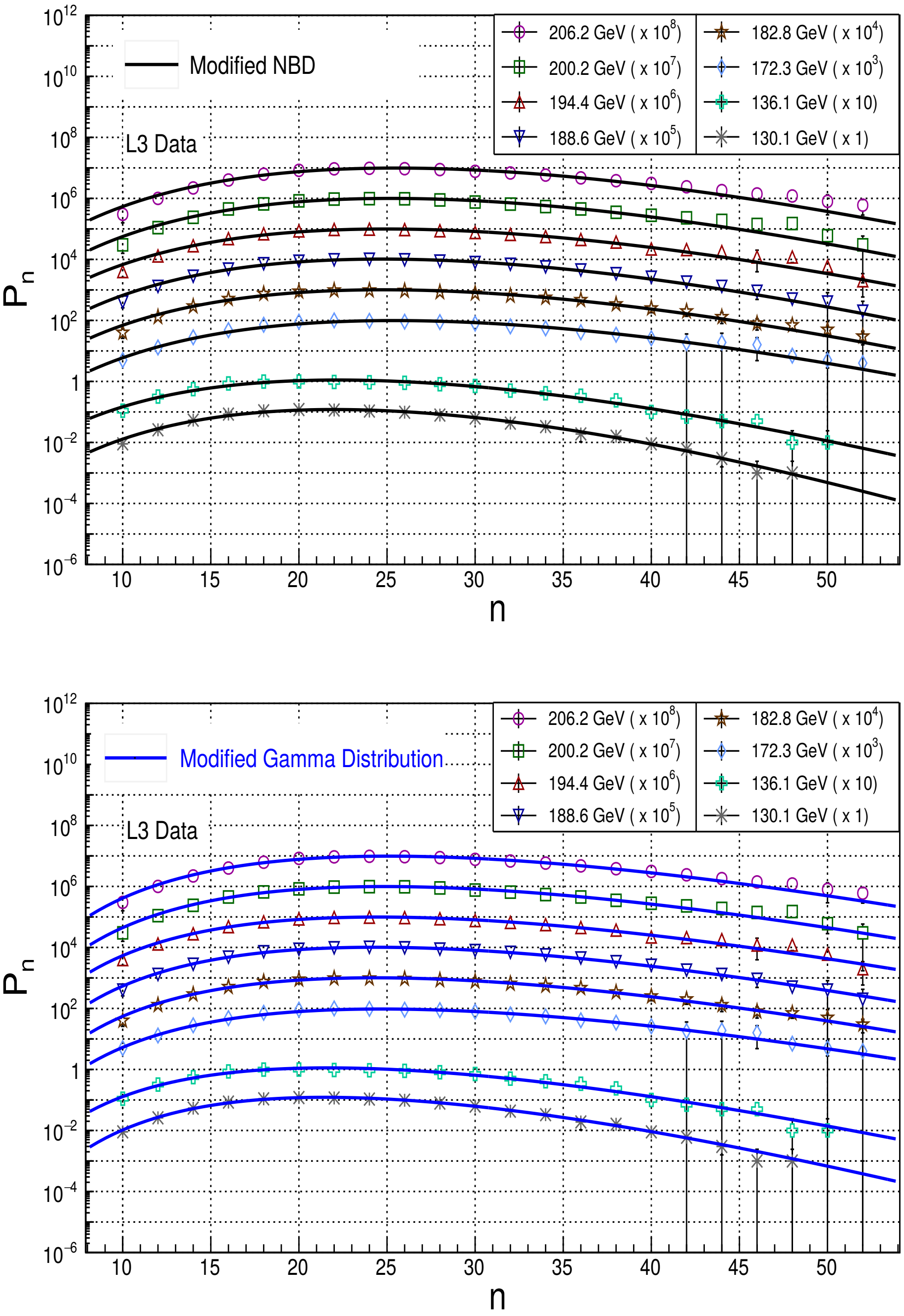

Figure 6.37: The charged particle multiplicity distributions in e^+e^- collisions by the L3 experiment and comparison of the experimental data with the Modified NBD and the Modified Gamma distributions.

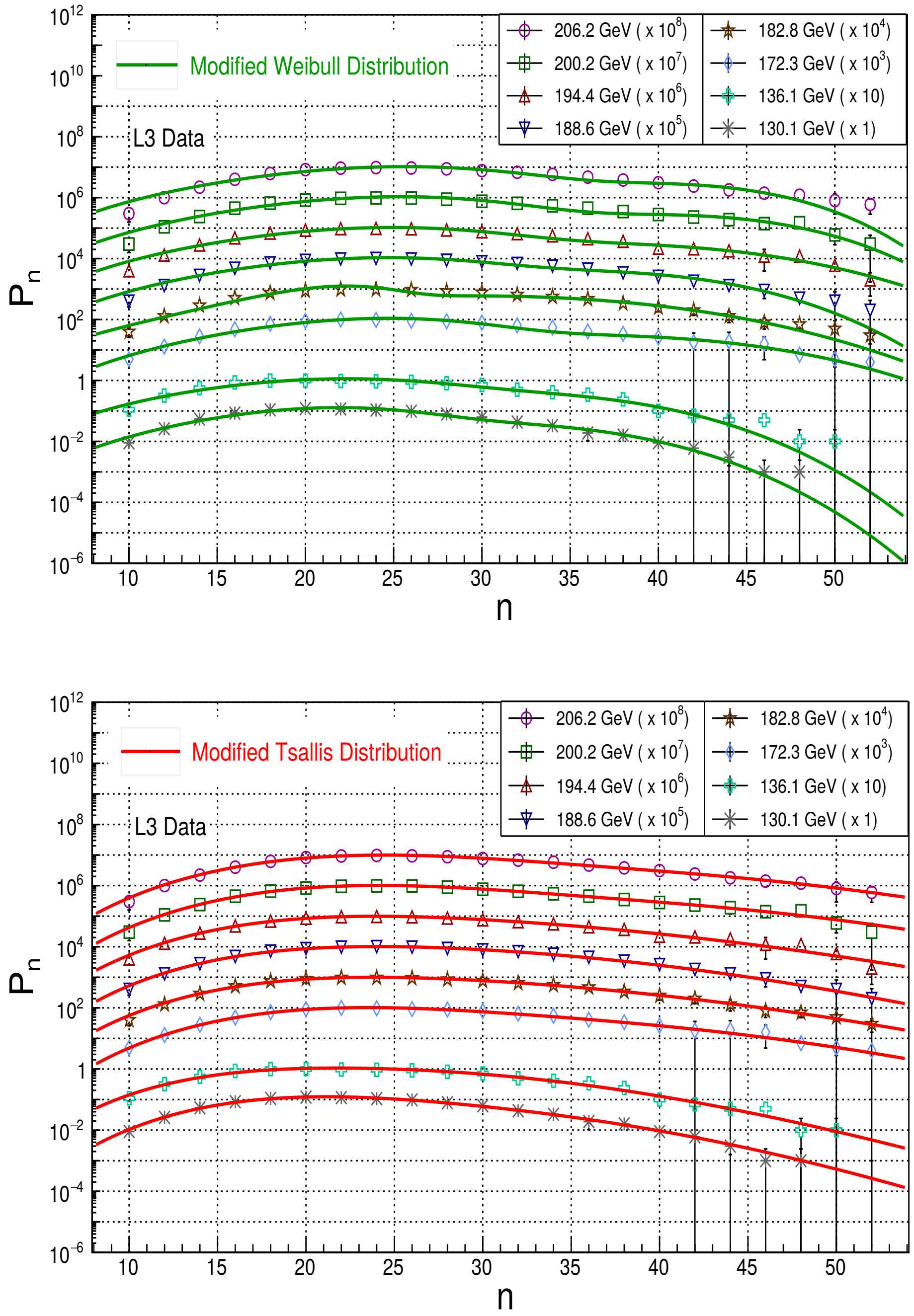

Figure 6.38: The charged particle multiplicity distributions in e^+e^- collisions by the L3 experiment and comparison of the experimental data with the Modified Weibull and the Modified Tsallis distributions.

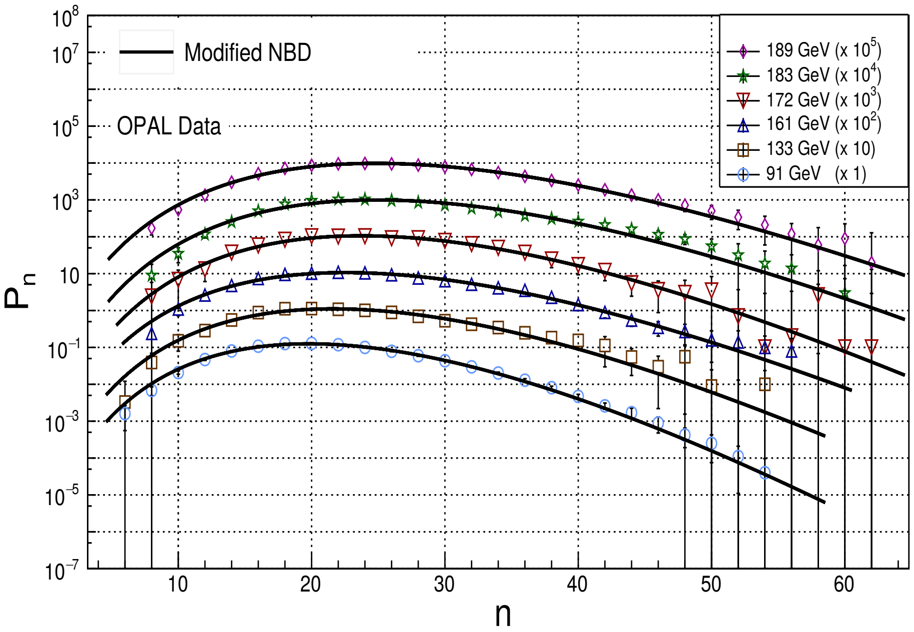

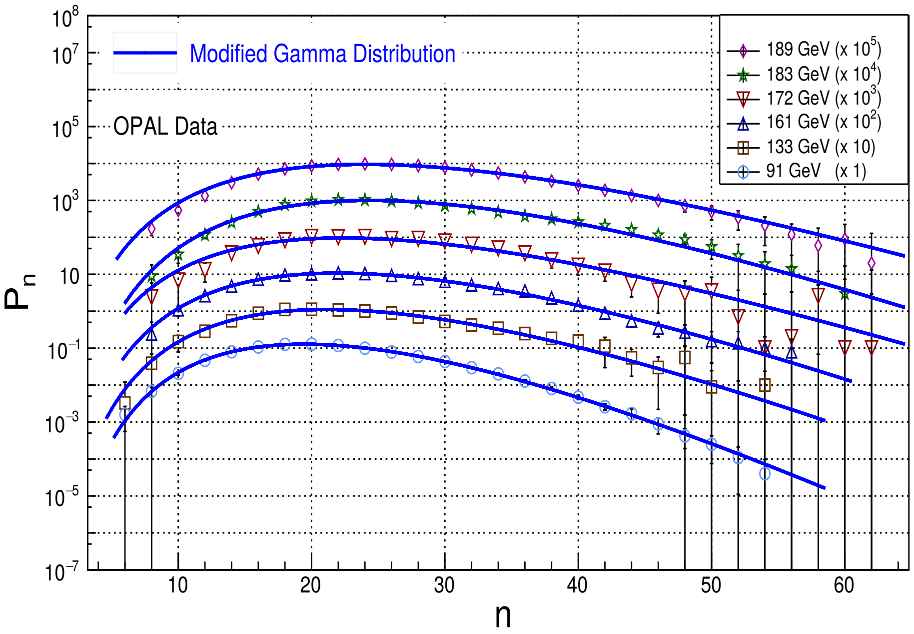

Figure 6.39: The charged particle multiplicity distributions in e^+e^- collisions by the OPAL experiment and the comparison of experimental data with the Modified NBD and the Modified Gamma distributions

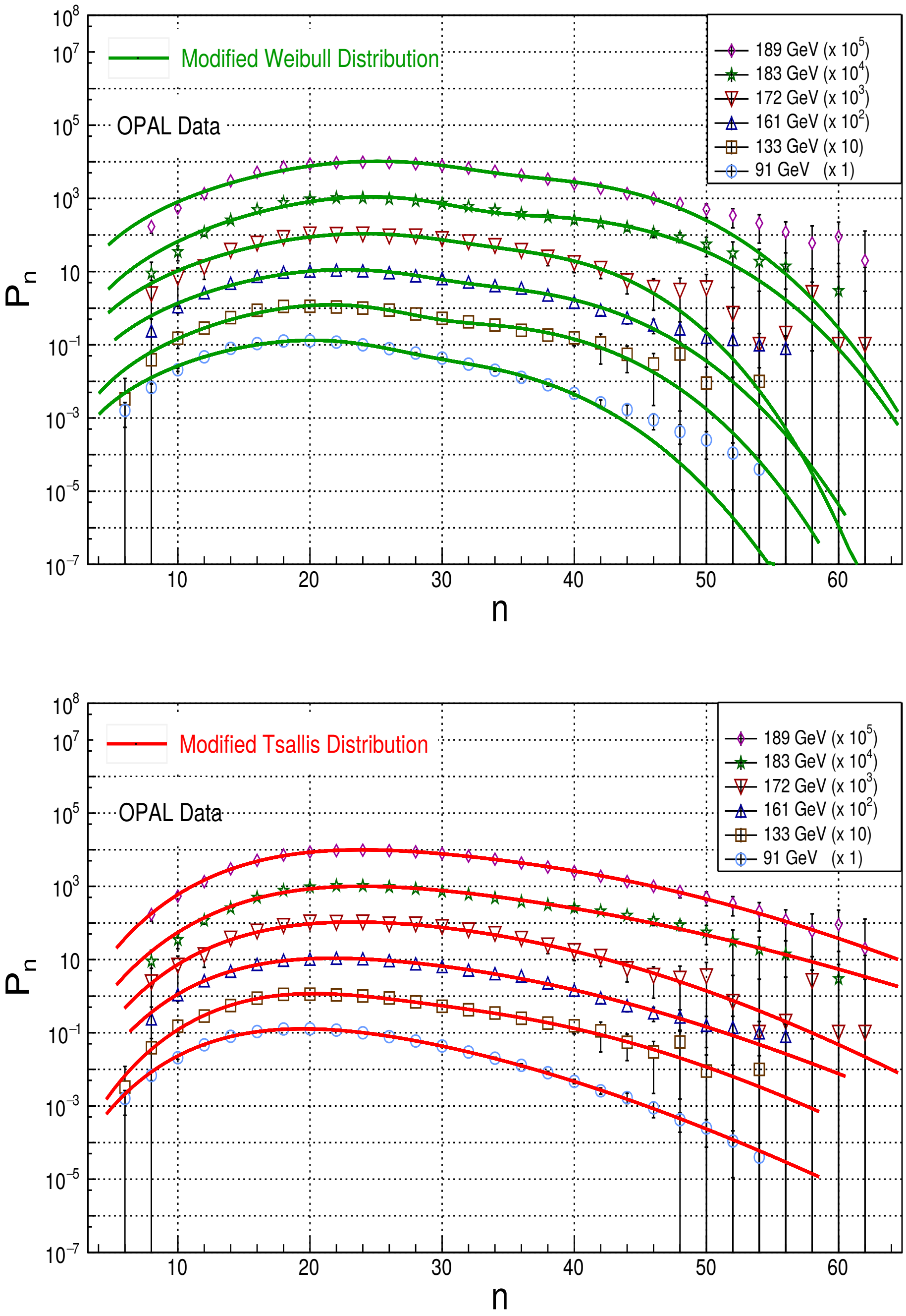

Figure 6.40: The charged particle multiplicity distributions in e^+e^- collisions by the OPAL experiment and comparison of the experimental data with the Modified Weibull and the Modified Tsallis distributions.

Experiment	Energy	NBD Distribution		Gamma Distribution		Weibull Distribution		Tsallis Distribution	
	(GeV)	χ^2/ndf	p value	χ^2/ndf	p value	χ^2/ndf	p value	χ^2/ndf	p value
OPAL	91	33.15/22	0.0598	4.16/22	1.0000	434.91/22	0.0001	33.13/20	0.0329
	133	12.72/22	0.1407	5.92/22	0.9997	66.88/22	0.0001	12.67/20	0.8899
	161	5.81/22	0.9988	3.14/22	1.0000	48.11/22	0.0011	5.81/20	0.9991
	172	3.90/25	1.0000	3.69/25	1.0000	17.87/25	0.8479	3.94/23	1.0000
	183	35.06/25	0.0871	19.28/25	0.7835	159.61/25	0.0001	35.13/23	0.0508
	189	15.94/25	0.9106	3.12/25	1.0000	183.63/25	0.0001	15.88/23	0.8595
L3	130.1	6.42/19	0.9967	2.86/19	1.0000	52.53/19	0.0001	6.42/17	0.9899
	136.1	19.26/19	0.4403	18.21/19	0.5085	41.64/19	0.0002	19.26/17	0.3138
	172.3	8.76/19	0.9773	3.34/19	1.0000	64.28/19	0.0001	8.78/17	0.9471
	182.8	16.98/19	0.5912	7.27/19	0.9926	98.71/19	0.0001	16.98/17	0.4557
	188.6	17.28/19	0.5709	5.47/19	0.9989	157.54/19	0.0001	17.28/17	0.4356
	194.4	19.19/19	0.4471	9.29/19	0.9683	108.70/19	0.0001	19.19/17	0.3177
	200.2	27.14/19	0.1014	13.64/19	0.8043	127.53/19	0.0001	27.14/17	0.0562
	206.2	32.42/19	0.0280	15.35/19	0.7001	168.91/19	0.0001	32.41/17	0.0134

Table 6.12: χ^2/ndf comparison and p values for different energies using different distributions in e^+e^- interactions.

Experiment	Energy (GeV)	α	Refer. for α	Mod. NBD Distribution		Mod. Gamma Distribution		Mod. Weibull Distribution		Mod. Tsallis Distribution	
				χ^2/ndf	p value	χ^2/ndf	p value	χ^2/ndf	p value	χ^2/ndf	p value
OPAL	91	0.657	[38]	1.23/20	1.0000	3.93/20	1.0000	72.78/20	0.0001	5.32/16	0.9940
	133	0.662	[33]	3.41/20	1.0000	5.88/20	0.9991	14.71/20	0.7933	2.40/16	1.0000
	161	0.635	[34]	4.91/20	0.9998	3.01/20	1.0000	12.20/20	0.9090	2.89/16	0.9999
	172	0.666	[37]	3.68/23	1.0000	3.50/23	1.0000	11.83/23	0.9730	3.31/19	1.0000
	183	0.675	[38]	1.71/23	1.0000	4.01/23	1.0000	28.80/23	0.1871	12.91/19	0.8437
	189	0.662	[38]	15.94/23	0.8578	1.72/23	1.0000	52.11/23	0.0005	2.73/19	1.0000
L3	130.1	0.654	[36]	6.11/17	0.9924	2.22/17	1.0000	9.75/17	0.9137	4.20/13	0.9889
	136.1	0.649	[36]	17.33/17	0.4322	13.97/17	0.6692	27.63/17	0.0495	16.61/13	0.2178
	172.3	0.657	[36]	7.01/17	0.9834	3.19/17	0.9999	11.26/17	0.8427	1.51/13	1.0000
	182.8	0.668	[36]	14.49/17	0.6322	6.88/17	0.9851	29.92/17	0.0269	5.72/13	0.9558
	188.6	0.670	[36]	15.83/17	0.5359	5.16/17	0.9973	40.93/17	0.0010	5.83/13	0.9521
	194.4	0.679	[36]	18.69/17	0.3466	9.03/17	0.9393	30.86/17	0.0208	6.94/13	0.9052
	200.2	0.661	[36]	23.98/17	0.1200	12.88/17	0.7442	29.01/17	0.0344	4.61/13	0.9828
	206.2	0.666	[36]	29.66/17	0.0289	14.31/17	0.6450	41.41/17	0.0008	4.12/13	0.9898

Table 6.13: χ^2/ndf comparison and p values for different energies using two component model for different distributions in e^+e^- interactions.

Energy (GeV)	NBD		Gamma		Weibull distribution		Tsallis distribution	
	K	$< n >$	α	β	k	λ	K_{TS}	q
91	21.401 ± 0.706	21.268 ± 0.065	10.863 ± 0.197	0.508 ± 0.009	3.548 ± 0.033	23.197 ± 0.073	21.397 ± 0.670	1.751 ± 0.325
133	19.888 ± 2.253	23.260 ± 0.316	10.191 ± 0.846	0.436 ± 0.038	4.029 ± 0.122	25.239 ± 0.374	19.891 ± 2.251	1.405 ± 0.562
161	17.981 ± 1.553	24.432 ± 0.272	10.270 ± 0.626	0.421 ± 0.024	3.542 ± 0.098	27.174 ± 0.300	17.983 ± 1.587	1.340 ± 0.093
172	21.270 ± 3.026	25.397 ± 0.408	11.472 ± 1.545	0.451 ± 0.059	3.813 ± 0.162	27.942 ± 0.479	21.274 ± 3.003	1.097 ± 0.075
183	19.755 ± 1.343	26.743 ± 0.237	10.921 ± 0.602	0.407 ± 0.024	4.069 ± 0.088	29.117 ± 0.277	19.749 ± 1.339	1.056 ± 0.023
189	17.806 ± 0.857	26.811 ± 0.177	10.209 ± 0.291	0.379 ± 0.011	3.994 ± 0.058	29.018 ± 0.197	17.795 ± 0.858	1.099 ± 0.096
130.1	23.51 ± 2.081	23.55 ± 0.201	11.73 ± 0.619	0.500 ± 0.025	3.655 ± 0.095	26.110 ± 0.215	23.513 ± 2.031	1.786 ± 0.846
136.1	18.30 ± 1.539	24.03 ± 0.220	10.27 ± 0.698	0.428 ± 0.027	3.513 ± 0.099	26.913 ± 0.235	18.309 ± 1.490	1.712 ± 0.831
172.3	18.81 ± 1.322	27.33 ± 0.254	10.67 ± 0.430	0.392 ± 0.018	4.033 ± 0.121	30.358 ± 0.296	18.813 ± 1.324	1.0001 ± 0.005
182.8	18.98 ± 1.332	26.69 ± 0.271	10.92 ± 0.007	0.409 ± 0.003	4.041 ± 0.101	28.590 ± 0.358	18.983 ± 1.332	1.0001 ± 0.001
188.6	19.88 ± 1.042	26.57 ± 0.183	11.09 ± 0.351	0.412 ± 0.014	4.066 ± 0.078	28.144 ± 0.251	19.883 ± 1.044	1.0010 ± 0.0006
194.4	18.53 ± 1.223	26.89 ± 0.242	10.58 ± 0.488	0.391 ± 0.019	3.998 ± 0.084	28.841 ± 0.266	18.533 ± 1.223	1.812 ± 0.585
200.2	20.09 ± 1.491	27.08 ± 0.287	10.92 ± 0.590	0.399 ± 0.025	4.271 ± 0.099	28.350 ± 0.322	20.092 ± 1.497	1.405 ± 0.060
206.2	19.63 ± 1.210	27.39 ± 0.234	10.92 ± 0.53	0.394 ± 0.022	4.151 ± 0.079	28.831 ± 0.262	19.631 ± 1.195	1.967 ± 0.041

Table 6.14: The parameters of the NBD, the Gamma, the Weibull and the Tsallis probability distribution functions for data samples of e^+e^- collisions at various energies from the OPAL and the L3 experiments.

Energy (GeV)	Modified Weibull				Modified Tsallis			
	k_1	λ_1	k_2	λ_2	K_{TS_1}	q_1	K_{TS_2}	q_2
91	4.556 ± 0.228	23.030 ± 0.471	4.684 ± 0.482	32.810 ± 0.544	22.140 ± 2.022	1.058 ± 0.153	50.001 ± 3.202	1.577 ± 0.776
133	4.810 ± 0.192	22.050 ± 0.418	4.811 ± 0.557	32.480 ± 0.775	68.540 ± 31.590	1.023 ± 0.129	46.340 ± 37.620	1.120 ± 0.541
161	4.412 ± 0.063	20.620 ± 0.119	4.221 ± 0.133	28.401 ± 0.168	24.890 ± 5.287	1.065 ± 0.160	50.001 ± 35.600	1.002 ± 0.551
172	4.537 ± 0.307	24.380 ± 0.691	5.363 ± 0.963	34.070 ± 0.928	33.920 ± 11.590	1.210 ± 0.229	50.002 ± 36.680	1.799 ± 0.838
183	5.025 ± 0.139	25.170 ± 0.310	5.157 ± 0.358	37.510 ± 0.516	17.970 ± 2.197	1.086 ± 0.065	50.001 ± 3.275	1.061 ± 0.059
189	4.629 ± 0.094	25.570 ± 0.260	5.121 ± 0.377	36.690 ± 0.405	32.101 ± 5.396	1.005 ± 0.013	37.410 ± 12.660	1.112 ± 0.097
130.1	4.811 ± 0.248	22.267 ± 0.469	4.696 ± 0.352	31.041 ± 0.438	25.032 ± 4.022	1.026 ± 0.019	50.027 ± 28.561	1.988 ± 0.887
136.1	4.286 ± 0.318	22.681 ± 0.858	4.808 ± 0.698	32.110 ± 0.575	24.591 ± 3.979	1.001 ± 0.025	50.021 ± 27.911	1.772 ± 0.539
172.3	5.054 ± 0.218	25.191 ± 0.624	4.631 ± 0.318	37.133 ± 0.602	33.573 ± 5.151	1.187 ± 0.052	50.007 ± 38.722	1.498 ± 0.232
182.8	4.757 ± 0.140	24.910 ± 0.322	5.315 ± 0.497	36.765 ± 0.570	31.388 ± 3.787	1.089 ± 0.171	50.001 ± 27.303	1.958 ± 0.922
188.6	4.721 ± 0.096	25.051 ± 0.184	5.445 ± 0.326	36.492 ± 0.422	30.031 ± 2.654	1.147 ± 0.154	50.004 ± 8.850	1.789 ± 0.680
194.4	4.695 ± 0.131	25.454 ± 0.299	4.659 ± 0.300	37.322 ± 0.601	31.455 ± 3.500	1.086 ± 0.037	50.006 ± 37.741	1.001 ± 0.100
200.2	4.915 ± 0.120	25.473 ± 0.248	5.197 ± 0.398	38.391 ± 0.670	34.391 ± 3.687	1.065 ± 0.151	50.005 ± 30.089	1.825 ± 0.767
206.2	4.846 ± 0.106	25.582 ± 0.226	5.602 ± 0.437	38.210 ± 0.564	33.101 ± 2.983	1.024 ± 0.060	50.012 ± 28.161	1.331 ± 0.364

Table 6.15: The parameters of the Modified Weibull and the Modified Tsallis probability distribution functions for data samples of e^+e^- collisions at various energies from the OPAL and the L3 experiments.

6.3.3 Results and Discussions

The probability distributions calculated from the Tsallis, Weibull, Gamma, NBD and their respective two component models have been implemented on e^+e^- experimental data. Confidence Level, CL or probability values, generally known as p values, are calculated for each χ^2/ndf value to determine the statistical significance of the results obtained from the models. The chi-square comparison and p values for different models and their respective two component approach are shown in tables 6.12 and 6.13. All the results for which $CL > 0.1$ % or 0.001 are statistically acceptable for these models. It is observed that the Weibull model fails to describe the multiplicity data at these energies. But Gamma and the Tsallis distributions are in agreement with the experimental data at almost all the energies with CL value > 0.1 %. For two component method it is found that this approach improves each fit by reducing the χ^2/ndf values significantly. The improvement in the value of χ^2/ndf due to two component is distinctly visible in the case of the Tsallis and the Weibull distributions. In the modified Tsallis model all the data sets which were excluded statistically in the Tsallis model due to low p values corresponding to $CL <$ 0.1% become statistically acceptable with values $CL > 0.1\%$. The Weibull distribution which itself could not describe the data, can explain the data well at both lower and higher energies except at $\sqrt{s} = 91$, 189 and 206 GeV using the Modified approach. The shape parameter, β, of the Gamma distribution shows very small decrease in the values with increasing energy and scale parameter α almost remains constant with the energy, as expected [14].

For the Weibull model shape parameter, k does not change much with energy and all the values are within limits of errors. This behaviour corresponds to the emission of soft gluons followed by the hadronization. Moreover, the shape parameter is associated with the nature of the fragmentation process. In leptonic interactions the dynamics of the fragmentation process does not vary much within the range of energy under study. But λ, which determines the width of distribution increases with the energy. This behaviour is expected as λ is related to the mean multiplicity $< n >$ which increases at higher energies as more number of particles are produced. The increasing trend of λ with the center of mass energy, $\sqrt{s}$ is the same as observed in the analysis of hadronic interactions. The increase can be described by the power law [39]. Figure 6.41 exhibits the dependence of λ

of the Weibull fit on the centre of mass energies of e^+e^- collisions for the OPAL and the L3 experiment.

The increase of λ with the centre of mass energy, $\sqrt{s}$ can be parameterised in terms of power law, $\lambda = \mu \sqrt{s}^{\nu}$, with μ and ν as the fit parameters. Values of the parameters μ and ν :

For OPAL experiment: $\mu = 5.84 \pm 0.23$ and $\nu = 0.30 \pm 0.010$,

For the L3 experiment: $\mu = 10.05 \pm 0.99$ and $\nu = 0.20 \pm 0.019$

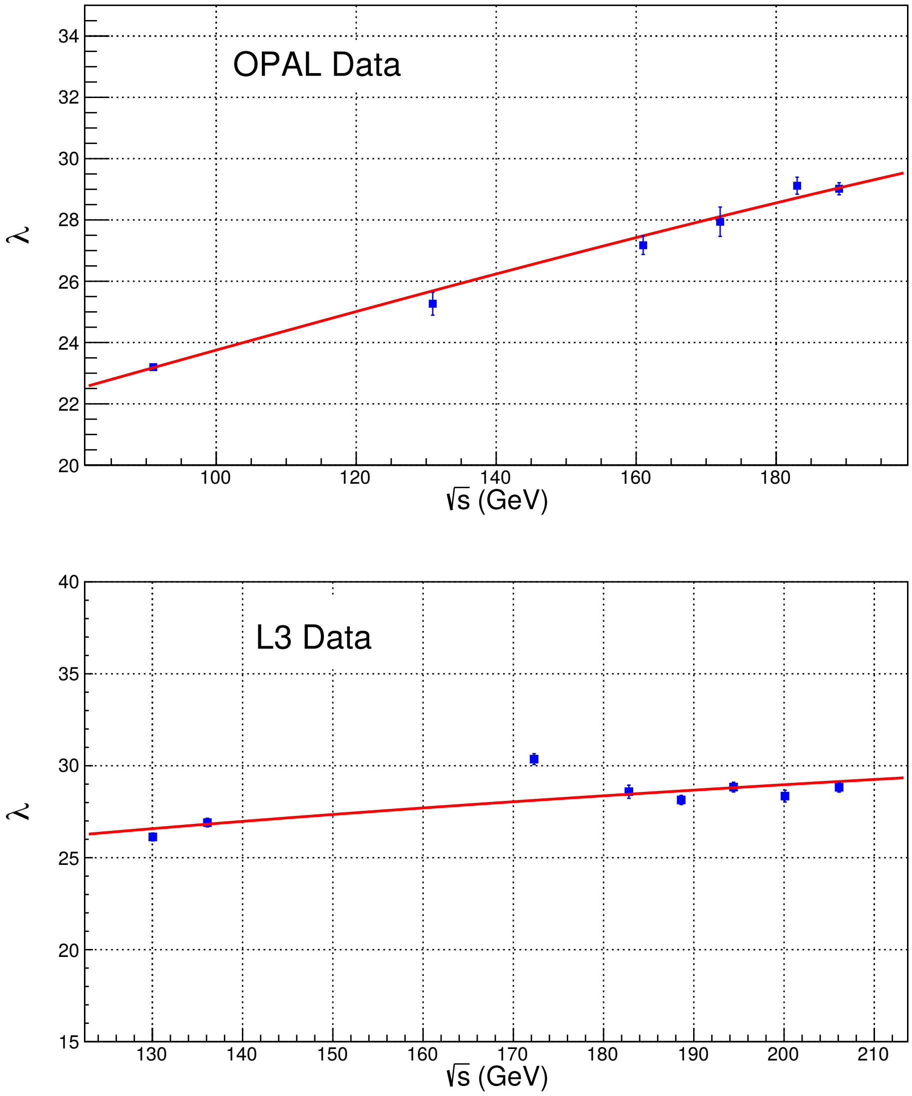

Figure 6.41: Dependence of the Weibull parameter, λ on energy for the OPAL and the L3 experiments.

From the tables above it is clear that for both the Tsallis and the Modified Tsallis, the entropic index, q which measures the departure of entropy from its extensive behaviour is found to be more than 1, in each case. This ensures the non-extensive behaviour of entropy in these interactions. The parameter K_{TS} of the Tsallis fit is related to q. K_{TS} measures the deviation from the Poissonian form and is related to the K parameter of the NBD which determines the width of the distribution. Thus the value of entropic index, $q > 1$ causes the width broadening of distribution which takes it closer to the experimental data. This value of entropic index, $q > 1$ is the basis of Tsallis statistics which was proposed because the standard BG distribution having $q = 1$ could not replicate the multiplicity distributions at higher energies. Due to the centre of mass energies being very closely spaced, the calculated q values from both the experiments are plotted together against energy $\sqrt{s}$ as shown in figure 6.42. One can observe a weak dependence of q on energy. It is found that almost all the q values lie well within the upper and the lower limit of confidence band. Figure 6.43 shows the q_1 and q_2 values as a function of $\sqrt{s}$. It is observed that there are few values which are outside this band. This is on account of the low statistics leading to the large errors on the q_1 and q_2. The mean value $< q >$ for the Tsallis Model and $< q_1 >$, $< q_2 >$ for the Modified Tsallis Model at these energies are found to be;

Tsallis: $< q > = \mathbf{1.388 \pm 0.095}$,

Modified Tsallis: $< q_1 > = \mathbf{1.077 \pm 0.017}$, and $< q_2 > = \mathbf{1.489 \pm 0.100}$.

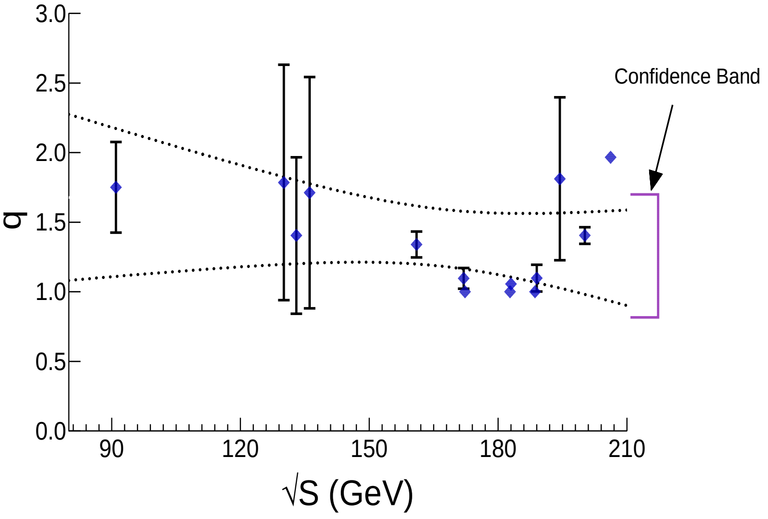

Figure 6.42: Dependence of the Tsallis non-extensive entropic index, q on $\sqrt{s}$

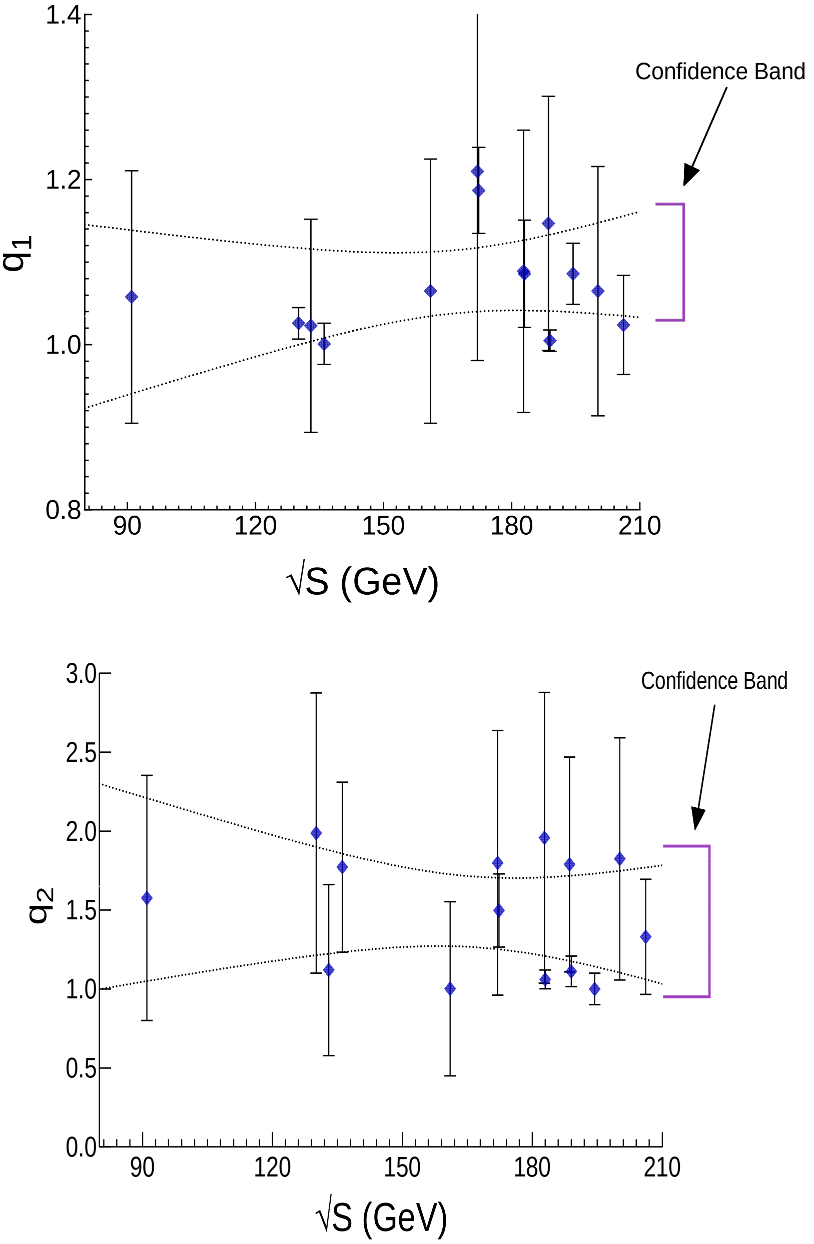

Figure 6.43: Dependence of the non-extensive entropic indexes, q_1 and q_2 of the Modified Tsallis model on $\sqrt{s}$.

6.3.4 Moments

The Tsallis gas model has been used to calculate the moments in order to understand the correlation of the final particles produced during the interaction process. The moments have been calculated by using the values of the Tsallis fits to the experimental data on multiplicity distributions and obtaining the multiplicity distribution as predicted by the Tsallis model at each of the energy. The dependence of C_q and F_q moments on the energy $\sqrt{s}$ for e^+e^- data is shown in figures 6.44 and 6.45. The moments from the OPAL and the L3 experiments are listed in tables 6.16 - 6.17 whereas the moments calculated using the Tsallis model are given in tables 6.18 and 6.19. It is observed that the F_q moments in each case is greater than unity, confirming the correlation between the produced particles [40]. It has been found that the moments C_q and F_q are independent to the centre of mass energy, $\sqrt{s}$. This behaviour indicates that there is no violation of the KNO scaling at the lower energies. Moments from the OPAL and L3 data are compared with the moments obtained from the Tsallis model and are found to be in good agreement.

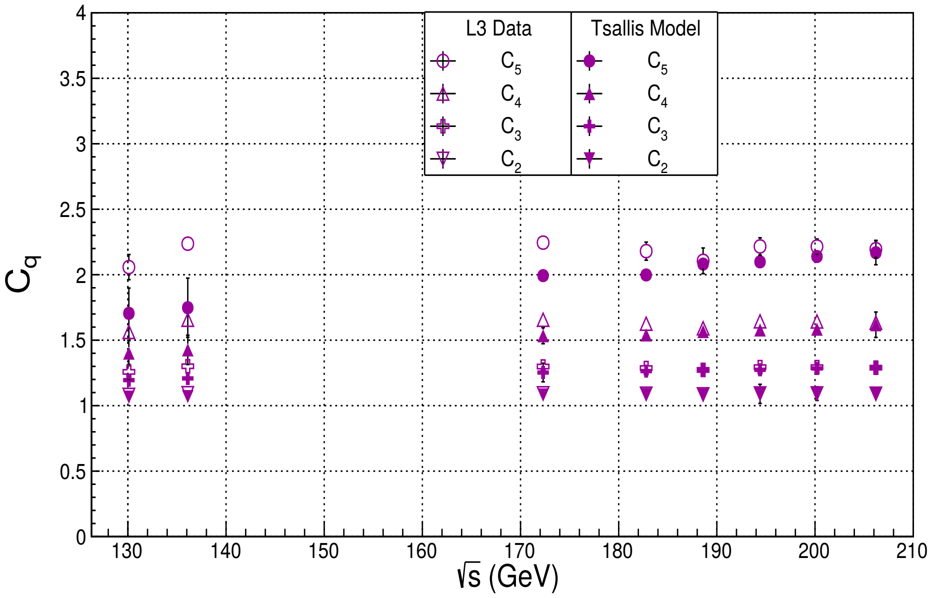

Figure 6.44: Dependence of C_q moments on the centre of mass energy, $\sqrt{s}$ and comparison of the moments obtained using the Tsallis model with the experimental values.

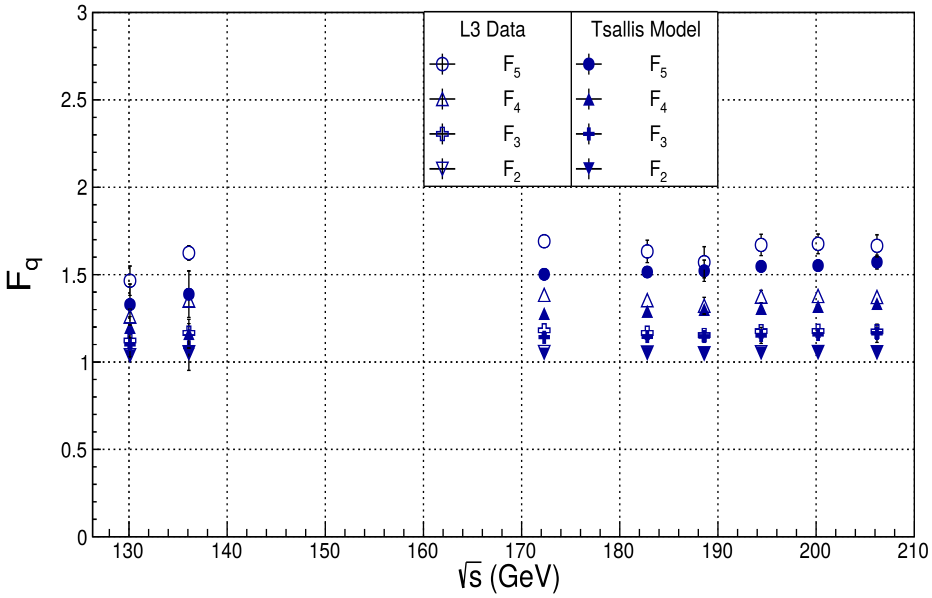

Figure 6.45: Dependence of F_q moments on the centre of mass energy, $\sqrt{s}$ and comparison of the moments obtained using the Tsallis model with the experimental values.

Experiment	Energy	Reduced Moments			
	(GeV)	C_2	C_3	C_4	C_5
OPAL	91	1.089 ± 0.003	1.287 ± 0.012	1.636 ± 0.029	2.218 ± 0.072
	133	1.095 ± 0.002	1.317 ± 0.021	1.716 ± 0.063	2.396 ± 0.147
	161	1.082 ± 0.002	1.277 ± 0.010	1.618 ± 0.023	2.180 ± 0.077
	172	1.080 ± 0.052	1.258 ± 0.061	1.565 ± 0.069	2.063 ± 0.074
	183	1.070 ± 0.026	1.257 ± 0.024	1.586 ± 0.044	2.126 ± 0.058
	189	1.063 ± 0.018	1.241 ± 0.019	1.549 ± 0.019	2.046 ± 0.015
L3	130.1	1.082 ± 0.014	1.258 ± 0.057	1.563 ± 0.042	2.058 ± 0.096
	136.1	1.095 ± 0.002	1.301 ± 0.007	1.656 ± 0.019	2.237 ± 0.045
	172.3	1.094 ± 0.004	1.299 ± 0.012	1.656 ± 0.021	2.245 ± 0.028
	182.8	1.091 ± 0.005	1.287 ± 0.016	1.626 ± 0.025	2.180 ± 0.069
	188.6	1.086 ± 0.007	1.273 ± 0.020	1.591 ± 0.047	2.106 ± 0.098
	194.4	1.093 ± 0.005	1.294 ± 0.017	1.644 ± 0.035	2.216 ± 0.066
	200.2	1.093 ± 0.004	1.294 ± 0.015	1.643 ± 0.032	2.215 ± 0.058
	206.2	1.091 ± 0.006	1.290 ± 0.016	1.634 ± 0.035	2.195 ± 0.067

Table 6.16: C_q moments from the OPAL and the L3 data for e^+e^- interactions

Experiment	Energy	Factorial Moments			
	(GeV)	F_2	F_3	F_4	F_5
OPAL	91	1.043 ± 0.003	1.139 ± 0.011	1.301 ± 0.026	1.549 ± 0.054
	133	1.052 ± 0.002	1.181 ± 0.024	1.402 ± 0.064	1.748 ± 0.133
	161	1.041 ± 0.002	1.148 ± 0.010	1.324 ± 0.031	1.589 ± 0.066
	172	1.041 ± 0.052	1.135 ± 0.043	1.287 ± 0.049	1.513 ± 0.036
	183	1.032 ± 0.025	1.140 ± 0.029	1.321 ± 0.033	1.594 ± 0.037
	189	1.026 ± 0.018	1.126 ± 0.017	1.288 ± 0.012	1.528 ± 0.004
L3	130.1	1.039 ± 0.005	1.123 ± 0.018	1.261 ± 0.041	1.465 ± 0.084
	136.1	1.054 ± 0.002	1.167 ± 0.008	1.352 ± 0.018	1.624 ± 0.040
	172.3	1.057 ± 0.005	1.181 ± 0.014	1.384 ± 0.025	1.691 ± 0.035
	182.8	1.053 ± 0.003	1.167 ± 0.017	1.354 ± 0.026	1.633 ± 0.064
	188.6	1.049 ± 0.005	1.154 ± 0.019	1.322 ± 0.048	1.571 ± 0.089
	194.4	1.056 ± 0.006	1.176 ± 0.018	1.374 ± 0.036	1.670 ± 0.061
	200.2	1.057 ± 0.005	1.178 ± 0.016	1.378 ± 0.032	1.676 ± 0.056
	206.2	1.056 ± 0.006	1.175 ± 0.018	1.372 ± 0.035	1.665 ± 0.063

Table 6.17: F_q moments from the OPAL and the L3 data for e^+e^- interactions

Experiment	Energy	Reduced Moments			
	(GeV)	C_2	C_3	C_4	C_5
OPAL	91	1.048 ± 0.011	1.141 ± 0.032	1.280 ± 0.069	1.472 ± 0.127
	133	1.068 ± 0.059	1.204 ± 0.181	1.416 ± 0.341	1.725 ± 0.153
	161	1.093 ± 0.021	1.293 ± 0.088	1.643 ± 0.157	2.225 ± 0.052
	172	1.095 ± 0.091	1.301 ± 0.161	1.659 ± 0.149	2.261 ± 0.129
	183	1.102 ± 0.108	1.313 ± 0.099	1.696 ± 0.202	2.341 ± 0.094
	189	1.110 ± 0.057	1.323 ± 0.193	1.715 ± 0.066	2.382 ± 0.115
L3	130.1	1.065 ± 0.012	1.195 ± 0.041	1.401 ± 0.096	1.705 ± 0.193
	136.1	1.069 ± 0.015	1.208 ± 0.046	1.426 ± 0.112	1.748 ± 0.226
	172.3	1.082 ± 0.002	1.253 ± 0.071	1.534 ± 0.061	1.993 ± 0.023
	182.8	1.084 ± 0.031	1.264 ± 0.011	1.540 ± 0.018	1.998 ± 0.046
	188.6	1.087 ± 0.011	1.269 ± 0.013	1.566 ± 0.027	2.081 ± 0.043
	194.4	1.090 ± 0.073	1.274 ± 0.007	1.578 ± 0.016	2.098 ± 0.038
	200.2	1.092 ± 0.052	1.284 ± 0.015	1.584 ± 0.029	2.139 ± 0.034
	206.2	1.093 ± 0.009	1.291 ± 0.036	1.618 ± 0.097	2.168 ± 0.092

Table 6.18: C_q moments obtained using the Tsallis model for e^+e^- interactions

Experiment	Energy	Factorial Moments			
	(GeV)	F_2	F_3	F_4	F_5
OPAL	91	1.009 ± 0.018	1.022 ± 0.024	1.079 ± 0.048	1.110 ± 0.077
	133	1.025 ± 0.051	1.069 ± 0.229	1.125 ± 0.247	1.187 ± 0.010
	161	1.036 ± 0.019	1.145 ± 0.103	1.306 ± 0.088	1.252 ± 0.065
	172	1.047 ± 0.072	1.157 ± 0.092	1.332 ± 0.109	1.352 ± 0.133
	183	1.051 ± 0.101	1.173 ± 0.041	1.368 ± 0.072	1.373 ± 0.014
	189	1.056 ± 0.031	1.175 ± 0.011	1.373 ± 0.026	1.381 ± 0.233
L3	130.1	1.034 ± 0.009	1.101 ± 0.072	1.199 ± 0.061	1.329 ± 0.117
	136.1	1.041 ± 0.009	1.086 ± 0.134	1.162 ± 0.082	1.388 ± 0.133
	172.3	1.045 ± 0.003	1.142 ± 0.006	1.278 ± 0.014	1.502 ± 0.023
	182.8	1.048 ± 0.010	1.145 ± 0.009	1.291 ± 0.010	1.515 ± 0.035
	188.6	1.050 ± 0.021	1.146 ± 0.008	1.301 ± 0.003	1.522 ± 0.061
	194.4	1.051 ± 0.005	1.152 ± 0.046	1.307 ± 0.017	1.547 ± 0.009
	200.2	1.053 ± 0.013	1.158 ± 0.011	1.319 ± 0.021	1.552 ± 0.030
	206.2	1.056 ± 0.012	1.164 ± 0.052	1.334 ± 0.033	1.572 ± 0.039

Table 6.19: F_q moments obtained using the Tsallis model for e^+e^- interactions

6.3.5 Average Multiplicity

The empirical relation has been used to study the variation of the mean multiplicity as a function of centre of mass energy . The average multiplicity values from the Tsallis model have been compared with the experimental values for e^+e^- interactions from the OPAL and the L3 experiment of the LEP. Both the values are listed in table 6.20 and found to be in good agreement. These values are shown in figure 6.46.

$$For \quad Data: \qquad <n> = \ 176.74 - 70.52(ln\sqrt{s}) + 7.99(ln\sqrt{s})^2 \tag{6.6}$$

$$For \quad Tsallis \quad Model: <n> = 134.85 - 53.11(ln\sqrt{s}) + 6.183(ln\sqrt{s})^2 \tag{6.7}$$

Experiment	Energy (GeV)	Average Charged Multiplicity $< n >$	
		Experiment	Tsallis Model
OPAL	91	21.40 ± 0.43	21.07± 0.21
	133	23.40 ± 0.65	23.17 ± 0.29
	161	24.46 ± 0.63	24.01 ± 0.47
	172	25.77 ± 1.05	24.98 ± 0.53
	183	26.85 ± 0.58	26.17 ± 0.39
	189	26.95 ± 0.53	26.33 ± 0.66
L3	130.1	23.28 ± 0.26	23.21 ± 0.35
	136.1	24.13 ± 0.29	23.53 ± 0.17
	172.3	27.00 ± 0.58	26.93 ± 0.25
	182.8	26.84 ± 0.34	26.77 ± 0.19
	188.6	26.84 ± 0.32	26.51 ± 0.08
	194.4	27.14 ± 0.42	26.87 ± 0.49
	200.2	27.73 ± 0.47	27.09 ± 0.31
	206.2	28.09 ± 0.33	27.38 ± 0.20

Table 6.20: Average multiplicity $< n >$ at $\sqrt{s} = 91$ GeV to 206 GeV for e^+e^- interactions. The values obtained from the Tsallis model are compared with the OPAL and the L3 experimental values

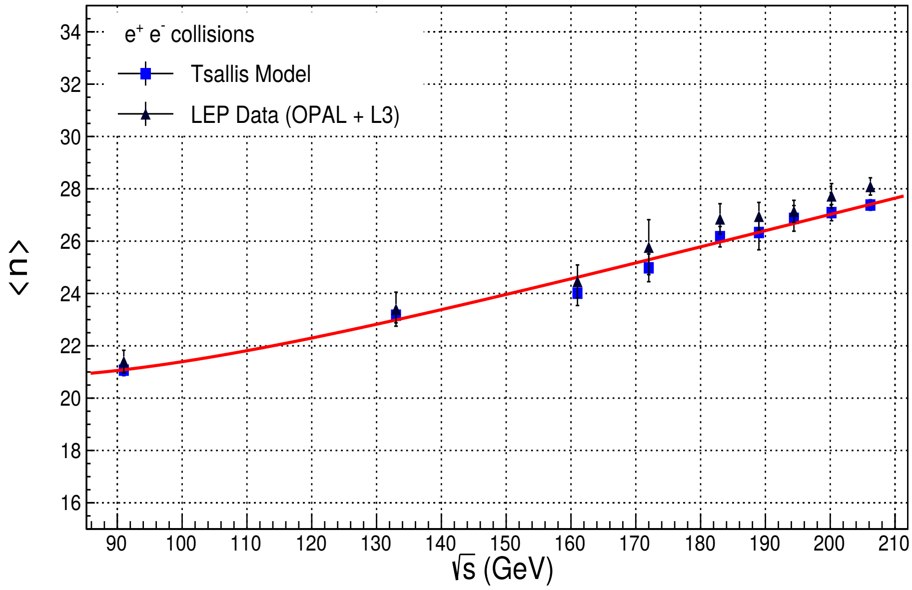

Figure 6.46: Dependence of the average multiplicity $< n >$ on the centre of mass energy, $\sqrt{s}$ for e^+e^- collisions and comparison with experimental values. The solid line corresponds to the equation (6.7)

6.4 Analysis of Hadron-Nucleus Interactions

The study of hadron-nucleus (hA) interactions [41] plays a significant role in understanding the mechanism of hadron production and their properties. In these interactions nuclear fragmentation products reflect in their characteristics the mechanism of production of new particles. It is quite promising to investigate the correlation between the various types of particles produced in the final state of an hA collision. The study of high energy hadron-nucleus interactions become very important to understand the particle-particle interactions and the phenomenon of particle production in heavy ions interactions in nuclear targets. Heavy ion interactions play a key role in the understanding of physics of formation of quark-gluon plasma (QGP) [42]. Nucleus-nucleus interactions can be explained as a superposition of hadron-nucleus interactions. Particles produced in the hA interactions are studied using various phenomenological models. In present study the experimental data from pion-emulsion and proton-emulsion interactions from different fixed target experiments from the energy range 27 to 800 GeV have been analysed [43]. It is interesting to revisit these old data for the models which successfully describe the present day data at higher energies.

6.4.1 Multiplicity Analysis using π^--Em and p-Em Data

The data under study on pion-nucleus interactions mainly come from the fixed target experiments using nuclear emulsions as the detector [44]. The passage of a charged particle through nuclear emulsion leaves behind a trail of ionization produced in AgBr crystals which are reduced to specks of silver. This trail of specks, known as track, is scrutinized under high power precision telescopes. In the present study π^--Em data at $P_{Lab} = 50$ GeV [45], 200 GeV [46], 340 GeV [47] and 525 GeV [48] have been analysed. Along with the π^--Em data, we have also analysed the data of proton-Emulsion, p-Em interactions at $P_{Lab} = 27$ GeV [49], 67 GeV, 200 GeV [50], 300 GeV [51], 400 GeV [52]and 800 GeV [53]. Various models described in the earlier sections, such as the NBD, the Gamma, Shifted Gamma, the Weibull and the Tsallis models have been used to obtain the multiplicity distribution at each of these energies. Results are compared with the experimental data. Figures 6.47 - 6.48 show the results of these fits for π^--Em data and figures 6.49 - 6.50

for the p-Em data.

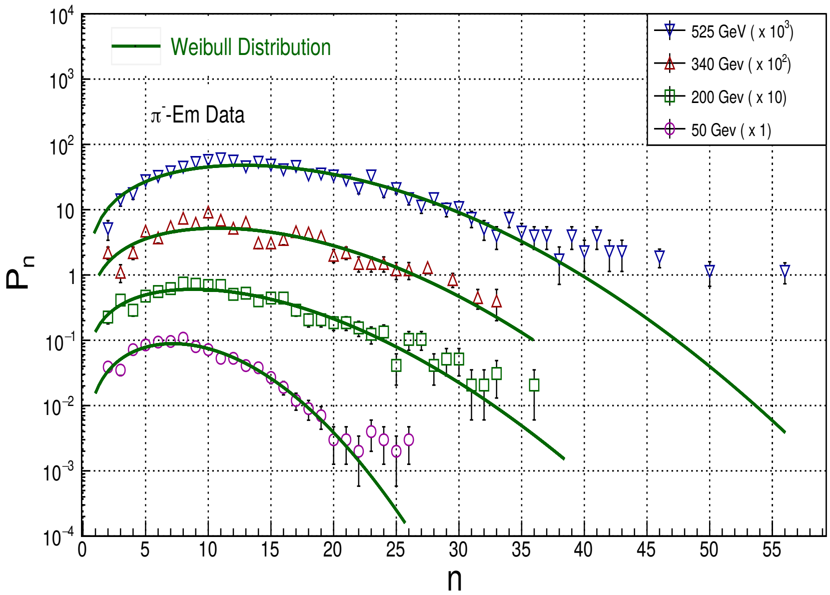

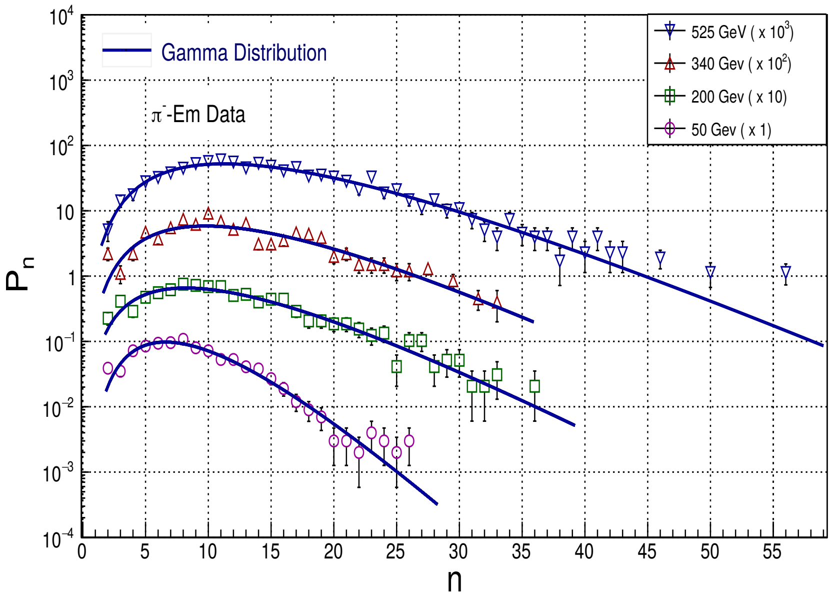

Figure 6.47: The charged particle multiplicity distributions in π^--Em interactions at various energies and comparison of the experimental data with the Weibull and the Gamma distributions.

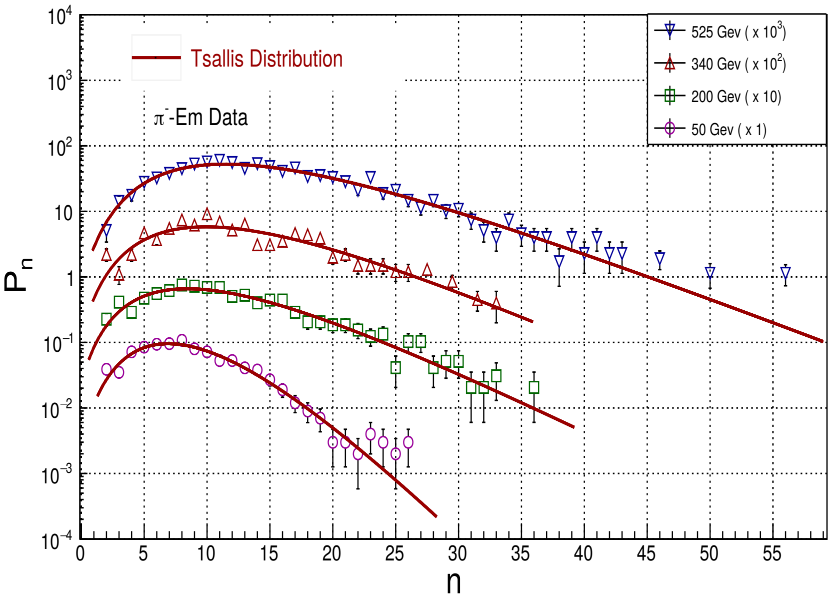

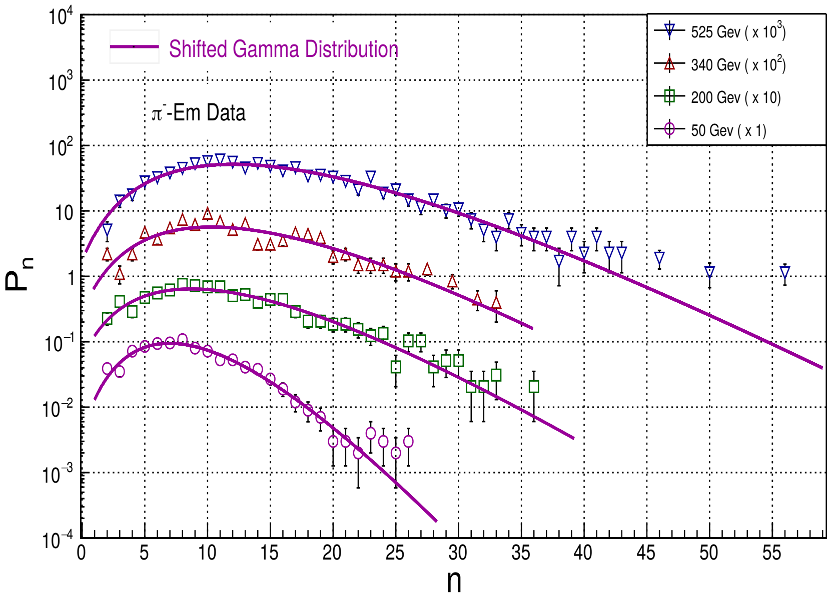

Figure 6.48: The charged particle multiplicity distributions in π^--Em interactions at various energies and comparison of the experimental data with the Tsallis and Shifted Gamma distributions.

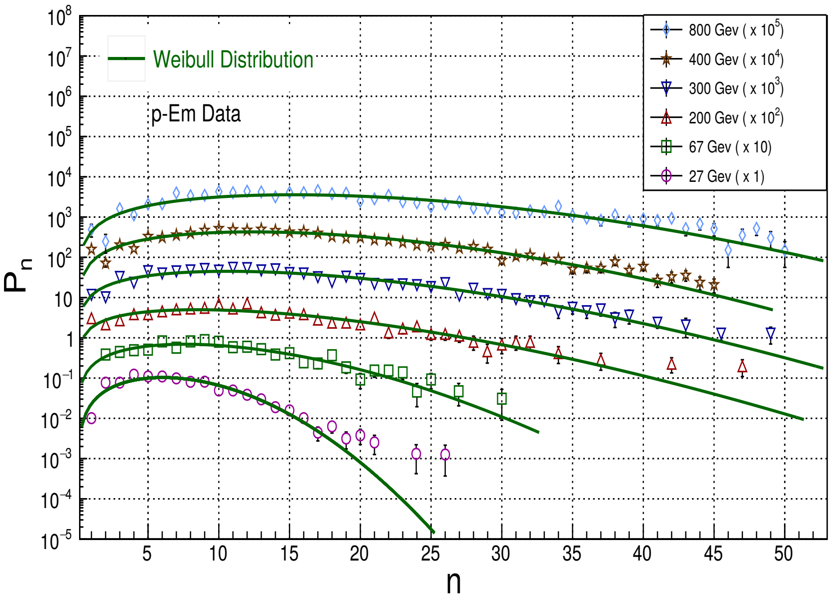

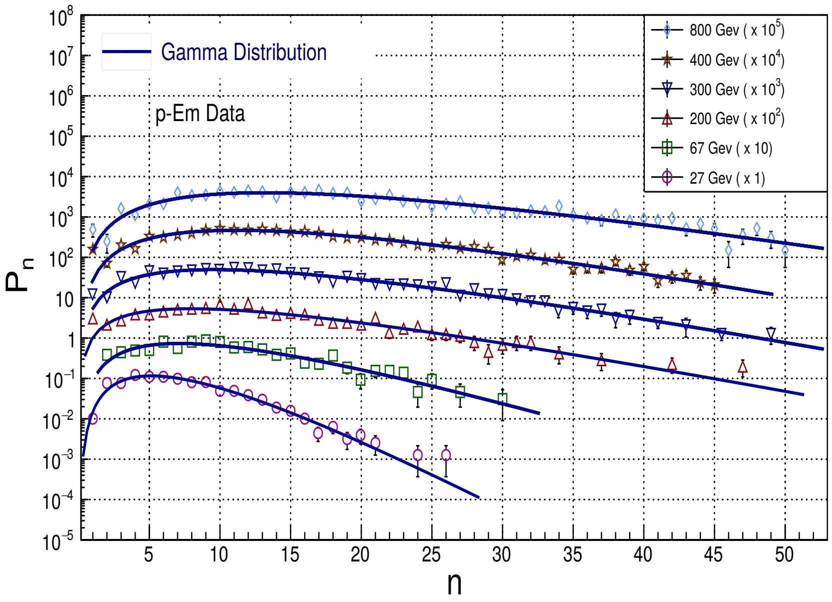

Figure 6.49: The charged particle multiplicity distributions in p-Em interactions at various energies and comparison of the experimental data with the Weibull and the Gamma distributions.

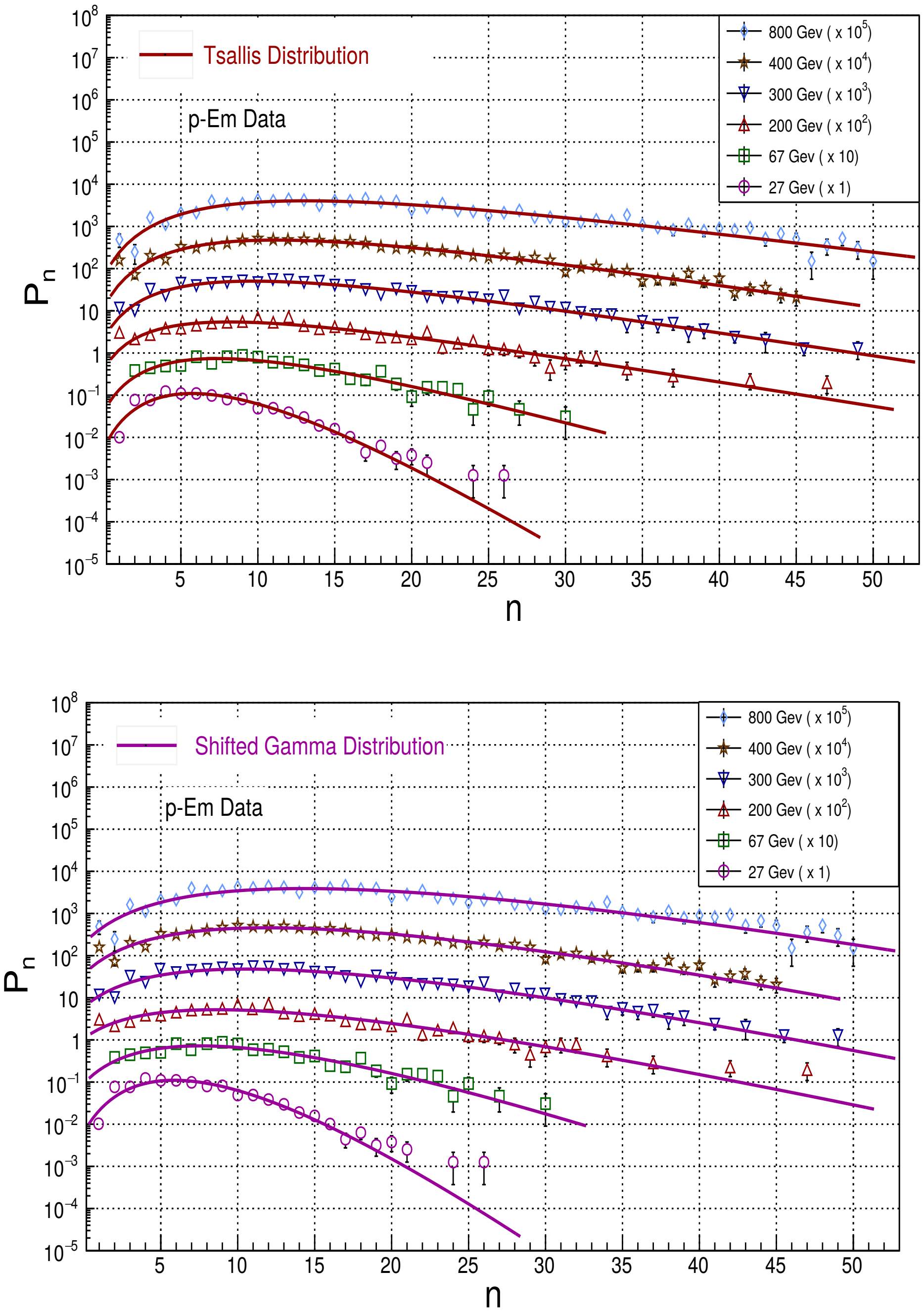

Figure 6.50: The charged particle multiplicity distributions in p-Em interactions at various energies and comparison of the experimental data with the Tsallis and Shifted Gamma distributions.

Energy,	NBD Distribution		Gamma Distribution		Shifted Gamma Distribution		Weibull Distribution		Tsallis Distribution	
P_{Lab} (GeV)	χ^2/ndf	p value	χ^2/ndf	p value	χ^2/ndf	p value	χ^2/ndf	p value	χ^2/ndf	p value
π^--Em										
50	37.22/23	0.0308	54.43/23	0.0002	35.26/23	0.0490	39.33/23	0.0182	38.33/23	0.0235
200	32.82/31	0.3778	41.16/31	0.1049	31.30/31	0.4512	38.85/31	0.1662	33.93/31	0.3281
340	72.89/26	0.0001	69.11/26	0.0001	74.70/26	0.0001	90.37/26	0.0001	68.83/26	0.0001
525	54.91/43	0.1052	54.55/43	0.1114	57.80/43	0.0652	92.42/43	0.0001	49.32/43	0.2352
p-Em										
27	67.45/20	0.0001	33.78/20	0.0277	71.30/20	0.0001	85.3/ 20	0.0001	63.89/20	0.0001
67	25.66/23	0.3172	28.23/23	0.2072	25.10/23	0.3452	27.37/23	0.2405	26.20/23	0.2915
200	36.88/33	0.3141	41.19/33	0.1549	35.68/33	0.3435	43.10/33	0.1119	36.94/33	0.2917
300	49.30/40	0.1487	49.65/40	0.1410	54.39/40	0.0641	71.31/40	0.0017	46.69/40	0.2167
400	74.75/42	0.0014	82.09/42	0.0002	76.34/42	0.0010	112.7/42	0.0001	72.42/42	0.0024
800	75.02/47	0.0058	66.40/47	0.0326	82.60/47	0.0010	111.3/47	0.0001	64.64/47	0.0447

Table 6.21: Comparison of χ^2/ndf and p values for the NBD, the Gamma, Shifted Gamma, the Weibull and the Tsallis distributions for charged hadron multiplicity spectra.

Energy (GeV)	NBD		Gamma		Shifted Gamma		Weibull		Tsallis
	K	$< n >$	α	β	α'	β'	k	λ	q
π^--Em									
50	6.760 ± 0.728	8.47 ± 0.145	3.873 ± 0.245	0.447 ± 0.028	6.696 ± 0.418	0.586 ± 0.036	2.072 ± 0.065	9.506 ± 0.159	1.006 ± 0.004
200	4.120 ± 0.350	11.70 ± 0.238	2.994 ± 0.193	0.251 ± 0.017	4.773 ± 0.152	0.327 ± 0.012	1.869 ± 0.059	13.011 ± 0.259	1.149 ± 0.017
340	4.665 ± 0.382	13.57 ± 0.301	3.460 ± 0.134	0.284 ± 0.018	5.203 ± 0.150	0.316 ± 0.012	2.008 ± 0.063	15.151 ± 0.321	1.069 ± 0.009
525	4.610 ± 0.221	15.62 ± 0.221	3.786 ± 0.216	0.219 ± 0.010	5.124 ±0.102	0.274 ± 0.007	2.076 ± 0.043	17.401 ± 0.243	1.258 ± 0.020
p-Em									
27	7.890 ± 0.642	0.210 ± 0.107	3.461 ± 0.085	0.480 ± 0.014	7.707 ± 0.140	0.756 ± 0.032	2.122 ± 0.041	8.145 ± 0.120	1.001 ± 0.002
67	4.100 ± 0.526	10.520 ± 0.284	2.932 ± 0.255	0.272 ± 0.026	4.780 ± 0.200	0.357 ± 0.017	1.844 ± 0.087	11.59 ± 0.302	1.034 ± 0.014
200	2.920 ± 0.250	13.480 ± 0.360	2.367 ± 0.176	0.169 ± 0.016	3.553 ± 0.270	0.220 ± 0.018	1.657 ± 0.062	14.79 ± 0.381	1.149 ± 0.241
300	3.291 ± 0.139	15.350 ± 0.232	2.617 ± 0.072	0.169 ± 0.005	3.856 ± 0.880	0.222 ± 0.008	1.757 ± 0.032	17.16 ± 0.254	1.369 ± 0.031
400	3.580 ± 0.131	16.800 ± 0.200	2.888 ± 0.050	0.170 ± 0.004	4.140 ± 0.070	0.210 ± 0.004	1.869 ± 0.029	18.64 ± 0.209	1.464 ± 0.018
800	3.670 ± 0.164	19.750 ± 0.350	2.971 ± 0.108	0.149 ± 0.007	4.237 ± 0.100	0.187 ± 0.005	1.945 ± 0.037	22.09 ± 0.372	1.633 ± 0.026

Table 6.22: Parameters of the NBD, the Gamma, Shifted Gamma, the Weibull and the Tsallis probability distribution functions at various energies for π^--Em and p-Em interactions.

6.4.2 Results and Discussion

The probability distribution functions calculated from the Tsallis, Weibull, Gamma and NBD models have been used for the π^--Em and p-Em experimental data. The χ^2/ndf values have been compared for all the four models and are shown in the table 6.21. The parameters of the fitted distributions corresponding to the data are shown in table 6.22. In π^--Emulsion data all the distributions explain the data well at all the energies except at $P_{Lab} = 340$ GeV. In p-Em data the Tsallis model, Gamma and Shifted Gamma distribution explain the data well at nearly all the energies except at $P_{Lab} = 27$ GeV. The Weibull distribution could explain the data upto $P_{Lab} = 300$ GeV and fails at higher energies. The most successful distribution corresponding to p values greater than 0.1 % is the Tsallis distribution. For the Weibull distribution shape parameter, k does not vary significantly with energy in both types of interactions. The scale parameter λ, which is associated with the mean multiplicity, as expected increases with increase in energy in both π^--Em and p-Em interactions as shown in figures 6.51 and 6.52. The increase of λ with the energy, P_{Lab} can be described in terms of power law, $\lambda = \mu\ P_{Lab}^{\nu}$, where μ and ν are the fit parameters.

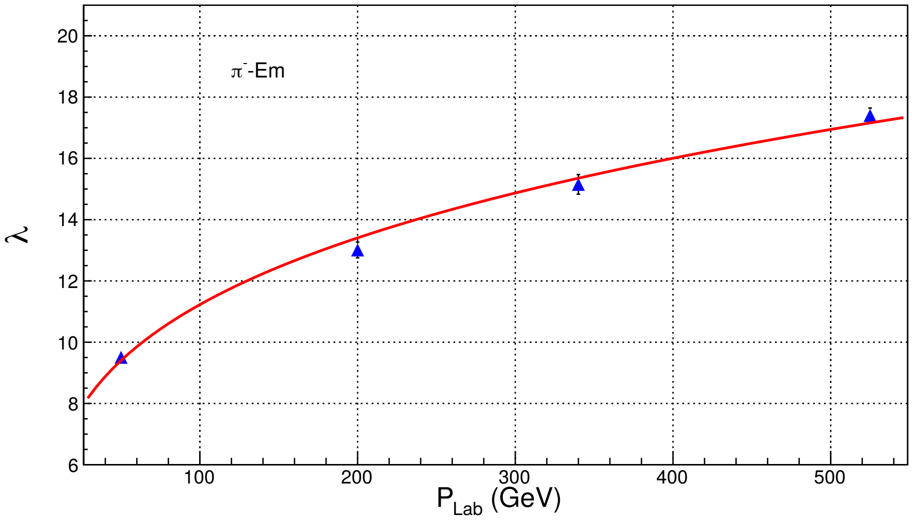

Figure 6.51: Dependence of the Weibull parameter, λ on energy, P_{Lab} for the π^--Em interactions

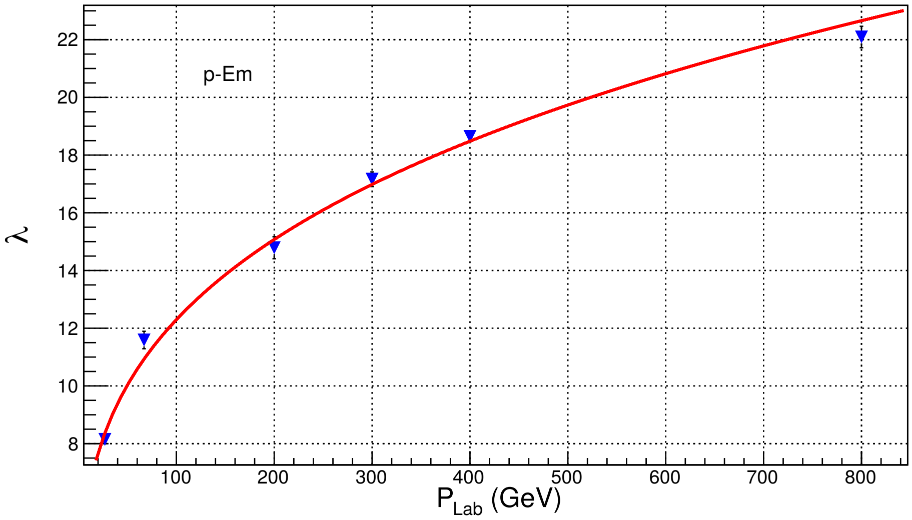

Figure 6.52: Dependence of the Weibull parameter, λ on energy, P_{Lab} for the p-Em interactions

The values of the parameters μ and ν are;

For π-Em Interactions; $\mu = 3.459 \pm 0.174$ and $\nu = 0.256 \pm 0.010$,

For p-Em Interactions; $\mu = 3.176 \pm 0.118$ and $\nu = 0.293 \pm 0.007$

The shape parameters, β, of the Gamma distribution and β' of Shifted Gamma distribution show very small decrease in the values with increasing energy for both π^--Em and p-Em data. The scale parameter, α, a numerical parameter of the Gamma distribution and α' of Shifted Gamma distribution which describes the shape of a distribution remains constant within limits with increase in energy. This behaviour is expected as the shape of distribution remains independent of the energy. The same behaviour was observed in the analyses of hadron-hadron and leptonic interactions. For the Tsallis model the non-extensive parameter q in every case is found to be greater than 1 and increases linearly with increase in energy, P_{Lab}. This trend has been observed in the multiplicity analyses of hadronic and leptonic interactions also as described in the previous sections. The variation of q with the lab energy is shown in figure 6.53.

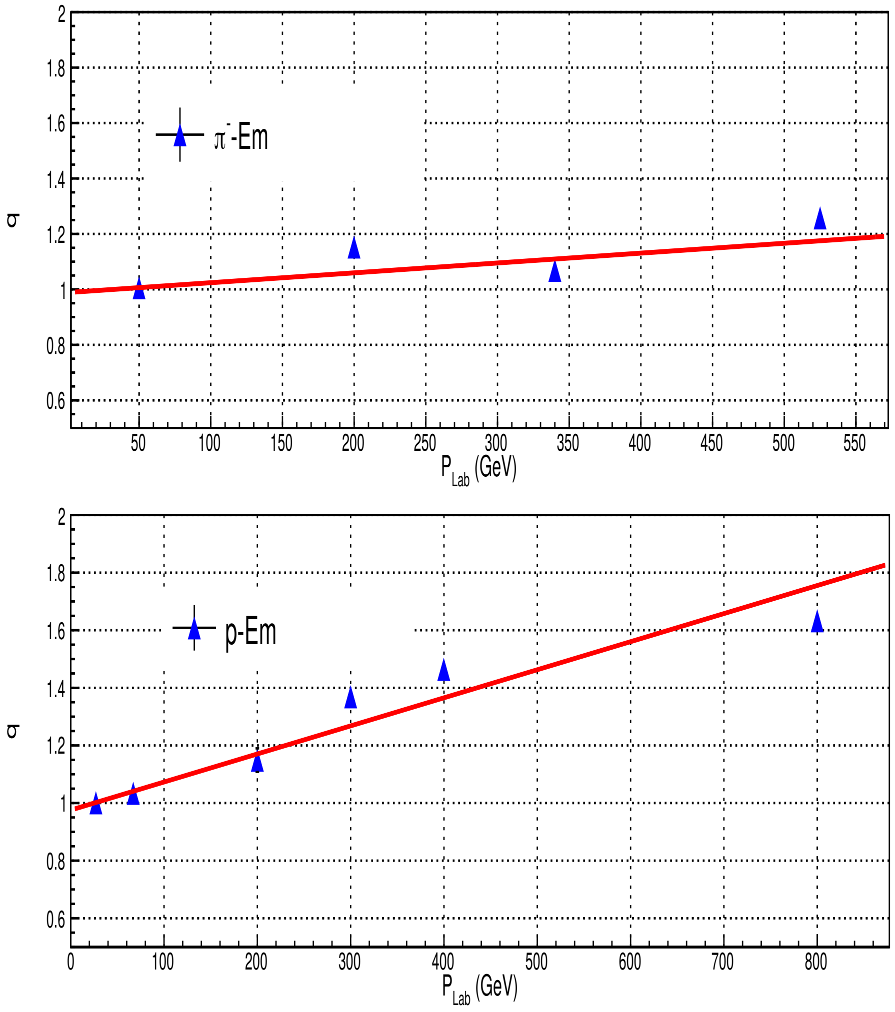

Figure 6.53: Dependence of the parameter q of the Tsallis statistics on energy P_{Lab}.

The rise in q values for the cases are given by equations;

$$q_{p-Em} = P_{Lab}(97.47 \pm 2.69)e^{-05} + (0.9755 \pm 0.002216)$$

$$q_{\pi-Em} = P_{Lab}(35.57 \pm 2.74)e^{-05} + (0.9885 \pm 0.004729)$$

The enhancement in the values of q with energy points to the increased disorder in a non-extensive manner in the interaction volume.

6.4.3 Moments

The Tsallis gas model has been used to calculate the moments in order to understand the correlation of the final particles produced during the interaction process. The dependence of C_q and F_q moments on the energy P_{Lab} for π^--Em and p- Em data are shown in figures 6.54 and 6.55 respectively. The moments form the data are listed in table 6.23 whereas the moments calculated using the Tsallis models are given in table 6.24. It is observed that the F_q moments in each case is greater than unity, confirming the correlation between the produced particles. It has been found that the moments C_q and F_q are independent to P_{Lab} in the case of π^--Em. However in the case of p- Em interactions a small decrease in the higher moments can be observed at $P_{Lab} > 200$ GeV. The overall behaviour indicates that there is no violation of the KNO scaling at the lower energies. Moments from the data are compared with the moments obtained from the Tsallis model and are found to be in good agreement.

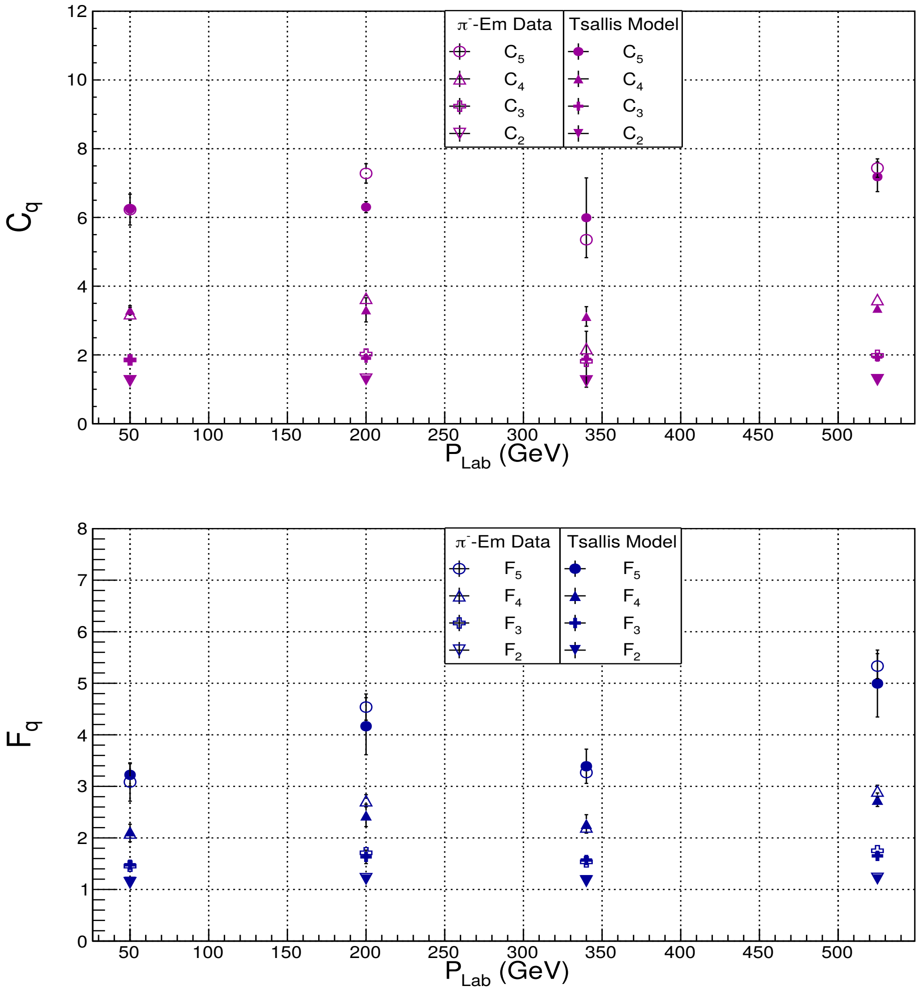

Figure 6.54: Dependence of C_q and F_q moments calculated from the Tsallis model on energy P_{Lab} for π^--Em interactions and comparison with the experimental data.

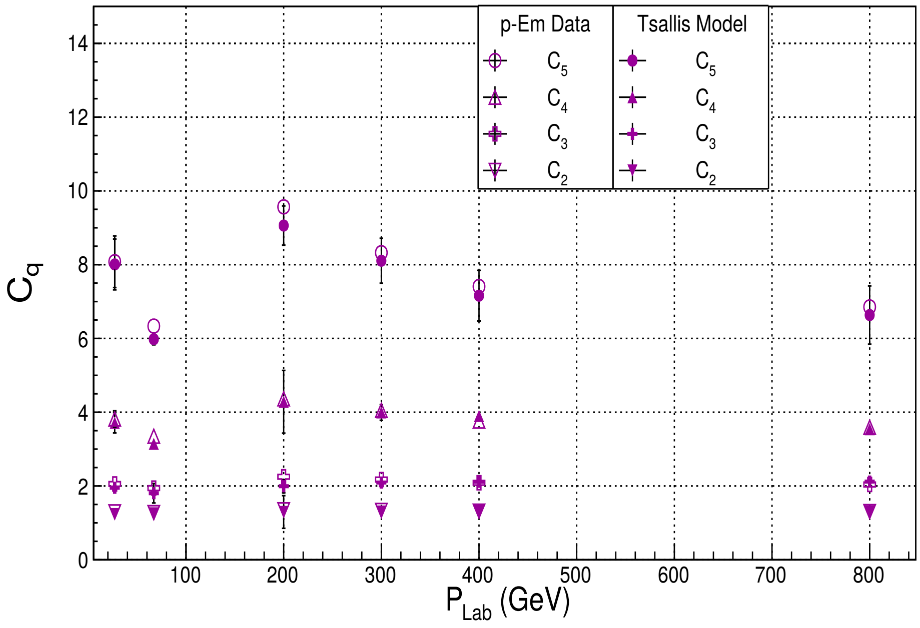

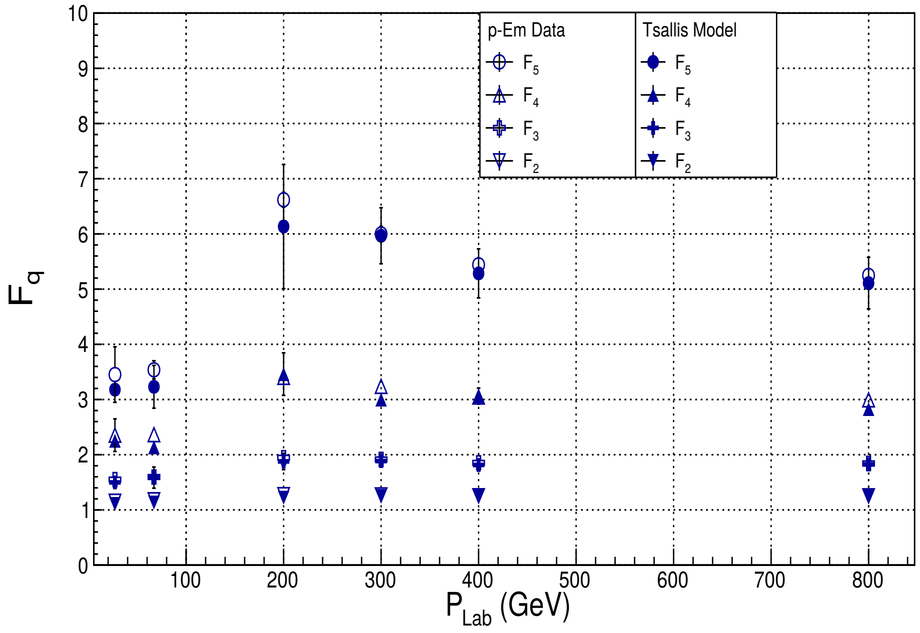

Figure 6.55: Dependence of C_q and F_q moments calculated from the Tsallis model on energy P_{Lab} for p-Em interactions and comparison with the experimental data.

Energy P_{Lab} (GeV)	Reduced Moments				Factorial Moments			
	C_2	C_3	C_4	C_5	F_2	F_3	F_4	F_5
π^--Em								
50	1.246 ± 0.020	1.854 ± 0.063	3.198 ± 0.188	6.228 ± 0.449	1.131 ± 0.019	1.453 ± 0.066	2.095 ± 0.169	3.085 ± 0.372
200	1.294 ± 0.012	2.024 ± 0.044	3.646 ± 0.117	7.281 ± 0.282	1.209 ± 0.015	1.711 ± 0.050	2.721 ± 0.118	4.538 ± 0.254
340	1.243 ± 0.007	1.815 ± 0.020	2.183 ± 0.034	5.352 ± 0.094	1.165 ± 0.008	1.536 ± 0.021	2.212 ± 0.044	3.268 ± 0.077
525	1.278 ± 0.013	1.986 ± 0.046	3.609 ± 0.115	7.436 ± 0.269	1.215 ± 0.013	1.751 ± 0.046	2.909 ± 0.113	5.333 ± 0.242
p-Em								
27	1.297 ± 0.015	2.055 ± 0.065	3.817 ± 0.221	8.080 ± 0.700	1.157 ± 0.018	1.549 ± 0.069	2.354 ± 0.295	3.452 ± 0.503
67	1.278 ± 0.009	1.943 ± 0.030	3.349 ± 0.077	6.335 ± 0.176	1.183 ± 0.009	1.596 ± 0.036	2.363 ± 0.079	3.538 ± 0.164
200	1.354 ± 0.009	2.251 ± 0.028	4.364 ± 0.065	9.568 ± 0.119	1.276 ± 0.011	1.946 ± 0.033	3.401 ± 0.072	6.618 ± 0.135
300	1.338 ± 0.008	2.175 ± 0.026	4.050 ± 0.062	8.325 ± 0.140	1.271 ± 0.010	1.915 ± 0.028	3.238 ± 0.067	5.998 ± 0.139
400	1.317 ± 0.007	2.087 ± 0.021	3.759 ± 0.051	7.410 ± 0.113	1.256 ± 0.008	1.853 ± 0.023	3.046 ± 0.053	5.440 ± 0.101
800	1.306 ± 0.007	2.041 ± 0.017	3.592 ± 0.031	6.854 ± 0.038	1.254 ± 0.008	1.843 ± 0.019	2.994 ± 0.036	5.247 ± 0.050

Table 6.23: C_q and F_q moments from the experimental data at various energies in π^--Em and p-Em interactions.

Energy P_{Lab} (GeV)	Reduced Moments				Factorial Moments			
	C_2	C_3	C_4	C_5	F_2	F_3	F_4	F_5
				π^--Em				
50	1.262 ± 0.011	1.852 ± 0.040	3.301 ± 0.131	6.242 ± 0.118	1.148 ± 0.016	1.479 ± 0.036	2.130 ± 0.080	3.223 ± 0.218
200	1.275 ± 0.024	1.901 ± 0.107	3.311 ± 0.351	6.301 ± 0.160	1.189 ± 0.017	1.633 ± 0.131	2.437 ± 0.217	4.167 ± 0.553
340	1.263 ± 0.021	1.874 ± 0.814	3.119 ± 0.285	5.991 ± 1.160	1.179 ± 0.016	1.571 ± 0.016	2.272 ± 0.179	3.390 ± 0.332
525	1.284 ± 0.019	1.934 ± 0.013	3.357 ± 0.027	7.183 ± 0.431	1.194 ± 0.007	1.652 ± 0.015	2.741 ± 0.131	4.995 ± 0.649
				p-Em				
27	1.237 ± 0.052	1.953 ± 0.095	3.714 ± 0.276	8.007 ± 0.689	1.108 ± 0.016	1.498 ± 0.049	2.252 ± 0.113	3.179 ± 0.105
67	1.258 ± 0.026	1.804 ± 0.265	3.145 ± 0.036	5.980 ± 0.152	1.133 ± 0.009	1.585 ± 0.192	2.133 ± 0.091	3.230 ± 0.387
200	1.299 ± 0.443	1.993 ± 0.178	4.283 ± 0.850	9.061 ± 0.532	1.221 ± 0.034	1.878 ± 0.148	3.460 ± 0.385	6.134 ± 1.125
300	1.307 ± 0.014	2.094 ± 0.073	3.995 ± 0.214	8.107 ± 0.609	1.252 ± 0.081	1.885 ± 0.055	2.998 ± 0.024	5.967 ± 0.507
400	1.319 ± 0.029	2.114 ± 0.055	3.899 ± 0.110	7.160 ± 0.685	1.259 ± 0.009	1.814 ± 0.032	3.062 ± 0.145	5.285 ± 0.444
800	1.312 ± 0.092	2.120 ± 0.063	3.539 ± 0.087	6.635 ± 0.790	1.267 ± 0.010	1.823 ± 0.049	2.827 ± 0.117	5.109 ± 0.467

Table 6.24: C_q and F_q moments calculated from the Tsallis model at various energies in π^--Em and p-Em interactions.

6.4.4 Average Multiplicity

The variation of the mean multiplicity as a function of energy, P_{Lab} has been studied according to the power law $< n > = a\ (P_{Lab})^b$. The average multiplicity values calculated from the Tsallis model are given in table 6.25. These values are compared with the experimental values for π^--Em and p-Em interactions and found to be in good agreement as shown in figure 6.56.

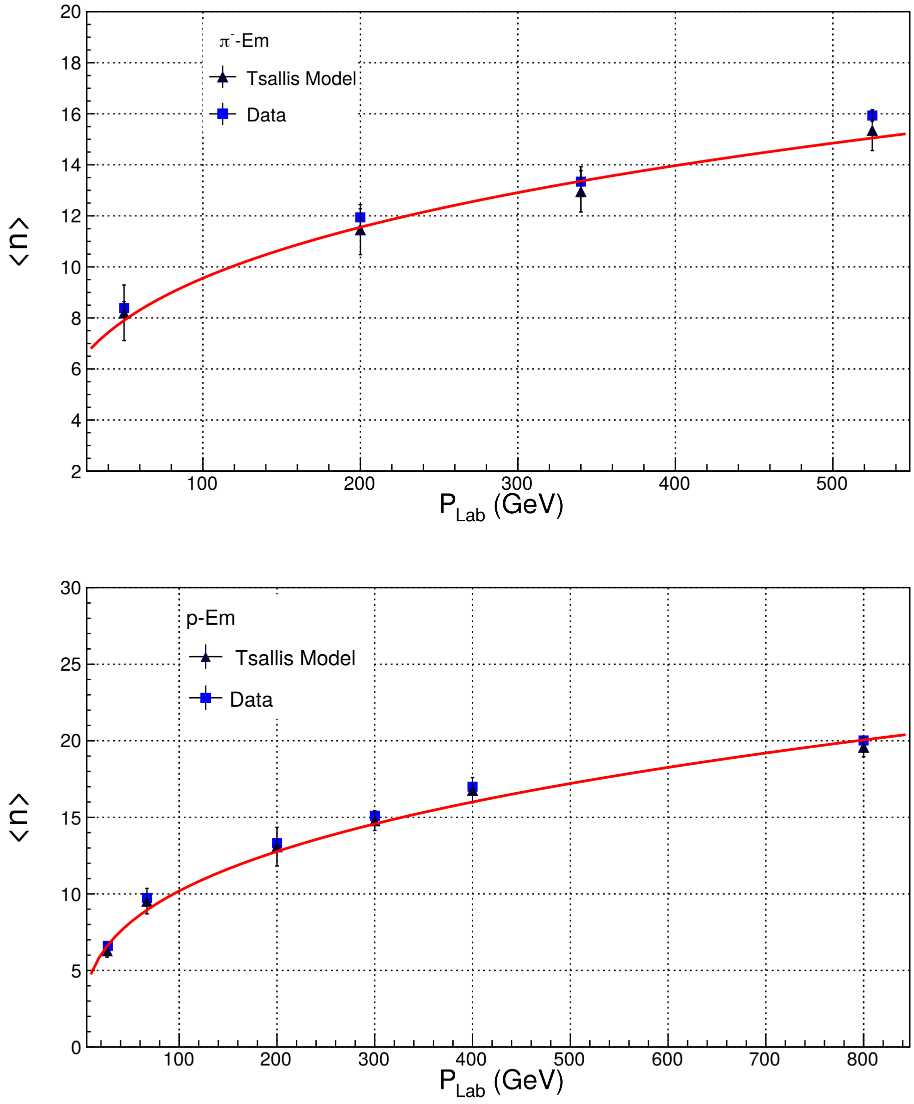

Figure 6.56: Dependence of the average multiplicity $< n >$ on energy, P_{Lab} for π^--Em and p-Em interactions and comparison with the experimental values. The solid line corresponds to the equations (6.9) and (6.11) respectively.

For π^--Em;

$$For\ \ the\ \ Data: \qquad <n> = 2.826(P_{Lab})^{0.226} \tag{6.8}$$

$$For\ \ the\ \ Tsallis\ Model: \quad <n> = 2.708(P_{Lab})^{0.274} \tag{6.9}$$

For p-Em;

$$For\ \ the\ \ Data: \qquad <n> = 2.281(P_{Lab})^{0.331} \tag{6.10}$$

$$For\ \ the\ \ Tsallis\ Model: \quad <n> = 2.276(P_{Lab})^{0.335} \tag{6.11}$$

Energy	Average Charged Multiplicity $< n >$	
P_{Lab} (GeV)	Experiment	Tsallis Model
π^--Em		
50	8.39 ± 0.25	8.20 ± 1.09
200	11.94 ± 0.34	11.46 ± 0.98
340	13.34 ± 0.59	12.96 ± 0.81
525	15.93 ± 0.22	15.36 ± 0.80
p-Em		
27	6.60 ± 0.10	6.29 ± 0.44
67	9.73 ± 0.23	9.53 ± 0.83
200	13.31 ± 0.28	13.09 ± 1.26
300	15.10 ± 0.20	14.74 ± 0.65
400	17.00 ± 0.21	16.77 ± 0.82
800	20.02 ± 0.29	19.59 ± 0.63

Table 6.25: Average multiplicity $< n >$ at various energies in π^--Em and p-Em interactions

Bibliography

[1] E. De Wolf, J. J. Dumont and F. Verbeure, “Comparative study of charged multiplicity distributions”, Nucl. Phys. B **87**, 325 (1975)

[2] J. F. Grosse-Oetringhaus, K. Reygers, “Charged-Particle Multiplicity in Proton-Proton Collisions”, J. Phys. G **37**, 083001 (2010)

[3] S. Chatrchyan et al., “The CMS experiment at the CERN LHC, JINST **3**, 508004 (2008)

[4] UA5 proposal, CERN/SPSC/78-70/P108; CERN/SPSC/78-107/P108 Add. I; CERN/SPSC/78-147/P108/Add. 2 (1978)

[5] J. Rushbrooke,“ ”The UA5 Streamer Chamber Experiment at the SPS p-pbar Collider” Physica Scripta **23**, 642 (1981)

[6] V. Khachatryan et al., “Charged particle multiplicities in pp interactions at $\sqrt{s}$ = 0.9, 2.36 and 7 TeV”, JHEP **01**, 79 (2011)

[7] F. Becattini and G. Passaleva, “Statistical hadronization model and transverse momentum spectra of hadrons in high energy collisions”, Eur. Phys. J. C 23, 551 (2002)

[8] A. Wolfgang, “Track and vertex reconstruction in CMS”, Nucl. Instrum. Meth. A **582**, 781 (2007)

[9] CMS Collaboration, “Tranverse momentum and pseudorapidity distributions of charged hadrons in pp collisons at $\sqrt{s} = 0.9$ and 2.36 TeV”, JHEP **02**, 041 (2010)

[10] CMS Collaboration, “Tranverse momentum and pseudorapidity distributions of charged hadrons in pp collisons at $\sqrt{s} = 7$ TeV”, Phys. Rev. Lett. 105, 022002 (2010)

[11] https://root.cern.ch/

[12] S. Greenland, S. J. Senn, K. J. Rothman et al., "Statistical tests, P values, confidence intervals, and power: a guide to misinterpretations", Eur. J. Epidemiol **31**, 337 (2016)

[13] A. K. Pandey, P. Sett and S. Dash, "Weibull distribution and the multiplicity moments in *pp* ($\bar{p}p$) collisions", Phys. Rev. D **96**, 074006 (2017)

[14] K. Urmossy, G. G. Barnafoldi and T.S. Biro, "Generalized Tsallis Statistics in Electron-Positron Collisions ", Phys. Lett. B **701**, 111 (2011)

[15] M. Gazdzicki and M. I. Gorenstein, "Power law in hadron production", Phys. Lett. B **517**, 250 (2001)

[16] G. J. Alner et al., "A New Empirical Regularity for Multiplicity Distributions in Place of KNO Scaling ", Phys. Lett. B **160**, 199 (1985)

[17] W. Thome et al., "Charged Particle Multiplicity Distributions in *pp* Collisions at ISR Energies ", Nucl. Phys. B **129**, 365 (1977)

[18] S. Sharma and M. Kaur, "Multiplicity spectra in *pp* collisions at high energies in terms of Gamma and Tsallis distributions", Phys. Rev. D **98**, 034008 (2018)

[19] G. J. Alner et al., "Antiproton-proton cross sections at 200 and 900 GeV c.m. energy", Z. Phys. C **32**, 153 (1986)

[20] R. E. Ansorge et al., "Charged Particle Multiplicity Distributions at 200 GeV and 900 GeV Center-Of-Mass Energy", Z. Phys. C **43**, 357 (1989)

[21] G. J. Alner et al., "An Investigation of Multiplicity Distributions in Different Pseudorapidity Intervals in anti-p p Reactions at a CMS Energy of 540-GeV ", Phys. Lett. B **160**, 193 (1985)

[22] R. Brandelik et al., "Rapid Growth of Charged Particle Multiplicity in High-Energy e^+e^- Annihilations", Phys. Lett. B **89**, 418 (1980)

[23] R. Brandelik et al., "Properties of hadron final states in e^+e^- annihilation at 13 GeV and 17 GeV center of mass energies", Phys. Lett. B **83**,261 (1979)

[24] S. Sharma, M. Kaur and S. Kaur, "Tsallis nonextensive entropy and the multiplicity distributions in high energy leptonic collisions", Int. J. Mod. Phys. E **25**, 1650041 (2016)

[25] S. Sharma, M. Kaur and S. Thakur, "Modified Tsallis and Weibull distributions for multiplicities in e^+e^- collisions", Phys. Rev. D **95**, 114002 (2017)

[26] W. Bartel et al., "Total cross section for hadron production by e^+e^- annihilation at petra energies", Phys. Lett. B **88**, 171 (1979)

[27] H. Boerner et al,"The Large Cylindrical Drift Chamber of Tasso", Nucl. Instrum. Meth. **176**, 151 (1980)

[28] S. Myers and E. Picasso, "The Design, construction and commissioning of the CERN Large Electron Positron collider", Contemp. Phys. **31**, 387 (1990)

[29] W. Braunschweig et al., "Charged multiplicity distributions and correlations in e^+e^- annihilation at PETRA energies", Z. Phys. C **45**, 193 (1989)

[30] G. Altarelli, T. Sjostrand and F. Zwirner, "Physics at LEP 2", CERN96-01(1996)

[31] S. Sharma, M. Kaur and S. Thakur, "Modified Weibull and Tsallis Distributions for multiplicities in e^+e^- collisions at LEP2 energies", arXiv:1708.09297

[32] P. D. Acton et al., "A study of charged particle multiplicities in hadronic decays of the Z^0", Z. Phys. C **53**, 539 (1992)

[33] G. Alexander et al., "QCD studies with e(+)e(-) annihilation data at 130 and 136 GeV", Z. Phys. C **72**, 191 (1996)

[34] K. Ackerstaff et al., "QCD studies with e^+e^- annihilation data at 161 GeV", Z. Phys. C **75**, 193 (1997)

[35] G. Abbiendi et al., "QCD studies with e^+e^- annihilation data at 172-189 GeV", Eur. Phys. J. C **16**, 185 (2000)

[36] P. Achard et al.,"Studies of hadronic event structure in e^+e^- annihilation from 30 to 209 GeV with the L3 detector", Phys. Rep. **399**, 71 (2004)

[37] M. Acciarri et al., “QCD studies and determination of α_S in e^+e^- collisions at $\sqrt{s} =$ 161 GeV and 172 GeV”, Phys. Lett. B **404**, 390 (1997)

[38] G. Abbiendi et al. (OPAL Collaboration) and P. Pfeifenschneider (JADE Collaboration), “QCD analyses and determination of α_S in e^+e^- annihilation at energies between 35 and 189 GeV”, Eur. Phys. J. C **17**, 19 (2000)

[39] S. Dash et al., “Multiplicity distributions for e^+e^- collisions using Weibull distribution”, Phys. Rev. D **94**, 074044 (2016)

[40] M. Praszalowicz, “Negative Binomial Distribution and the multiplicity moments at LHC”, Phys. Lett. B **704**, 566 (2011)

[41] N. Dobrotin, “Hadron-Nucleus and Nucleus-Nucleus Interactions at Accelerator Energies”, ICRC **10**, 456 (1977)

[42] H. Bohr, H. B. Nielsena, “Hadron production from a boiling quark soup: quark model predicting particle ratios in hadronic collisions”, Nucl. Phys. B. **128 (2)**, 275 (1977)

[43] S. Sharma, M. Kaur and S. Thakur, “Statistical hadronization and multiplicities in high-energy hadron-nucleus collisions”, Int. J. Mod. Phys. E **26**, 1750006 (2017)

[44] G. P. S. Occhialini, C. F. Powell, “Nuclear Disintegrations Produced by Slow Charged Particles of Small Mass”, Nature **159**, 453 (1947)

[45] V. Kumar et al., “Study of Charged Particle Multiplicity in 50 GeV/c π^--Emulsion Interaction”, Phys. Soc. Jpn. **44**, 1078 (1978)

[46] Z. V. Anzon et al.,“A Study of Inelastic Pion-Nucleus Interactions at 200-GeV/c in an Emulsion”, Nucl. Phys. B **129**, 205 (1977)

[47] M. El-Nadi et al., “Inelastic Interactions of 340-GeV/c PI- with Emulsion Nuclei”, Phys. Rev. D **27**, 12 (1983)

[48] M. L. Cherry et al., “Measurements of 525-GeV pion interactions in emulsion”, Phys. Rev. D **50**, 4272 (1994)

[49] A. Barbaro-Galtieri et al., “Experimental results on the proton-nucleus collisions at 27 GeV in emulsion”, Nuovo Cimento **21**, 469 (1961)

[50] J. Babecki et al., "Multiplicity distributions in proton-nucleus collisions at 67 and 200 GeV", Phys. Lett. B **47**, 268 (1973)

[51] J. Hbert et al., "Nuclear interactions of 300-GeV protons in emulsion", Phys. Rev. D **15**, 1867 (1977)

[52] E. G. Boos et al., "Investigation of inelastic interactions of 400 GeV protons with emulsion nuclei", Nucl. Phys. B **143**, 232 (1978)

[53] A. Abduzhamilov et al., "Charged-particle multiplicity and angular distributions in proton-emulsion interactions at 800 GeV", Phys. Rev. D **35**, 3537 (1987)

Chapter 7

Summary and Conclusion

In high energy particle collisions several elementary particles are produced primarily due to the gluon-gluon, quark-quark and quark-gluon interactions between the constituent quarks and gluons of the colliding particles. One of the most important and interesting observables to describe the mechanism of particle production is the charged particle multiplicities. It makes an important tool to understand the underlying mechanism of particle production in these high energy interactions. In the present work detailed analyses of charged particle production in hadron-hadron, lepton-lepton and hadron-nucleus interactions has been carried out. Data from two basic kind of experiments were used. For the study of hadronic and leptonic interactions, data from various colliding beam experiments have been analysed. For the study of hadron-nucleus interactions, data from the fixed target experiments have been analysed. The phenomenological study of high energy collisions requires a knowledge of the theoretically predicted basic parameters and their experimental verifications. For instance, behaviour of the charged particle multiplicity distributions in full phase space as well as in restricted phase space, momenta spectra, correlations among produced particles, variation of average multiplicity with energy etc. are a few parameters which require special mention. In the present study various phenomenological approaches, statistical distributions and thermal models like the negative binomial distribution (NBD), the Gamma distribution, Shifted Gamma distribution, the Weibull and the Tsallis gas model have been used to analyse the data from few GeV upto the LHC energies.

The current study has been done using three kinds of interactions as described in above section. In hadronic interactions analyses of the charged particle multiplicities have been done at different pseudorapidity intervals in *pp* collisions at $\sqrt{s}$ = 0.9 to 7.0 TeV, the data collected by the CMS experiment at the LHC and in $\bar{p}p$ collisions at $\sqrt{s}$ = 200 to 900 GeV,the data collected at the UA5 experiment at the Proton-Antiproton Collider. In study using *pp* collision data it has been observed that Weibull model provides the best description for the experimental data on each pseudorapidity interval, at each energy with $CL > 0.1$ %. Except at pseudorapidity intervals $|\eta| < 0.5$ and 1.0 for 7 TeV, results from Tsallis model are statistically acceptable with the value of $CL > 0.1$ %. The entropic index, q, of Tsallis statistics which measures the departure of entropy from its extensive behaviour is found to be more than 1 in each case. This ensures the non-extensive behaviour of entropy at higher energies. Whereas in $\bar{p}p$ collision data it has been found that the prediction from the Tsallis gas model describes the experimental data successfully at all pseudorapidity intervals at all energies with $CL > 0.1$ %. It has been observed that the non-extensive parameter of the Tsallis model, q increases with energy. This increase in the q value indicates that the non-extensive behaviour of entropy becomes more pronounced at higher energies. The dependence of q with the energy can be well understood using power law which is inspired by the observation that single particle energy distribution obeys a power law behaviour. The average multiplicity value calculated from the Tsallis model has been compared with the experimental values and found to be in good agreement with them. At $\sqrt{s}$ = 7 TeV, the Tsallis model predicted the value of average multiplicity, $< n >_{TS} = \mathbf{31.231 \pm 3.042}$ compared to the CMS experimental value, $< n >_{CMS} = \mathbf{30.516 \pm 3.660}$ at highest pseudorapidity interval, $|\eta| < 2.4$. The average multiplicity predicted by the Tsallis model at $\sqrt{s}$ = 200 GeV and 900 GeV are found to be, $< n >_{TS} = \mathbf{20.50 \pm 0.14}$ and $< n >_{TS} = \mathbf{32.51 \pm 0.92}$ compared to the UA5 experimental values of $< n >_{UA5} = \mathbf{20.17 \pm 2.65}$ and $< n >_{UA5} = \mathbf{32.73 \pm 1.39}$ respectively. Using the Tsallis model and the energy dependence of q parameter, the prediction for multiplicity distribution at centre of mass energy, $\sqrt{s}$ = 14 TeV has been made as shown in figure 7.1. The q value and $< n >$ corresponding to the multiplicity distribution predicted at $\sqrt{s}$ = 14 TeV at $|\eta| < 1.5$, are found to be;

$$q = \mathbf{1.476 \pm 0.108} \qquad \textbf{and} \qquad < n > = \mathbf{24.492 \pm 2.571}$$

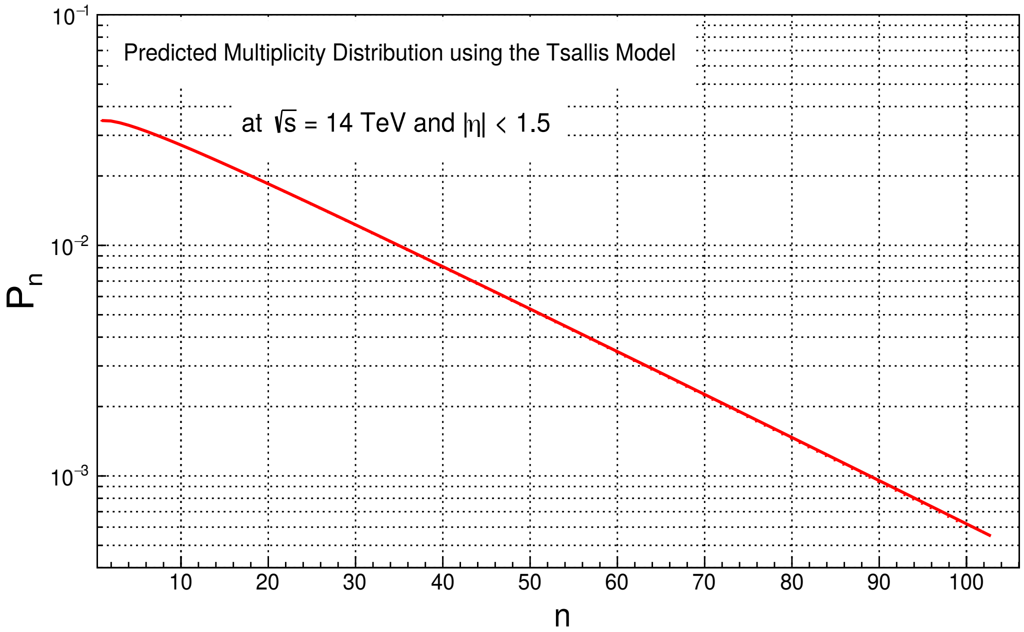

Figure 7.1: The multiplicity spectrum predicted for pp collisions at $\sqrt{s} = 14$ TeV at $|\eta| < 1.5$.

The particles produced in the final state of interactions are not independent of each other. The dynamical fluctuations arising due to random cascading processes in particle production can lead to correlations amongst the particles. The study of higher-order moments of the distribution is very important tool to understand the correlation between particles. The deviation from independent production can be understood if the factorial moments are greater or less than unity. The violation or holding of KNO scaling at higher energies can also be studied and understood correctly by using the normalized moments. The KNO scaling implies the energy independence of these moments whereas energy dependence of these moments implies KNO scaling violation. Moreover the energy dependence of higher-order moments has been used to improve or reject different Monte Carlo and statistical models of particle production. The normalised and factorial moments have been calculated using the Tsallis gas model and compared with the experimental values. The obtained values of moments found to be in good agreement with the experimental values within experimental uncertainties. The values obtained from the Tsallis gas model confirm the violation of KNO scaling as observed in the experimental values at higher energies.

A detailed analysis and comparison for the charged particle multiplicity distributions for e^+e^- collisions at LEP II energies from $\sqrt{s} = 91$ to 206 GeV has been done using the NBD, Gamma, Shifted Gamma, Weibull and Tsallis gas model. The two component model which is associated with the two jet and multi-jet production has also been implemented to describe the multiplicity distribution. It has been observed that the Tsallis model and Gamma distribution provide the best description for the experimental data and are successful at each energy with $CL > 0.1$ %. Use of two component model improves the predictions of all the models to explain the experimental data. Weibull distribution which fails to justify the experimental data becomes successful with the use of two component approach. The average multiplicity predicted by the Tsallis model at $\sqrt{s} = 206.2$ GeV is in good agreement with the experimental value and is found to be, $< n >_{TS}$ $\mathbf{= 27.38 \pm 0.20}$ compared to the L3 experimental values of $< n >_{L3}$ $\mathbf{= 28.09 \pm 0.33}$. q, the entropic index, of Tsallis statistics in each case is found to be more than 1 and increases very weakly with the energy. The mean values of q of the Tsallis model and q_1, q_2 of the two component approach are calculated, and found to be;

Tsallis: $< q > \mathbf{= 1.388 \pm 0.095}$

Modified Tsallis: $< q_1 > \mathbf{= 1.077 \pm 0.017}$ and $< q_2 > \mathbf{= 1.489 \pm 0.100}$

We have also analysed the experimental data on multiplicity distributions of particles produced in the interactions of proton with emulsion nuclei at incident energies between $P_{Lab} = 27$ GeV to 800 GeV and interaction of pion with emulsion nuclei at $P_{Lab} = 50$, 200, 340 and 525 GeV. The data have been compared with the various models and the Tsallis model is found to be best amongst all in describing the experimental data with $CL > 0.1$ %. The average multiplicity predicted by the Tsallis model at $P_{Lab} = 525$ GeV is found to be, $< n >_{TS}$ $\mathbf{= 15.36 \pm 0.80}$ compared to the experimental values of $< n >_{\pi-Em}$ $\mathbf{= 15.93 \pm 0.22}$ whereas in case of proton emulsion interactions the $< n >$ using the Tsallis model at $P_{Lab} = 800$ GeV is found to be $< n >_{TS}$ $\mathbf{= 19.59 \pm 0.63}$ compared to the experimental value of $< n >_{p-Em}$ $\mathbf{= 20.02 \pm 0.29}$. For the Tsallis model the non-extensive parameter q in every case is found to be greater than 1 and increases linearly with increase in energy, P_{Lab}. This linear increase can be described well using the relations described below;

$$q_{p-Em} = P_{Lab}(0.0009747 \pm 2.691\mathrm{e}^{-05}) + (0.9755 \pm 0.002216)$$

$$q_{\pi-Em} = P_{Lab}(0.0003557 \pm 2.738\mathrm{e}^{-05}) + (0.9885 \pm 0.004729)$$

Another important feature of multiparticle states in high energy interactions is evolution of mean charged multiplicity with energy. In the present analyses it is observed that dependence of average charged multiplicity can be described well using an empirical relation, $< n > = a + b \ln\sqrt{s} + c \ln^2 \sqrt{s}$ for hadronic and leptonic interactions whereas it follows power law in the case of lower P_{Lab} energies $< n > = a\ P_{Lab}^b$.

In the present study it has been observed that the Tsallis Model is the best in describing the experimental data at both lower and higher energies in all kinds of interactions. The success of the Tsallis model points us towards the predominance of non-extensive behaviour of entropy as we go towards the higher energies. Our various analyses results on hadronic, leptonic and hadron-nucleus interactions have been published in the international journals like *Physical Review D* and *International Journal of Modern Physics E.* The complete list of the publications is provided at the end of this chapter.

Thus study of multiplicity distributions, their moments and dependence of average multiplicity on the energy provide the interesting features of particle production and help us in understanding the mechanism of particle production at higher energies. When the data at higher LHC energies at $\sqrt{s} > 13$ TeV will become available in future it will be interesting to test the behaviour of these models which may highlight the better and new aspects of particle production mechanism.

List of Publications/Conferences

- **Papers in International Journals**

  1. S. Sharma and M. Kaur, "Multiplicity spectra in *pp* collisions at high energies in terms of Gamma and Tsallis distributions", Phys. Rev. D **98**, 034008 (2018)
  2. S. Sharma, M. Kaur and S. Thakur, "Statistical Hadronisation in High Energy Particle Collisions", Springer Proc. Phys. **203**, 771 (2018)
  3. S. Sharma, M. Kaur and S. Thakur, "Modified Tsallis and Weibull distributions for multiplicities in e^+e^- collisions", Phys. Rev. D **95**, 114002 (2017)
  4. S. Sharma, M. Kaur and S. Thakur, "Statistical hadronization and multiplicities in high-energy hadron-nucleus collisions", Int. J. Mod. Phys. E **26**, 1750006 (2017)
  5. S. Sharma, M. Kaur and S. Kaur, "Tsallis nonextensive entropy and the multiplicity distributions in high energy leptonic collisions", Int. J. Mod. Phys. E **25**, 1650041 (2016)

- **Papers presented in Conferences, Workshops and Symposiums**

  1. S. Sharma et al., "Multiplicity Distributions at LHC energies for p-p Collisions in Tsallis q-statistics", **12th Chandigarh Science Congress, CHASCON 2018**, 12-14 February, 2018, Panjab University, Chandigarh, India.
  2. S. Sharma et al., "Statistical Hadronisation in High Energy Particle Collisions", **XXII DAE-BRNS High Energy Physics Symposium 2016**, 12-16 December, 2016, Delhi, India.

3. S. Sharma et al., “Generalised Tsallis Distributions in Leptonic & Hadron-Nucleus Collisions”, **International Workshop on Frontiers in Electroweak Interactions of Leptons and Hadrons**, 2-6 November, 2016, Aligarh, India
4. S. Sharma et al., “Non-Extensivity of Entropy in Multiparticle Production at High Energy”, **3rd IAPT National Student Symposium on Physics**, 17-19 September, 2015, Chandigarh, India

- **Conferences, Schools and Workshops attended**

1. **9th International Workshop on Multiple Partonic Interactions at the LHC**, 11-15 December 2017, Shimla, India
2. **Workshop on Physics at LHC Run II**, August 26-28, 2016, Saha Institute of Nuclear Physics, Kolkata, India
3. **X SERC School on Experimental High Energy Physics**, April 19 to May 09, 2016, Department of Physics and Astrophysics, University of Delhi, India
4. **National School cum Workshop in Accelerator Physics**, March 15-18, 2016, Department of Physics, Panjab University, Chandigarh, India

- **CMS Publications** [1]

1. CMS Collaboration, “Studies of $\mathrm{B}^{*s2}(5840)^0$ and $\mathrm{B}_{s1}(5830)^0$ mesons including the observation of the $\mathrm{B}^{*s2}(5840)^0 \to \mathrm{B}^0\mathrm{K}^0_\mathrm{S}$ decay in proton-proton collisions at $\sqrt{s} = 8\,\mathrm{TeV}$,” Eur. Phys. J. C **78**, no. 11, 939 (2018)
2. CMS Collaboration, “Performance of reconstruction and identification of τ leptons decaying to hadrons and ν_τ in pp collisions at $\sqrt{s}$ = 13 TeV”, JINST **13**, no. 10, P10005 (2018)
3. CMS Collaboration, “Search for physics beyond the standard model in high-mass diphoton events from proton-proton collisions at $\sqrt{s}$ = 13 TeV”, Phys. Rev. D **98**, no. 9, 092001 (2018)

---

[1] I am a co-author of more than 100 Journal Articles with the Collaboration. The full list of publications can be found at http://inspirehep.net/search?ln=en&ln=en&p=exactauthor %3AS.Sharma.15&of=hb&action_search=Search&sf=earliestdate&so=d&rm=&rg=250&sc=0e CMS Collaboration

4. CMS Collaboration, “Charged-particle nuclear modification factors in XeXe collisions at $\sqrt{s_{\mathrm{NN}}} = 5.44$ TeV,” JHEP **1810**, 138 (2018)
5. CMS Collaboration,“Observation of Higgs boson decay to bottom quarks”, Phys. Rev. Lett. **121**, no. 12, 121801 (2018)
6. CMS Collaboration, “Search for a charged Higgs boson decaying to charm and bottom quarks in proton-proton collisions at $\sqrt{s} = 8$ TeV”, JHEP **1811**, 115 (2018)
7. CMS Collaboration,‘Search for long-lived particles with displaced vertices in multijet events in proton-proton collisions at $\sqrt{s}$ =13 TeV”, Phys. Rev. D **98**, no. 9, 092011 (2018)
8. CMS Collaboration,“Searches for pair production of charginos and top squarks in final states with two oppositely charged leptons in proton-proton collisions at $\sqrt{s} = 13$ TeV”, JHEP **1811**, 079 (2018)
9. CMS Collaboration, ‘Measurements of the differential jet cross section as a function of the jet mass in dijet events from proton-proton collisions at $\sqrt{s} = 13$ TeV”, JHEP **1811**, 113 (2018)
10. CMS Collaboration, “Precision measurement of the structure of the CMS inner tracking system using nuclear interactions”, JINST **13**, no. 10, P10034 (2018)
11. CMS Collaboration, “Measurement of charged particle spectra in minimum-bias events from protonproton collisions at $\sqrt{s} = 13\,\mathrm{TeV}$”, Eur. Phys. J. C **78**, no. 9, 697 (2018)
12. CMS Collaboration,“Search for the decay of a Higgs boson in the $\ell\ell\gamma$ channel in proton-proton collisions at $\sqrt{s} = 13$ TeV”, JHEP **1811**, 152 (2018)
13. CMS Collaboration, “Search for dark matter produced in association with a Higgs boson decaying to $\gamma\gamma$ or $\tau^+\tau^-$ at $\sqrt{s} = 13$ TeV”, JHEP **1809**, 046 (2018)
14. CMS Collaboration, “Observation of the Z$\rightarrow \psi\ell^+\ell^-$ decay in pp collisions at $\sqrt{s} = 13$ TeV”, Phys. Rev. Lett. **121**, no. 14, 141801 (2018)
15. CMS Collaboration,“Search for resonant pair production of Higgs bosons decaying to bottom quark-antiquark pairs in proton-proton collisions at 13 TeV”, JHEP **1808**, 152 (2018)

16. CMS Collaboration, "Search for a singly produced third-generation scalar leptoquark decaying to a τ lepton and a bottom quark in proton-proton collisions at $\sqrt{s} = 13$ TeV", JHEP **1807**, 115 (2018)
17. CMS Collaboration,"Search for pair-produced resonances each decaying into at least four quarks in proton-proton collisions at $\sqrt{s} = 13$ TeV", Phys. Rev. Lett. **121**, no. 14, 141802 (2018)
18. CMS Collaboration, "Measurement of the weak mixing angle using the forward-backward asymmetry of Drell-Yan events in pp collisions at 8 TeV", Eur. Phys. J. C **78**, no. 9, 701 (2018)
19. CMS Collaboration,"Search for narrow and broad dijet resonances in proton-proton collisions at $\sqrt{s} = 13$ TeV and constraints on dark matter mediators and other new particles", JHEP **1808**, 130 (2018)
20. CMS Collaboration, "Search for beyond the standard model Higgs bosons decaying into a $\mathrm{b\overline{b}}$ pair in pp collisions at $\sqrt{s} = 13$ TeV", JHEP **1808**, 113 (2018)
21. CMS Collaboration,"Search for new physics in dijet angular distributions using protonproton collisions at $\sqrt{s} = 13$ TeV and constraints on dark matter and other models", Eur. Phys. J. C **78**, no. 9, 789 (2018)
22. CMS Collaboration,"Evidence for associated production of a Higgs boson with a top quark pair in final states with electrons, muons, and hadronically decaying τ leptons at $\sqrt{s} = 13$ TeV", JHEP **1808**, 066 (2018)
23. CMS Collaboration, "Measurements of differential cross sections of top quark pair production as a function of kinematic event variables in proton-proton collisions at $\sqrt{s} = 13$ TeV", JHEP **1806**, 002 (2018)
24. CMS Collaboration,"Electroweak production of two jets in association with a Z boson in protonproton collisions at $\sqrt{s} = 13$ TeV", Eur. Phys. J. C **78**, no. 7, 589 (2018)
25. CMS Collaboration,"Search for Physics Beyond the Standard Model in Events with High-Momentum Higgs Bosons and Missing Transverse Momentum in Proton-Proton Collisions at 13 TeV", Phys. Rev. Lett. **120**, no. 24, 241801 (2018)